Abrasion and Friction in Parallel-lay Rope Terminations.

Ian Fraser BROWN

Dissertation submitted to the University of Cambridge

in partial fulfilment of the requirements for the

Degree of Doctor of Philosophy.

Examiners

Professor K. L. Johnson, University of Cambridge

Professor M. A. Crisfield, Imperial College, London

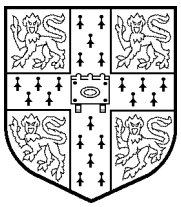

St. John's College

March 1997

Abrasion and Friction in Parallel-lay Rope Terminations.

Ian Fraser Brown.

Summary.

Ropes made from parallel aramid yarns have been used for many years due to their light weight, good electrical properties and utilisation of the material's stiffness. The standard termination for these parallel-lay ropes is a "spike-and-barrel" developed by the rope manufacturer. The terminations perform very well under static loading but fail due to abrasion of the rope near the nose of the spike when exposed to cyclic stresses.

Spike-and-barrel terminations for parallel-lay ropes are much more complex than they first appear. The functioning of the termination is heavily influenced by geometry, the material properties of both the termination and fibre, and the frictional properties. Any alteration to one of these factors alters the behaviour of the whole termination. Over their 25 year history, Parafil terminations have evolved into a sophisticated design which works well most of the time. To improve on their performance this study has looked inside the terminations and exposed hitherto unknown mechanisms and processes of slip and wear.

No straightforward analysis is possible because the simplifying assumptions mask the subtleties of the design. The use of a modified Howell's equation for friction, $\tau = a\sigma^{\beta}$, is proposed here as a valid means of modelling the friction between polymeric materials. This re-expression in terms of stress, enables its use in a finite element analysis. Experiments on Kevlar 49 yarns over aluminium capstans were performed to determine the stick and slip coefficients of friction. Experiments on pads of 1000 yarns were also performed to determine the non-linear transverse stress-strain properties of Kevlar 49. Two sets of transverse moduli can be derived, one for first-loading, and a much stiffer set for unloading-reloading. This data is integrated into the analysis via subroutines written by the engineer.

Using the Kevlar 49-on-aluminium abrasion tests performed here, a general formula has been devised for lifetime, in terms of contact pressure, amplitude of slip and thickness to be abraded. This formula is coupled with the calculated severities in 6 and 60 tonne terminations, to predict lifetimes for ropes under various cyclic regimes. These predictions are very close to those reported in the literature.

The predictions from the finite element model compare favourably with strain-gauge and displacement readings measured here on an actual 60 tonne spike-and-barrel termination; so this work, which focussed on understanding behaviour, can be extended to optimise the design in terms of materials and geometry for bigger and longer lasting ropes.

The design procedures developed in this work, may be used as a model for the development of similar procedures for terminations for other very high strength materials.

Keywords: parallel-lay ropes, Parafil, Kevlar, friction, abrasion, aramid, non-linear, finite element, Abaqus, Howell.

Declaration.

Except for commonly understood knowledge and generally accepted concepts, or where specific reference has been made to the work of others, the content of this dissertation is my own original work and includes nothing which is the outcome of work done in collaboration.

This work was carried out in the Engineering Department of the University of Cambridge between October 1990 and March 1997. It has not been submitted previously, in part or in whole, to any University or Institution for any degree, diploma, or other qualification.

The full length of this dissertation is 52,000 words.

Acknowledgements.

I would like to thank my supervisor, Dr. Chris Burgoyne, for his advice and guidance during my period of research, and a special thank you to Dr. Earl Lancaster for the constructive proof reading of this thesis.

My appreciation to all the technical staff of the Structures Research Laboratory; especially to Martin Touhey for helping with the preparation and testing of the 60 tonne ropes, and to Roger Denston for his help and advice with the small scale experiments and his expert knowledge of strain-gauging and instrumentation.

My thanks to the Science and Engineering Research Council for the initial funding, and to Derek Kingston of Linear Composites Limited for generously donating the materials used.

I am indebted to my family for their untiring support, emotionally and financially, and to all my friends.

Nomenclature.

A	contact area, or a constant.
a	ratio of τ to σ^β for modified Howell's friction.
a_d a_s	dynamic and static ratios of τ to σ^β.
a_o	amplitude of cycle between bodies in contact.
$\hat{a_o}$	normalised amplitude of cycle $= a_o/d$.
B	a constant.
C	ratio involved with the asperity contact area.
C_{qp}	stiffness matrix relating the stresses σ_q to strains ϵ_p with $p = 1, 2...6$ and $q = 1, 2...6$.
c	clearance for zero pressure.
d	yarn diameter.
E	Young's modulus.
E_1 E_2 E_3	moduli in the 1, 2 and 3 directions.
E11	separation of the surfaces, in the normal direction.
E12	relative tangential displacement of the surfaces.
E_L E_T	longitudinal and transverse moduli of the fibre.
F	frictional force.
G	shear modulus, $G = E/2(1+\nu)$
G_{12} G_{13} G_{23}	shear moduli between the 1-2, 1-3 and 2-3 directions.
G_{LT}	longitudinal shear modulus of the fibre.
h	over-closure between the two surfaces, or thickness of material.
I	second moment of area.
K	ratio of F to N^β for Howell's friction.
k K_0 K_1 K_2	constants.
k_s	stiffness in stick, ratio of τ_{crit} to γ_{crit}.
l	a length.
M	bending moment.
N	normal force, or number of cycles to failure.

$n_1\ n_2\ n_3$	indices in abrasion equation.
p^0	contact pressure at zero clearance.
Q	size of the rope in tonnes.
R	radius of disc.
$r\ r_i\ r_o$	radius, inner radius, outer radius.
S	shear breaking strength of asperities
S11	pressure transmitted between the contact surfaces.
S12	shear stress transmitted between the contact surfaces.
S_{pq}	compliance matrix relating stresses σ_q to strains ϵ_p
	with $p = 1, 2...6$ and $q = 1, 2...6$
T	tension in yarn.
T_i	incoming yarn tension, the side moving in towards the contact zone.
T_o	outgoing yarn tension, the side moving out away from the contact zone.
t	'time' in the finite element analysis, or contact width
UTS	ultimate tensile strength.
W	a load.
z	length along the axis of the spiral for a given α.
β	normal force and stress are raised to the power of β for Howell's friction.
γ_1^{el}	elastic tangential slip in Abaqus.
$\overline{\gamma}_1^{el}$	elastic slip at the start of the increment, before slipping.
γ_1^{sl}	tangential slip in Abaqus.
$\gamma_{12}\ \gamma_{13}\ \gamma_{23}$	shear strains between the 1-2, 1-3 and 2-3, directions.
γ_{crit}	maximum allowable elastic slip.
$\gamma_{xy}\ \gamma_{xz}\ \gamma_{yz}$	shear strains between the x-y, x-z and y-z, directions.
Δ	change in, e.g. $\Delta\epsilon$ is the change in ϵ.
δ	thickness of material to be abraded.
$\hat{\delta}$	normalised thickness of material to be abraded, or a deflection.
	$=\delta/d$.
ϵ	strain.
$\epsilon_{11}\ \epsilon_{22}\ \epsilon_{33}$	strains in the 1, 2 and 3, directions.
$\epsilon_{xx}\ \epsilon_{yy}\ \epsilon_{zz}$	strains in the x, y and z directions.

κ	curvature.
θ	angle subtended by a yarn around a capstan,
	or distance in the hoop direction.
λ	stretch ratio, the ratio of current length to original length.
	or percentage load factor, (100×load/breaking load).
λ_{max} λ_{min}	maximum and minimum percentage load factor applied.
μ	effective coefficient of friction, ratio of frictional force to normal load.
μ_d μ_s	dynamic and static effective coefficients of friction.
ν	Poisson's ratio.
ν_{12} ν_{13} ν_{23}	Poisson's ratios between the 1-2, 1-3 and 2-3, directions.
ν_{LT}	The longitudinal Poisson's ratio of the fibre.
ν_{TT}	The transverse or in-plane Poisson's ratio of the fibre.
σ	contact stress.
$\hat{\sigma}$	normalised contact stress $=\sigma/\sigma_y$
$\overline{\sigma}$	mean contact stress in the contact zone.
σ_{11} σ_{22} σ_{33}	stresses in the 1, 2 and 3, directions.
σ_{xx} σ_{yy} σ_{zz}	stresses in the x, y and z, directions.
σ_y	yield stress.
σ_r σ_θ	radial and hoop stresses.
τ	shear stress or either frictional stress.
τ_1	shear stress in direction 1.
τ_1^{pr}	extrapolated prediction of shear stress in direction 1.
τ_{12} τ_{13} τ_{23}	shear stresses between the 1-2, 1-3 and 2-3, directions.
τ_{crit}	critical shear stress at which slipping starts.
τ_d	dynamic frictional stress.
τ_i	interface shear stress at node i.
τ_s	static frictional stress.
τ_{xy} τ_{xz} τ_{yz}	shear stresses between the $x-y$, $x-z$ and $y-z$, directions.
τ_y	shear yield stress.
ϕ	angle between principal axes and gauge axes.
ϕ_f	limiting angle of friction ($\tan^{-1}(F/N)$).
ψ	half angle of the spike.

Contents

Chapter 1

Introduction.

Ropes made from parallel Kevlar yarns have been used for many years due to their light weight, good electrical properties and utilisation of the material's stiffness. The best method found for terminating parallel-lay ropes is to clamp the rope between a spike and a barrel, as developed by Linear Composites Limited. This has the advantage that as the rope is loaded, the spike is drawn into the barrel, thereby clamping the rope even more tightly. The uses and advantages of parallel-lay Kevlar ropes are discussed in Chapter 2.

For static loading, spike-and-barrel terminations utilise 100% of the capacity of the individual yarns, although problems may arise if the termination is not assembled correctly. When the rope is subjected to cyclic loading, abrasion occurs between the rope and the termination which can ultimately lead to failure. Anomalous spike movement has also been reported when the load is increased after a period of cyclic loading. To date there has been no detailed analysis of spike-and-barrel terminations; their design has evolved via a build-it-and-see approach. This approach is not reasonable for the design of large terminations; fabrication of ropes with a breaking load of 10,000 tonnes has been proposed for the offshore industry.

Aim of this project.

The main aim of this study is to provide an insight into the workings of a parallel-lay spike-and-barrel termination. To achieve this, a finite element model was developed to follow the stresses, strains and displacements within a termination subjected to a cyclic loading history. This is compared with

strains and displacements gathered from tests performed here on an actual 60 tonne Parafil G rope. Comparisons are then drawn up between long term cyclic fatigue tests performed elsewhere and those extrapolated from yarn-on-capstan tests using the finite element model. To formulate the finite element model it was necessary to determine the bulk transverse properties of Kevlar 49, and the frictional properties of Kevlar 49-on-aluminium.

Outline of the dissertation.

Chapter 2 contains a review of parallel-lay ropes, indicating the advantages they have over the two other main types of rope construction; twisted and braided. A brief synopsis of the current applications for parallel-lay ropes is included. A discussion of alternative termination methods is presented. The advantages and problems associated with a spike-and-barrel design are explained, including literature data on the lifetimes of Parafil G ropes under cyclic loadings.

A brief literature review of friction in polymeric materials is presented in **Chapter 3**; which is then extended to propose a new formulation relating the frictional and contact stresses, $\tau = a\sigma^{\beta}$, for inclusion in the finite element modelling. Experimental results of Kevlar 49-on-aluminium performed here are presented. The associated subject of abrasion is then presented along with the experimental data gathered here for Kevlar 49-on-aluminium abrasion. A formula is fitted to this data relating the lifetime with the contact pressure, the amplitude of slip, and the thickness to be abraded.

As the spike moves further into the termination on loading, the rope is progressively compressed. In **Chapter 4**, experimental stress-strain curves for the transverse compression of pads of 1,000 yarns of Kevlar 49 are presented. A literature review of the other properties of Kevlar 49 is discussed along with the rearrangement for inclusion in the finite element model.

Chapter 5 outlines the formulation of the finite element model to use the Abaqus package, and its friction and material subroutine options. The complicated process of establishing contact between surfaces is outlined.

The results from the finite element model for a loading history including two load cycles are presented in detail in **Chapter 6**.

The finite element results are compared with the tests performed here on actual 60 tonne Parafil G ropes in **Chapter 7**. This chapter also ties up the abrasion data from Chapter 3 with the predicted severities from Chapter 6 to predict lifetimes for ropes under cyclic loading, these are compared with the literature presented in Chapter 2.

Chapter 8 contains a discussion of the various issues brought to light by this research, including avenues that may be followed to optimise the performance.

Finally, a summary of the factors involved in analysing spike-and-barrel terminations is presented in **Chapter 9**, along with recommendations for further work.

(Kevlar, Kevlar 29 and Kevlar 49 are trade names of E.I. DuPont de Nemours for aramid fibres. Kevlar 49 is stiffer than Kevlar 29. Parafil F and Parafil G are trade names of Linear Composites Ltd, for parallel-lay ropes made from Kevlar 29 and Kevlar 49 respectively.)

Chapter 2

Parallel-lay ropes

This chapter contains a review on the various types of rope available, detailing why parallel-lay ropes are the most suitable for certain engineering applications. Methods of terminating parallel-lay ropes are discussed, along with the problems that remain to be resolved with the design analysed here, the spike-and-barrel termination. The two main problems are a loss of prestress due to spike bed-down, and failure due to abrasive wear within the termination when exposed to cyclic loading.

2.1 Types of rope.

In general, ropes can be separated into three categories: twisted, braided, and parallel-lay (Figure 2.1).

The oldest form of rope is formed from a twisted construction, because this utilises short filaments. The load is transferred between filaments by friction: the filaments are forced together by the twist, generating an inter-filament pressure which increases the limiting frictional force between filaments. The disadvantages are that a torque is set up under load which tends to unravel the rope if one end is free, with subsequent kinking and looping when unloaded.

These problems are avoided in braided ropes, in which the yarns are aligned in many directions. They are very flexible but this comes at the expense of high inter-yarn abrasion when the load is cycled. Their properties are

dependent on the braid construction and braid angle. As with twisted ropes, the axial properties of braided ropes suffer from the yarns being at an angle to the rope axis. This leads to a lower rope stiffness and lower breaking stress compared with the constituent yarns.

Parallel-lay or parallel filament (Parafil) ropes were first developed in the 1960s to meet a requirement for low weight non-corrodible cables for mooring deep water platforms [Kingston, 1988], and only became feasible with the advent of continuous yarns. They contain a core of polyester or aramid (Kevlar 29 or Kevlar 49) [Linear Composites, 1977], encased in a polymeric thermoplastic sheath to maintain the rope structure and shield the aramid from the harmful effects of sunlight [Chambers, 1986]. In the future other fibres may be used, for example: the new aramids; Kevlar 149 (which has a modulus comparable to steel, 210kN/mm^2), Twaron made by Enka, and Technora made by Teijin; or others like Spectra, a high modulus polythene, and Vectran, a liquid crystal polyester [Beers and Ramirez, 1990; Dobb and Robson, 1990; Flory et al., 1990a; Kalantar and Drzal, 1990; Stidd, 1990; van Leeuwen et al., 1990]. Aramid fibres are also called polyaramid, poly aromatic amide, poly para-phenylene terephthalamide, and PPTA.

Parallel-lay ropes are torque free and do not kink. They are good for applications where creep is critical; due to the axial alignment they suffer less creep than the other two constructions. Because all the yarns are aligned axially, this type of rope has the highest strength efficiency (the ratio of the rope strength to the cumulative strength based on the individual yarns). The strength efficiency is still only 72%, however, as the weakest yarns always reduce the strength of the bundle [Amaniampong, 1992]; this figure depends on the variability of the yarns. The larger the bundle is, the lower the strength efficiency of the rope will be, as shown in Figure 2.2 [Guimarães, 1988]. The efficiencies of twisted and braided ropes are comparatively 55% and 49% respectively [Chambers, 1986].

The amount of twist in the individual yarns is set such that a trade-off is established between the fibres slipping over one another at low twist, and the fibres breaking at high twist due to an inability to share the load between the fibres [Hearle et al., 1967].

Aligning the yarns parallel to each other has the added advantage that they do not rub over each other on loading, so no inter-yarn abrasion occurs within the main body of rope. The only abrasion that occurs is within the termination, or where the path of the rope is deviated over a sheave [Burgoyne et al., 1989].

2.2 Uses of Parafil rope.

Parafil rope, made with Kevlar 49, is six times more expensive than cold drawn steel wire per tonne carried in the rope [Burgoyne, 1988], so its applications are limited to those where its lightness, ease of fabrication, and resistance to corrosion come to the fore. A number of examples follow.

2.2.1 Resistance to corrosion.

Several trial studies have been performed using Parafil as an externally prestressed tendon for concrete beams. [Burgoyne et al., 1991, Chambers, 1986; Guimarães, 1988]. No concrete cover is needed, so less concrete is required; hence a significant reduction in the dead load can be achieved when this reduction is fed back into the design. The stress in the tendon is high but constant; so abrasive wear within the termination is not a problem. However, any unpredictable spike bed-down can dramatically affect the prestress in the rope. Parafil is ideal for externally prestressing old bridges due to its light weight.

Trials have been carried out on prestressed brickwork [Garrity and Garwood, 1990; Sinha, 1990]; the low modulus of Parafil A (polyester) is an advantage here [Burgoyne, 1988]. Tests are also in progress for using Parafil ropes as ground anchors [Haji-Dehabadi and White, 1988].

2.2.2 Light weight.

In civil engineering, Parafil's lightness enables it to be 'man-handled' during construction, for example to reinforce cracked cooling towers [Burgoyne, 1988] and the ensuing increase in dead-load is minimal. Its lightness can also present cost advantages in long cable stayed and suspension bridges [Aminian and White, 1988; Burgoyne, 1988], and for cable supported roofs [De Witte, 1990; Hanaor, 1990; Schierle, 1990]. At Aberfeldy [Richmond and Sham, 1994], a footbridge across the Tay with a 63m main span has been constructed using parallel-lay Kevlar cables and a GFRP decking. Due to the low dead-load of the structure, the live-load plays a significant part in the load in the cables, imparting a large cyclic stress. This introduces the factor of abrasion in the terminations.

In electrical engineering, Parafil ropes have been used for over 30 years as insulating guys, catenaries, and support systems; their electrical inertness is also an advantage here [Linear Composites, 1977].

In marine engineering, Parafil ropes have been used for buoy moorings in 6000m deep water, for ship and yacht rigging, and for guard rails and tow ropes [Baxter, 1988; Driscoll, 1990; Linear Composites, 1977]. If water is prevented from entering the core then the rope will float due to the air surrounding the fibres.

In aeronautical engineering, parachute rigging is actively being developed from Kevlar [Peterson, 1990].

2.3 Termination design.

Regardless of the rope type, all the load in the rope has to be transferred to the anchorages via some form of termination. For Parafil ropes the most efficient and elegant solution takes the form of a spike-and-barrel design (Figure 2.3). In the current design the barrel has a 3° straight internal taper, and the spike has a more complex geometry with a taper angle of about 3.5°. High tensile steel cables have been secured between spike and barrel terminations since the work by Freyssinet in 1940 [Naaman, 1982], although these have grooves running along the length of the spike to keep the individual wire strands in position. The design was extended to parallel-lay ropes by the patent of Kingston and Mattrass [1973], replacing an earlier design which consisted of a cone and locking ring.

The other main possibility is that of a 'potted' termination; the rope splays out into a tapered barrel where it is encased in a resin. However uniformity in fabrication for such a design is very hard; even if all the fibres are uniformly coated in resin, on cycling the load much abrasion will occur where the yarns and the resin separate due to their differing stiffnesses.

Clamping the rope with external wedges that are pulled into a tapered barrel, in the manner used for steel cables [e.g. O'Brien and Dixon, 1995], cannot generate the friction necessary to take the load out of the rope uniformly over its cross section; the middle of the rope slips relative to the edges. Such relative slip also occurs in the rope between the spike and the barrel, but to a negligible degree (Chapter 6).

The static and cyclic performances of spike-and-barrel terminations will be discussed in this section.

2.3.1 Static failure.

Chambers [1986] carried out 46 ultimate load tests on straight 6 tonne Parafil G ropes: the majority of failures occurred away from the terminations. In some of the ropes the outer sheath was pulled back from a termination to reveal a few broken yarns. In one test the ultimate load was reduced (by 5%) by failure near a termination, but no failures occurred inside the terminations.

The only other static problems arise from the viscoelastic nature of the Kevlar fibres, which are susceptible to creep-rupture at high stresses [Guimarães and Burgoyne, 1996].

2.3.2 Spike bed-down.

When a Parafil rope is loaded for the first time, the spike is pulled into the barrel by the rope; it "beds-down" (Figure 7.21). If a rope is being used to prestress a concrete beam for example, then the loss of prestress caused by any additional slipping of the spike is detrimental to the beam's performance (Figure 2.4). The spike can also slip after a long period of time when the rope is subjected to a uniform load (Figure 2.5), which may be due to stress-relaxation in the transverse compression of the rope between the spike and the barrel (see Chapter 8).

If the rope is not loaded directly to failure however, but is first subjected to a cyclic regime, then when the load is increased further the spike has been observed to jump, leading to a loss of prestress. Chambers [1986] observed the spike to jump in to the barrel by about 0.3mm (Figure 2.6). Whereas here a jump backwards was observed (Figure 7.21).

Undesirable bedding-down during service can be virtually eliminated by pre-tensioning the rope to a load greater than it is expected to experience.

2.3.3 Cyclic fatigue.

Any abrasion that occurs will take place in the terminations, since the parallel yarns do not rub over each other in the main body of the rope. The abrasion within terminations is discussed in Chapter 7, whilst abrasion in general is discussed in Chapter 3.

At high stresses, creep-rupture may be a significant factor. Kenney et al. [1985] have carried out a multitude of tests on nylon fibres, yarns and small ropes, subjecting them to a cyclic axial stress. They found that their yarns and single fibres fail by a creep-rupture mode (i.e. they creep to failure) which depends on the total time that the loads are applied rather than the number of cycles. They also showed that the behaviour of other oriented fibres including polyester and aramid (e.g. Kevlar) agrees with this cumulative time under load model.

Lyons et al. (reported in [Hearle, 1967]) have shown that there are two distinct regions in the strain – cycles-to-failure curve, with extremely long lives occurring for low strains. Kenney et al. cycled across these two regions, thus masking this phenomenon.

Crawford and McTernan [1988] performed low-load cyclic tests at different frequencies, thus subjecting the ropes to different times under load. They found no discernible difference in the lifetimes. Cyclic loading at high stresses is not on the agenda for the uses in Section 2.2, so creep-rupture has not been examined further in this thesis.

2.4 Abrasion data for Parafil G ropes.

Very little data has been published for the abrasion lifetimes of Parafil ropes. Some data has been obtained for tests performed at the National Engineering Laboratory on Parafil G ropes. These include tests on 6 tonne ropes

with cyclic ranges of 5-35%, 10-50%, 25-55%, 20-60%, 10-70% [Technomare, 1996], 15-45%, 5-55% [McTernan, 1986], and 15-65% [McTernan, 1992]; and 60 tonne ropes cycled between 5-30%, 5-35%, 5-40%, 5-50%, 5-70% [McTernan, 1986a]. Here and throughout the thesis, reference to an x% load, refers to x% of the nominal breaking load of the rope (6 or 60 tonnes for the ropes considered in this thesis).

There is no overall scheme to this data, since different maximum and minimum load limits were used throughout. The data for these 6 and 60 tonne Parafil G ropes is plotted in Figure 2.7; the y-axis is taken to be the maximum load. (The ranges do not form smooth zones because the minima are different.) It is clear that the 60 tonne ropes have a much shorter lifetime than the 6 tonne ropes. This is due to the larger amplitude of abrasion that is occurring within them.

For the 6 tonne rope, the greatest lifetimes are achieved by the regimes having a 30% cycle (λ=5 to 35, 15 to 45 then 25 to 55 (where λ is the percentage ratio of load to maximum static strength)); next come the regimes with 40% cycles (λ=10 to 50 then 20 to 60) followed by 50% (λ=5 to 55 and 15 to 65) then finally the 10 to 70% cycle. This indicates that it is the amplitude of the cycle, both in terms of load and therefore slip, that is more significant than the maximum load. All the 25 to 55% tests outlived all the 10 to 50% tests, due to their smaller amplitude, despite having a greater maximum load. They also outlived the 5 to 55% tests by an order of magnitude.

2.5 Summary.

Parallel-lay Kevlar ropes will play a large part in the lightweight structures of the future once they can be specified with more confidence. This confidence will only come once the behaviour of the terminations is better understood.

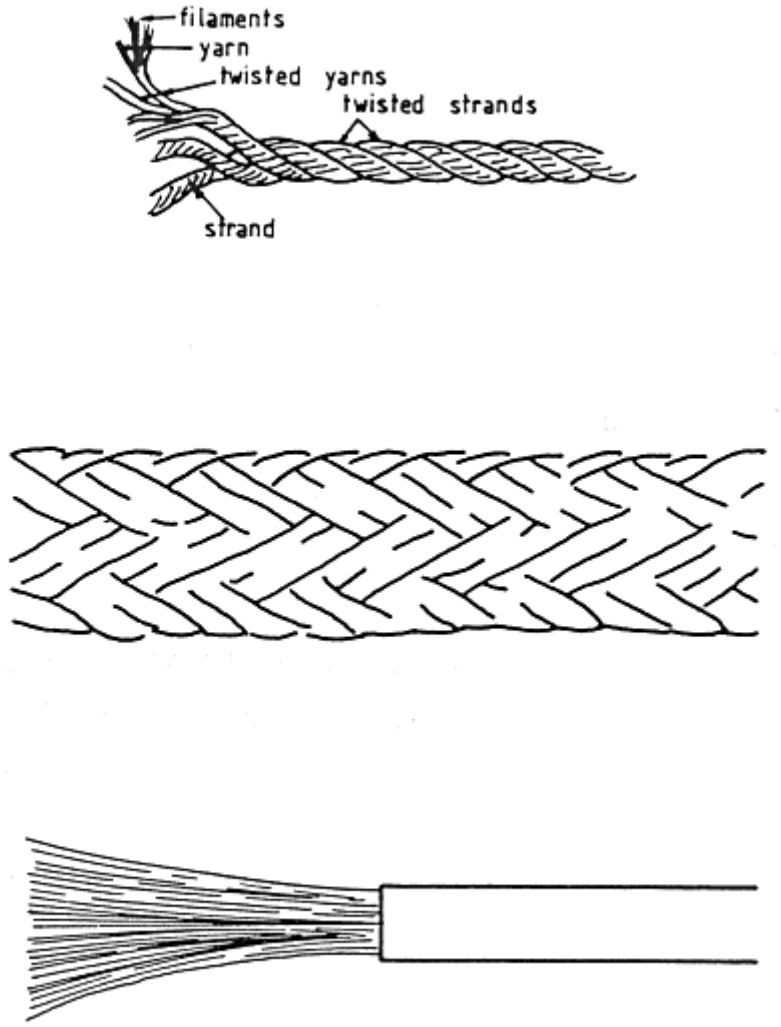

Figure 2.1: Types of rope: twisted, briaded, parallel-lay. [Chambers, 1986]

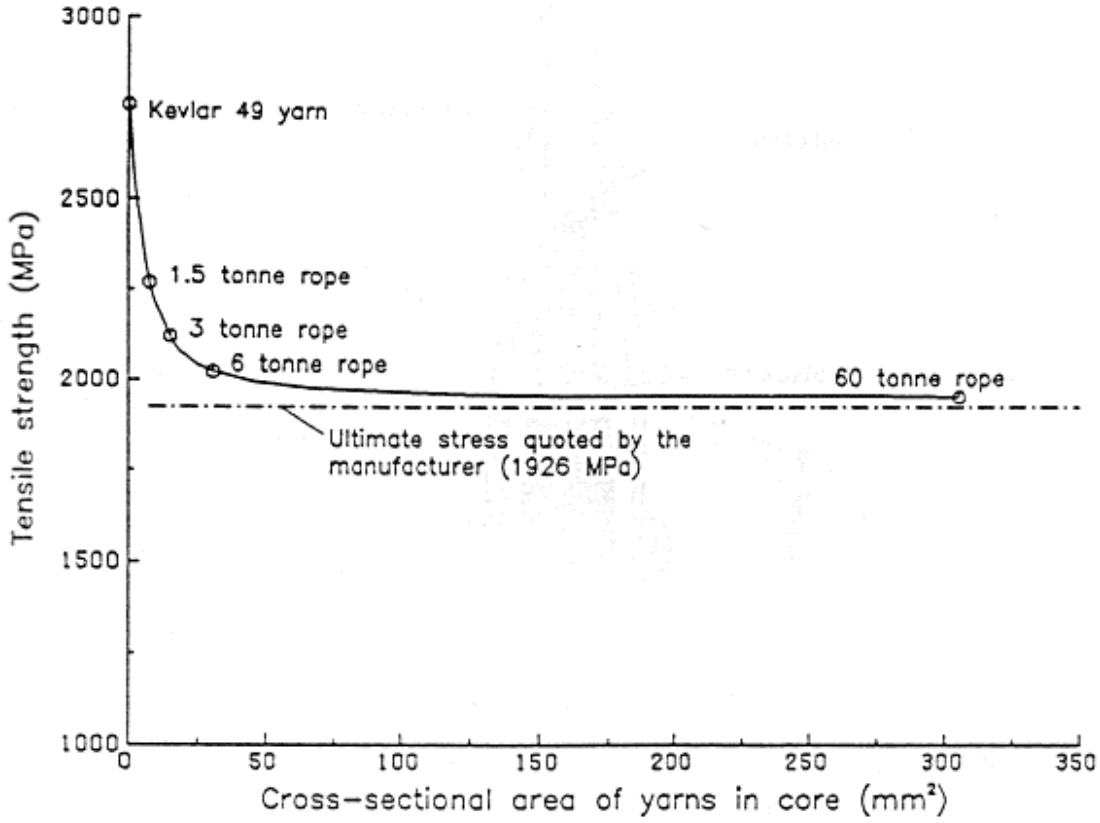

Figure 2.2: Effect of size on the tensile strength of Parafil G (Kevlar 49) rope. [Guimaraes, 1988]

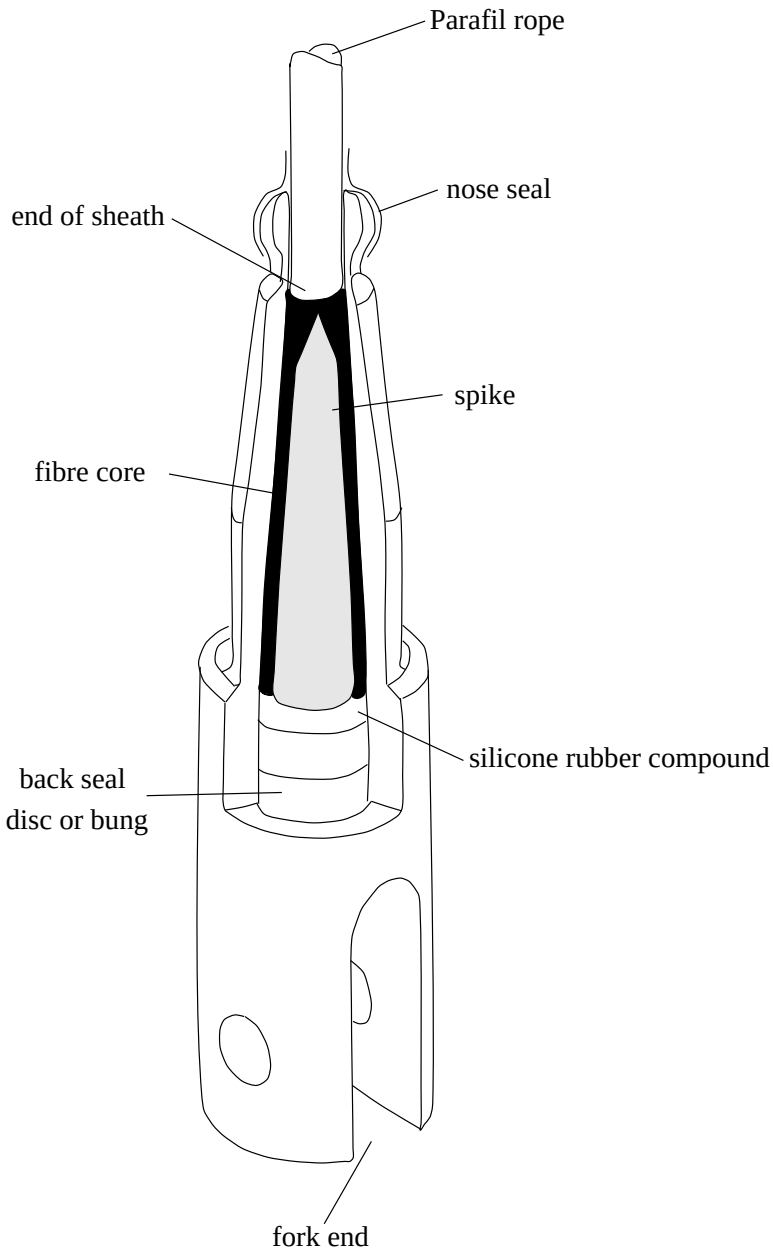

Figure 2.3: Spike-and-barrel Parafil termination. [Linear Composites, 1977]

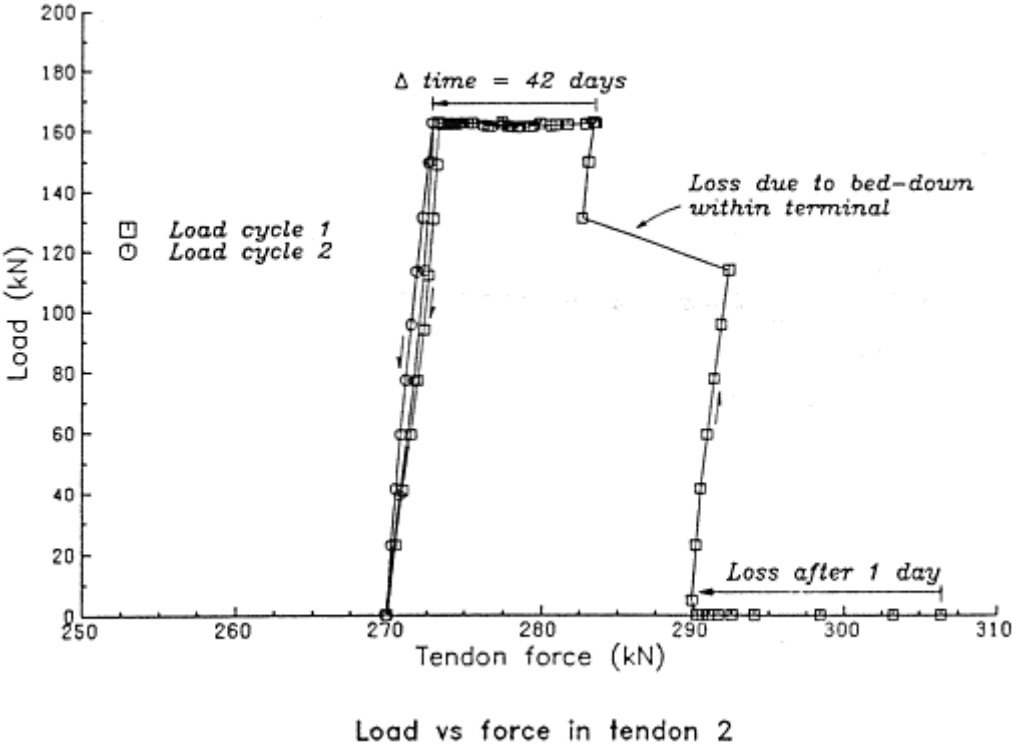

Figure 2.4: Loss of prestress due to slip of spike. [Guimaraes, 1988]

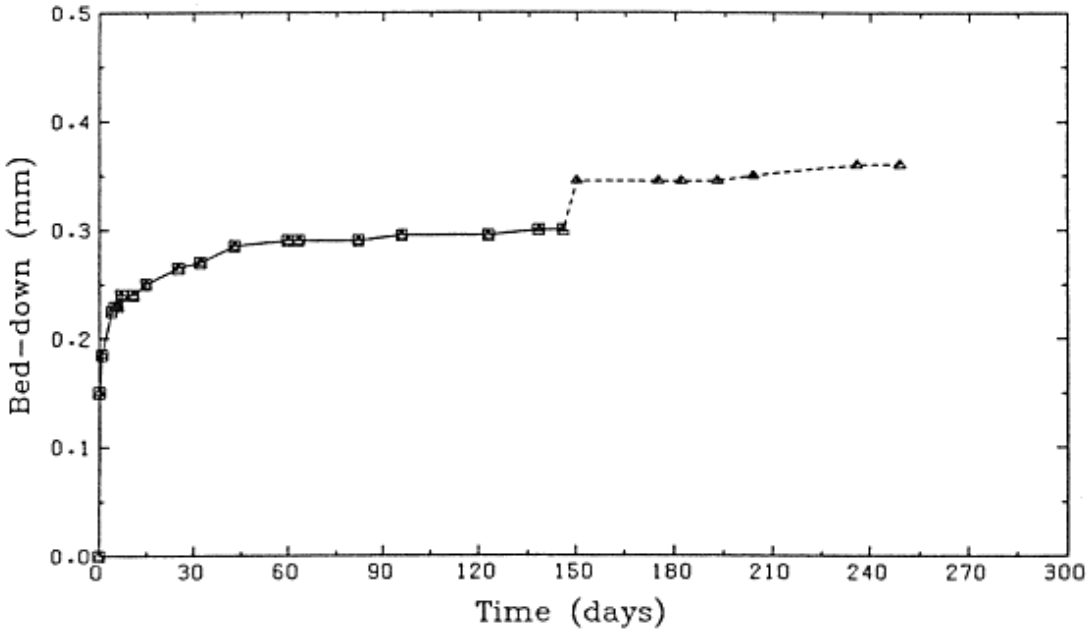

Figure 2.5: Spike bed-down within a 3 tonne Parafil G rope at 57.3% UTS. [Guimaraes, 1988]

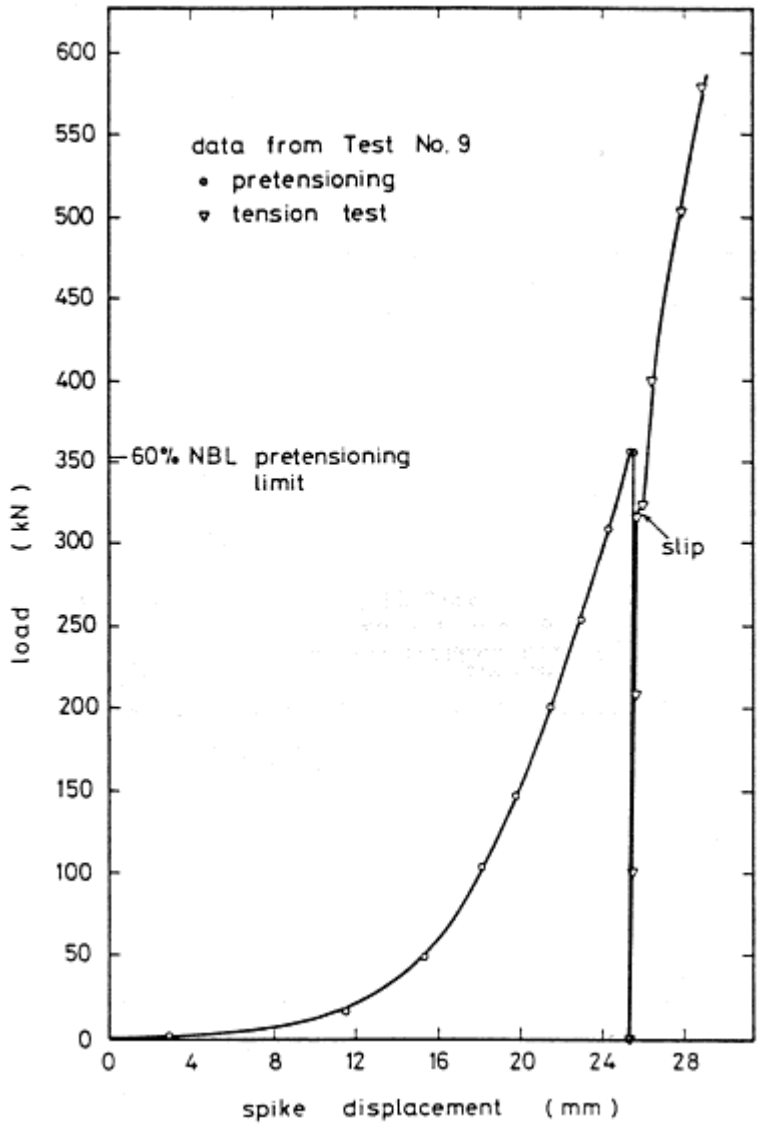

Figure 2.6: Total movement of a steel spike in a 60 tonne aluminium barrel, for Parafil G rope. The rope is pretensioned to 60%, unloaded, then reloaded to failure. On reloading to 320kN the spike jumps in by about 0.3mm. [Chambers, 1986]

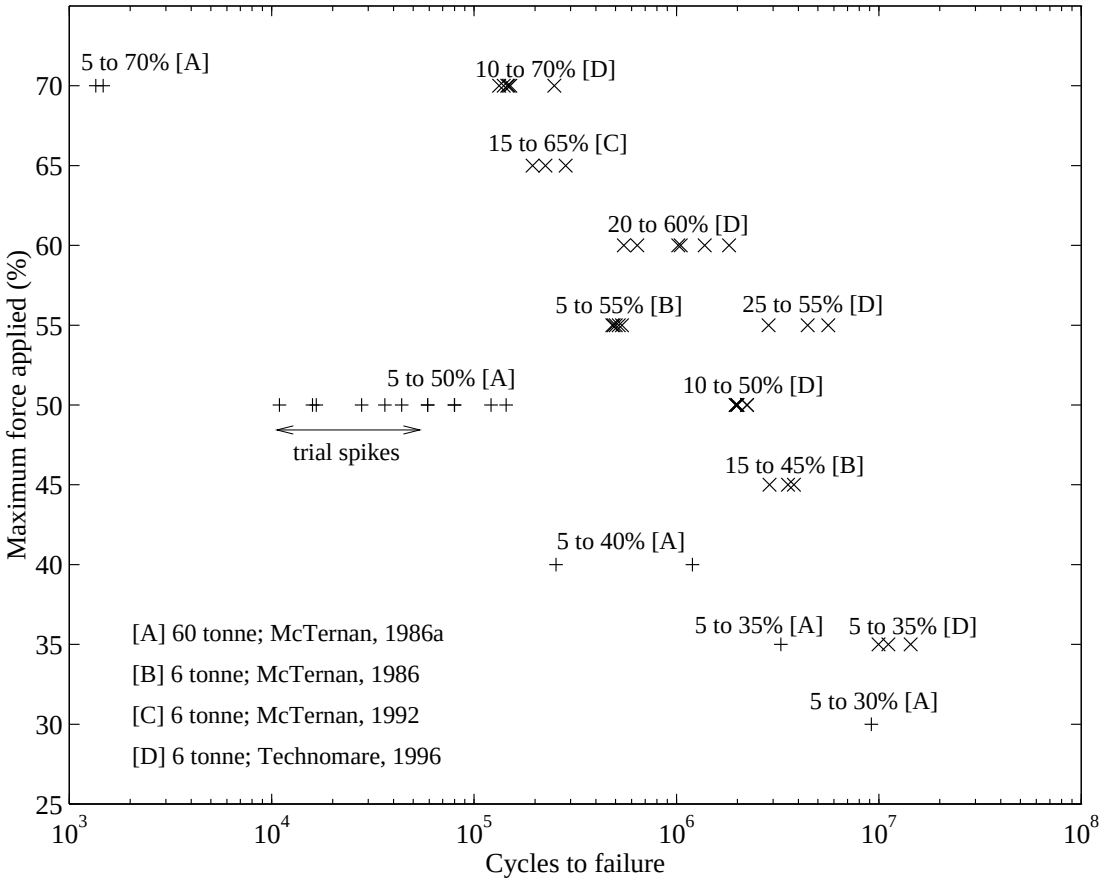

Figure 2.7: The lifetimes of 6 and 60 tonne Parafil G ropes subjected to cyclic loading.

Chapter 3

Friction and abrasion of synthetic fibres.

3.1 Introduction.

This chapter starts with a literature review on the friction that inevitably arises when two surfaces slide over one another. In particular the friction of polymers is discussed. Experimental data gathered here for Kevlar 49-on-aluminium friction is then presented, along with a frictional stress – contact pressure relationship for use in the finite element model. The chapter then moves on to polymer abrasion and concludes with an analysis of Kevlar 49-on-aluminium abrasion, presenting a model relating the lifetime to the severity, based on experiments performed here. This relationship is later used in Chapter 7 to accurately predict the lifetimes of full size ropes under cyclic loading.

3.2 Friction.

3.2.1 Classical friction.

In 1699, Amontons rediscovered Leonardo da Vinci's two laws of friction: the frictional force is directly proportional to the normal load, and the size

of the bodies does not affect the friction [Bowden and Tabor, 1950; 1974]. Desaguliers introduced the idea that adhesion also plays a part, which was later verified by Coulomb. The surface of any solid, no matter how polished, has many asperities sticking out (Figure 3.1). It is these asperities that make contact with the other surface: "putting two solids together is rather like turning Switzerland upside down and standing it on Austria – the area of intimate contact will be small." [Bowden and Tabor, 1974]

When two metal surfaces are brought together the area of asperity-to-asperity contact is extremely small so the pressure is very high. Even at small contact loads plastic deformation occurs at the asperities, while the underlying metal still deforms elastically. As the normal load is increased the asperities deform and fracture, thus increasing the real area of contact, the sum of all the surface irregularities that touch and support the load. This is much less than the apparent area which remains unchanged. Use of the usual assumption that the local plastic yield pressure σ_y is constant, gives the real area of contact for one asperity under a load N_i to be $A_i = N_i/\sigma_y$, so the total real contact area is:

$$A_r = A_1 + A_2 + ...A_i = \frac{N_1}{\sigma_y} + \frac{N_2}{\sigma_y} + ...\frac{N_i}{\sigma_y} = \frac{N}{\sigma_y} \tag{3.1}$$

where N is the total normal force. Hence, for a metal, the real area of contact is proportional to the load and independent of the size of the surfaces.

To shear these two bodies apart by sliding, a force $F = S\,A$ is needed, where S is the shear breaking strength of the contacts. Hence $F = S\,N/\sigma_y = \mu N$ and hence Amontons' law.

Assuming a von Mises yield surface $((\sigma_{11} - \sigma_{22})^2 + (\sigma_{22} - \sigma_{33})^2 + (\sigma_{33} - \sigma_{11})^2 = 2\sigma_y^2)$ gives $S = \sigma_y/\sqrt{3}$. Alternatively, assuming a Tresca yield surface $(max[|\sigma_{11}-\sigma_{22}|, |\sigma_{22}-\sigma_{33}|, |\sigma_{33}-\sigma_{11}|] = \sigma_y)$ gives $S = \sigma_y/2$. (From a Mohr's circle for simple shear, $\sigma_{11} = S$ and $\sigma_{22} = -S$.) Experimental data on metals fall between the two surfaces, but in general are closer to the von Mises yield surface [e.g. Lu, 1996]. Assuming pure metal on metal contact and a von Mises yield surface would lead to $\mu = 1/\sqrt{3} = 0.58$.

Most metal surfaces are covered by a thin film of oxide, water vapour and other absorbed impurities. Where the asperities contact, the metal surfaces weld together to form junctions. The shear strength of these junctions is heavily dependent on the shear strength of the surface films. Thus it is the surface oxide layer that determines the coefficient of friction and not, in general, the parent metal [Ashby and Jones, 1980].

If the actual area of contact is increased, for example by heating the metals in a vacuum [Bowden and Tabor, 1974] (or by applying a large electric field for nylon on glass [Bradbury and Reicher, 1952]), then the coefficient of friction can be increased by an order of magnitude. Table 3.1 from Ashby and Jones [1980] lists ranges of μ for various materials.

3.2.2 Friction of polymers.

When either or both of the surfaces are polymers, Equation 3.1 no longer applies. Polymers deform viscoelastically: the deformation depends not only on the normal load N but also on the geometry and time of loading. With fixed geometry and duration of loading, the area of true contact is proportional to N^{β} where $\frac{2}{3} \leq \beta \leq 1$. For a truly elastic solid (for example rubber), $\beta = \frac{2}{3}$ [Lincoln, 1952].

From Figure 3.2 for $\beta = \frac{3}{4}$ (typical for a hard sphere on a Plexiglas surface), a 16-fold increase in load from 1 to 16 pounds produces an 8-fold increase in frictional force, hence the coefficient of friction is halved. This is a general feature of polymers; the effective coefficient of friction reduces at higher loads.

Howell and Mazur [1953] performed some of the first experiments to study the effect that the elastic behaviour of the asperity-to-asperity contact has on the nature of sliding for polymeric materials. The stress-strain curves of three hypothetical materials are shown in Figure 3.3. The dashed lines represent the stress range in the contacting asperities. The asperities of material (a) deform plastically, so Amontons' law applies. The asperity-to-asperity

contact in material (b) is elastic; so the true asperity-on-asperity contact area will be of the form $CN^{2/3}$ where C involves the modulus and dimensions of the asperities, hence $F = SCN^{2/3}$ (where S is the shear breaking strength). Increasing the normal stress would cause plastic deformations as for material (a).

For material (c) the deformation of the asperity contact starts with a linear elastic region followed by a gradual yield; the true asperity-on-asperity contact area is thus likely to lie between the bounds of materials (a) (plastic $A \propto N$) and (b) (elastic $A \propto N^{2/3}$). Therefore a possible equation for the friction could be the empirical one, $F = KN^{\beta}$, where $\frac{2}{3} \leq \beta \leq 1$. Most synthetic polymers used in ropes correspond most closely to material (c) where the actual mechanism of asperity deformation is indeterminate.

The relationship $F = KN^{\beta}$ fits Howell and Mazur's test results very well; some of their results are shown in Table 3.2 and Figure 3.4.

Howell's equation for friction can be re-written as $F = (KN^{\beta-1})N$, where $(KN^{\beta-1})$ is the "equivalent coefficient of friction". For use in the finite element analysis it was decided that expressing this relationship in terms of stresses would make modelling possible. Therefore, it is proposed here that Howell's equation can be re-expressed as; $\tau = a\sigma^{\beta}$, where τ is the frictional stress, σ is the contact pressure, and a and β are frictional constants.

Due to the viscoelastic properties of polymers, when a polymer is in contact with another surface for a period of time, the asperities start to creep under the normal load. This increases the actual area of contact, thereby increasing the frictional limit. This creep explains why contact involving polymers typically has a greater difference between static and dynamic coefficients of friction, than for metal-to-metal contact.

3.2.2.1 Summation of friction components.

An alternative view of friction is put forward by Kragelsky et al. [1982]. They support the hypothesis that the coefficient of friction is the sum of two terms; molecular and mechanical, i.e.;

$$\mu = \mu_{molecular} + \mu_{mechanical} \tag{3.2}$$

Molecular interaction processes take place in the surface 'film' and affect the surface layers to a depth of a few hundredths of a micron. Mechanical interaction takes place in layers with a thickness of a few tenths of a micron. As these processes occur at different levels they are largely uncorrelated and hence can be separated.

This equation suggests a very complex relationship between the normal load and the coefficient of friction; both components of μ include a pressure term, as well as extra terms for the hysteresis loss during sliding, the surface roughness, and the strength of the molecular bond, amongst others.

The additional complexity of Kragelsky's model does not seem justified; Howell's equation has been shown to adequately represent experimental data. Therefore a modified Howell's equation, $\tau = a\sigma^{\beta}$, is used.

3.2.2.2 Effect of spin finish on friction.

Spin finish is a surface coating, added to the fibres during manufacture, for the purpose of gluing together the fibres during the processing of the yarn [Piller, 1973]. This prevents them being snagged by the guides and thus being broken or drawn out of the yarn. The finish also evens out, and so improves, the running properties and friction coefficients, as well as removing any electrostatic charge; these keep the draw-off conditions as even as possible.

Yarn sizes are also used; these coat the yarn with a protective film to reduce the abrasion damage during processing and service.

By selecting the right finish, the abrasion resistance of the yarn can be increased [Beers and Ramirez, 1990; Crawford and McTernan, 1988; Schick, 1975, 1977]. The yarns used in the tests referred to in this chapter are from spools used to make Parafil ropes and so carry the finishes present in actual ropes.

3.3 Kevlar-on-aluminium friction.

Very little published data is available on the coefficients and indices of friction between Kevlar and itself, and between Kevlar and other materials. To model the friction in spike-and-barrel terminations for Parafil ropes, data for Kevlar-on-aluminium contact has been measured as detailed in this section.

3.3.1 Measurement of yarn-on-capstan friction.

The simplest method of measuring the friction between a yarn and a solid is by the **capstan method**. Here the yarn is pulled over a cylinder of radius R through an angle θ and the end tensions measured (Figures 3.5 and 3.6). Amontons' law leads to [see for example, Meredith and Hearle, 1959]:

$$T_o = T_i \, \mathrm{e}^{\,\mu\,\theta} \tag{3.3}$$

which is often referred to as the capstan equation and is independent of R. T_i, the incoming tension, is the tension in the yarn entering the contact zone, between the weights and the capstan. T_o, the outgoing tension, is the tension in the yarn leaving the capstan, between the capstan and the tensometer. μ is the coefficient of friction.

Howell's [1953] equation ($F = KN^{\beta}$) leads to:

$$T_o^{1-\beta} = T_i^{1-\beta} + (1-\beta)\, K\, \theta\, R^{1-\beta} \tag{3.4}$$

Thus the radius of the capstan now comes into the equation [Lyne, 1955]. If a modified Howell's equation $\tau = a\sigma^{\beta}$ is used then an alternative equation

can be derived. (Note: β is a dimensionless index, but a has dimensions of $(\mathrm{FL}^{-2})^{(1-\beta)}$. Therefore care must be taken if the units of σ are changed, as this will change the value of a.)

Consider a small element of yarn subtending an angle $\mathrm{d}\theta$ around a capstan, as shown in Figure 3.5. The radius is R, the contact width is t, the contact pressure is σ, and the frictional stress is $\tau = a\sigma^{\beta}$. A resolution of forces along the yarn gives:

$$a\sigma^{\beta} t R \mathrm{d}\theta = \mathrm{d}T \tag{3.5}$$

Resolving perpendicular to the contact surface gives:

$$2T\frac{\mathrm{d}\theta}{2} = \sigma t R \mathrm{d}\theta \tag{3.6}$$

Eliminating σ from these two equations gives:

$$a t^{1-\beta} R^{1-\beta} \mathrm{d}\theta = \frac{1}{T^{\beta}} \mathrm{d}T \tag{3.7}$$

This can be integrated between $\theta = 0$ to θ, and $T = T_i$ to T_o, yielding:

$$T_o^{1-\beta} = T_i^{1-\beta} + (1-\beta)\, a\, t^{1-\beta}\, R^{1-\beta}\, \theta \tag{3.8}$$

This equation is then fitted to experimental values of T_o and T_i to give the coefficients a and β that are used in the finite element analysis.

For this analysis, and for the abrasion analysis in Section 3.7, the contact width was taken to be 1mm. This is consistent with observations of the yarns on the various sized capstans.

3.3.2 Apparatus.

The basic apparatus consists of an aluminium capstan over which a Kevlar yarn is pulled, as shown in Figure 3.6. The tension in the yarn leaving the contact zone, (the outgoing tension, T_o), is measured by means of the Howden tensometer to which the yarn is tied. The tension in the yarn entering the contact zone, (the incoming tension, T_i), is derived from the free weights

applied plus an allowance for the friction in the two pulleys. This allowance is calculated by pulling loaded yarns over two pulleys with no capstan present. For a given incoming tension the tensometer is moved upwards, stretching the yarn between it and the capstan until the force in the yarn is sufficient to overcome friction and the yarn slips. The use of short lengths of yarn (less than 500mm connecting the tensometer to the capstan), ensures that little energy is stored, so when slipping occurs it is continuous, and not a series of stick-slip jumps.

For the test shown in Figure 3.7 the yarn was stopped to allow it to stick, then re-pulled to see if the new force to initiate sliding was the same as the initial one. It could be argued that subsequent forces would differ as the distribution in tension, and hence contact pressure, around the capstan varies slightly between the two. This variation may arise if the incoming tension has not initially worked its way around the capstan, but it can be seen from Figure 3.7 that all the static peaks have similar magnitudes.

It is possible to cycle the tensometer in both directions, such that it measures incoming and outgoing tensions, however this practice excessively reuses one portion of yarn more than the rest. This leads to fairly rapid abrasion with a fine powder building up on the capstan which affects the measurements taken. So the yarn is pulled in one direction only which results in a continuous intake of clean yarn.

At the start of a test the apparatus is set up with the lowest free weight in place and the tensometer head is raised until slipping takes place. More free weights are added, and the procedure repeated until the yarn snaps, usually at the knot attaching it to the tensometer. Then the test is repeated with a new yarn, ensuring that the earmarked contacting portion is not handled. Between tests the contact area is cleaned with acetone to remove any Kevlar powder that has built up. After many tests it was seen that the aluminium surface had become polished from abrasion. Six tests were each performed on capstans of radii, 10, 20, 30, 40, 50, 60, 70 and 80mm; each test giving

between 4 and 6 readings depending on how many loads were applied. 216 readings were taken in total.

3.3.3 Experimental equivalent coefficient of friction, μ.

Many of the experimental points correspond to low contact stresses, which are not of interest in this analysis. To remove their effect, it is necessary to quantify the contact stresses. A simple analysis for this will suffice, as this is only an indication of the contact stress; Equation 3.8 takes into account the variation in contact stress along the length of the contact zone for each and every test.

A mean contact stress, $\overline{\sigma}$, was obtained by assuming a uniform contact pressure around the contacting half of the capstan. Resolving forces on the yarn around the capstan, in a direction parallel to the incoming and outgoing yarns, gives:

$$\overline{\sigma} = (T_o + T_i)/2Rt \tag{3.9}$$

as shown in Figure 3.8. To get a mean frictional stress, $\overline{\tau}$, it was assumed that the frictional stress was constant, so looking at the whole contact area gives:

$$\overline{\tau} = (T_o - T_i)/\pi Rt \tag{3.10}$$

If one were to assume that Amontons' law applies, then an application of (Equation 3.3) to the 216 readings of T_o and T_i gives Figure 3.9, the contact stress being calculated using Equation 3.9. It can be seen that the greater the contact stress the lower the coefficient of friction; this nullifies the assumptions made in deriving this graph, so Amontons' law is not a good model for Kevlar-on-aluminium friction.

Figure 3.10 shows a plot of $\overline{\tau}$ versus $\overline{\sigma}$. The data points are in pairs; a circle corresponds to a static measurement, and the cross below it corresponds to the accompanying dynamic measurement. It can be seen that the points

do not lie on a straight line — at greater contact pressures the effective coefficient of friction reduces.

3.3.4 Experimental coefficients of friction, a and β.

A best fit equation of the form given in Equation 3.8 to all the measured data points (216 static and 216 dynamic) leads to the following two equations:

$$\tau_s = 0.087\sigma^{0.88} \tag{3.11}$$

$$\tau_d = 0.084\sigma^{0.88} \tag{3.12}$$

However if an equation of the form given in Equation 3.8 is fitted only to the points most relevant to a Parafil termination, which here is taken to be all those greater than 6N/mm^2 (21 static and 21 dynamic), then the following refined equations are obtained (where τ and σ are in kN/mm^2):

$$\tau_s = 0.099\sigma^{0.91} \tag{3.13}$$

$$\tau_d = 0.095\sigma^{0.91} \tag{3.14}$$

These equations are plotted in Figure 3.10, the solid line being the static friction and the dashed line the dynamic. Because the static and dynamic indices are the same, these equations give a static friction greater than the dynamic one for all contact stresses. Note, the axes show mean contact and frictional stresses as a means of visualising the experimental data; the stresses continuously vary along the length of the contact zone, a fact which is included in this analysis.

3.3.4.1 Expressing μ in terms of a and β.

Equations 3.13 and 3.14 can be re-expressed to give equivalent coefficients of friction, μ, as follows:

$$\text{static} \quad \mu_s = a_s\sigma^{\beta_s - 1} = 0.099\sigma^{-0.09} \tag{3.15}$$

$$\text{dynamic} \quad \mu_d = a_d\sigma^{\beta_d - 1} = 0.095\sigma^{-0.09} \tag{3.16}$$

These curves are plotted in Figure 3.11 for the range of stress encountered in the finite element analysis.

3.4 Yarn-on-yarn friction for Kevlar 49.

There is no published data in the literature for the yarn-on-yarn friction for Kevlar 49, nor for the shear yield stress. However, because there is minimal yarn-on-yarn slip within a Parafil termination, this parameter is not critical. This is unlike the yarn-on-solid friction, which is a major factor in the functioning of the terminations.

For use in the finite element analysis, a coefficient of friction of μ=0.3 was assumed for the Kevlar-on-Kevlar friction. Chapter 5 details how the rope is modelled as three separate layers, to allow for any relative slip. However, it is seen in Chapter 6 that the shear stress in these layers remains below 25N/mm^2, a value which is believed to be used in the design of Parafil terminations. No slip between these rope layers is indicated in the analysis, so this value is a reasonable assumption. If a lower value of μ was to be used, then slipping would occur before the shear stress could rise to this limiting value; if a higher value was set, then the analysis would be unaffected.

3.5 Abrasion of polymeric fibres.

Abrasive wear is said to happen when there is a progressive loss of material from the softer surface when two surfaces are rubbed back and forth. In a 'clean' environment this is most often caused by the hard protuberances of one surface gouging grooves in the softer surface as they are reciprocated under normal loading. The swarf is initially pushed to one side but after many cycles it is removed altogether. If grit is present then this process is speeded up, but the terminations are usually sealed to prevent water penetration, so

no grit will be able to get in. In polymers, strong adhesion occurs at the points of contact of the asperities; when sliding occurs, fragments are torn from the softer surface and are left deposited on the harder one [Meredith and Hearle, 1959].

As stated in Section 3.2, the laws of friction (including Howell's equation) have been largely substantiated. However wear has no satisfactory quantitative laws. This is because any small change in one of the parameters; for example, speed, area of contact, load, amplitude, etc. can completely alter the contribution of each factor to any overall wear equation [Bowden and Tabor, 1974]. Most research has looked at microscopic sliding (20-300μm) or macroscopic sliding (>25mm); none has looked at the intermediate range of 0.1-1mm that occurs in Parafil terminations.

As mentioned in Chapter 2, the method of failure for Parafil ropes cycled under load was either by abrasion at the terminations or sheaves.

Fretting is a name given to abrasive wear at very small amplitudes, typically less than 0.3mm. The loss of material from the softer material is very low at these amplitudes but rises rapidly with increase in amplitude, as abrasion takes over, Figure 3.12. It can be seen from this figure that on rubbing two metals together, very little material loss occurs below 0.1mm, with a dramatic increase above this amplitude. It is likely that a similar situation occurs for polymers.

There may also be structural changes taking part in the fibres themselves due to the work being done on them. Delamination is very common amongst polymeric fibres although aramids are less susceptible. Super-molecular structures in polypropylene are altered during frictional contact, as observed by Bely [reported in Kragelski et al., 1982]; this may also occur for the super-molecular structures in Kevlar fibres (see Section 4.2).

As reported in Chapter 4, the shear yield strength of Kevlar 49 is 160N/mm^2 [Kawabata and Sera, 1993]. Taking the uniaxial yield stress of the aluminium

alloy used for the termination to be 600N/mm^2, then its shear yield strength is 300N/mm^2 [Ashby and Jones, 1980]. Therefore the Kevlar fibres are the softer material and will suffer most of the abrasion.

Very little research has been published on the problems of small amplitude abrasion of polymer fibre-on-fibre or polymer fibre-on-solid (whether metal or plastic). What little there is, is presented in this section.

3.5.1 Experimental results on abrasion in the literature.

Research has been carried out on polymeric abrasion by Goksoy [1986] and Wu [1990]. However, the lowest stroke used by Wu was 25mm and Goksoy predominantly used 50mm, so neither could be classified as doing any experiments on fretting — they were both interested in large amplitude abrasion. Therefore their actual results are not of direct relevance here, and neither used Kevlar 49, but the phenomena they identified are of interest.

Goksoy identified two regimes of 'abrasion' (Figure 3.13); a gradual abrasion at a low severity of testing, and a catastrophic regime at a high severity. Wu has elaborated on this and has classified these regimes as mechanical abrasion and thermal failure respectively.

3.5.1.1 Mechanical abrasion.

Mechanical abrasion occurs at a low frequency or low applied load (<10% yield), the fibres being gradually worn away by frictional action. There is little heat generated and little thermal degradation. Away from the contact region the fibres are unaffected. Just before failure the friction between the ropes rises by about 20% due to the severe surface roughness.

3.5.1.2 Thermal failure.

Thermal failure occurs for a high frequency or where there is a poor heat transfer (e.g. in still air). For polyester and nylon, the heat generated actually melts some of the fibres and the remaining ones suffer thermal degradation with a dramatic drop in residual strength. Just before failing the friction drops due to the smoothness of the melted surfaces.

Thermal failure can be avoided (and hence lifetimes improved dramatically) if adequate cooling is provided either by a fan or by water. For Kevlar 29, Dupont [1976; 1988] have recorded only small reductions in the tensile strength up to 180°C of about 20% followed by large reductions above this; Kevlar 49 is similar.

Even at the very high stresses, 5-70%, and frequencies, 0.33Hz, to which Crawford and McTernan [1988] subjected a 150 tonne Parafil F (Kevlar 29) rope, the temperature did not rise above 100°C due to Kevlar's low hysteresis and the absence of lay geometry. Thermocouples were inserted into the rope core at the front face of the termination. Thermal failure would not be expected to occur at this temperature, and the ropes failed by mechanical abrasion. They reported only split fibres, which would be expected in a fretting failure at low amplitudes of motion.

Since the amplitude and frequency of the motion expected within a termination are low, all the tests done here are in Wu's mechanical abrasion zone. As with most abrasion data, a logarithmic plot of severity, either amplitude or contact stress, against lifetime, should produce a straight line.

3.6 Yarn-on-yarn abrasion.

A detailed analysis of yarn-on-yarn abrasion was not performed here. When the yarns fail by rubbing against the spike or the barrel, they will recoil

away from the abrasion zone thus exposing fresh yarns to be abraded. So yarn-on-solid abrasion is assumed to be the dominant failure mechanism.

3.7 Kevlar 49-on-aluminium abrasion.

A comprehensive study of abrasion of Kevlar 49 yarn on aluminium has been undertaken. There are many variables that may affect the lifetime of a yarn rubbing on a solid; the amplitude of the cycle, the contact pressure, the maximum load and hence the amount of yarn to be abraded, the surface finishes of the materials including the 'size' that is applied to the yarn, the temperature, the presence of debris and the presence of water. For this analysis it was assumed that only the amplitude, the contact pressure and the thickness to be abraded, are significant variables. The maximum load is also a factor, but this will be encompassed in the lifetime equation by calculating the thickness that needs to be abraded; the greater the maximum load the less the thickness that needs to be abraded before the tensile stress is reached in the remaining yarns. For this analysis, the intention was to model what is currently happening, therefore the experiments were kept as close as possible to the severities in an actual termination. Actual rope yarns were used, with no alteration made to their surface coatings; the materials were kept as clean and dry as possible, and all tests were performed at room temperature (although the temperature in a rope under cyclic loading may rise to 100°C). A relationship of the following form is therefore assumed:

$$N \propto a_o^{n_1} \sigma^{n_2} \delta^{n_3} \tag{3.17}$$

where N is the number of cycles to failure, a_o is the amplitude of cycle, σ is the contact stress, δ is the thickness to be abraded, and n_1, n_2 and n_3 are the indices that need to be determined.

By performing a set of tests with various amplitudes, whilst keeping σ and δ uniform, the value of n_1 can be determined from the gradient of a plot of $\log(N)$ against $\log(a_o)$. Unfortunately, not enough tests were performed

keeping both δ and a_o constant to provide a meaningful estimate for n_2 in this manner. Instead, this is derived by fitting the above equation to all the tests performed. For this analysis it is assumed that $n_3 = 1$, i.e. the rate of wear is uniform throughout a test. This is a reasonable assumption to make as the Kevlar debris is removed from the aluminium surface by the rubbing of both the yarns in these tests and the yarns in the rope terminations, thus ensuring fresh material is always in contact. Also, the Kevlar away from the contact zone moves as one and does not abrade against itself, so whilst it is away from the aluminium surface it is unaffected by the number of cycles accrued.

In order to non-dimensionalise this equation; the amplitude, and thickness to be abraded, are arbitrarily divided by the diameter of a fully compressed yarn, d, (0.357mm); and the contact stress is divided by the yield stress of a Parafil rope, σ_y, (1926N/mm^2). For convenience, $\hat{a_o}$ is defined to be a_o/d, $\hat{\delta}$ is defined to be δ/d, and $\hat{\sigma}$ is defined to be σ/σ_y.

3.7.1 Apparatus.

Figure 3.14 shows a schematic view of one station on the abrasion tester that was built to perform lifetime tests on 8 stations simultaneously. Unfortunately, it was soon found that when the first station failed the others would rapidly follow due to the shock loading from a 20kg mass being released from the system. All the abrasion tests were therefore performed on one station running alone.

A yarn was passed over a disc of the desired radius, to make the desired contact angle. For small angles of contact the exact value is not relevant in determining the contact pressure, however the contact zone should be long enough such that a portion of yarn is subjected to the entire regime. If a piece of yarn passed outside the contact zone at both ends of the cycle then no part of the yarn would be fully abraded. The contact length must also

be short enough that the tension in the yarn does not rise too much, due to friction, to affect the contact pressure. A contact angle of 10° was used throughout.

Considering a small element of yarn passing over the disc and resolving normal to the surface, $\sigma R\theta t = 2.T.\theta/2$, or $\sigma = R/Tt$. R is the radius of curvature, T is the yarn tension, σ is the contact stress, and t is the width of the contact zone, which was assumed to be 1mm here.

The yarn was guided over the disc by means of pulleys such that it was free to move along its axis only. One end was driven by a motor via an eccentric axle, which gave rise to a sinusoidal oscillation. The movement was constrained with bearings to translate this rotation into a linear motion. The other end was loaded by a free weight. To stop the free weight spinning and hence removing all the twist present in the yarn, it was loosely tied to a cut-off switch with a piece of thick wire. The weight would rotate round by a quarter of a turn until the wire exerted enough torque to prevent the yarn untwisting further; the wire was set such that it provided no axial load into the system. When the yarn eventually broke, this piece of wire would pull a block out of a cut-off switch thus stopping both the motor and the counter. The counter was driven by a reed switch and a magnet attached to the shaft of the motor.

A marker was attached to the yarn just above the weight, and the upper and lower limits of this marker noted by lining up the cross hairs of a travelling microscope; the position was read from the vernier scale on the side of the microscope. These readings were repeated six times and a mean taken to give the amplitude of each cycle.

All the abrasion tests were performed using Kevlar 49 yarn from a bobbin used to make Parafil ropes provided by Linear Composites Ltd. Therefore the number of fibres present, the amount of twist and the size applied to the yarns are all representative of those within a Parafil termination. When assembling the apparatus care was taken to ensure that the number of twists

in the yarn remained constant (there are about 45 twists per metre.) The aluminium discs were prepared by sawing a template out of Dural, then turning this in a lathe.

The actual surface of an aluminium 60 tonne Parafil G spike has small shallow score marks running around it every 0.25mm. It was not practical to machine these on the discs used here, as they are a by-product of the turning process in manufacturing the spike. Experiments were done with marks running perpendicular to the direction of slip, but it was not possible to create the smooth score marks that are found on the spike, and so the lifetimes were exceedingly short.

The discs here were smoothed as much as possible for the first test, and after several abrasion tests were performed it could be seen that the already smooth surface was polished even more by the abrasion from the Kevlar. A fine yellow dust was present around the contact zone from the debris.

The yarn is clamped at both ends between aluminium plates that are screwed together; this is a very efficient method of restraining the ends, as this restraint remains effective regardless of the number of fibres that have broken. It was found to be impractical to glue the ends as it was very difficult to achieve a uniform coating on all the fibres whilst maintaining their geometry within the yarn. A speed of 120rpm was chosen, this being the highest speed possible before dynamic effects from the flexibility of the rig became significant. The change in tension due to the dynamic loading on the free weight is negligible at this speed.

For the fixed amplitude experiments the amplitude was fixed at 0.68mm and the contact pressure and thickness to be abraded were altered by using discs of radii 27.5mm and 79.5mm, with loads of 50.0, 100.2, 150.0 and 199.8N. Other experiments were done using amplitudes of 0.12, 0.68 and 2.90mm, as detailed in Table 3.3.

3.7.2 Contribution from the thickness to be abraded.

For this analysis it is assumed that under a certain severity, determined by the contact pressure and the amplitude, the rate of wear of the Kevlar 49 is constant. This is not necessarily true; the rate may slow down due to a build-up of debris which will act as a lubricant and as a barrier, and conversely the rate may speed up due to damage being accumulated above the contact zone from inter-fibre fretting.

The non-dimensionalising factor used here is arbitrarily taken to be the yarn diameter, calculated as the sum of all the fibre areas, which gives a value of $d = 0.357$mm. The exact value of this factor does not affect the analysis so long as consistency is maintained throughout the analysis. The cross sectional area of the yarn, however, is greater than this value of d would imply, due to the low transverse pressures used here — the cross sectional area is taken to be 0.23mm^2. This area correlates with the breaking load of 440N (taken from a mean of 6 tensile tests using Amaniampong's jaws [1992]) and the rope's ultimate tensile stress of 1926N/mm^2. It is assumed that the yarn deforms over the capstan into a rectangle 1mm wide and 0.23mm thick, which is consistent with observations for all the severities measured.

For the yarn experiments, the thickness that needs to be abraded before failure occurs is related to the maximum tension in the yarn. For a larger tension less material needs to be abraded before the remaining yarn reaches its breaking stress. The proportion of yarn that has abraded at failure is (1-$\lambda_{max}/100$) where λ_{max} is the percentage ratio of the maximum load to the breaking load. From this, the non-dimensionalised thickness to be abraded, $\hat{\delta}$, can be deduced:

$$\hat{\delta} = \frac{h(1 - \lambda_{max}/100)}{d} \tag{3.18}$$

where h is the total thickness of the Kevlar, and d is the non-dimensionalising yarn diameter. For the yarns used here with a breaking load of 440N and a

maximum cyclic load of T_{max} this can be re-written as:

$$\hat{\delta} = \frac{0.23 \times (1 - T_{max}/440)}{0.357} = 1.464 \times 10^{-3}(440 - T_{max}) \tag{3.19}$$

3.7.3 Contribution from the amplitude of cycling.

As with most abrasion data, an exponential relationship is seen, so a log-log plot is the most appropriate. Figure 3.15 shows a plot of $\log(\hat{a_o})$ against $\log(N)$. A straight line can be drawn between these points, with a least squares best fit gradient of $-\frac{1}{2.8}$. Therefore it can be deduced that n_1=-2.8 and:

$$N \propto \frac{1}{\hat{a_o}^{2.8}} \tag{3.20}$$

3.7.4 Overall lifetime equation.

As stated earlier in this section, not enough data for constant $\hat{\delta}$ and $\hat{a_o}$ was gathered to provide a meaningful estimate of n_2 from a plot of $\log(\hat{\sigma})$ against $\log(N)$. Instead this is derived from all the data points; using n_1=-2.8 and n_3=1.0, Equation 3.17 can be rewritten as:

$$N = k(\hat{a_o})^{-2.8}(\hat{\sigma})^{n_2}(\hat{\delta}) \tag{3.21}$$

and taking logarithms gives:

$$\log(N) = \log(k) + n_2 \log(\hat{\sigma}) - 2.8 \log(\hat{a_o}) + \log(\hat{\delta}) \tag{3.22}$$

where k is a constant. k and n_2 were varied to find the least-squares best-fit using a Matlab regression analysis for Equation 3.22. Figure 3.16 shows the predicted lifetimes with the calculated best-fits of k=355 and n_2=1.1. The predicted lifetimes (the right hand side of Equation 3.22) are on the y-axis, the actual lifetimes (the left hand side) are on the x-axis. The points straddle the line $x = y$ therefore Equation 3.23 is a good predictor for the lifetimes of yarns on capstans.

These values of k and n_2 can be substituted into Equation 3.21 to yield:

$$N = 355 \frac{\hat{\delta}}{\hat{\sigma}^{1.1} \hat{a_o}^{2.8}} \tag{3.23}$$

3.8 Summary.

With the appropriate experiments it is possible to gather the friction data that is required for a finite element analysis of a Parafil termination. For Kevlar 49-on-aluminium this takes the form $\tau_s = 0.099\sigma^{0.91}$ and $\tau_d = 0.095\sigma^{0.91}$. Kevlar 49-on-Kevlar 49 is not so critical in the mechanics of the terminations so an assumed value of $\tau_s = 0.30\sigma$ is used.

In a similar way, Kevlar 49-on-Kevlar 49 abrasion is not assumed to be the critical factor in the lifetimes of terminations, Kevlar 49-on-aluminium abrasion is. Kevlar 49-on-aluminium abrasion can be expressed in terms of three factors; the amplitude of slip, the contact pressure, and the thickness to be abraded. These are related by the non-dimensionalised expression $N = 355\hat{\delta}/\hat{\sigma}^{1.1}\hat{a_o}^{2.8}$. This equation is later used in Chapter 7 to accurately predict the lifetimes of actual terminations.

Material	μ
Perfectly clean metals in vacuum	seizure $\mu > 5$
Clean metals in air	0.8-2
Clean metals in wet air	0.5-1.5
Steel on dry bearing materials	0.1-0.5
(e.g. lead, bronze)	
Steel on ceramics	0.1-0.5
(e.g. sapphire, diamond, ice)	
Ceramics on ceramics	0.05-0.5
(e.g. carbides on carbides)	
Polymers on polymers	0.05-1.0
Metals and ceramics on polymers	0.04-0.5
Boundary lubrication of metals	0.05-0.2
Hydrodynamic lubrication	0.001-0.005

Table 3.1: Coefficients of friction for various materials. [Ashby and Jones, 1980]

Material	K	β
cellulose acetate	0.60	0.96
viscose rayon	0.49	0.91
drawn nylon	0.92	0.80
undrawn nylon	0.85	0.90

Table 3.2: Coefficients and indices of friction for various polymers. [Howell, 1953]

Tension (N)	Radius (mm)	Amplitude (mm)	Contact pressure (N/mm^2)	Thickness to be abraded (mm)	Cycles to failure
199.8	27.5	2.90	7.26	0.125	152
199.8	27.5	2.90	7.26	0.125	468
199.8	27.5	2.90	7.26	0.125	1,270
199.8	27.5	2.90	7.26	0.125	239
199.8	27.5	2.90	7.26	0.125	507
199.8	27.5	2.90	7.26	0.125	203
199.8	27.5	2.90	7.26	0.125	432
199.8	27.5	2.90	7.26	0.125	224
199.8	79.5	0.68	2.51	0.125	11,600
199.8	79.5	0.68	2.51	0.125	30,600
199.8	79.5	0.68	2.51	0.125	36,800
199.8	79.5	0.68	2.51	0.125	13,000
199.8	79.5	0.68	2.51	0.125	17,900
199.8	79.5	0.68	2.51	0.125	20,800
199.8	79.5	0.68	2.51	0.125	24,100
199.8	79.5	0.68	2.51	0.125	15,400
199.8	79.5	0.68	2.51	0.125	9,490
150.0	79.5	0.68	1.88	0.151	25,200
150.0	79.5	0.68	1.88	0.151	59,200
150.0	79.5	0.68	1.88	0.151	21,700
100.2	79.5	0.68	1.26	0.177	150,000
100.2	79.5	0.68	1.26	0.177	88,000
100.2	79.5	0.68	1.26	0.177	50,000
50.0	79.5	0.68	0.62	0.203	308,000
50.0	79.5	0.68	0.62	0.203	285,000
50.0	79.5	0.68	0.62	0.203	462,000
50.0	79.5	0.68	0.62	0.203	653,000
199.8	27.5	0.68	7.26	0.125	5,140
199.8	27.5	0.68	7.26	0.125	902
199.8	27.5	0.68	7.26	0.125	5,790
199.8	27.5	0.68	7.26	0.125	6,940
199.8	27.5	0.68	7.26	0.125	12,500
50.0	27.5	0.68	1.81	0.203	111,000
199.8	27.5	0.12	7.26	0.125	1,200,000
199.8	27.5	0.12	7.26	0.125	3,260,000

Table 3.3: Kevlar 49 on aluminium abrasion.

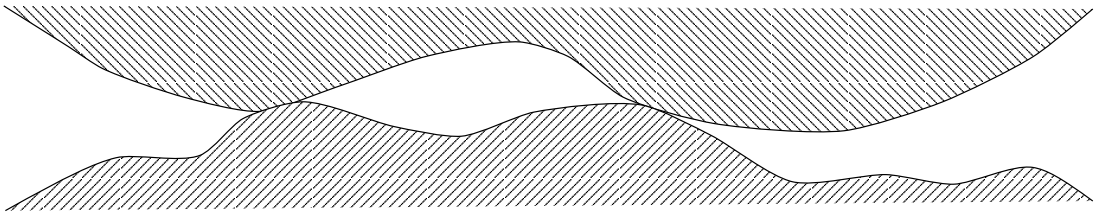

Figure 3.1: Contact of two surfaces, "like turning Switzerland upside down and standing it on Austria".

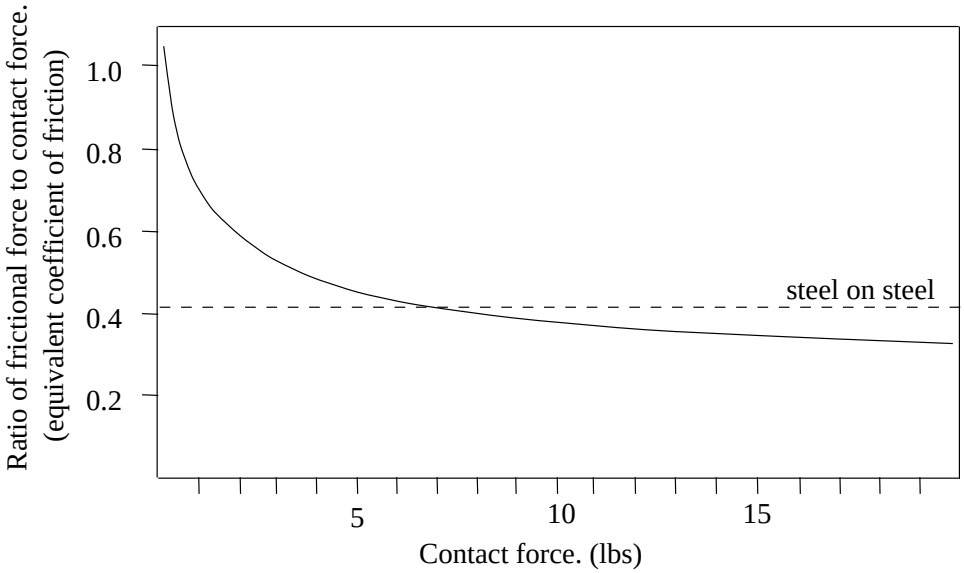

Figure 3.2: Friction of a hard sphere sliding over a clean flat surface of Plexiglas. As the contact force is increased the ratio of frictional force to contact force is reduced, this is a general feature of polymeric materials. [Bowden and Tabor, 1974]

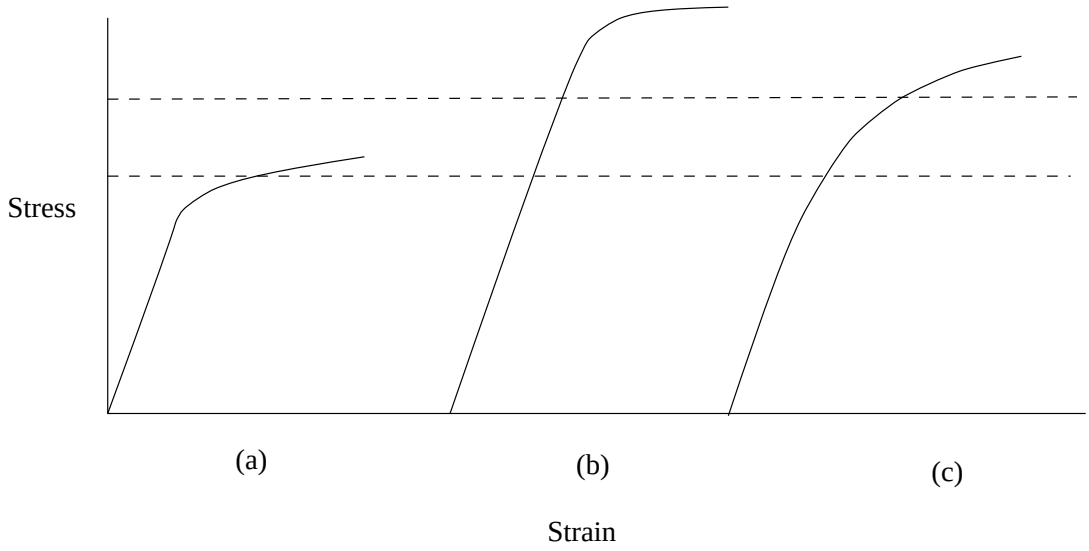

Figure 3.3: Stress-strain curves for various hypothetical asperity models [Howell, 1953]. The dashed lines represent the stress range in the contacting asperities. The models are:
(a) plastic deformation of asperities, so Amontons' law applies,
(b) elastic deformation of asperities, so $F \propto N^{2/3}$,
(c) elastic and plastic deformation of asperities, so $F \propto N^{\beta}$.

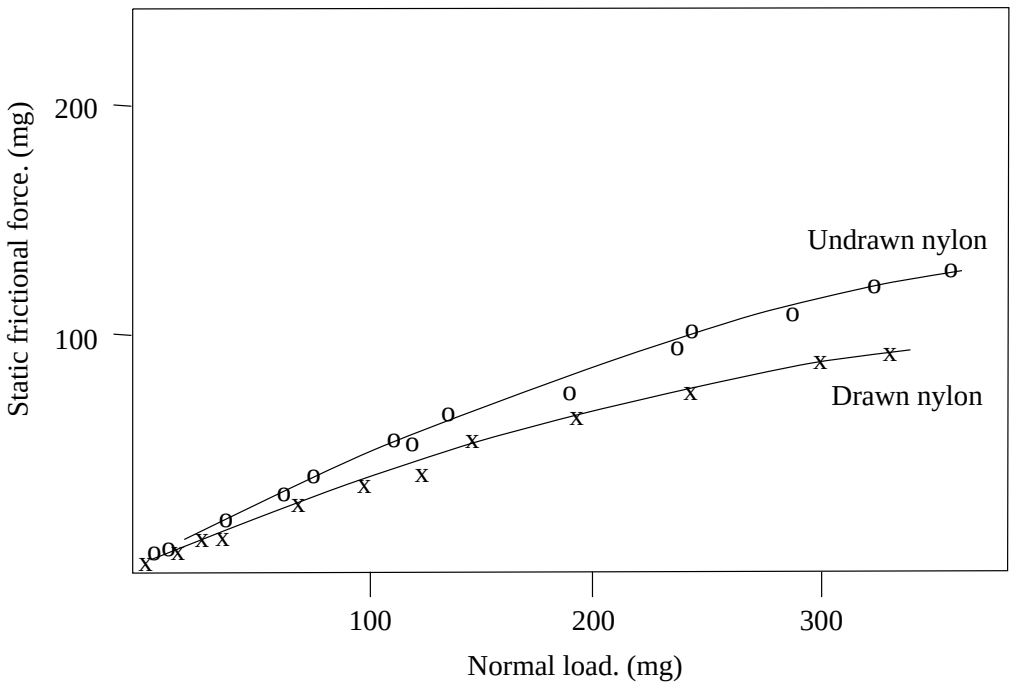

Figure 3.4: Frictional behaviour of nylon-on-nylon contact [Howell, 1953]. Best fits were obtained for drawn nylon with $F = 0.92N^{0.80}$, and for undrawn nylon with $F = 0.85N^{0.90}$, where F is the static frictional force and N is the normal load. It can be seen that the F-N curve falls below a straight line; the ratio of F to N decreases with load.

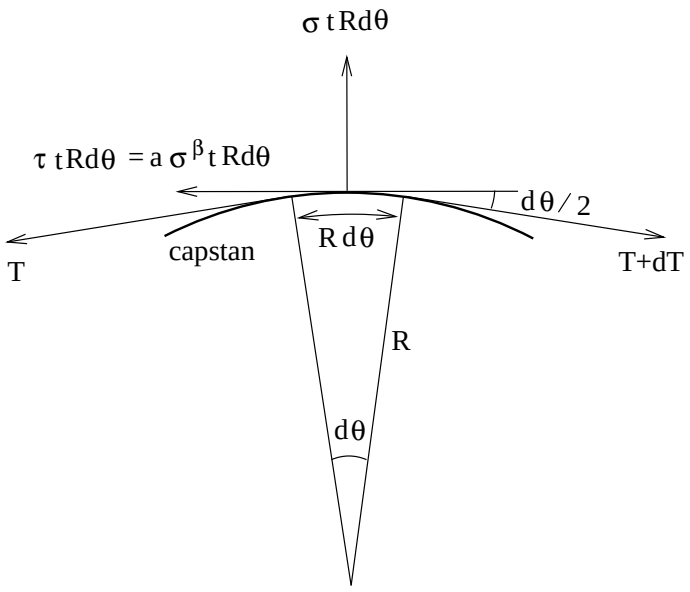

Figure 3.5: Forces acting on a segment of yarn running over a capstan of angle dθ and radius R. The tension in is T, the tension out is $T = T+\mathrm{d}T$. The contact force over length $R\mathrm{d}\theta$ is $\sigma t R\mathrm{d}\theta$, where t is the contact width, and σ the contact pressure. The frictional force is $\tau t R\mathrm{d}\theta$ where the τ is frictional stress, $\tau = a\sigma^{\beta}$.

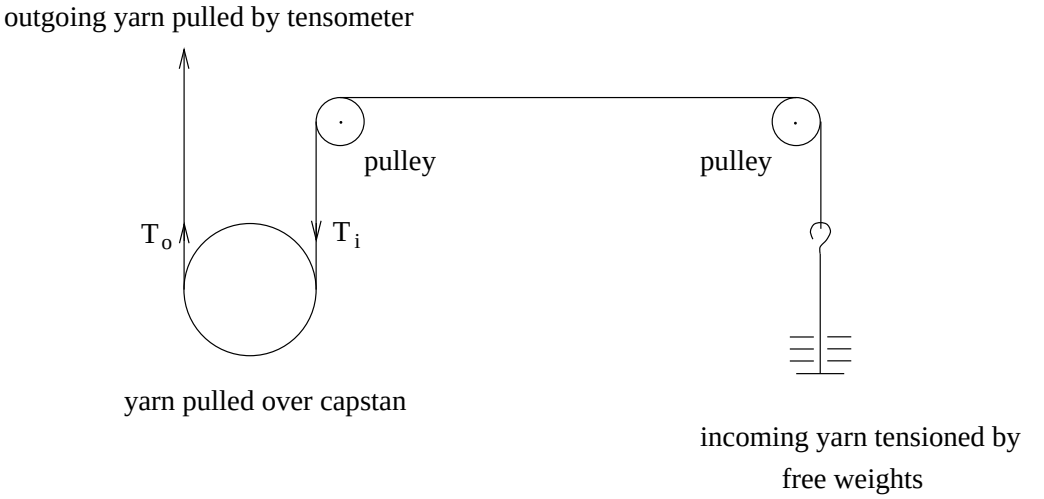

Figure 3.6: Apparatus used to measure yarn on solid friction. The yarn is tensioned by free weights which are increased at intervals during the test to vary T_i, the incoming tension. The yarn is pulled over a capstan by displacing the other end which is attached to a tensometer; this outgoing tension is T_o.

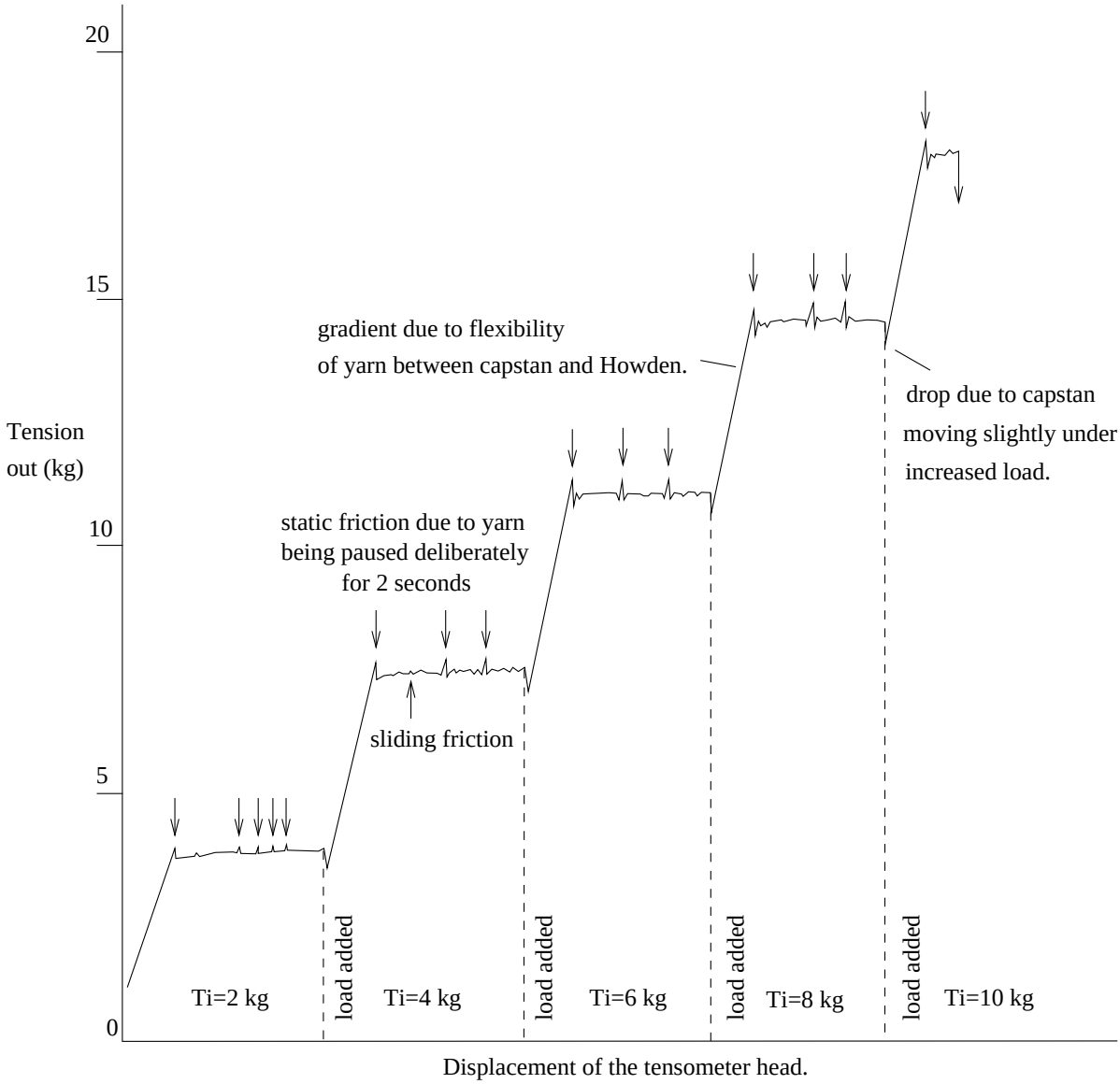

Figure 3.7: Plot of the outgoing tension for Kevlar pulled over a 30mm aluminium capstan at 10mm/min. This shows that the effect of stopping the sliding for 2 seconds and then restarting, is negligible. Hence for other tests only the initial static friction was taken. For a given T_i; the static value of T_o is the peak, the dynamic value is the slipping plateau.

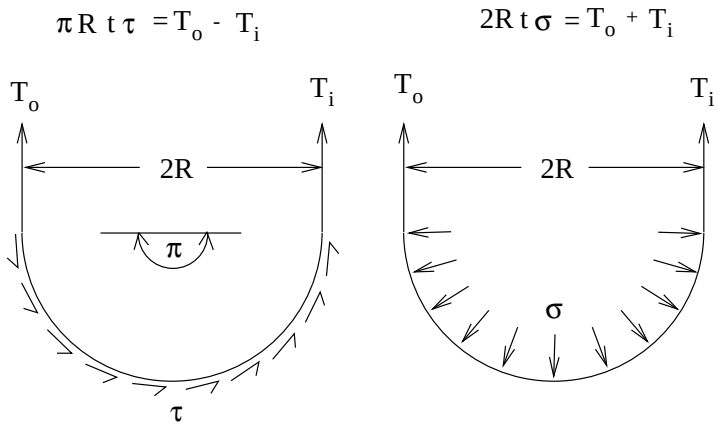

Figure 3.8: Estimation of average contact and frictional stresses on a capstan. Due to the non-linear nature of the friction, τ and σ will vary around the capstan, but for the visualisations in Figures 3.9 and 3.10, average values can be estimated. If a uniform distribution is assumed then $\tau = (T_o - T_i)/(\pi Rt)$ and $\sigma = (T_o + T_i)/(2Rt)$.

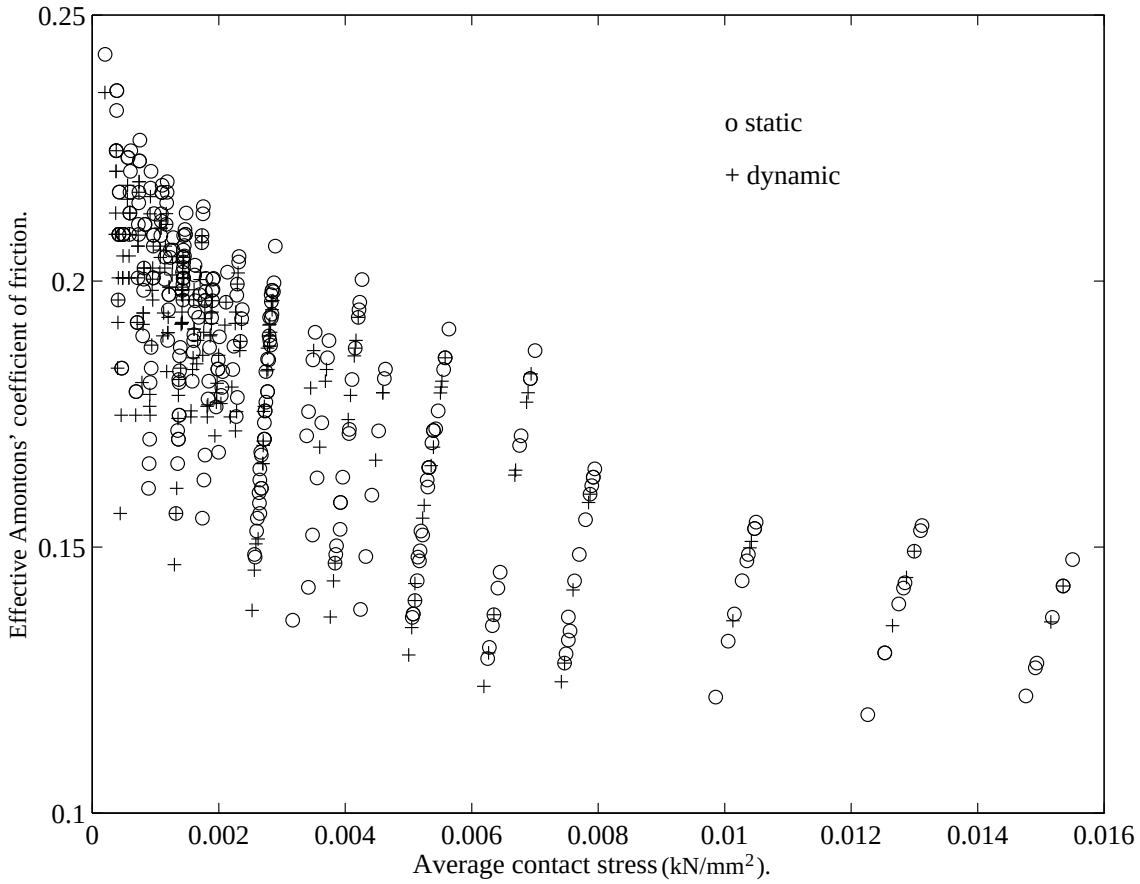

Figure 3.9: Effective Amontons' coefficient of friction, μ, for Kevlar 49-on-aluminium assuming μ is constant. The average contact stress is defined in Equation 3.9 for visualisation purposes. It can be seen that μ drops with increasing σ therefore this graph invalidates the assumptions made in generating it, and so Amontons' law is not a good model for Kevlar 49 on aluminium contact. The vertical lines represent the range of μ gathered for a given radius and incoming tension. For a greater outgoing tension; the value of μ will be larger, and the average contact stress will also increase slightly.

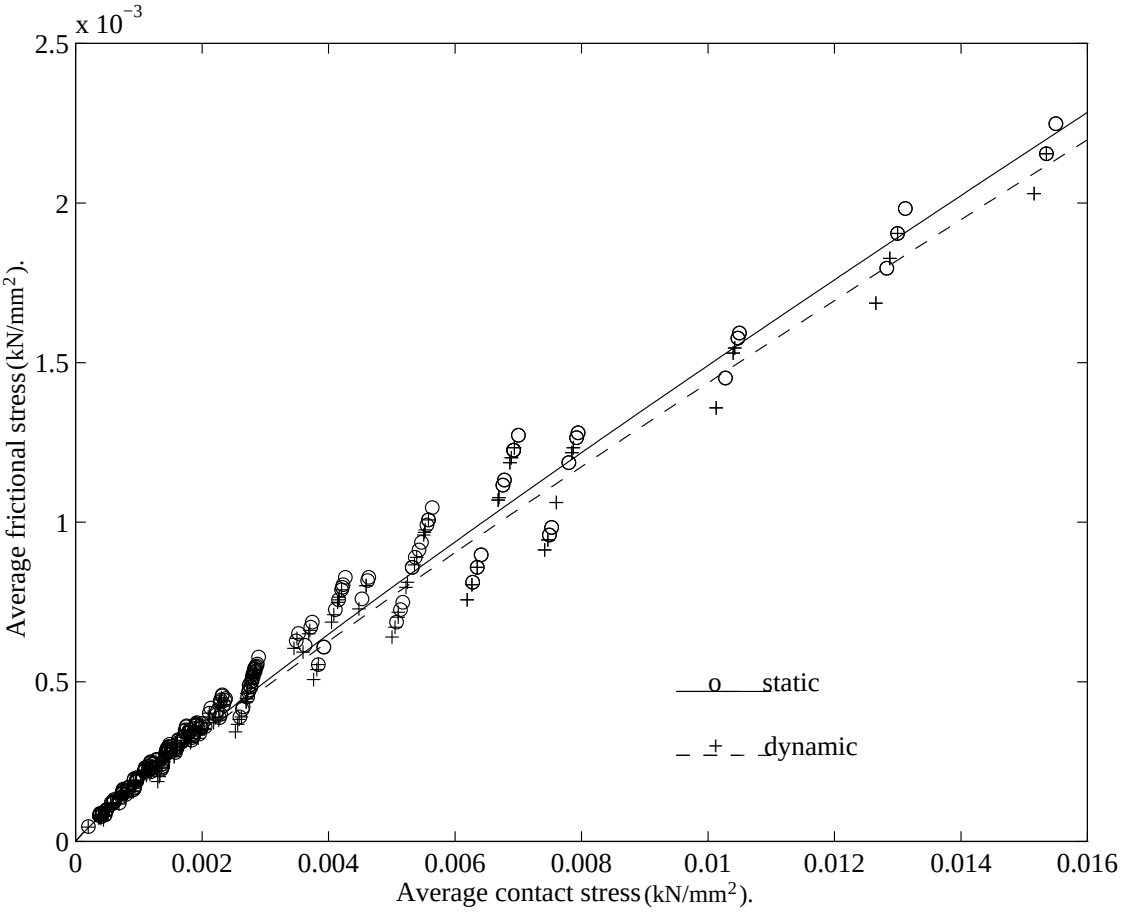

Figure 3.10: Visualisation of the average frictional stress versus average contact stress. If Amontons' law ($\tau = \mu\sigma$) applies then these points would lie on two straight lines, however they fall below the initial line at higher contact stresses and can be seen to closely follow the modified Howell's curves, $\tau_s = 0.099\sigma^{0.91}$ and $\tau_s = 0.095\sigma^{0.91}$.

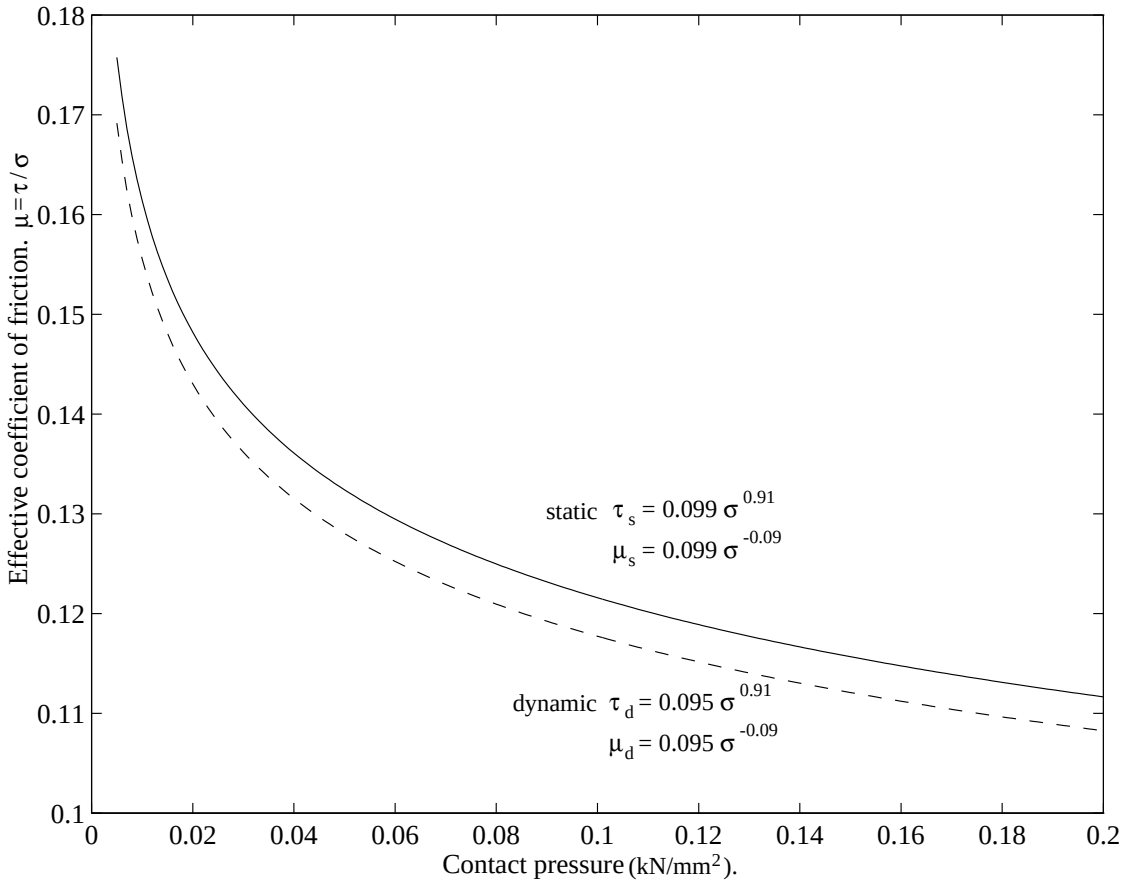

Figure 3.11: Equivalent Amontons' coefficients of friction ($\mu = \tau/\sigma$) for Kevlar 49-on-aluminium used in the finite element analysis. This demonstrates how the ratio of friction to contact pressure drops when using a modified Howell's equation ($\tau = a\sigma^{\beta}$) for the stress range encountered in a Parafil termination.

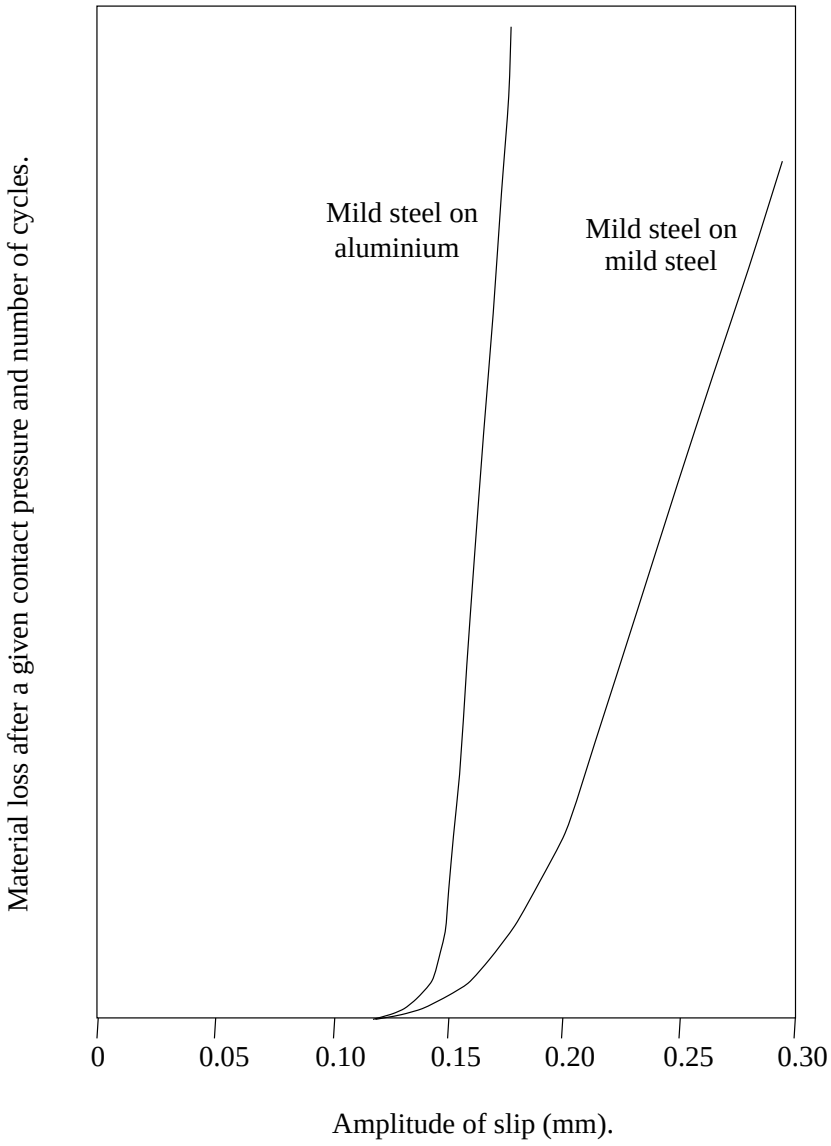

Figure 3.12: Loss of material versus amplitude of sliding [Sarkar, 1980]. At small amplitudes, less than 0.12mm, there is negligible loss of material. Above this amplitude the abrasion rapidly increases. The minimum amplitude applied in the tests in this chapter (Table 3.3) is 0.12mm.

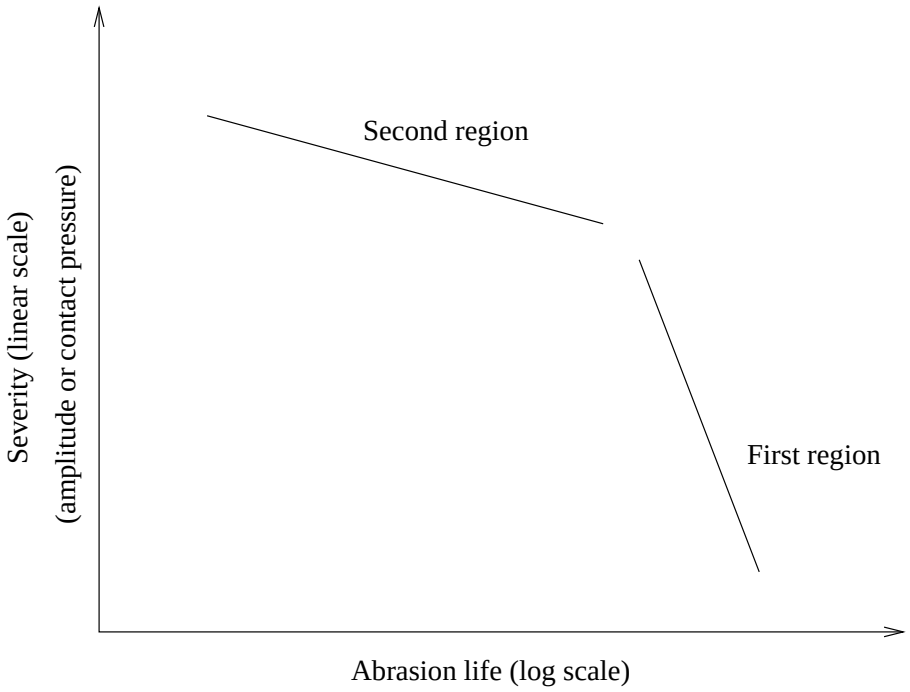

Figure 3.13: The regimes of 'abrasion' presented by Goksoy [1986]. Goksoy broadly identified two regimes for abrasion between nylon and polyester yarns. A first region at a medium severity with long lifetimes, and a second region at a higher severity with dramatically lower lifetimes.

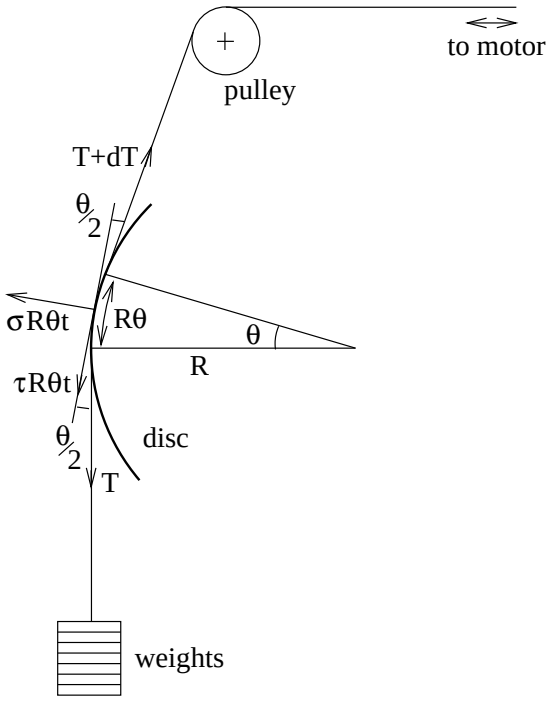

Figure 3.14: Schematic of apparatus used to determine yarn-on-solid abrasion. The nomenclature is consistent with that of Figure 3.8. The angle θ is kept small to reduce the change in tension dT during the cycle, but large enough such that a portion of yarn remains within the contact zone.

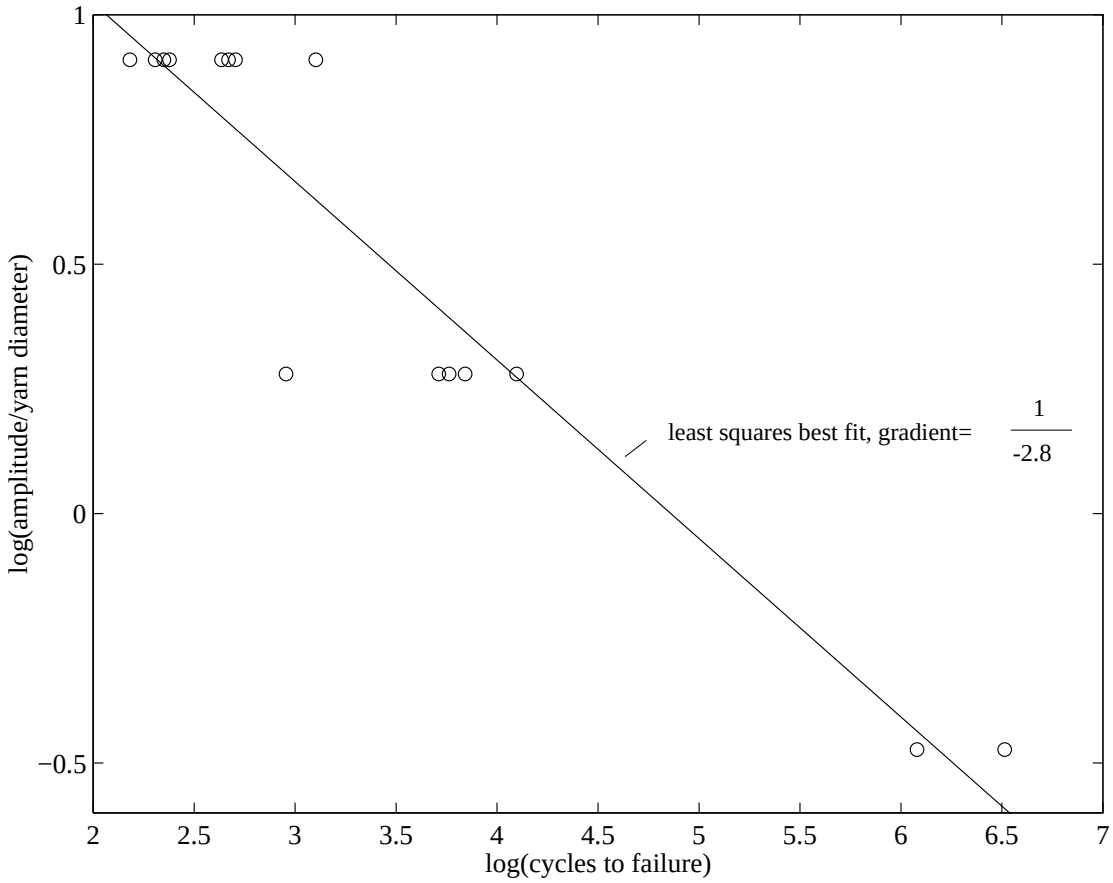

Figure 3.15: Lifetime data for Kevlar 49 yarns abraded at a contact pressure of 7.26N/mm^2, over an aluminium capstan of radius 27.5mm, with amplitudes of 0.12, 0.68 and 2.90mm. A straight line can be fitted through these points to give the equation $N \propto 1/\hat{a_o}^{2.8}$ where $\hat{a_o}$ is the ratio of amplitude to yarn diameter.

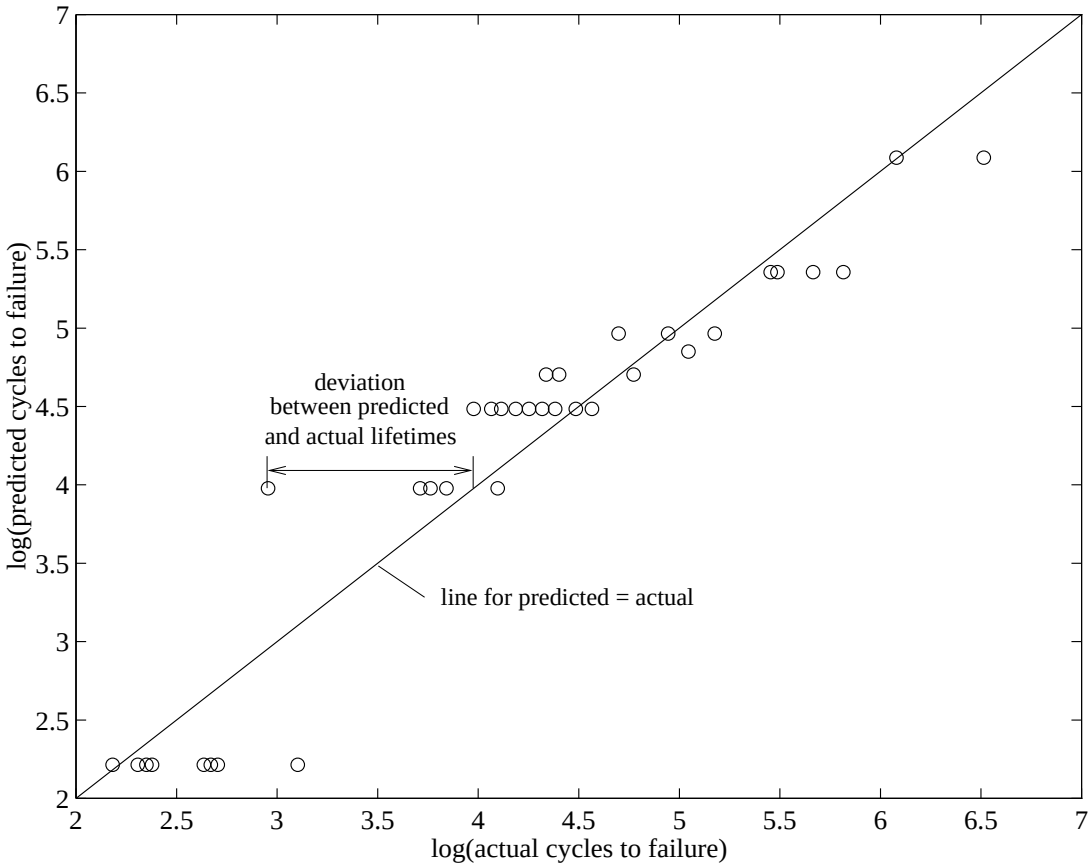

Figure 3.16: Predicted versus actual cycles to failure for Kevlar 49-on-aluminium abrasion. The experimental data points are compared to the predictions from the best fit equation $N = \hat{\delta}/\hat{\sigma}^{1.1}\hat{a_o}^{2.8}$. There is no significant deviation from the straight line that equates the predictions to the experimental values; therefore this equation gives a good prediction of the lifetimes.

Chapter 4

Anisotropy of synthetic fibres.

4.1 Introduction.

A study of the material properties of Kevlar fibres is needed in order to carry out a detailed finite element analysis of a spike-and-barrel Parafil rope termination. This chapter starts with a brief outline of the equations applicable to elastic materials, leading to those which apply to Kevlar. Material data for Kevlar 49 from the literature is then presented. This is followed by a description of the experiments carried out here to quantify the bulk transverse moduli of Kevlar 49, concluding with the results from these in a form suitable for insertion into the finite element analysis.

4.2 Elasticity in materials.

Due to the alignment of the Kevlar molecules within the fibres and the alignment of the fibres within the rope, the material properties of the rope differ in the axial and transverse directions. This is an example of anisotropy.

At small (and therefore elastic) strains, the mechanical behaviour of a solid material can be expressed by up to thirty six independent elastic compliances, all of which can be measured. The more symmetry there is, the fewer independent compliances there will be. These are defined by the generalised

Hooke's law as follows [e.g. Hearman, 1956]:

$$\begin{aligned} \epsilon_p &= S_{pq} \quad \sigma_q \\ \sigma_q &= C_{qp} \quad \epsilon_q \end{aligned} \tag{4.1}$$

where S_{pq} and C_{qp} are the compliance and stiffness constants relating the stresses σ_q to strains ϵ_p with $p = 1, 2...6$ and $q = 1, 2...6$. Compliance constants are normally used because they can be found more readily. (The stiffness matrix can be found by taking the inverse of the compliance matrix.)

Anisotropy has many forms; an example of general anisotropy is the crystal structure shown in Figure 4.1, where the distances between the atoms in the three directions of the crystal lattice are different, and the directions themselves are not orthogonal. No rotation about any axis other than 360° will map the lattice onto itself. If an elastic linear stress-strain relationship (Hooke's law) is assumed, the following compliance matrix (S_{pq}) applies:

$$\begin{pmatrix} \epsilon_{xx} \\ \epsilon_{yy} \\ \epsilon_{zz} \\ \gamma_{yz} \\ \gamma_{xz} \\ \gamma_{xy} \end{pmatrix} = \begin{pmatrix} S_{11} & S_{12} & S_{13} & S_{14} & S_{15} & S_{16} \\ S_{21} & S_{22} & S_{23} & S_{24} & S_{25} & S_{26} \\ S_{31} & S_{32} & S_{33} & S_{34} & S_{35} & S_{36} \\ S_{41} & S_{42} & S_{43} & S_{44} & S_{45} & S_{46} \\ S_{51} & S_{52} & S_{53} & S_{54} & S_{55} & S_{56} \\ S_{61} & S_{62} & S_{63} & S_{64} & S_{65} & S_{66} \end{pmatrix} \begin{pmatrix} \sigma_{xx} \\ \sigma_{yy} \\ \sigma_{zz} \\ \tau_{yz} \\ \tau_{xz} \\ \tau_{xy} \end{pmatrix} \tag{4.2}$$

However, the structure of the Kevlar fibre will appear identical after a rotation of 180° about its fibre axis or at right angles to this (see Figure 4.2). This type of anisotropy is called orthotropy. The symmetry of an orthotropic material requires that there is no interaction between the various shear components or between the shear and normal components when the xyz axes are

parallel to the symmetry axes. Thus the stress-strain matrix reduces to:

$$\begin{pmatrix} \epsilon_{xx} \\ \epsilon_{yy} \\ \epsilon_{zz} \\ \gamma_{yz} \\ \gamma_{xz} \\ \gamma_{xy} \end{pmatrix} = \begin{pmatrix} S_{11} & S_{12} & S_{13} & 0 & 0 & 0 \\ S_{12} & S_{22} & S_{23} & 0 & 0 & 0 \\ S_{13} & S_{23} & S_{33} & 0 & 0 & 0 \\ 0 & 0 & 0 & S_{44} & 0 & 0 \\ 0 & 0 & 0 & 0 & S_{55} & 0 \\ 0 & 0 & 0 & 0 & 0 & S_{66} \end{pmatrix} \begin{pmatrix} \sigma_{xx} \\ \sigma_{yy} \\ \sigma_{zz} \\ \tau_{yz} \\ \tau_{xz} \\ \tau_{xy} \end{pmatrix} \tag{4.3}$$

A special case of orthotropy, which does not apply to Kevlar, is when the material has equal properties in all three orthogonal directions, which happens if the crystal has a cubic structure. Many metal crystals are cubic, for example sodium. A cubic structure simplifies further to:

$$\begin{pmatrix} \epsilon_{xx} \\ \epsilon_{yy} \\ \epsilon_{zz} \\ \gamma_{yz} \\ \gamma_{xz} \\ \gamma_{xy} \end{pmatrix} = \begin{pmatrix} S_{11} & S_{12} & S_{12} & 0 & 0 & 0 \\ S_{12} & S_{11} & S_{12} & 0 & 0 & 0 \\ S_{12} & S_{12} & S_{11} & 0 & 0 & 0 \\ 0 & 0 & 0 & S_{44} & 0 & 0 \\ 0 & 0 & 0 & 0 & S_{44} & 0 \\ 0 & 0 & 0 & 0 & 0 & S_{44} \end{pmatrix} \begin{pmatrix} \sigma_{xx} \\ \sigma_{yy} \\ \sigma_{zz} \\ \tau_{yz} \\ \tau_{xz} \\ \tau_{xy} \end{pmatrix} \tag{4.4}$$

Most materials used on a commercial scale are polycrystalline, and consequently have approximately isotropic properties, even if the underlying crystal structure is itself not cubic. The elastic parameters are usually independent of the direction of measurement because the value observed is an average for all directions in the various crystals of the specimen. The elastic constants can then be expressed in terms of Young's modulus, E, and Poisson's ratio, ν; $S_{11} = 1/E$, $S_{12} = -\nu/E$, $S_{44} = 2(1+\nu)/E$. (A shear modulus, G, can also be defined where $G = E/2(1+\nu)$.)

4.3 Published values for Kevlar.

There have been two studies that relate to the transverse properties of Kevlar; an early study by Phoenix and Skelton [1974], and a more recent one led by Kawabata [1993].

Kevlar 49, like all oriented synthetic fibres, exhibits orthotropy; the moduli and compliances are different in the longitudinal and transverse directions. This is due to the inherent asymmetry of the organic molecules that make up the fibres and the drawing that takes place during fibre manufacture. The difference in moduli can be up to a factor of 170 for Kevlar 49 [Phoenix and Skelton, 1974] or a factor of 52 according to Kawabata et al. [1993]. By comparison, polyester exhibits a twenty-fold difference [Hadley et al., 1969].

Values of the axial Young's modulus have been determined for bulk yarns and Parafil ropes, as well as single fibres of Kevlar 49 and polyester. Because there is little twist of the fibres in each yarn, and no twist of the yarns in the rope, the differences between the axial moduli are small. ($129.6 kN/mm^2$ for the fibre [Kawabata et al., 1993], $126.5 kN/mm^2$ for the rope [Linear Composites, 1979].) However, there is no published data for the elastic and plastic properties of the bulk fibres in the transverse direction.

The rope has many voids between the individual fibres and hence initially does not behave as a solid, so elastic compliances are inappropriate. Fortunately, Kevlar 49 fibres deform plastically under transverse loading whilst maintaining most of their axial strength [Phoenix and Skelton, 1974], so the rope will continue to be squashed until there are no voids left, at which point the rope will behave like a solid. The compliances of the rope will then be equal to the compliances of a single fibre. It has been observed in a Parafil spike and barrel termination that the fibres are compressed together so tightly that no water can penetrate along the fibres, and the position of the spike after bed-down is consistent with all the voids being squeezed out of the rope. The fibres themselves probably take up various polygonal shapes

with correspondingly large unrecoverable plastic strains. Before this void ratio is reached, however, it is assumed that the fibre's elastic compliances provide a good estimate for the overall material behaviour. This behaviour is approximated by discrete linear-elastic portions having the same E_L, ν_{TT}, ν_{LT} and G_{LT}, as the fibres but with different values for E_T. The values of E_T are determined by the transverse compression of pads of fibres.

4.3.1 Nomenclature used here.

If the material is transversely isotropic, the strain can be expressed by the following equation [Kawabata and Sera, 1993], where x and y lie perpendicular to the fibre axis, and z lies along it (see Figure 4.3):

$$\begin{pmatrix} \epsilon_{xx} \\ \epsilon_{yy} \\ \epsilon_{zz} \\ \gamma_{yz} \\ \gamma_{xz} \\ \gamma_{xy} \end{pmatrix} = \begin{pmatrix} \frac{1}{E_T} & \frac{-\nu_{TT}}{E_T} & \frac{-\nu_{LT}}{E_L} & 0 & 0 & 0 \\ \frac{-\nu_{TT}}{E_T} & \frac{1}{E_T} & \frac{-\nu_{LT}}{E_L} & 0 & 0 & 0 \\ \frac{-\nu_{LT}}{E_L} & \frac{-\nu_{LT}}{E_L} & \frac{1}{E_L} & 0 & 0 & 0 \\ 0 & 0 & 0 & \frac{1}{G_{LT}} & 0 & 0 \\ 0 & 0 & 0 & 0 & \frac{1}{G_{LT}} & 0 \\ 0 & 0 & 0 & 0 & 0 & \frac{2(1+\nu_{TT})}{E_T} \end{pmatrix} \begin{pmatrix} \sigma_{xx} \\ \sigma_{yy} \\ \sigma_{zz} \\ \tau_{yz} \\ \tau_{xz} \\ \tau_{xy} \end{pmatrix} \tag{4.5}$$

The elastic parameters are:

E_L The longitudinal modulus of the fibre, found by measuring the extension of a fibre when pulled axially.

E_T The transverse modulus of the fibre, found by compressing a fibre under a microscope and relating its change in diameter to the applied load.

G_{LT} The longitudinal shear modulus of the fibre, found by relating the shear stress to the shear strain when a fibre is twisted in a torsion tester.

ν_{LT} The longitudinal Poisson's ratio of the fibre. This relates the strains of longitudinal extension with transverse contraction when the fibre is uniaxially stretched along its axial direction. It can be determined by

measuring under a microscope the diameter and length changes of a fibre under axial extensions.

ν_{TT} The transverse or in-plane Poisson's ratio of the fibre. This relates the strains of transverse extension with transverse contraction when the fibre is uniaxially stretched in the plane of its cross section. It can be found by making a composite plate with a high volume fraction of fibres, which is then strain gauged and loaded.

4.3.2 Correlation of fibre and Abaqus parameters.

The parameters needed for the Abaqus analysis (Chapter 5) are defined by:

$$\begin{pmatrix} \epsilon_{11} \\ \epsilon_{22} \\ \epsilon_{33} \\ \gamma_{12} \\ \gamma_{13} \\ \gamma_{23} \end{pmatrix} = \begin{pmatrix} \frac{1}{E_1} & \frac{-\nu_{12}}{E_1} & \frac{-\nu_{13}}{E_1} & 0 & 0 & 0 \\ \frac{-\nu_{12}}{E_1} & \frac{1}{E_2} & \frac{-\nu_{23}}{E_2} & 0 & 0 & 0 \\ \frac{-\nu_{13}}{E_1} & \frac{-\nu_{23}}{E_2} & \frac{1}{E_3} & 0 & 0 & 0 \\ 0 & 0 & 0 & \frac{1}{G_{12}} & 0 & 0 \\ 0 & 0 & 0 & 0 & \frac{1}{G_{13}} & 0 \\ 0 & 0 & 0 & 0 & 0 & \frac{1}{G_{23}} \end{pmatrix} \begin{pmatrix} \sigma_{11} \\ \sigma_{22} \\ \sigma_{33} \\ \tau_{12} \\ \tau_{13} \\ \tau_{23} \end{pmatrix} \tag{4.6}$$

Where direction 2 lies parallel to the fibres, direction 1 is perpendicular to the fibres in the plane of analysis, and direction 3 is perpendicular to this plane (the hoop direction) (see Figures 4.4 and 5.2). The local axes for the rope are aligned with the individual elements, which are themselves angled relative to the global axes by between 3° and 3.5°, the taper angles of the barrel and spike.

By comparing like terms between the fibre matrix and the Abaqus matrix, the following identities can be derived. The values quoted are taken from Kawabata et al. [1993] and relate to single filaments:

Abaqus nomenclature	Fibre nomenclature	Kawabata's value
E_1	E_T	2.49kN/mm^2
E_2	E_L	129.6kN/mm^2
E_3	E_T	2.49kN/mm^2
ν_{12}	$\nu_{LT}\frac{E_T}{E_L}$	0.0119
ν_{13}	ν_{TT}	0.31
ν_{23}	ν_{LT}	0.62
G_{12}	G_{LT}	2.01kN/mm^2
G_{13}	$\frac{E_T}{2(1+\nu_{TT})}$	0.924kN/mm^2
G_{23}	G_{LT}	2.01kN/mm^2

4.4 Transverse compression of a pad of fibres.

Tests to obtain transverse properties on single filaments are not relevant to bulk fibres, which will interact laterally. It might be possible to conduct tests on a limited number of filaments suitably constrained, but the practical difficulties of doing so and the uncertainty of its relevance to the bulk properties makes it not worthwhile.

Instead, it was decided to carry out tests on the bulk fibre, as far as possible retaining the fibre orientation used in the actual termination. Blocks of fibre were placed in a chamber which constrained them in one transverse direction, but left them free axially. The fibres were then compressed transversely and the force and displacement measured. The blocks of fibre were about 15mm high before loading, with various figures for the length and width. Thus, many thousands of fibres would be present and the exact orientation of the individual fibres could not be guaranteed.

The fibres were allowed to be free axially such that there would be no axial buckling. (In the termination itself, the fibres remain in tension throughout (Figure 6.32), so they do not buckle either.) When the spike beds down in

the termination, the gap between the spike and the barrel will significantly reduce.

As in the termination geometry (Figure 4.4), the greatest strains in the pad will occur in the transverse x direction across the pad, and the transverse radial direction across the rope. There will be minimal strain in the other transverse (hoop) direction in the rope, and zero y strain in the pad. There will, of course, be significant stresses in the circumferential transverse direction and these will also appear in the finite element model.

4.4.1 Sizing of rig.

The larger the cross sectional area of the fibre pad, the larger the force needed to squash the fibres. The compression machine used for these experiments had a capacity of 50kN. However, by increasing the cross sectional area, any misalignment errors due to the difficulties in placing the fibres in the rig are minimised.

The larger the height of the specimen the greater the value of displacement to be measured, so accuracy is improved. However, if the height is too large, the whole specimen may buckle in the free direction rather than crush.

Several trial runs were performed with a plunger of size 19x3mm (i.e. 19mm in the axial direction and 3mm transversely), but this proved to be too narrow. The resistance due to the plunger rubbing on the sides due to the plunger bowing was reasoned to be of the same order of magnitude as the force transmitted to the fibres. Therefore a more stocky plunger of size 20×20mm was used, and when squashed outside the rig it showed no signs of buckling under the maximum load.

To minimise friction, the sides of the plunger were lightly oiled. At the maximum load of the tester this plunger gives a stress of 125N/mm^2. Higher stresses were achieved by using plungers of sizes 20×10mm and 10×10mm. The values for the common lower stresses are compared.

4.4.2 Experimental set-up.

The rig consisted of two blocks of steel bolted together by four M8 bolts. A shape was milled out of one block such that it acted both as a guide for the plunger and as a receptacle for the fibres as shown in Figure 4.5.

A slice of the steel plunger was attached to the bottom of the receptacle, directly below the plunger, to give an exact cross section to the specimen of fibres. The fibres were cut slightly longer than the width of the plunger (by about 2mm) so that they would protrude slightly rather than be too short. The extra length of the protruding fibres barely affected the cross section as they were unconstrained at the top and bottom and therefore splayed out carrying negligible load.

It was found that the easiest way to cut the fibres to the right length and ensure that they were aligned as parallel as possible was to saw off the correct length from a piece of 30 tonne Parafil G (Kevlar 49) rope, then cut through the plastic sheath and remove the fibres en masse.

As many fibres as possible were laid in the receptacle before the two halves of the rig were bolted together. The fibres were then compacted by hand and more added through the top of the rig, care being taken to ensure that the fibres were correctly aligned and were level across the depth of the specimen.

The plunger was then inserted and the rig placed centrally in a compression machine. Curves of force–displacement for the plunger were recorded by a plotter attached to the machine.

4.4.3 Observations.

As can be seen from Figure 4.6, (a plot of force-displacement for a Kevlar pad), the unloading and reloading curves are markedly different due to hysteresis.

From the load displacement curve three stiffnesses can be assigned for a load **F** as shown in Figure 4.7:

stiffness A, the tangent to the curve on loading, which is applicable to the modelling of the spike bed down during the first loading of the rope.

stiffness B, the slope of the force-displacement curve on unloading from this load. This is applicable to modelling the unloading behaviour.

stiffness C, the slope of the force-displacement curve on reloading back to this load after unloading. This would be applicable to modelling the reloading behaviour when the maximum load experienced was **F**. However as seen in Chapter 6 (Figure 6.31), the compression across the fibres hardly drops on unloading. Therefore the hysteresis will be much lower than for a total unloading. So the Kevlar does not follow **B** down and **C** up, but just goes down and up **B** a small way.

4.4.3.1 Speed.

Due to the viscoelastic behaviour of Kevlar the rate of loading is important. Tests were carried out at various speeds to quantify this effect — no significant dependence of modulus on speed was noted for the speeds liable to be encountered in the stressing of the terminations for curve **A**. However for curve **B** the faster the pad was loaded, the greater the stress relaxation when the plunger was stopped to cycle the load, so the tests were performed very slowly, with a plunger movement of 0.01mm/min (a strain rate of $60\mu\epsilon$/min).

When loaded at a faster rate of 0.5mm/min, for the 20×20mm pad, shown in Figure 4.6, the total loading procedure took about 30 minutes. On maintaining the maximum plunger displacement for 5 minutes, the force in the specimen dropped from 50kN to 45kN due to stress relaxation. When loaded back to 50kN the specimen had compressed by a further 0.1mm.

When loaded at 0.01mm/min, the runs took up to 10 hours, and no noticeable

change was observed when the full load was left applied for 24 hours. So this loading rate was used for the determination of the transverse moduli as it is representative of the loading rate used in the 60 tonne rope tests presented in Chapter 7. A further discussion of the effect of the transverse viscoelasticity is contained in Chapter 8.

4.4.3.2 Calibration.

There is a small amount of flexibility in the rig and compression machine; this was compensated for by compressing the rig alone, with no fibres present, and measuring the deflection output by the transducer. As can be seen from Figure 4.6 the apparatus stiffens up at about 1kN and then has an almost linear force–deflection graph up to the maximum load of 50kN. A separate calibration curve for each plunger was used to obtain the compression curves for the fibres alone.

4.4.3.3 Plasticity.

As the specimen is compressed, the fibres slip past each other so an irreversible deformation takes place. The fibres will also yield plastically. For Kevlar it has been noted [Phoenix and Skelton, 1974] that a large transverse plastic deformation can be sustained whilst still maintaining significant axial tensile strength.

Eventually all the voids will be filled and for further deformation the specimen will have to strain in the axial direction so the stiffness will rise by many orders of magnitude. This would suggest that the deformation of the sample will be asymptotic to the height of the fully compressed sample, which was observed (Figure 4.8). (The number of yarns in each sample was counted and since the number of fibres in each yarn is known, as is the fibre diameter, then the height of the fully compressed sample can be determined.)

4.4.3.4 Compression of a fibre to a rectangle using a finite element analysis.

A small finite element analysis was performed using Abaqus to model the elastic-plastic compression of a fibre to a rectangle. The plain strain elements used are shown in Figure 4.9, as is the deformed state when compressed to 75% of the original height. The material properties used were; Young's modulus 2490N/mm^2, Poisson's ratio 0.31, and a perfectly plastic yield stress of 320N/mm^2 (The shear yield strength is 160N/mm^2 [Kawabata and Sera, 1993], so the transverse yield stress was assumed to be twice this [Ashby and Jones, 1980].) Because of the symmetry there is zero friction along the boundaries. In Figure 4.8 the mean stress compressing the fibre is plotted against its height, normalised relative to the height of the same material occupying a rectangular shape of the same width.

There is reasonable agreement between this analysis and the actual test results, indicating that these fibres may be compacting to a rectangular rather than a perfectly hexagonal shape.

4.4.3.5 Yield line analysis of a fibre compressing to a hexagon.

A simple yield line analysis was performed assuming the pattern in Figure 4.10. The resulting force displacement curve is plotted in Figure 4.8.

This analysis starts off with all the fibres perfectly packed, so at low stresses it differs greatly from the tests which are packed much more loosely at the start. However at higher stresses the curves converge, but the test curves are not asymptotic to the yield line analysis because this does not take into account the elasticity of the fibres, shown by curve 'z'. If an allowance is made for the elasticity, then combining curves 'y' and 'z' will provide a reasonable asymptote for the experimental results.

4.4.3.6 Young's modulus on first loading (Curve A).

Figure 4.11 shows a typical force-displacement curve for the Young's modulus on first loading (Curve A) for Kevlar 49. Due to the unloaded height of the specimen changing as it is compressed, an 'effective height' for use in determining the modulus can be obtained by extrapolating the tangent back to the x axis. By taking the tangents to the respective force-displacement curves, the modulus (derived using the nominal strain) can be calculated. Figure 4.12 shows several loading modulus versus maximum stress curves, for plungers of size 20×20, 20×10 and 10×10mm. As can be seen from the figure, at the lower stresses, the curves for the three plunger sizes are superimposed. Only the stresses up to 140N/mm^2 are of interest as this covers the range of compressive stresses indicated by the finite element analysis. The values found in the literature are also shown for comparison purposes.

These moduli are not of direct use for the Abaqus analysis however, since Abaqus uses Cauchy (or true) stress and log strain ($f(\lambda) = \ln(\lambda)$) rather than the more common nominal (or Biot's) strain ($f(\lambda) = \lambda - 1$), where λ is the stretch ratio, the ratio of current height to original height. Figure 4.13 shows the graphs of the effective stress applied versus the log strain. The initial height of the samples was taken to be the height at a stress of 10N/mm^2, which was chosen so that the effects of the initial compaction by hand would be diminished, but it was also small enough not to affect the curves greatly. One curve had a blip at 10N/mm^2 and is therefore offset relative to the others. Taking the tangents to these curves $\partial\Delta\sigma/\partial\Delta\epsilon$, gives the moduli for use in the analysis which are listed in Table 4.1. (An 'effective height' is not needed because the moduli are determined directly from the stress–strain curve.)

4.4.3.7 Young's modulus on unloading-reloading (Curve B).

As can be seen from Figure 4.14, on unloading-reloading a small way, the curves **B** and **C** are superimposed, so only one stiffness is needed to model this part of the loading.

Figure 4.15 shows the curves of the effective stress versus the log strain derived by digitising three loading-unloading curves. By taking tangents to the unloading-reloading portions the stiffnesses for the analysis are derived. These are given in Table 4.2.

4.5 Values for use in the finite element model

All the values stated in Section 4.3.2 were used for the analysis except for the transverse moduli E_T, which are derived from curves **A** and **B**. Tables 4.1 and 4.2 show the values used.

4.6 Summary.

Most of the elastic properties of Kevlar 49 are reported in the literature with the exception of large-scale transverse compression which has not been significantly studied before. The transverse compression is a major factor in the functioning of Parafil terminations and therefore transverse compression tests on pads of fibres were carried out.

It is seen that there are two distinct ranges of transverse modulus; one set for first loading which applies to the initial loading of the Parafil rope, and another set with a much higher modulus for the unloading-reloading which applies to the cyclic loading of the rope.

The moduli increase as the specimen is loaded due to the void ratio decreasing. It is possible to match these moduli by discretising the loading curves for insertion into the finite element analysis described in Chapter 5.

Maximum stress less than: (N/mm^2)	Modulus taken to be: (kN/mm^2)	Used for first loading to:
27	0.27	30%
72	0.45	60%
136	0.85	100%

Table 4.1: Transverse Moduli E_T for initial loading.

Maximum stress less than: (N/mm^2)	Modulus taken to be: (kN/mm^2)	Unloading-reloading from:
72	5.8	60%
136	16.4	100%

Table 4.2: Transverse Moduli E_T for unloading-reloading.

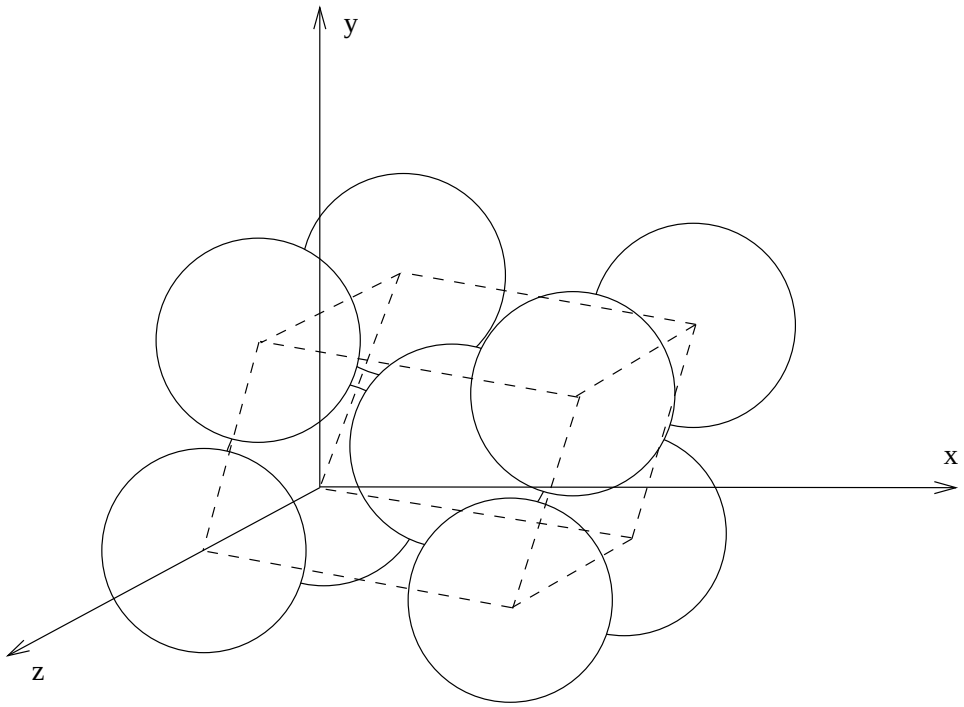

Figure 4.1: An anisotropic metal crystal structure, where the lattice axes are not orthogonal, and the atom separations along each axis are different.

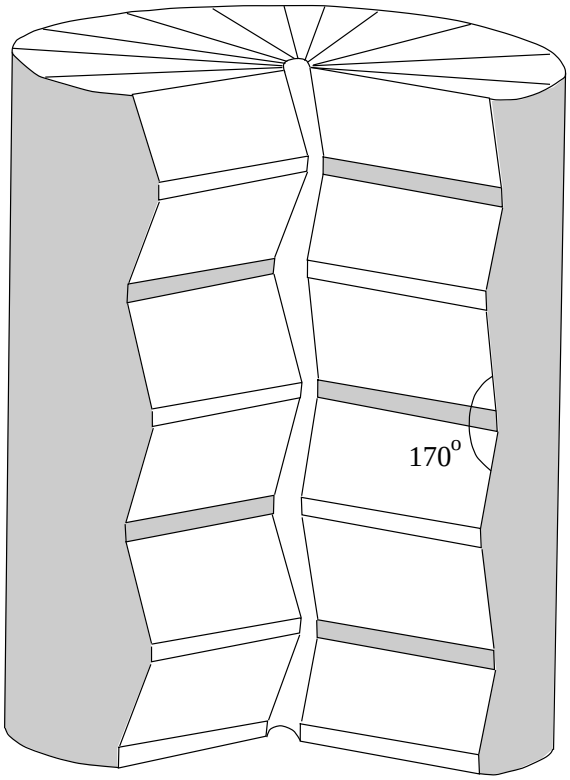

Figure 4.2: The structure of a Kevlar fibre, showing the difference between the transverse and axial properties [Dobb and Robson, 1990].

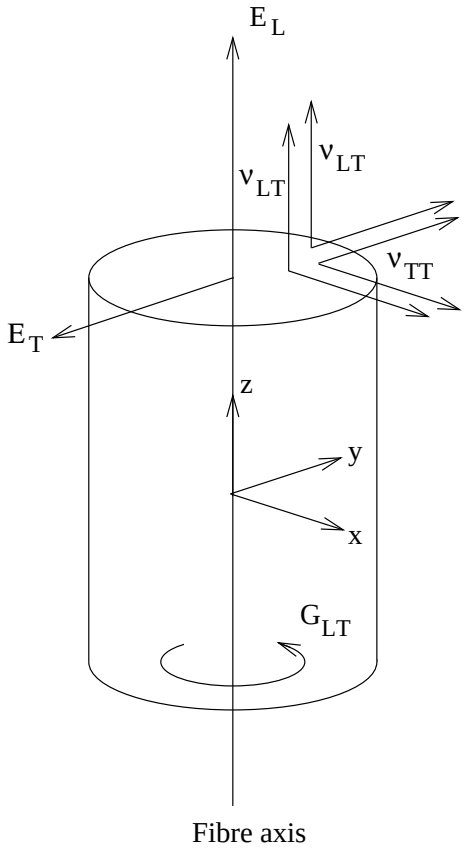

Figure 4.3: Nomenclature for expressing the elastic parameters of a fibre.

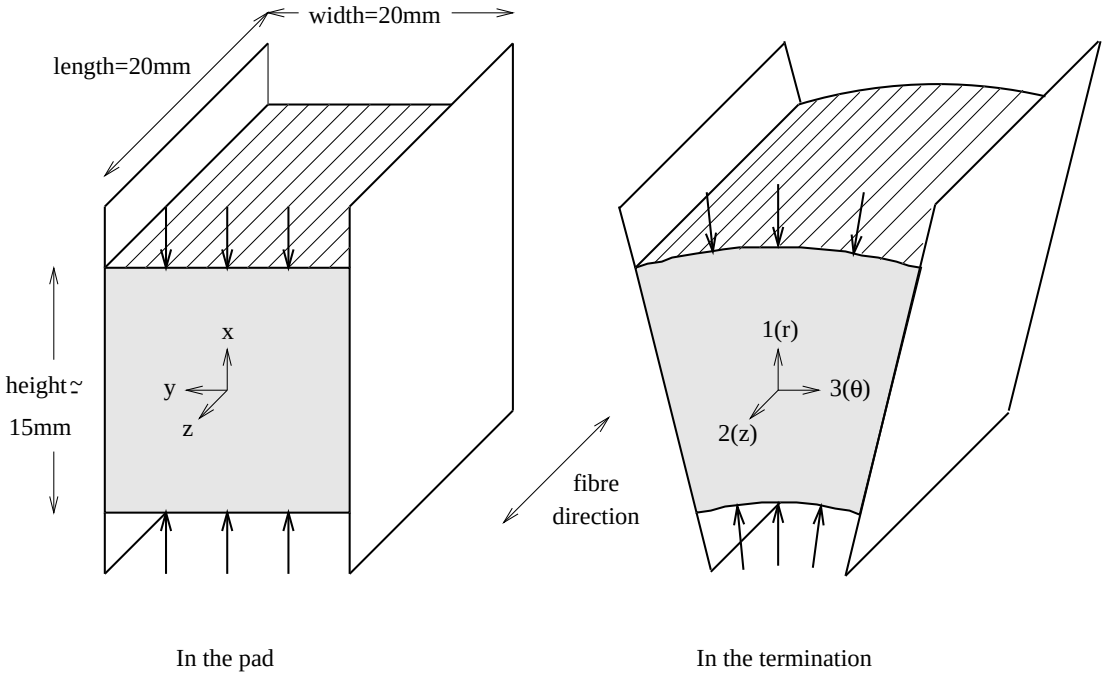

Figure 4.4: Similarities between the fibres in the termination and in the pads; the fibres are aligned in the z directions and transversely compressed in the x and r directions, with no or negligible strain in the third direction.

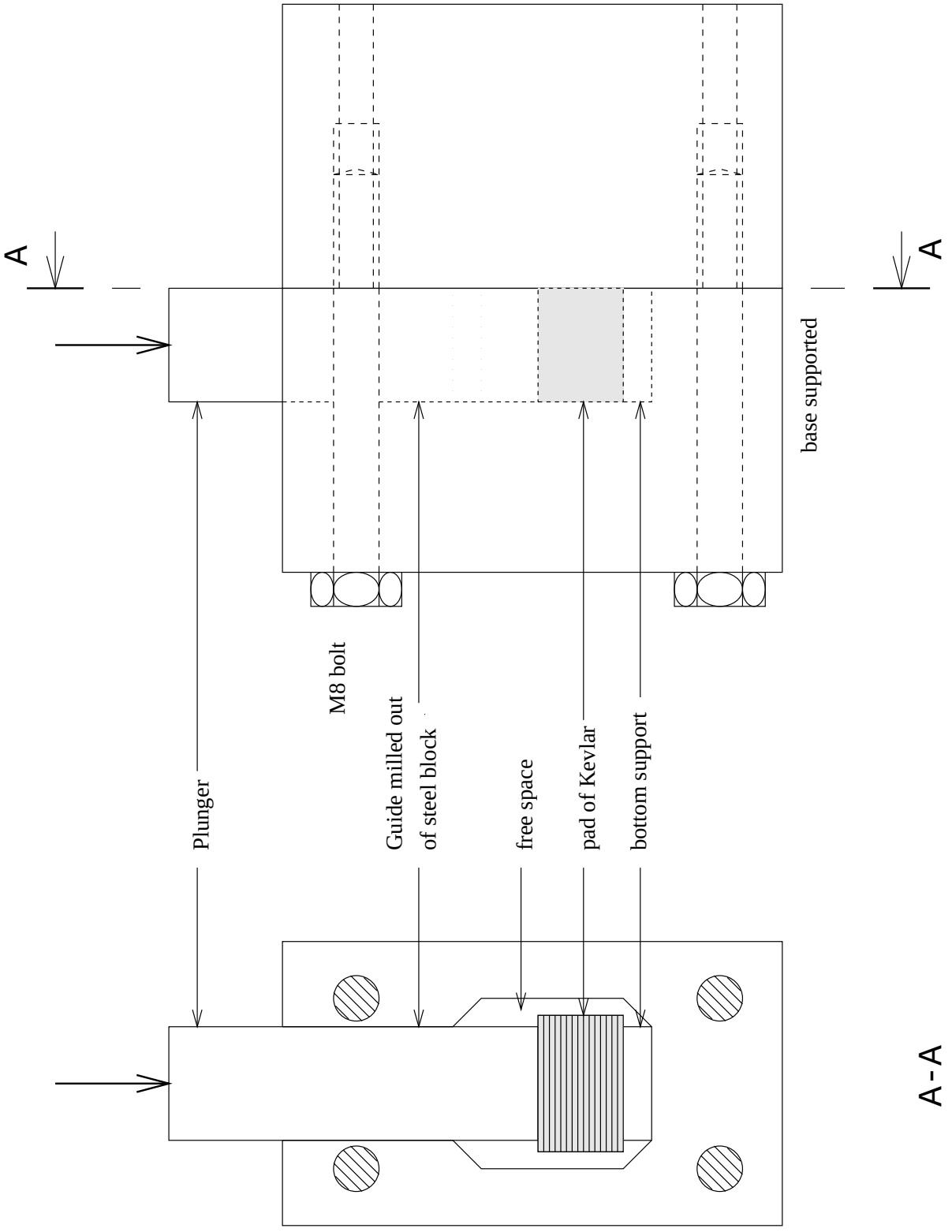

Figure 4.5: The rig used for the transverse compression of pads of fibres, consisting of two steel blocks that are bolted together, the fibres occupy a void in one block where they are compressed by a steel plunger.

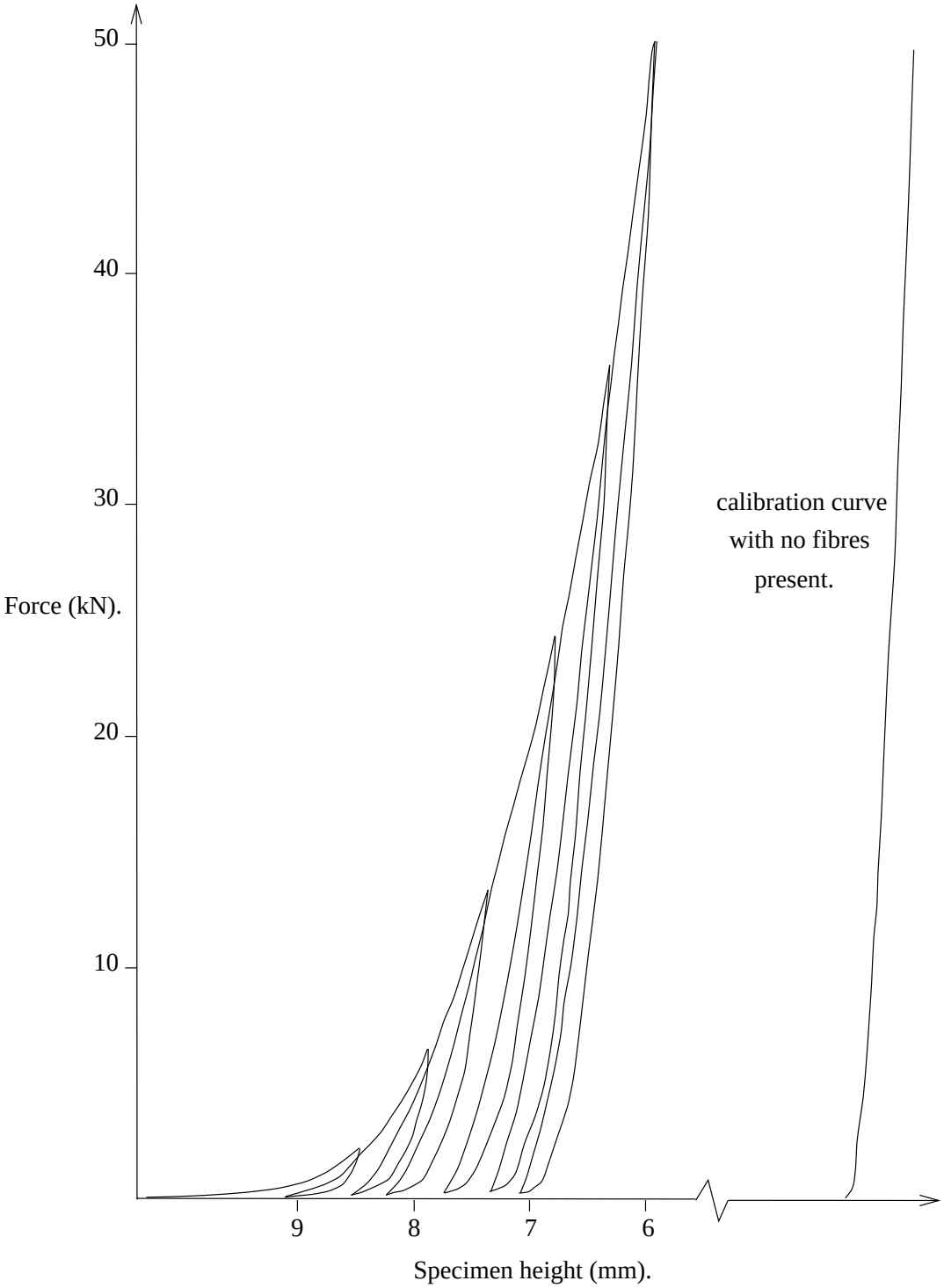

Figure 4.6: A typical load-displacement curve for a transversely compressed Kevlar pad showing the reduction in height as the load is increased and the hysteresis in the unloading-reloading curves. This test had a plunger of 20×20mm and was loaded at 0.5mm/min.

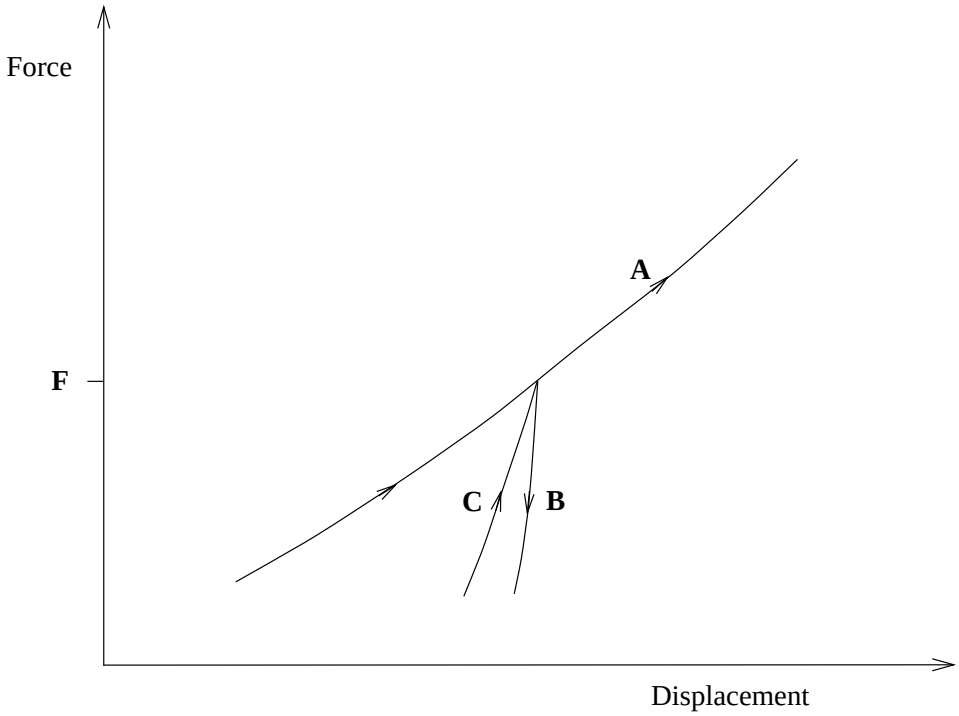

Figure 4.7: The load-displacement curve for a given load **F** of a transversely compressed pad of Kevlar 49 fibres; curve **A** represents the modulus on first loading, curve **B** the modulus on unloading, and curve **C** the modulus on reloading.

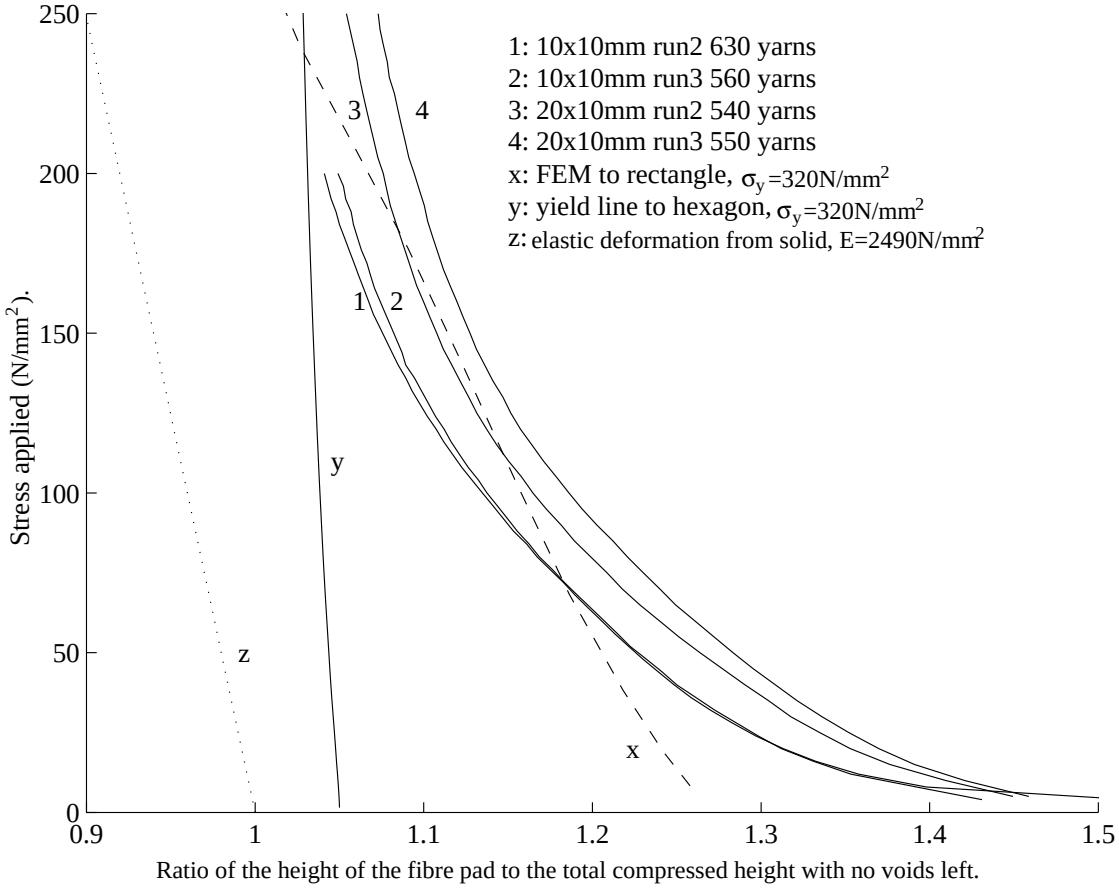

Figure 4.8: Compression of Kevlar pads towards a zero void ratio. Four experimental curves 1-4 correlate well with a simple finite element analysis, curve x, of a fibre deforming into a rectangle. Curve y represents a yield line analysis for hexagonal packing, and curve z represents the elastic compression of a zero void specimen.

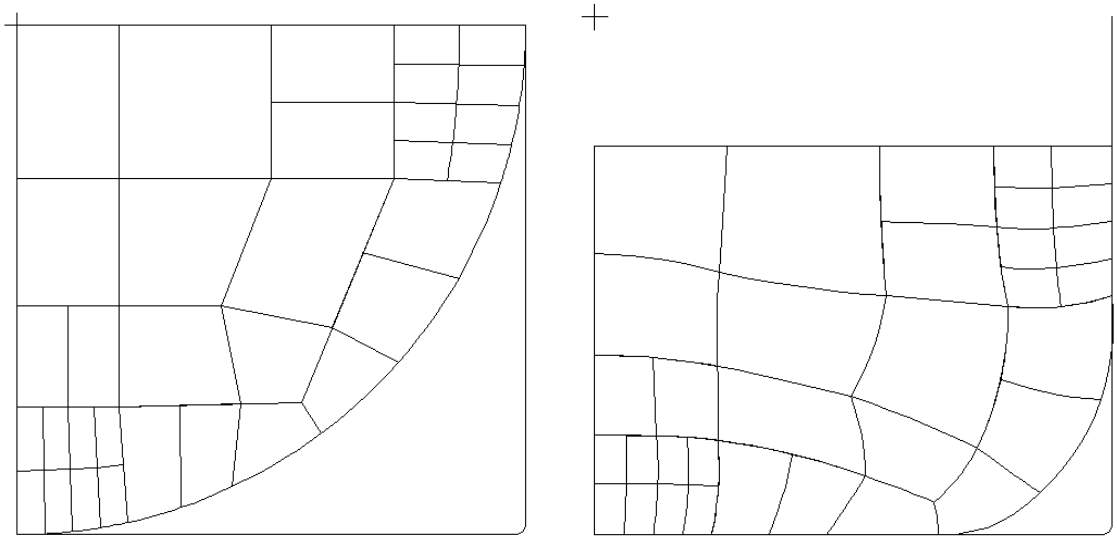

Figure 4.9: Finite element analysis of the transverse compression of a fibre into a rectangular packing arrangement. E=2490N/mm^2, σ_y=320N/mm^2, ν_{TT}=0.31, the deformed state is at a load of 250N/mm^2.

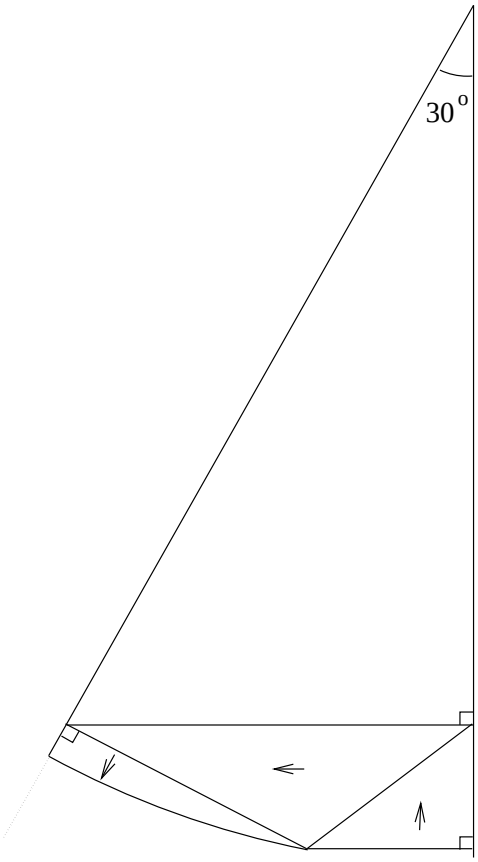

Figure 4.10: Yield lines assumed for the analysis of a fibre transversely compressed into a hexagonal packing arrangement. The axes of symmetry subtend an angle of 30°.

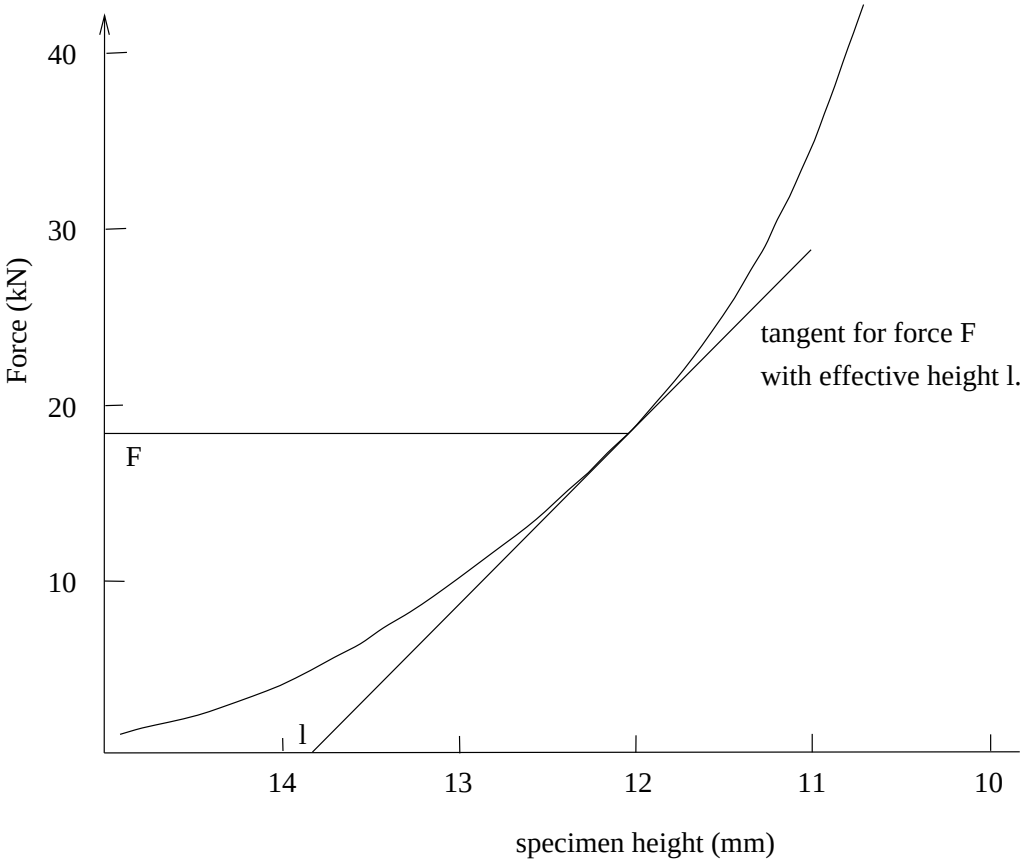

Figure 4.11: Curve **A**, typical force-displacement curve for first loading of a transversely compressed pad of Kevlar 49 fibres. At a given load **F**, the elasticity is determined by the tangent to the curve with an effective initial pad height of l. (540 yarns in a 20×10mm cross-section loaded at 0.5mm/min, after the correction is applied for the flexibility in the rig.)

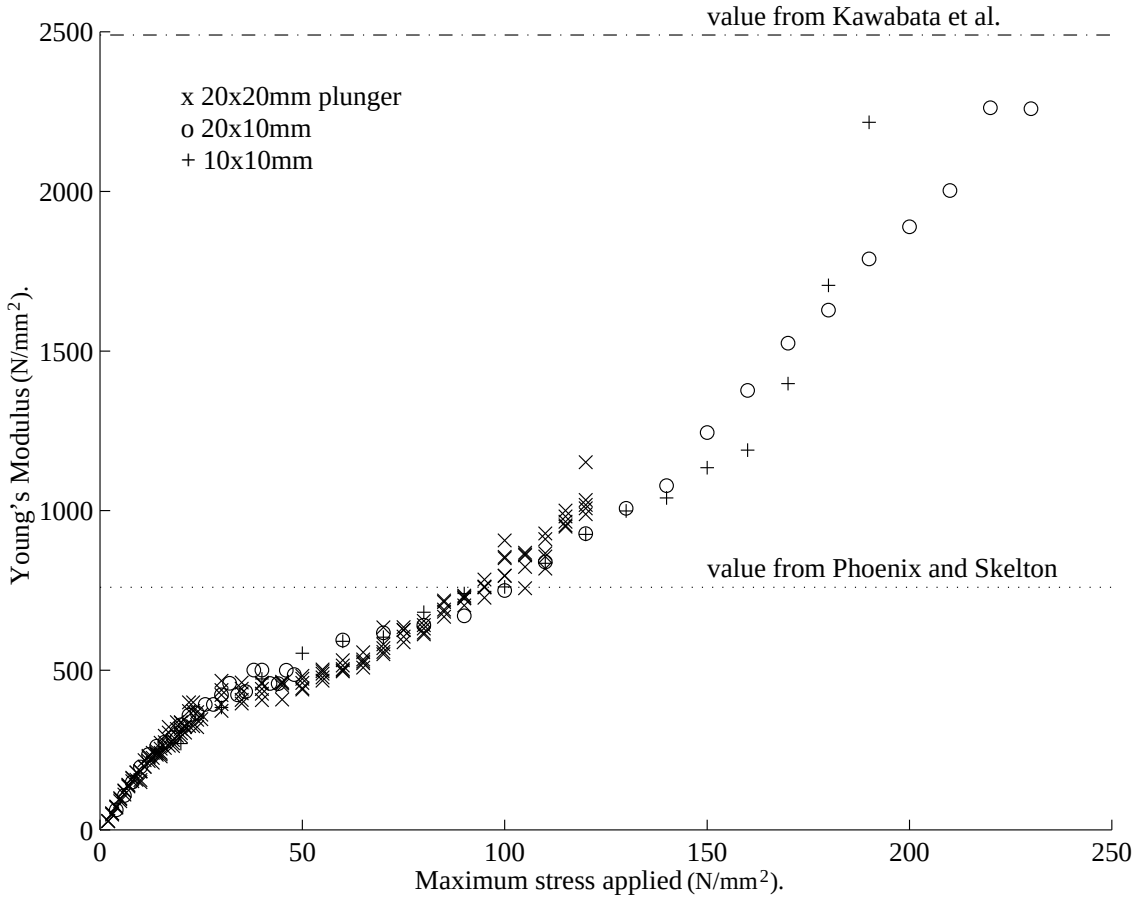

Figure 4.12: Transverse Young's modulus on first loading versus maximum stress applied, for a pad of Kevlar 49 fibres. The modulus increases as the void ratio is progressively reduced on loading.

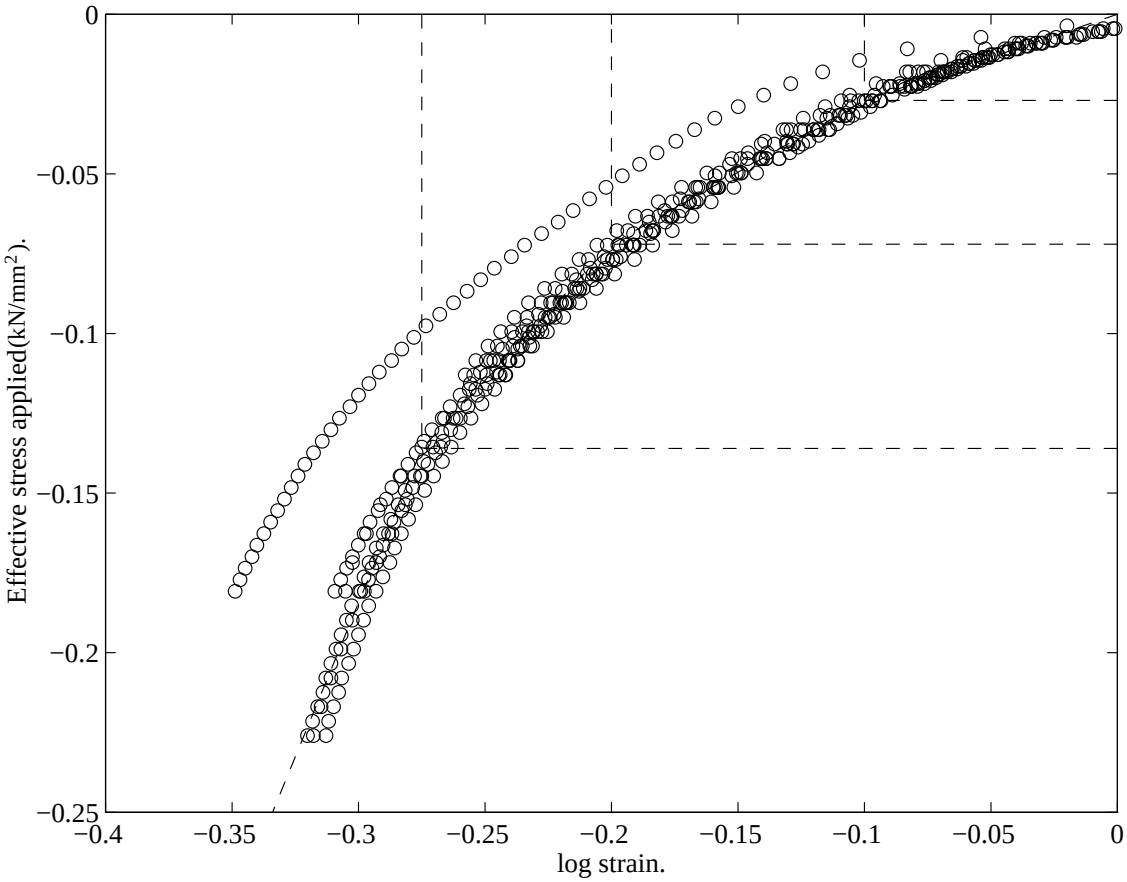

Figure 4.13: Transverse stress – log strain curves for the first loading of pads of Kevlar 49 fibres. The dotted lines represent the zones that are applied in the finite element analysis of a Parafil termination, Table 4.1.

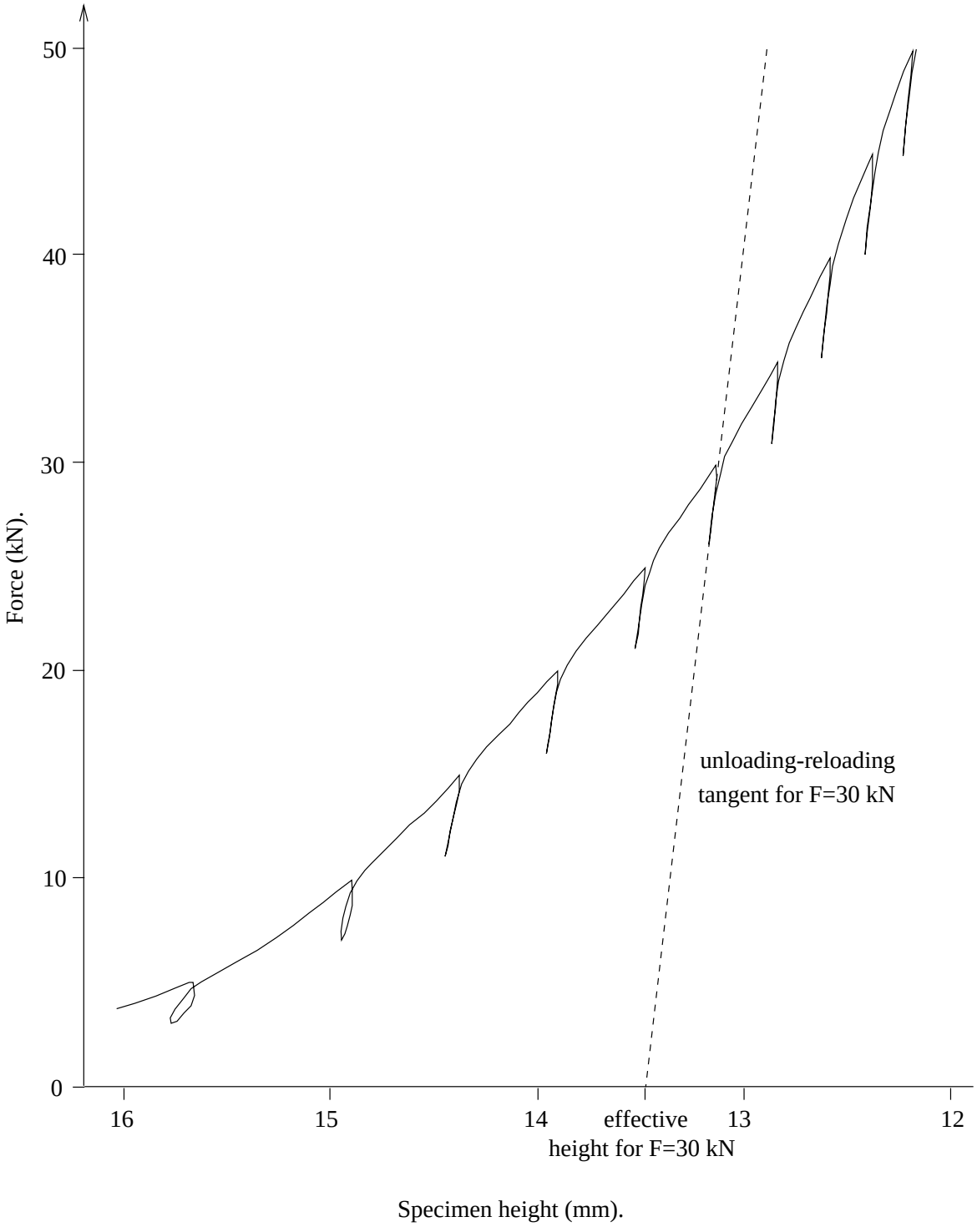

Figure 4.14: Curve **B/C**, typical force-displacement curve for the transverse unloading-reloading of a pad of Kevlar 49 fibres. The modulus can be derived from the tangent to the curve, and the effective height of the pad, obtained by extrapolating back to the axis. (This curve is a 20×10mm pad loaded at 0.01mm/min, with a correction due to the rig flexibility applied.)

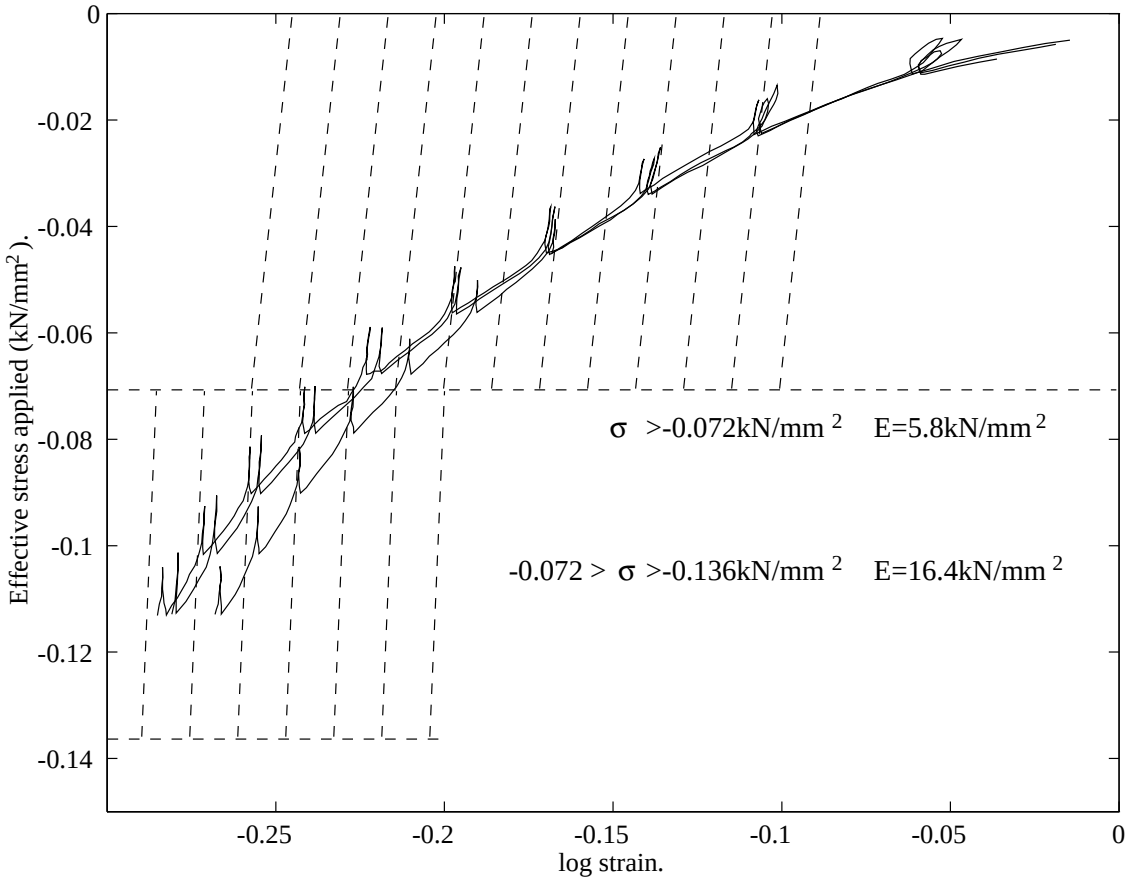

Figure 4.15: Transverse stress — log strain curves for the unloading-reloading of pads of Kevlar 49 fibres. The two zones (Table 4.2) used in the finite element analysis of a Parafil termination are indicated.

Chapter 5

Finite element modelling of a parafil termination.

5.1 Introduction.

This chapter outlines the finite element analysis used to study Parafil rope terminations. In order to model the complexities of a polymeric material like Kevlar, it was necessary to write user-subroutines for use in Abaqus to model the stick-slip friction and the material properties. The data used in these subroutines was found by experiment as detailed in Chapters 3 and 4.

The implementation of these subroutines is discussed here. A discussion then follows detailing the geometry; both the element selections, and the mesh sizing. The chapter concludes by describing the method for accomplishing the most difficult part of the analysis – the initial contact.

5.2 Alternatives to finite elements.

Finite elements are not the sole means of analysis available. Before computers were available, problems in elasticity and continuum mechanics were best expressed in terms of partial differential equations. However, solutions are only available for simple loadings and geometries, so many assumptions would have to be made before analysing a termination.

It is possible to analyse the termination on the assumption that the rope is uniformly compressed along its length, the barrel and the spike are rigid, and the principle of equilibrium holds. These are the principles that are used to design barrels and spikes. However this analysis does not take into account the elastic, and perhaps plastic, deformation of the various components. Nor is there any indication of the magnitude of slip and the contact pressure where slip occurs, which are important variables in determining the life of a termination subjected to cyclic loading.

The development of sufficiently powerful computers has enabled the practical use of large scale discrete methods. These usually take two forms; finite difference models and finite element models. They produce algebraic equations rather than differential equations, but in such abundance that a computer is needed to solve them. A finite element may be visualised more easily as an identifiable portion of the structure, with nodes on its boundaries. Adjacent elements are connected at the nodes. In contrast, the nodes of a finite difference molecule do not bound a region, and the connectivity is of an interlocking type. For some engineering structures, for example beams on equidistant supports, a finite difference approach offers advantages over finite elements. Finite differences use an approximating Taylor series to obtain a representation of $\mathrm{d}^n y/\mathrm{d}x^n$ which is obtained by truncation. Finite difference analyses are faster to set up than if a new finite element has to be written, but if appropriate finite elements are available, they are more easily applied to general problems. The finite element approach offers more generality, permitting easy modelling of arbitrary shapes, with arbitrary loadings and boundary conditions, which is why it is used here. Finite elements also have the advantage that they can be visualised whereas differential operators can not.

5.3 The finite element approach.

The basic concept is to replace a solid continuum with a mesh of small elements. The mesh is coarse at areas of low stress concentration to save on computation and refined to a fine mesh at areas of high stress concentration to facilitate convergence to the true stresses.

There are many shapes and sizes of finite element available, but for this analysis an eight-noded axisymmetric quadrilateral was chosen for the solid regions of the mesh. This element has the advantage of a mid-sided node to enable the element to map complex shapes, and the quadratic shape function means that there are fewer discontinuities than for four smaller four-noded elements. Quadrilaterals were chosen over triangles because the termination has a quadrilateral shape, so the mesh is easier to generate.

5.4 An Abaqus finite element analysis of a Parafil termination.

5.4.1 Introduction.

Abaqus is a powerful general purpose finite element package, including the main program Abaqus/Standard, and an interactive post-processor Abaqus/Post, which provides displays and output lists from restart and results files written by Abaqus/Standard. Abaqus comes with comprehensive manuals which should be studied before any analyses are performed. Only the special coding used to model the contact and material properties is given in this chapter; details of how to operate Abaqus on a 'day-to-day' level are available elsewhere.

Abaqus runs as a batch application. The main input is a file which indicates which options are required, and gives the data associated with those options. There may also be supplementary files, such as restart or results files, or

auxiliary data files. The main input is discussed in the terminology of a card image file; each line of the file represents a card that, many years ago, would have been used to input data. For analysis the file consists of two sections, model input and history input. The model input defines the geometry and materials used, and the history defines the loading sequences applied. The loading is divided by the user into a series of steps, each step being the response to a type of loading. The definition of a step includes the procedure type (static), control parameters for time integration or for the non-linear solution procedures, the loading, and output requests. What constitutes a step is a matter of choice for the user. For example, a static load might be applied in one step, or if more detailed output is required at higher load levels the same analysis might be broken into two steps so that the output requests can be changed.

This section outlines how the input data file for the analysis of the termination has been prepared.

The spike-and-barrel termination is modelled by axisymmetric elements as the termination itself is axisymmetric. The solid elements used are `CAX8` (an eight noded biquadratic rectangular element) for the majority of the spike, rope, and barrel (see Figure 5.1 for numbering of element), and `CAX6` (a six noded quadratic triangular element) for mesh refinement in the spike.

5.4.2 Geometry.

The geometries of the barrel and spike were determined by measuring an actual 60 tonne aluminium spike-and-barrel termination. This was performed in the metrology laboratory in CUED. A probe is inserted into the barrel or traversed around the spike, and touched against four points on the circumference; these coordinates are then used to calculate the centre of the circle and the radius. This is repeated at various sections along the length to build up the total geometry. As shown in Figure 7.4, the barrel is 320mm long, it has an outside diameter of 110mm and a uniform inner taper of approximately

3° along its inner contact surface; the inner surface is cylindrical at each end of the barrel, as seen in Figure 5.4. The spike is 232mm long with a varying taper of approximately 3.5°.

In the model there are a total of 2363 elements and 4864 nodes.

Figure 5.2 shows a schematic representation of an axisymmetric 'wedge' of a Parafil termination.

5.4.2.1 Spike.

The spike is made up of 229 elements, numbered in the range 40003 to 41071, and 862 nodes numbered between 40005 and 41641 as illustrated in Figure 5.3. The majority of the spike has four elements across its half width, with mesh refining at the base where the rope curls over the end, and at the bottom of the threaded hole. The numbering in Abaqus does not matter as the program renumbers everything internally to reduce the bandwidth of the stiffness matrix. In general everything is numbered such that different bodies have their own region of numbering as this makes reading the output easier.

The nodes along the axis are given the node set `AXIS` to enable them to be moved in unison during the initialisation.

5.4.2.2 Barrel.

There are 390 elements in the barrel, with elements numbers between 30001 and 30590, and 1423 nodes with numbers between 30001 and 36015. They are generated in a similar manner to the spike, see Figure 5.4. There is mesh refinement along the inner surface to model the contact zone in detail (see Section 5.4.2.6).

5.4.2.3 Rope.

The rope is modelled as three separate layers to highlight any relative slipping between the layers that may occur near the nose of the spike (Figure 5.5). Each layer is one `CAX8` element thick. Although this may look crude, tests on various densities of elements (Section 5.4.6) showed that a rope layer one element thick gives the exactly same contact conditions as a layer three elements thick. The coordinates were set such that an aspect ratio less than 5 was in effect for all the rope elements throughout the analysis.

The initial coordinates of the elements are determined by calculating outwards from the spike surface assuming one third of the rope's cross sectional area goes into each layer; the nodes within each layer are also spaced such that there is an equal area between each. There is also an offset applied to each layer as detailed in Section 5.4.7.1 to separate them at the start of the analysis. The initial cross sectional area of the rope is taken to be the area after a pressure of $10N/mm^2$ has been applied, in order to be consistent with the data obtained from the transverse compression of pads of fibres (see Chapter 4). For a 60 tonne Parafil G rope this area was taken to be $427.7mm^2$, which was back calculated from the total compressed area of fibres (given as $305.5mm^2$); the transverse compression data in Chapter 4 gives a factor of 1.4 for the ratio of areas at $10N/mm^2$ to fully compressed.

When the rope was modelled as one body, significant shear forces were observed in the analysis within the rope. Therefore the rope was remodelled as three separate layers; each layer being one element wide by 74 elements long. The inner layer has element numbers between 1100 and 1392 and node numbers between 1000 and 8408. The numbering is shown in Figure 5.5. The middle layer has element numbers between 2100 and 2392 and node numbers between 11008 and 18416. The outer layer has element numbers between 3100 and 3392 and node numbers between 21016 and 28424.

In an ideal analysis, the modelling of the rope would start in the main body of

rope outside the termination and continue through past the base of the spike. However, so much shear deformation and compaction occurs at either end of the contact zone that modelling these zones is more complicated than the rest of the analysis. For this analysis the rope is cut just short of either end of the contact zone, which means that there is bare metal in the termination where there would, in reality, be contact; the error on the spike and barrel should be minimal as these regions are small.

At the nose of the spike, it is assumed that the axial stress on the rope is uniform across its cross section, but this is not necessarily true. At some point in the body of the rope away from the termination the stress will be uniform due to the effects of yarn-on-yarn friction. However the geometry of the termination affects the way the rope splays out from the contact zone into the main body of rope, and this in turn affects the load transfer from the rope to the termination.

5.4.2.4 Interface elements.

Interface elements are used between the various surfaces of the model as explained further in Section 5.4.3.1. The elements are numbered as follows.

Elements 4001 to 4147 separate the spike and the inner layer of rope.

Elements 4501 to 4647 connect the inner and middle layers of rope.

Elements 4701 to 4847 connect the middle and outer layers of rope.

Elements 4201 to 4347 separate the barrel and the outer layer of rope.

5.4.2.5 Springs.

There are four spring elements, all of type `SPRING1`, with a stiffness of 10^{-6}kN/mm; i.e. there is a force of 10^{-6}kN in the spring for a relative displacement in the axial direction of the end node of 1mm from its initial

position. Element 1 is connected to the spike, 2 to the inner rope, 5 to the middle, and 6 to the outer layer of rope. They are required to prevent rigid body movement at the start of the analysis before any loads are applied.

5.4.2.6 Mesh refinement.

The mesh was refined where the stress concentrations were the greatest to improve the accuracy of the result; this was done on the contact surfaces of the spike and barrel, at the spike base on the trailing edge of the contact zone, and at the shoulder at the base of the threaded hole. There are several methods of mesh refinement; a common one is to deform the elements in such a way that extra ones can be fitted in, but this is best done by mesh generation software which can calculate all the coordinates and numbering. The best software also adapts the mesh, reducing the size of the elements according to the local stress concentrations. A mesh can also be refined by introducing triangular elements, which make it easier to cram extra elements in. But for simplicity the mesh refinement here was done by the alternative standard technique of marrying two smaller elements onto one larger one, whilst retaining the overall rectangular shape of the elements. The nodes of the smaller elements were tied to lie along the edge of the larger one by means of multi-point constraints (`MPC`).

This option allows constraints to be imposed between different degrees of freedom of the model. Here the `QUADRATIC` definition is used, which is the standard method for mesh refinement for these second-order elements. The `MPC` constrains each degree of freedom at node_1 or node_2 to be interpolated quadratically from the corresponding degrees of freedom at node_a, node_b and node_c (see Figure 5.6). Node_a, node_b and node_c are intrinsic to both large and small elements and so do not need tying.

5.4.3 Contact.

Between layers of rope, the interface element `INTER3A` is used, which allows for small sliding. Between the rope and the spike, and between the rope and the barrel, interface elements `ISL22A` are used with slide lines set up on the metal surfaces, which allows for finite sliding. This formulation allows for arbitrary separation, sliding and rotation of the two surfaces. One of the surfaces, usually the stiffer one, in this case the spike or the barrel, is designated the master surface. (The aluminium bodies have a higher stiffness in the radial direction, the direction of contact.) The other surface, the rope, is the slave; all the nodes on the slave surface must conform to the master surface, as shown in Figure 5.7.

5.4.3.1 Gap elements INTER3A.

To allow for any relative slip between the yarns in the rope at the end at which it is pulled, the rope is modelled as three distinct layers; the layers are separated by `INTER3A` elements. Abaqus specifies that gap element `INTER3A` should be used where there is "contact over parts of surfaces, where only small relative sliding of the surfaces may occur," and this is what occurs in the rope. Abaqus checks for contact by measuring how closely surface A approaches surface B along the positive normal, $\mathbf{n}$, which Abaqus generates pointing from surface A to surface B. Care should be taken to ensure that surfaces A and B are the right way around or the gaps operate incorrectly; that is, they over-close and do not open.

The separation of the surfaces is measured by how far the (4-5-6) face lies above the (1-2-3) face along positive $\mathbf{n}$. There are three integration points per element (see Figure 5.8).

5.4.3.2 Interface element ISL22A and slide lines.

To model the large slip that occurs between the spike and the rope and between the rope and the barrel, 'slide lines' are used. Slide lines allow the modelling of the interaction between deformable structures, where separation and sliding of finite amplitude, and arbitrary rotation of the surfaces may arise. One surface is coated with interface elements and the nodes on the other surface are assigned to a slide line with the `*SLIDE LINE` option.

Abaqus version 5.5 now offers the use of a `*SURFACE DEFINITION` option, which supersedes the use of 'slide lines'. However when this option was introduced in version 5.4 it was not possible to apply surfaces over parts of bodies; Abaqus would apply the surface to the whole circumference making the desired analysis too big to fit into memory. If the analysis is re-run using more rope layers then this option will make modelling easier.

5.4.3.3 Pressure-clearance relationship.

A pressure-clearance relationship is defined between contacting surfaces of interface elements. This helps the solution numerically, by adding some smoothing such that the gaps do not repeatedly open and close on successive increments. Figure 5.9 shows the relationship that is used here; clearance for zero pressure, $c = 0.03$mm, and pressure at zero clearance, $p^0 = 0.03\text{kN/mm}^2$. For the stresses encountered here, Abaqus has two definitions for the contact pressure; if the over-closure, $h \leq$ -0.03, then there is no contact, the contact pressure, σ, being given by

$$\sigma = 0 \tag{5.1}$$

$$\frac{\mathrm{d}\sigma}{\mathrm{d}h} = 0 \tag{5.2}$$

For greater over-closures -0.03 $< h <$ 0.18 (i.e. 0.03mm 'apart' to 0.18mm over-closed) then contact is defined to occur and the following softening

relationship is imposed:

$$\sigma = \frac{p^0}{\exp(1)-1}\left[\left(\frac{h}{c}+1\right)\left(\exp\left(\frac{h}{c}+1\right)-1\right)\right] \tag{5.3}$$

$$\frac{\mathrm{d}\sigma}{\mathrm{d}h} = \frac{p^0}{\exp(1)-1}\left[\frac{1}{c}\left(\frac{h}{c}+2\right)\exp\left(\frac{h}{c}+1\right)-\frac{1}{c}\right] \tag{5.4}$$

5.4.4 Friction subroutine.

The easiest way of modelling the friction is to use Amontons' law of friction, $F = \mu N$, with the same coefficient for sticking and slipping. However in most polymeric materials (and Kevlar is no exception) a more realistic prediction is obtained by Howell's equation, $F = KN^{\beta}$, or $\tau = a\sigma^{\beta}$, with different coefficients for sticking and slipping.

The Kevlar-on-Kevlar friction is taken to be $\tau_s = \tau_d = 0.30\sigma$ (see Chapter 3); this is not so important in the analysis as the yarn-on-solid friction, due to the small magnitude of the yarn-on-yarn movement.

The Kevlar-on-aluminium frictions are determined to be:

$$\tau_s = 0.099\sigma^{0.91} \tag{3.13 bis}$$

$$\tau_d = 0.095\sigma^{0.91} \tag{3.14 bis}$$

The user-supplied subroutine used in Abaqus works in such a way that the main program supplies estimated values of shear stress and the increment in sliding motion (τ_1 and $\Delta\gamma_1$). These estimates are based on the discretised partial differentials that are generated by `FRIC` during the previous increment ($\partial\Delta\tau_1/\partial\Delta\gamma_1$ and $\partial\Delta\tau_1/\partial\Delta\sigma$). The subroutine then generates new values for these differentials and values for τ_1 and $\Delta\gamma_1^{sl}$ (the increment in non-recoverable sliding motion that occurs in this increment). If equilibrium is not established for the whole model then Abaqus re-iterates the increment using modified estimates until equilibrium is achieved. The value of $\Delta\gamma_1^{sl}$ from the previous increment can be used to determine whether the integration point was sliding or sticking, which is important in determining the magnitude of critical shear stress, sticking giving a greater stress than sliding.

5.4.4.1 Elastic stick.

In reality, when two bodies are stuck there is negligible relative motion, but it is easier to model sticking friction by a stiff elastic behaviour. This can be justified in real terms by considering that although the tiny asperities on both contacting surfaces have stuck together, these asperities actually lie on larger protuberances which themselves deform elastically. As an approximation, the behaviour is idealised to be linear elastic according to the equation $\tau_1 = k_s \gamma_1^{el}$ where τ_1 is the interface shear stress, γ_1^{el} is the elastic slip (the reversible relative tangential motion from the point of zero shear stress), and k_s is the current 'stiffness in stick' (see Figure 5.10).

This model is based on the material modelling work of Oden and Pires [1983], although Abaqus uses it in name only; the true value of γ_{crit} (the critical value of elastic slip before true slip occurs) will be an order of magnitude less than the value used in the finite element model, which uses "stiffness-in-stick" as a numerical convenience. (The separation between asperities on a finely machined metal surface is of the order of 0.02mm [Ashby and Jones, 1980], so it can be reasoned that any elastic deformation of an individual asperity will be an order of magnitude less (for a strain of 0.1). Therefore the physical value of γ_{crit} will be of the order 0.002mm (c.f. γ_{crit} in this model of 0.06mm))

The stiffness, k_s, is chosen such that the relative motion from the position of zero shear stress is bounded by the value γ_{crit} which is specified in the subroutine `FRIC` (Figure 5.12):

$$k_s = \frac{\tau_{crit}}{\gamma_{crit}} = \frac{a_s \sigma^{\beta_s}}{\gamma_{crit}} \tag{5.5}$$

Since τ_{crit} is pressure dependent, k_s will change during the analysis. The elastic slip expression can thus be written as:

$$\tau_1 = \frac{a_s \sigma^{\beta_s}}{\gamma_{crit}} \gamma_1^{el} \tag{5.6}$$

Abaqus is able to deal with two dimensional slip planes, however there is only one slip direction in an axisymmetric termination. Therefore the only

subscript used here is $_1$; the use of the subscript is maintained for compatibility with the Abaqus manuals.

The behaviour remains elastic as long as the equivalent stress does not exceed the critical stress, and whilst elastic the following applies (see Figure 5.10):

$$\gamma_1^{el}(t+\Delta t) = \gamma_1^{el}(t) + \Delta\gamma_1 \tag{5.7}$$

The elastic slip expression (Equation 5.6) can be linearised to yield:

$$\mathrm{d}\tau_1 = \frac{a_s\sigma^{\beta_s}}{\gamma_{crit}}\mathrm{d}\gamma_1^{el} + \frac{a_s\beta_s\sigma^{\beta_s-1}\gamma_1^{el}}{\gamma_{crit}}\mathrm{d}\sigma \tag{5.8}$$

from which the partial differentials needed for subroutine `FRIC`, `DDTDDG(1,1)` and `DDTDDP(1)`, can be deduced (also using $\gamma_1 = \gamma_1^{el}$):

$$\texttt{DDTDDG}(1,1) \equiv \frac{\partial\Delta\tau_1}{\partial\Delta\gamma_1} \equiv \frac{\partial\mathrm{d}\tau_1}{\partial\mathrm{d}\gamma_1^{el}} = \frac{a_s\sigma^{\beta_s}}{\gamma_{crit}} \tag{5.9}$$

$$\texttt{DDTDDP}(1) \equiv \frac{\partial\Delta\tau_1}{\partial\Delta\sigma} \equiv \frac{\partial\mathrm{d}\tau_1}{\partial\mathrm{d}\sigma} = \frac{a_s\beta_s\sigma^{\beta_s-1}\gamma_1^{el}}{\gamma_{crit}} \tag{5.10}$$

5.4.4.2 Slip.

If the frictional stress exceeds the critical stress, slip must be taken into consideration so that the equation $\tau_1 = \tau_{crit}$ is satisfied. This can be linearised to yield:

$$\mathrm{d}\tau_1 = \mathrm{d}\tau_{crit} \tag{5.11}$$

but $\tau_{crit} = \pm a_d\sigma^{\beta_d}$ therefore $\mathrm{d}\tau_{crit} = \pm a_d\beta_d\sigma^{\beta_d-1}\mathrm{d}\sigma$ so:

$$\mathrm{d}\tau_1 = \pm a_d\beta_d\sigma^{\beta_d-1}\mathrm{d}\sigma \tag{5.12}$$

therefore `DDTDDG(1,1)` and `DDTDDP(1)` are given by:

$$\texttt{DDTDDG}(1,1) \equiv \frac{\partial\Delta\tau_1}{\partial\Delta\gamma_1} \equiv \frac{\partial\mathrm{d}\tau_1}{\partial\mathrm{d}\gamma_1^{el}} = 0 \tag{5.13}$$

$$\texttt{DDTDDP}(1) \equiv \frac{\partial\Delta\tau_1}{\partial\Delta\sigma} \equiv \frac{\partial\mathrm{d}\tau_1}{\partial\mathrm{d}\sigma} = \pm a_d\beta_d\sigma^{\beta_d-1} \tag{5.14}$$

For the stuck scenario, the program takes care of itself. However as τ_{crit} is set independently, the signs for the slipping partial differentials need to be

carefully considered. This is accomplished in the subroutine by checking the direction of slip and setting the sign accordingly.

A flowchart for the subroutine is given in Figure 5.12.

To determine whether the current point is slipping or sticking the variable `DSLIP` is analysed. This holds the value of slipping that was set during the previous increment. If `DSLIP` is non-zero then slip was occurring and τ_{crit} is set using the slipping coefficients (a_d and β_d). If `DSLIP` is zero then the integration point was stuck during the last increment and a higher τ_{crit} is set using the stuck coefficients (a_s and β_s).

If the magnitude of the incoming value of τ_1 is less than τ_{crit} then it can be deduced that stick will now occur, and the outgoing value of τ_1 is calculated from Equation 5.8. If this new value, or the incoming value of τ_1, is greater than or equal to τ_{crit} then slip in the positive direction will be occurring; similarly if either is less than or equal to $-\tau_{crit}$, then negative slip occurs, and the appropriate equations are then applied.

5.4.5 Material subroutine.

The termination has been modelled as five separate `SOLID SECTION`s, one for the spike, one for the barrel and three for the rope. Each `SOLID SECTION` is composed of one mesh of adjoining elements, and assigned a `MATERIAL` (the actual material properties may vary from element to element if the subroutine `UMAT` defines them to do so, but in general they are uniform throughout the section). The separate `SOLID SECTION`s are connected by means of contact elements.

The spike and barrel are defined to be aluminium, which for simplicity is modelled as a linear elastic isotropic material, with Young's Modulus of 70.0kN/mm^2 and a Poisson's Ratio of 0.33.

5.4.5.1 Kevlar — orthotropic.

The orthotropic parameters needed for Abaqus are defined by:

$$\begin{pmatrix} \epsilon_{11} \\ \epsilon_{22} \\ \epsilon_{33} \\ \gamma_{12} \end{pmatrix} = \begin{pmatrix} \frac{1}{E_1} & \frac{-\nu_{12}}{E_1} & \frac{-\nu_{13}}{E_1} & 0 \\ \frac{-\nu_{12}}{E_1} & \frac{1}{E_2} & \frac{-\nu_{23}}{E_2} & 0 \\ \frac{-\nu_{13}}{E_1} & \frac{-\nu_{23}}{E_2} & \frac{1}{E_3} & 0 \\ 0 & 0 & 0 & \frac{1}{G_{12}} \end{pmatrix} \begin{pmatrix} \sigma_{11} \\ \sigma_{22} \\ \sigma_{33} \\ \tau_{12} \end{pmatrix} \qquad (4.6 \text{ bis})$$

As stated in Chapter 4, most of the values recorded by Kawabata will be used except for the transverse moduli E_1 and E_3 which are derived from the transverse compression of pads of fibres.

On first-loading to 30%, a transverse modulus of 0.27kN/mm^2 was used for all three rope layers. The radial stresses were then checked and found to lie in the range 27-72N/mm^2 and so the radial and hoop stiffnesses were increased to 0.45kN/mm^2 for the rest of the preloading up to 60%.

At 60% the radial stresses in the rope were all in the region around 72N/mm^2, so the unloading-reloading modulus of 5.8kN/mm^2 was applied for the unloading. Throughout the cycling regime all the stresses in the rope remained in the same zone, so the moduli were left unchanged.

On loading beyond 60% the first-loading modulus of 0.85kN/mm^2 was used throughout, and the unloading modulus of 16.4kN/mm^2 was used for unloading from 100% to 0%.

To obtain the compliance matrix that is needed in the subroutine `UMAT`, the stiffness matrix formed from all the material parameters is inverted using Matlab. During the analysis this subroutine is called at each material calculation point of each element (see Figure 5.1) in the rope, and is used to define the mechanical constitutive behaviour.

For example, for first-loading from 60% to 100% a transverse modulus of 0.85kN/mm^2 is used which gives the following relationship (obtained by

substituting values into Equation 4.6):

$$\begin{pmatrix} \epsilon_{11} \\ \epsilon_{22} \\ \epsilon_{33} \\ \gamma_{12} \end{pmatrix} = \begin{pmatrix} 1.172 & -0.0048 & -0.3634 & 0 \\ -0.0048 & 0.0077 & -0.0048 & 0 \\ -0.3634 & -0.0048 & 1.172 & 0 \\ 0 & 0 & 0 & 0.4975 \end{pmatrix} \begin{pmatrix} \sigma_{11} \\ \sigma_{22} \\ \sigma_{33} \\ \tau_{12} \end{pmatrix} \tag{5.15}$$

This is inverted to give:

$$\begin{pmatrix} \sigma_{11} \\ \sigma_{22} \\ \sigma_{33} \\ \tau_{12} \end{pmatrix} = \begin{pmatrix} 0.9483 & 0.7721 & 0.2971 & 0 \\ 0.7721 & 130.6 & 0.7721 & 0 \\ 0.2971 & 0.7721 & 0.9483 & 0 \\ 0 & 0 & 0 & 2.010 \end{pmatrix} \begin{pmatrix} \epsilon_{11} \\ \epsilon_{22} \\ \epsilon_{33} \\ \gamma_{12} \end{pmatrix} \tag{5.16}$$

Two variables need to be defined in this subroutine; `DDSDDE(4,4)` and `STRESS(4)`. `DDSDDE(4,4)` is the Jacobian matrix of the constitutive model, $\partial\Delta\sigma/\partial\Delta\epsilon$, where $\Delta\sigma$ are the stress increments and $\Delta\epsilon$ are the strain increments. `DDSDDE(I,J)` defines the change in the I^{th} stress component at the end of the time increment caused by an infinitesimal perturbation of the J^{th} component of the strain increment array. $\partial\Delta\sigma/\partial\Delta\epsilon$ is found by taking partial derivatives of the equations represented in Equation 5.16, which simply leads to the elements of the matrix in Equation 5.16.

`STRESS(4)` is passed in as the stress tensor at the beginning of the increment and is updated to the stress tensor at the end of the increment. The measure of stress used in Abaqus is 'true' or Cauchy stress; the strains are logarithmic. The new values for `STRESS(4)` are derived by incrementing the old values using Abaqus' values for the changes in strain for the current increment `DSTRAN(4)`, and the current stiffnesses.

`STRESS(4)` is encoded by:

```
      DO 20 K1=1,NTENS
        DO 10 K2=1,NTENS
           STRESS(K2)=STRESS(K2)+DDSDDE(K2,K1)*DSTRAN(K1)
10        CONTINUE
20      CONTINUE
```

5.4.5.2 Orientation.

The `*ORIENTATION` option is used to align the material properties defined in the subroutine `UMAT` for each individual element to lie parallel with its outer face as the elements themselves lie parallel to the rope. If a set of local axes was not defined, then the material properties would be aligned with the global axes; this does not matter for the spike and barrel which are isotropic, but is incorrect for the rope.

The rope is in contact with the spike which has a varying slope of approximately 3.5° to the global 2 axis, and in contact with the barrel which has a slope of 3°, so the the angle of inclination for the local axes varies along and across the rope.

`DEFINITION=OFFSET TO NODES` is the Abaqus option for doing this. It is used to define the local 1 axis to lie parallel to the face containing nodes 1 and 2 (see Figure 5.13), and the local 2 axis to lie parallel to the face containing nodes 2 and 3.

5.4.6 Verification of the subroutines.

In order to verify that the subroutines work correctly, several small tests were run using one body to simulate the rope sliding over another body simulating the spike. They were joined by interface elements as in the full scale analysis. Figure 5.14 shows the two configurations tested, one model has one element for the 'rope', one for the 'spike', and one interface element between them. The other model is more detailed, with 18, 25 and 6 elements for the rope, spike and interface respectively. Two models are used to investigate the differences obtained by refining the mesh size. The overall dimensions and boundary conditions are the same for each model. Each model was also run with different values of γ_{crit} to investigate the effect that this also has on the behaviour.

The material properties of the rope were rotated 3° using the `*ORIENTATION` option, and defined via the `UMAT` user subroutine. Stick-slip Howell's friction was applied to the interface with the `FRIC` user subroutine.

The rope segment and the spike are initially separate, and are brought together in the first step by displacing the outer nodes of the rope element towards the spike. These outer nodes are then restrained to move axially only, to maintain the contact pressure throughout the analysis. This initial contact is a much simplified version of the one used in the actual analysis which is explained in detail in Section 5.4.7.

Springs are attached to one end of the rope to moderate the axial motion, and a pressure applied to the other end of the rope to pull it over the spike. In one direction this action squashes the rope radially, thus increasing the contact force as it slides along; this is useful to check how the frictional force changes with the normal reaction. In the other direction the contact pressure drops off; for this test the same modulus of elasticity is used throughout. After pulling in one direction, the pressure is reversed and the rope is pushed backwards, which allows the behaviour of the reversal of stick-slip friction to be checked. Finally the rope is pulled in the initial direction again to complete the cycle.

Three different magnitudes of the elastic slip limit, γ_{crit}, are used, in order to compare the accuracy lost by increasing γ_{crit}. Two values are used for each model; for the coarse mesh these are 0.6 and 0.06mm, and for the fine mesh they are 0.06 and 0.006mm. When expressed as percentages of element length these equate to 4% and 0.4%; 2.4% and 0.24% respectively.

With a small γ_{crit}, typically 0.5% or less of a typical element length, the best accuracy is obtained with the stick-slip friction being followed closely; this is the value recommended for use in Abaqus. As γ_{crit} is increased, the 'elastic slip' becomes large compared to any real slip that might be occurring in the increment and accuracy is lost. However, because the amount of elastic slip is constant from one slipping increment to the next, there is no difference

in the overall behaviour whilst slipping. Increasing γ_{crit} leads to a faster solution; decreasing γ_{crit} leads to a closer following of the real slip-reversal behaviour: a trade-off has to be sought between the two.

Figure 5.15 shows how the contact stress and frictional stress vary against the relative slip during the test; all the data is taken from the middle node of the interface region. On establishing contact, the pressures for all tests rise equally, whilst the friction and the slip remain close to zero.

On pulling the rope segment, the contact pressures for all tests rise linearly along the same curve, the value of γ_{crit} having no effect on the contact pressure.

On first pulling, and when the direction of pull is reversed, the tests follow an initial 'elastic slip' region (shown as 'STICK'). Only when the elastic slip limit has been exceeded does true slip occur. During the elastic slip phase the frictional stress is proportional to relative slip; the smaller the value of γ_{crit}, the larger the 'stiffness in stick'. This effect can be seen where the $\gamma_{crit} = 0.06$ and 0.006 curves rise to reach the slipping plateau with a steep gradient, whereas the $\gamma_{crit} = 0.6$ curve has a shallow gradient. Each curve plateaus after its respective γ_{crit} has been exceeded.

The true slip plateaus for all the curves are the same, as they are all governed by the equation $\tau_d = 0.095\sigma^{0.91}$. As the contact pressure rises, so the limiting frictional stress also rises.

When the rope is pushed in the opposite direction, all the curves exhibit the same 'elastic slip'-true slip behaviour; this time moving a distance of $2\gamma_{crit}$ before true slip starts. The contact stresses follow the same curve down, and continue along a linear extrapolation, as the element moves past its initial starting point. (In the actual termination, the contact stress remains constant due to the non-linearity of the transverse material properties, and the different geometry.) All frictional stresses again follow the same true slipping curve, this time along $\tau_d = -0.095\sigma^{0.91}$.

It can be seen that once the critical slip has been exceeded, the value of γ_{crit} is insignificant — all the tests follow the same path. Therefore the value of γ_{crit} chosen for the analysis should be as large as possible to decrease the time taken, whilst remaining less than the actual magnitude of slip to maintain the accuracy. It was found that $\gamma_{crit} = 0.06$mm was the optimum value for the actual analysis of the termination for this to occur (compare Figure 5.15 with Figures 6.8 and 6.22).

It is also seen that the behaviour of the stick-slip transition is solely dependent on γ_{crit} and not on the size of the elements. In general, for finite element analyses the smaller the element size the closer the analysis will come to calculating the exact stress state. For the rope, where there are no stress raisers, such as sharp corners or material discontinuities, there is no benefit to be gained by refining the size of the mesh. The stresses measured for these tests are the same whether the rope is one or three elements thick. A refined mesh has the major draw-back of increasing the size of the analysis by a power of 2. Such that if the number of elements across a rope layer is increased from one to three, and the aspect ratio is maintained, then the analysis will be nine times larger. Not only will this take nine times longer to run, but it will also require nine times more memory for the analysis to proceed. The number of elements near the spike and the barrel contact zones are important though, as will be seen in Section 6.4.3, where localised fluctuations in the stress occur when the rope elements move relative to the spike and barrel. Refining the mesh next to the contact zone as seen in Section 5.4.2 minimises this.

Table 5.1 shows the effect that the various factors have on the speed of the analysis. Comparing the two runs with γ_{crit}=0.06, it can be observed that increasing the number of elements from 3 to 49 (a factor of 16) increases the analysis time fifteen-fold. The number of increments needed is determined by the contact condition and not the number of elements and thus remains unaffected, 215 c.f. 217. For both models reducing the size of γ_{crit} by a factor

Number of interface elements	γ_{crit} (mm)	Total number of increments in the analysis	Total CPU time for the analysis (seconds on `tw900`) (an HP 755)
1	0.6	44	3
1	0.06	215	13
6	0.06	217	197
6	0.006	688	707

Table 5.1: Relative analysis times for the verification runs.

of 10, increases the total time roughly four-fold.

5.4.7 Establishing contact.

The most complicated stage of the entire analysis is bringing all the surfaces together. The surfaces can not start in a touching configuration as there are too many redundancies in the contact stresses along the surfaces, and if they are brought together too imprecisely the gaps can chatter between open and closed in successive iterations. The best way of establishing contact between several surfaces was found to be the methodology detailed in Abaqus-Answers [1993].

This describes how to model a generic metal forming problem involving multiple rigid surfaces. The model consists of a plane strain mesh with a punch, die and blank holder. The punch is pushed down to form an S-bend into a steel plate blank (see Figure 5.16).

The rigid surfaces must be smooth, which is easily achieved by using the `SMOOTH` parameter on the `*RIGID SURFACES` option, and the rigid surfaces must also extend beyond the mesh to ensure that nodes do not slide off the end of the surface.

The first stage of the process is to get the blank held between the holder and the die. The punch is initially positioned a small distance above the blank to ensure that it does not cause problems at this stage.

At first sight it would appear best to fix the die, and move the holder down onto the blank by applying a force to the reference node of the holder. However this method would almost certainly give rise to a number of problems.

Firstly, at the start of the increment, no contact has yet been established, even if the surfaces of the blank and die, and blank and holder, are initially co-planar. Without additional constraints on the blank there is zero stiffness in the vertical direction and a numerical singularity results.

Secondly, if the surfaces are not co-planar, the blank may be able to move between the holder and the die and so the contact condition between the three bodies is ill defined. Abaqus attempts to solve the contact between the blank and the die, and the blank and the holder, but the code may end up flipping between the two contact conditions. This phenomenon is known as 'chattering' and it commonly occurs in multiple surface contact analyses. In this example chattering is easily prevented by fixing the mid-plane of the blank in the vertical direction to prevent the motion of the blank as a whole.

The mid-plane of the blank is chosen because it is away from the contact area. Care is required in applying constraints to nodes on contact elements. If a node is constrained in the direction of contact, and the node comes into contact, there are two constraints on one degree of freedom and zero-pivot errors result.

The third problem is that if a force is applied to the holder before contact is established, there is no vertical constraint on the reference node and a singularity results.

Hence, contact is established by moving the holder down by means of a `*BOUNDARY` command, ensuring a firm contact condition with no possibility of singularities or chattering. The die is also moved up slightly to establish

contact between the die and the blank. Then the boundary is removed from the mid-plane of the blank and the blank material settles between the die and the holder. Finally the punch is brought down to form the S-bend in the blank.

Most text books and manuals espouse the benefits of using small time steps, as they allow the analysis to follow the loading curve more accurately. However, it was found here, and reiterated in a recent discussion (October 1996) on the American Society of Mechanical Engineers' Finite Elements mailing list [`fea-l@mecheng.asme.org`] that the smaller the time step becomes, the more the analysis is likely to become stuck. When the time step is reduced the program spends more time overcoming minor blips on the loading curve.

Because of the way the loading cycle is projected from the last step, when the direction of loading is changed or something starts slipping there can be problems with the analysis proceeding. A smaller step size might give a more accurate result, but if the size is too small then the analysis can not overcome ripples on the loading curve.

The disadvantage of using a larger step size is that the loading curve is not followed as accurately, and the loading may progress beyond the desired final level, as the step size is not modified to reach an ultimate value. Thus getting the loading to finish exactly at a load is very difficult to do, since some overshoot is always present. The analysis would be re-run two or three times with different starting step sizes to get close to the desired end load. It is difficult to control Abaqus' estimates of the next time step, so if an analysis did become stuck, it would be re-attempted with different starting values for the initial, minimum and maximum step sizes.

5.4.7.1 Initial contact within the termination.

An analogy with the forming process example, would suggest an initial fixing of the mid-nodes of the rope layers, then bringing the spike and barrel into

contact with the rope. But there is the problem that the spike and barrel cannot be pushed directly together to squash the rope as they have to slide relative to each other. Therefore contact is established by sliding the rope and spike into the barrel by displacing lines of nodes parallel to the axis. These lines of nodes lie along the centrelines of the rope layers, and along the axis of the spike. This is done using the `*BOUNDARY` option. These lines of nodes are constrained to prevent chattering whilst contact is established. When contact has been established these fixed displacements are removed to prepare the model for the loading process.

If the initial contact is done with friction in place then problems arise with partial contact, so either the friction should be removed until contact has been firmly established, or the better but more complicated approach used here is to control the contact precisely such that chattering does not occur.

The use of softened surfaces also presents problems; when the surfaces of the rope portions have a zero separation, there will exist a pressure between them. Starting the analysis in this configuration presents iteration problems; this is overcome using Abaqus' `*CONTACT INTERFERENCE` option which 'shrinks' one overlapping surface onto another over the course of a step such that at the end of the step everything is established correctly.

The problems of initial contact are further compounded by the fact that the spike and barrel can squeeze the rope at the nose and the base of the spike whilst gaps still exist near the middle of the spike. This arises due to the conical geometry. This lack of contact is overcome by superimposing a parabolic displacement to the mid-layer nodes such that the central nodes are moved up more than the nodes at the nose and base of the spike. (Maximum central displacements of 0.025, 0.050, 0.075mm, are applied to the inner, middle and outer layers, respectively; with zero radial displacement at the nose and base.) These displacements are calculated by a Matlab program then brought in to the `.inp` file. Using this displacement regime ensures that the transverse stresses the rope experiences are uniform — if the rope were

simply slid into the barrel the transitory pressures near the nose and the base would far exceed those in the middle.

The following steps outline the initialisation process to establish contact within the model. (This is also shown schematically in Figure 5.17).

step 1 Establish contact between touching rope-rope and rope-spike interfaces using `*CONTACT INTERFERENCE` (no movement).

step 2 Move both the rope and the spike in 11.5mm, so that barrel face to spike face = 41.2mm (the rope is moved in and up simultaneously).

step 3 Move the spike in further, face to face = 45.7mm.

step 4 Release inner layer of rope.

step 5 Release middle layer of rope.

step 6 Release outer layer of rope.

step 7 Release spike.

At the end of this initialisation process the transverse stress acting on all the rope is between zero and 27N/mm^2. This is the minimum range in Table 4.1 and so the modulus is taken to remain at 0.27kN/mm^2, the value set throughout the initialisation.

At points during this initialisation the transverse stress does exceed 27N/mm^2 due to the enforced displacements. However this excess was a by-product of this modelling rather than an actual stress state, and so use of the first initial loading modulus should be continued. Because subroutine `UMAT` applies the moduli in a linear-elastic manner, this excess stress does not affect the analysis because it falls back to the desired initial state with no plastic deformation or increase in modulus, once step 7 has been completed.

5.4.8 Loading history.

The termination is first pretensioned to 60%, with a pause at 30% to increase the moduli, and then unloaded to 5%. This matches the pretensioning that is typically applied to ropes. A loading cycle between 5-50% of the ultimate

tensile stress is then applied for two complete cycles. Finally the rope is taken to the failure load before unloading.

This regime was chosen to obtain data to compare with the lifetime data for real 60 tonne Parafil G ropes tested to failure between these loads as presented in Chapter 7. All the steps were run using the Riks algorithm.

step 8 Pull rope to 30% of the ultimate breaking load.

step 9 Pull rope to 60%.

step 10 Unload rope to 5%.

step 11 Pull rope to 50%.

step 12 Unload rope to 5%.

step 13 Pull rope to 50%.

step 14 Unload rope to 5%.

step 15 Pull rope to 60%.

step 16 Pull rope to 100%.

step 17 Unload rope to 0%.

5.5 Summary.

A finite element analysis of a Parafil termination is feasible provided great care is taken to set up the model correctly. The non-linear transverse stress-strain behaviour of the rope must be followed to accurately calculate the contact stress. This is achieved by encoding the transverse compression data presented in Chapter 4 with the `UMAT` subroutine.

This contact stress is in turn crucial for the determination of the frictional stress, which is encoded using the subroutine `FRIC` and the frictional data presented in Chapter 3. This allows stick-slip friction of the form $\tau = a\sigma^{\beta}$ and slip reversal to be followed.

The other main requirement is that the rope-rope, rope-spike and rope-barrel contact are all firmly established as discussed in Section 5.4.7, before the actual loading sequence can be applied.

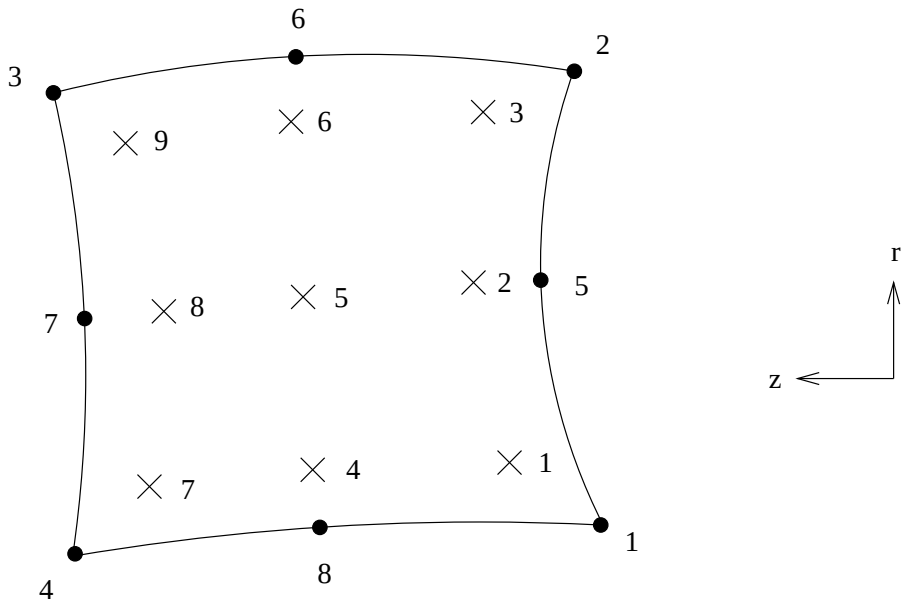

Figure 5.1: Element CAX8, 8 nodes and 9 integration points. This element is used for modelling the solids; the spike, the barrel, and three layers of rope.

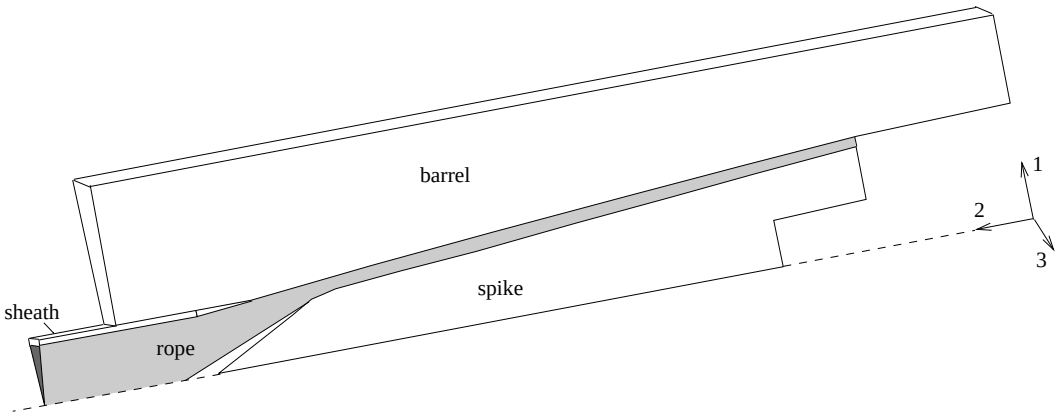

Figure 5.2: Representation of an axisymmetric 'wedge' through a Parafil termination. For the modelling, the rope is truncated at the end of its contact zone with the spike.

Figure 5.3: The elements in the spike, showing typical node and element numbering in the middle of the spike. There is mesh refinement at the ends of the spike and along the contact surface with the rope, using multi-point constraints as shown. The nodes along the axis are constrained to move axially only.

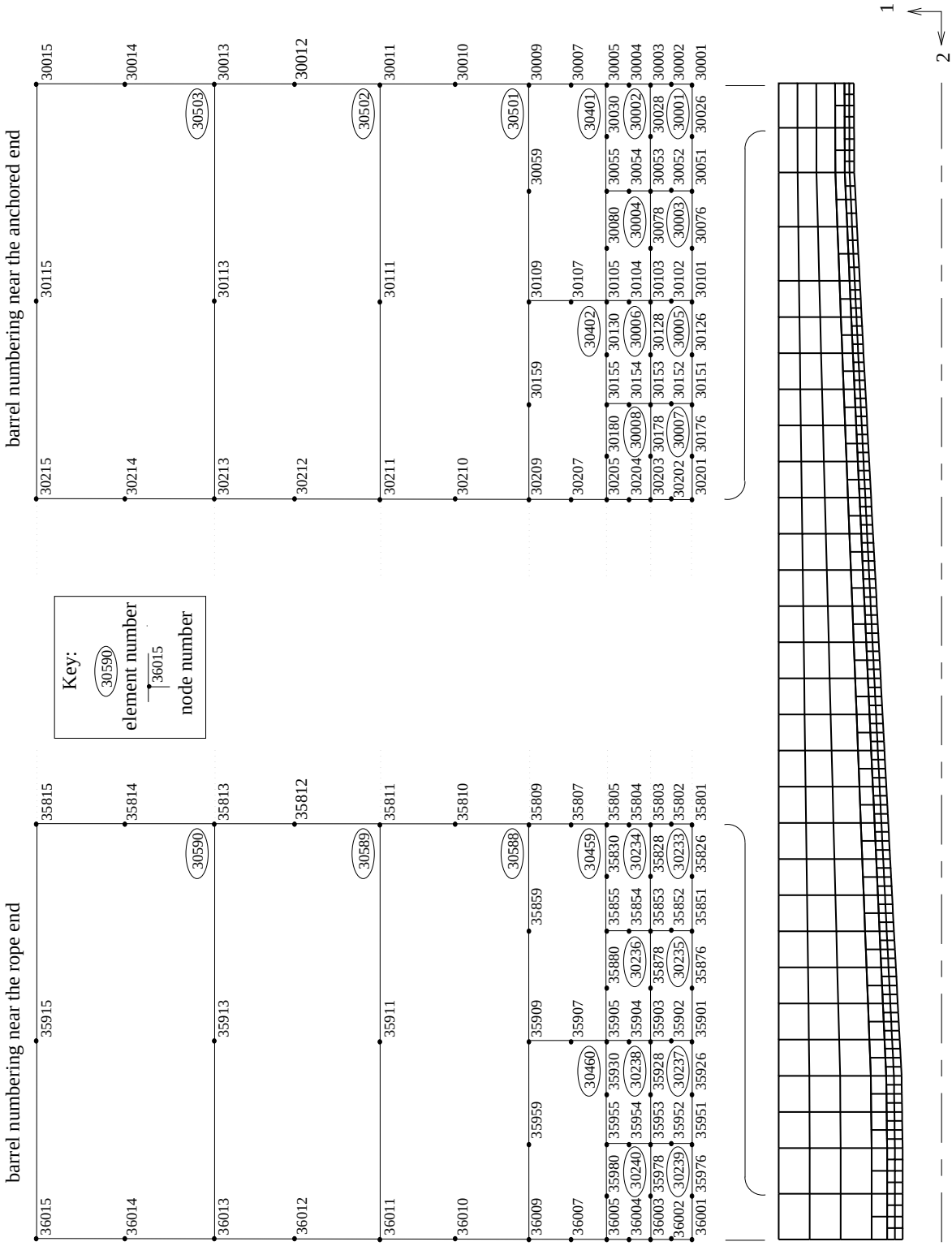

Figure 5.4: The elements in the barrel, showing typical node and element numbering at either end. There is mesh refinement along the inner surface where the rope makes contact. The barrel is restrained along its outside edge at nodes 30015, 30115... 30815, the rope exits the other end past element 30239.

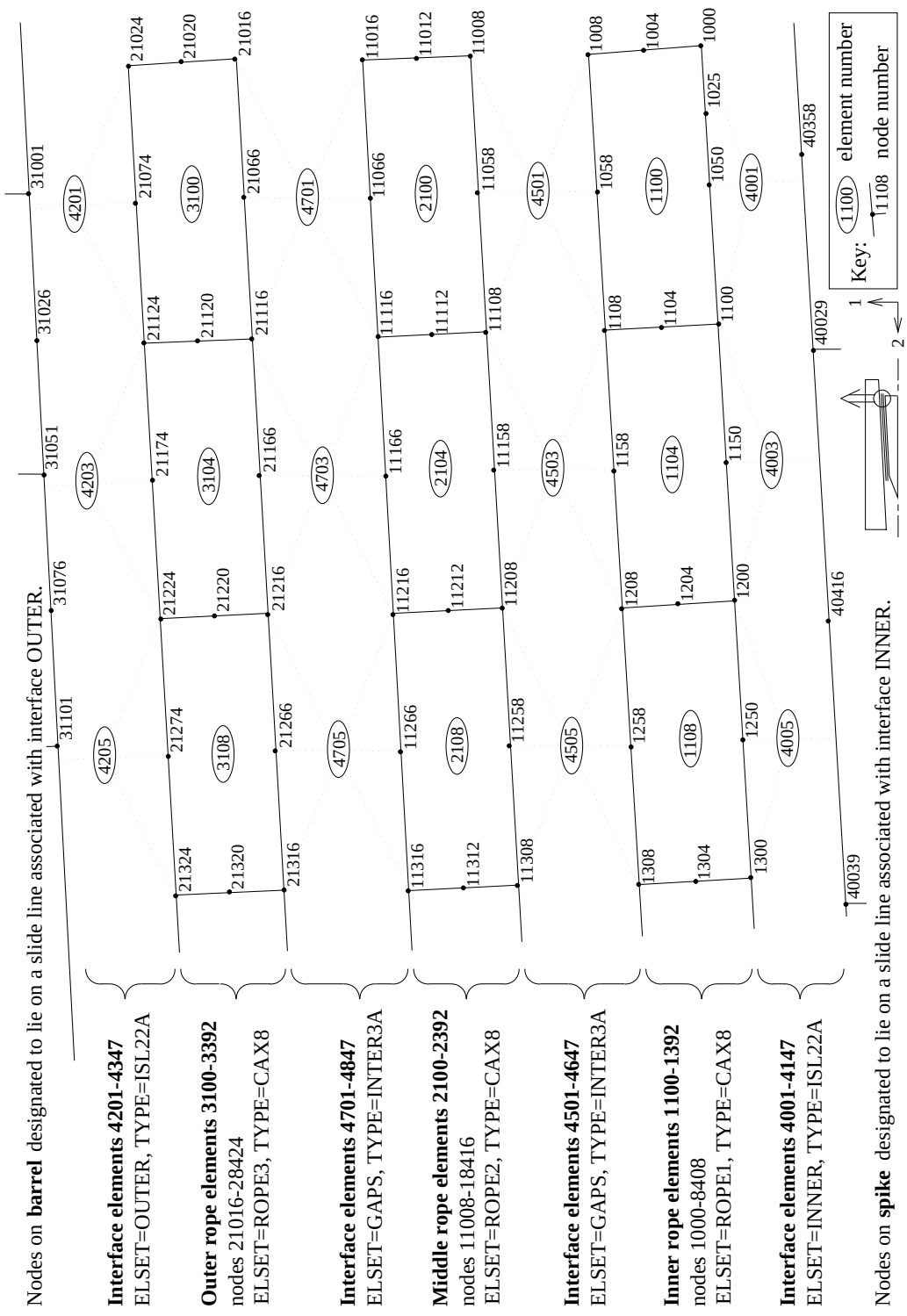

Figure 5.5: Schematic diagram of the contact between the rope layers with the rope layers shown separated for clarity. The use of interface elements ISL22A and INTER3A is detailed.

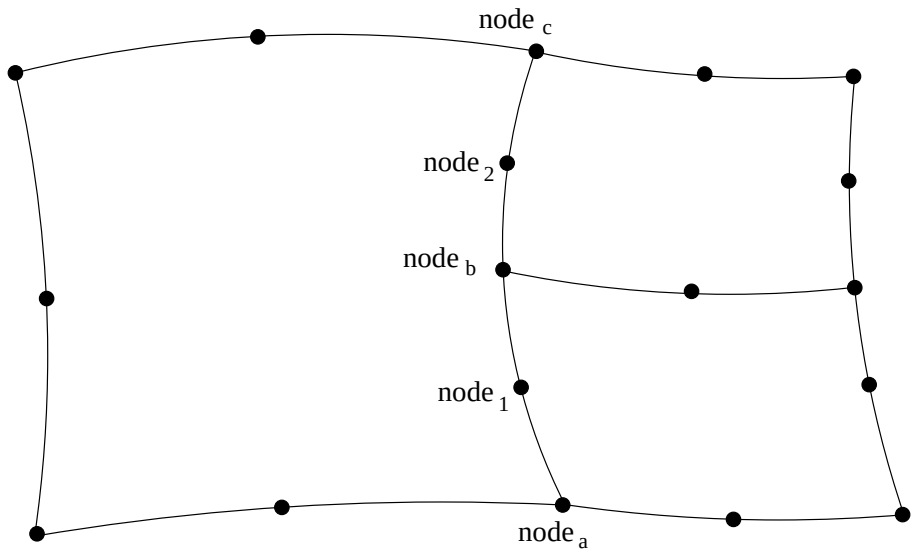

Figure 5.6: Mesh refinement using multi-point constraints (MPC), nodes 1 and 2 are constrained to lie along the parabolic line passing through nodes a, b and c.

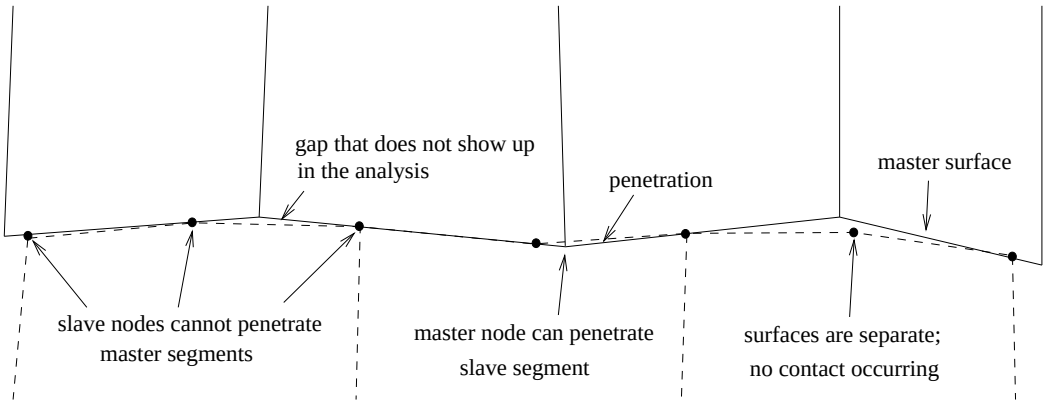

Figure 5.7: Master-slave surface interaction; the slave nodes lie on or above the master surface which they can not penetrate.

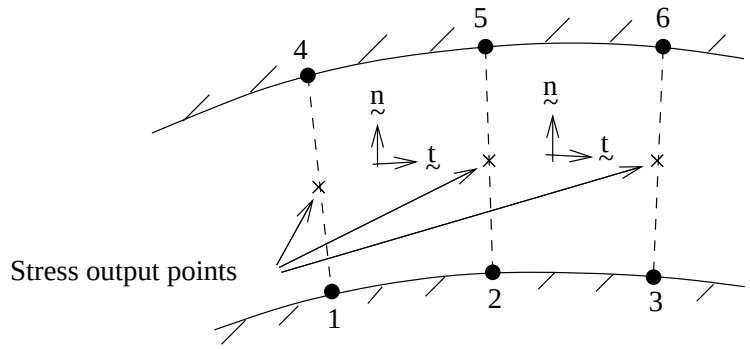

Figure 5.8: Interface element INTER3A, 6 nodes and 3 integration points. This element is used for modelling the small sliding between the layers of rope.

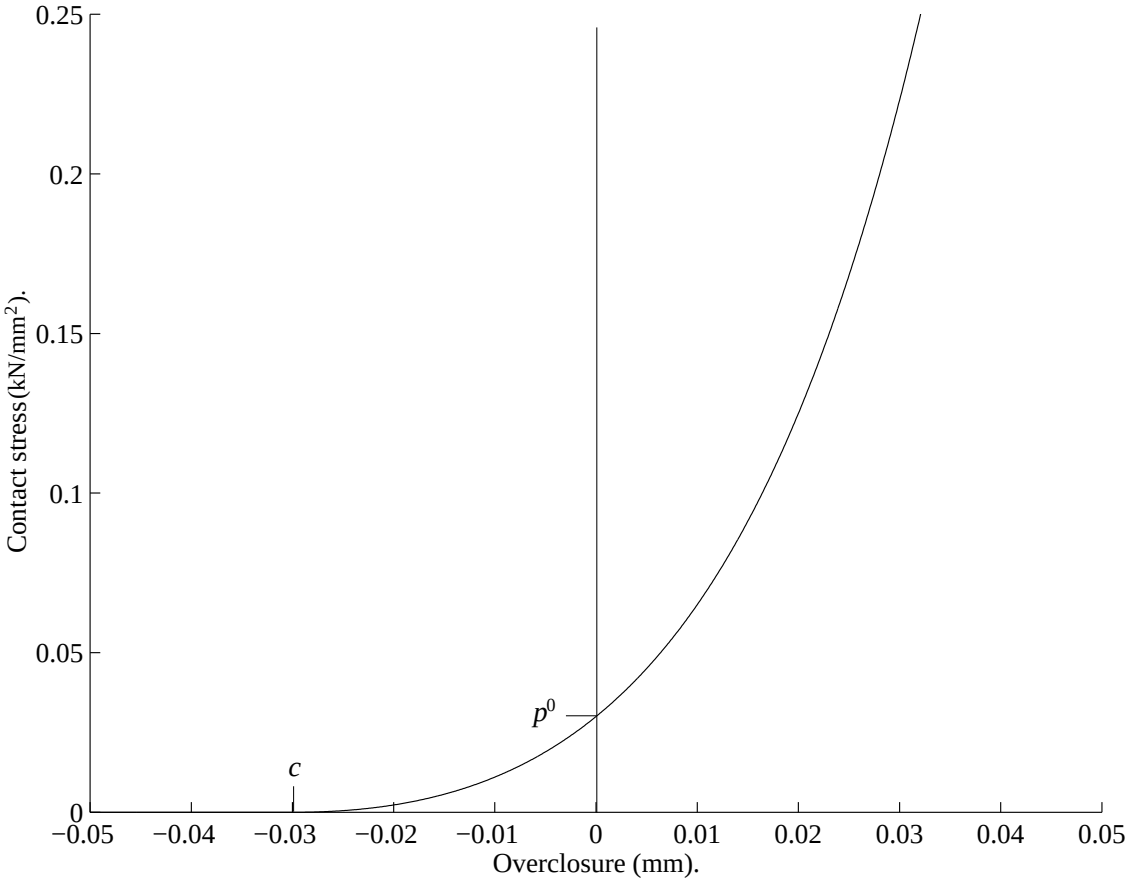

Figure 5.9: Contact pressure using soft contact, where p^0=0.03, c=0.03. When the two surfaces have zero separation the contact pressure is 0.03kN/mm^2. At a typical contact pressure inside a Parafil termination of 0.1kN/mm^2 the surfaces are over-closed by the very small amount of 0.016mm.

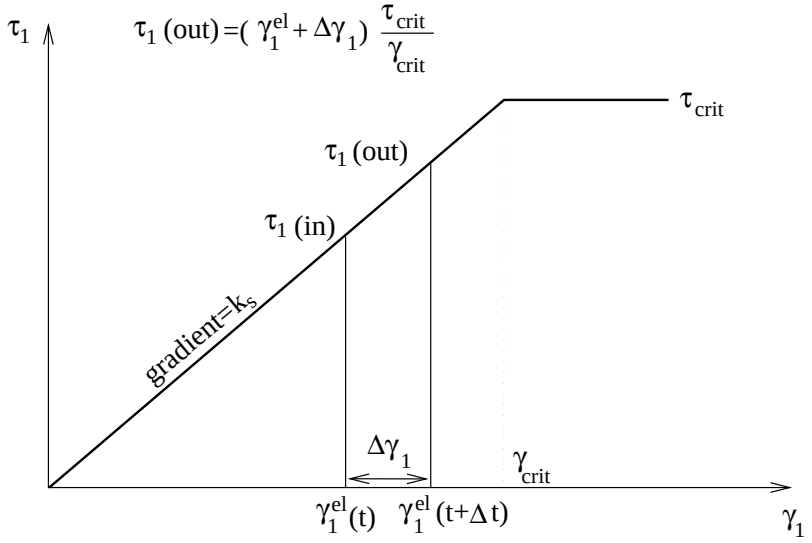

Figure 5.10: Frictional stress – displacement whilst stuck. At the start of the increment the frictional stress is τ_1(in) and the elastic slip is $\gamma_1^{el}(t)$; at the end these become τ_1(out) and $\gamma_1^{el}(t + \Delta t)$. The change in elastic slip is $\Delta\gamma_1$ and the change in friction is determined from the current 'stiffness in stick'.

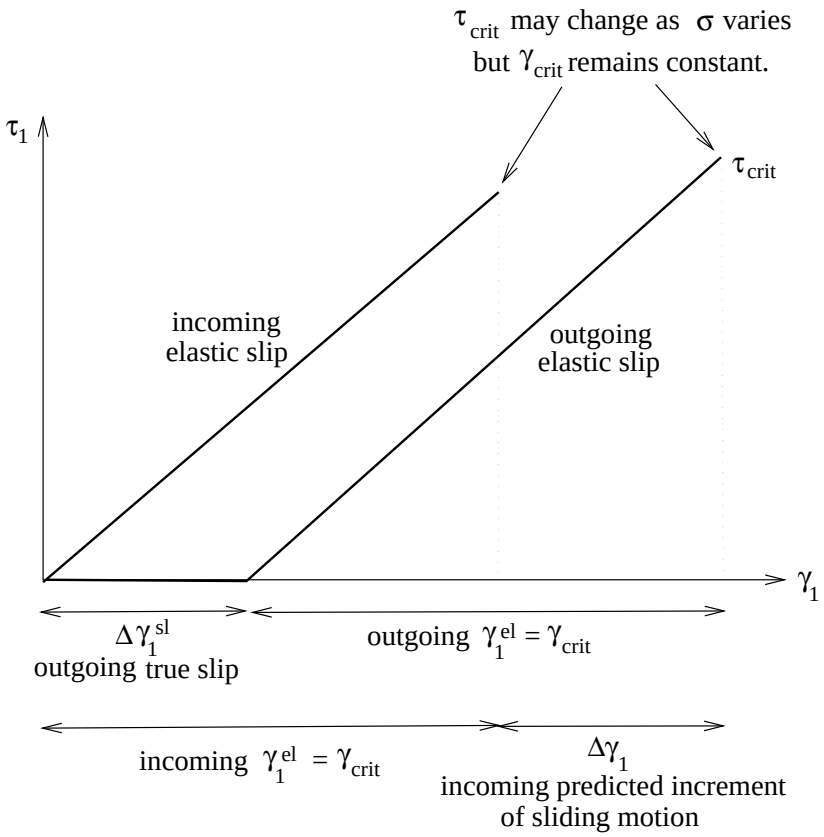

Figure 5.11: Relationship between the frictional stress and the displacements when slipping at the start and end of the increment in the finite element analysis.

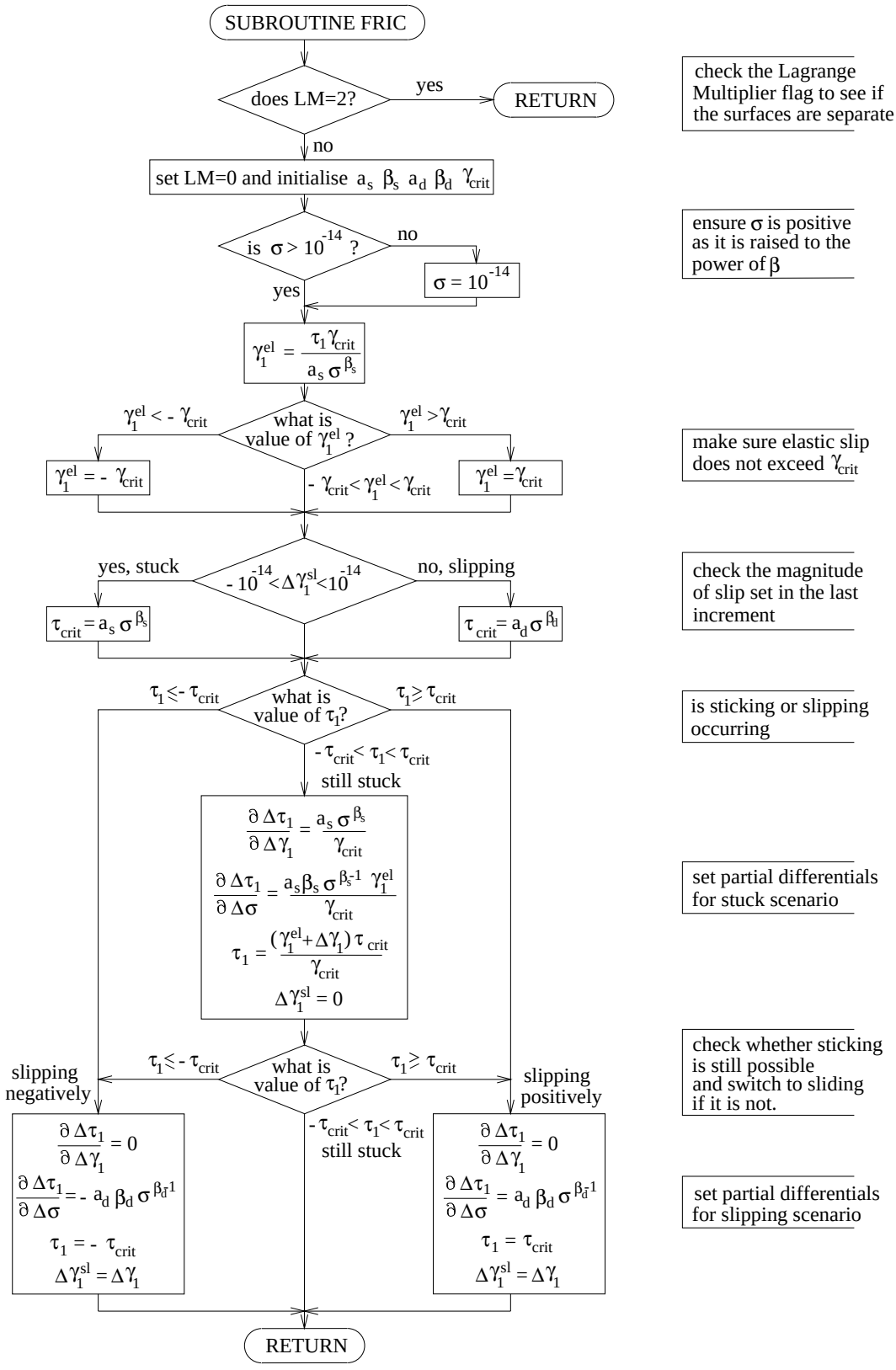

Figure 5.12: Flowchart for the subroutine FRIC. This subroutine is used to apply the stick and slip modified Howell's equations for friction ($\tau_s = a_s\sigma^{\beta_s}$ and $\tau_d = a_d\sigma^{\beta_d}$), it determines the state of friction and sets the required parameters accordingly.

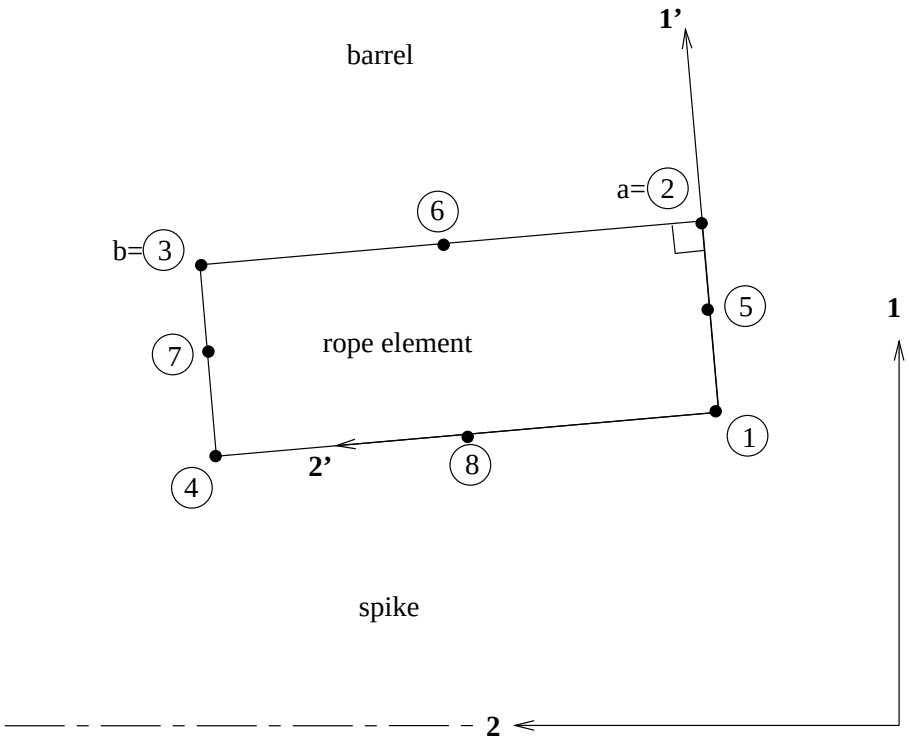

Figure 5.13: Relationship of local (1',2') and global (1,2) axes in the rope. The `ORIENTATION` option is used to align the material properties of the rope with each individual rope element.

1 ‘‘rope’’ element, 1 interface element, 1 ‘‘spike’’ element

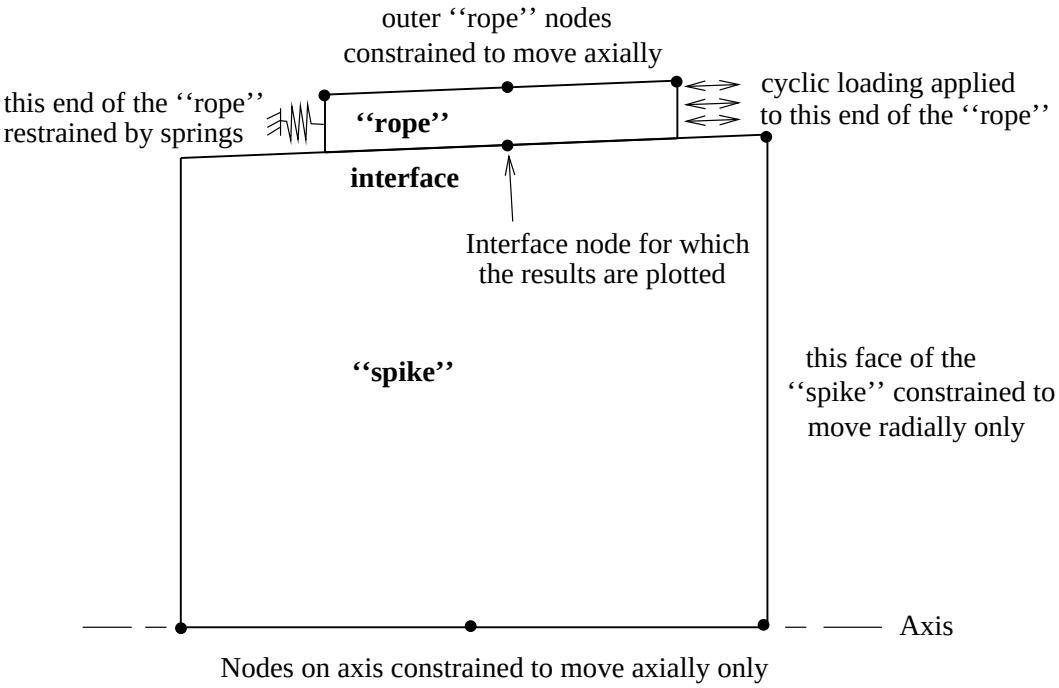

18 ‘‘rope’’ elements, 6 interface elements, 25 ‘‘spike’’ elements

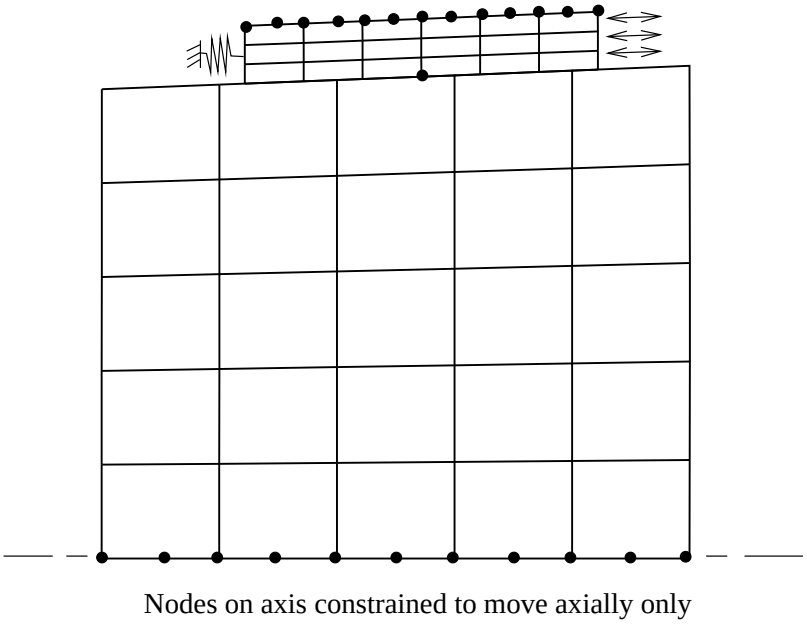

Figure 5.14: The two models that are used in the verification of the subroutines, and in the demonstration of the effect of changing γ_{crit}. The coarse mesh has just three elements simulating the rope, spike and an interface element, the refined mesh has 49 elements.

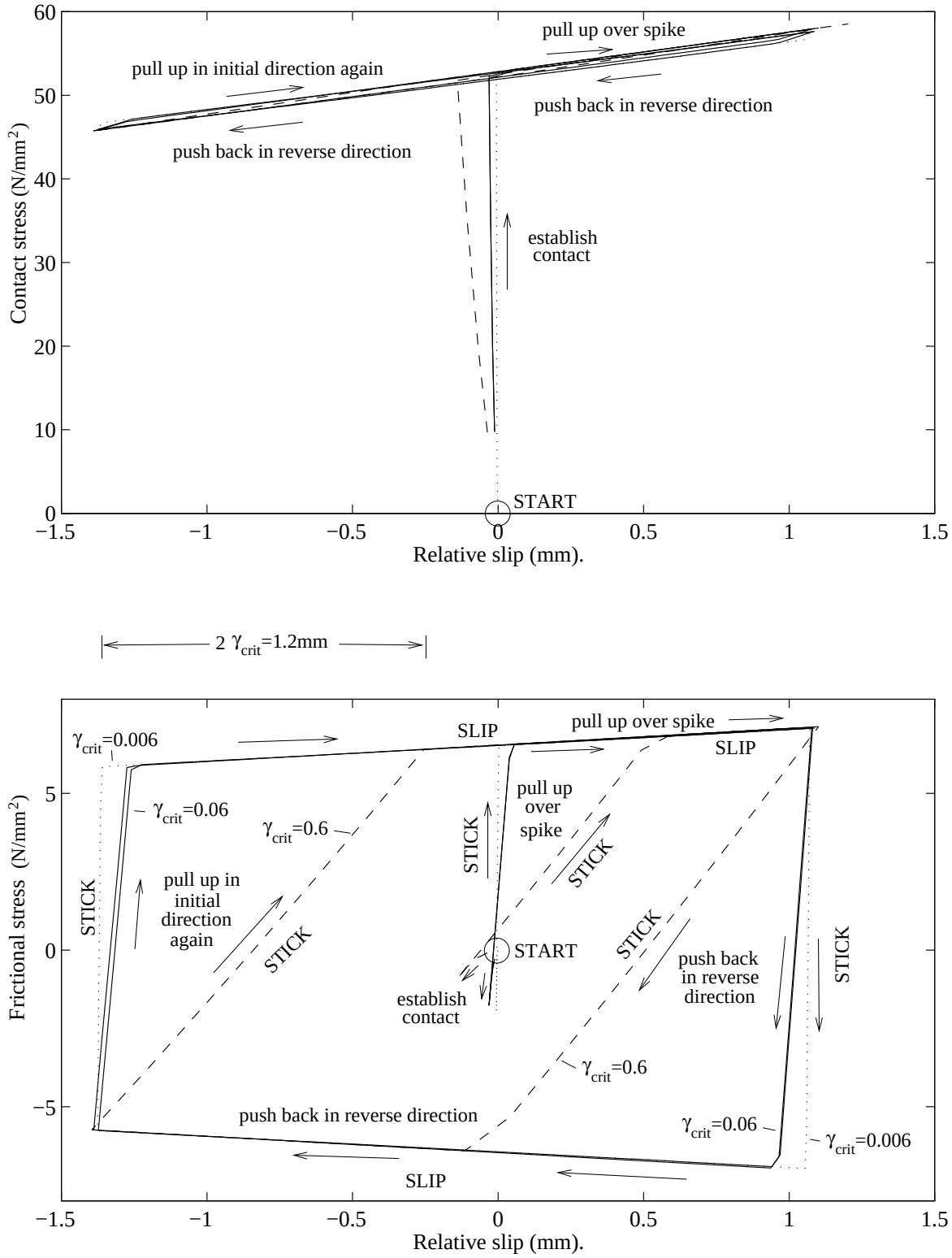

Figure 5.15: Contact stress and frictional stress behaviour for the verification runs. The frictional stress exhibits hysteresis due to the slip-reversal; the smaller the value of γ_{crit} the more closely the run resembles 'real' stick-slip behaviour, but with the penalty of a greater computational time. At either end of the slip regime, all models have the same frictional and contact stresses.

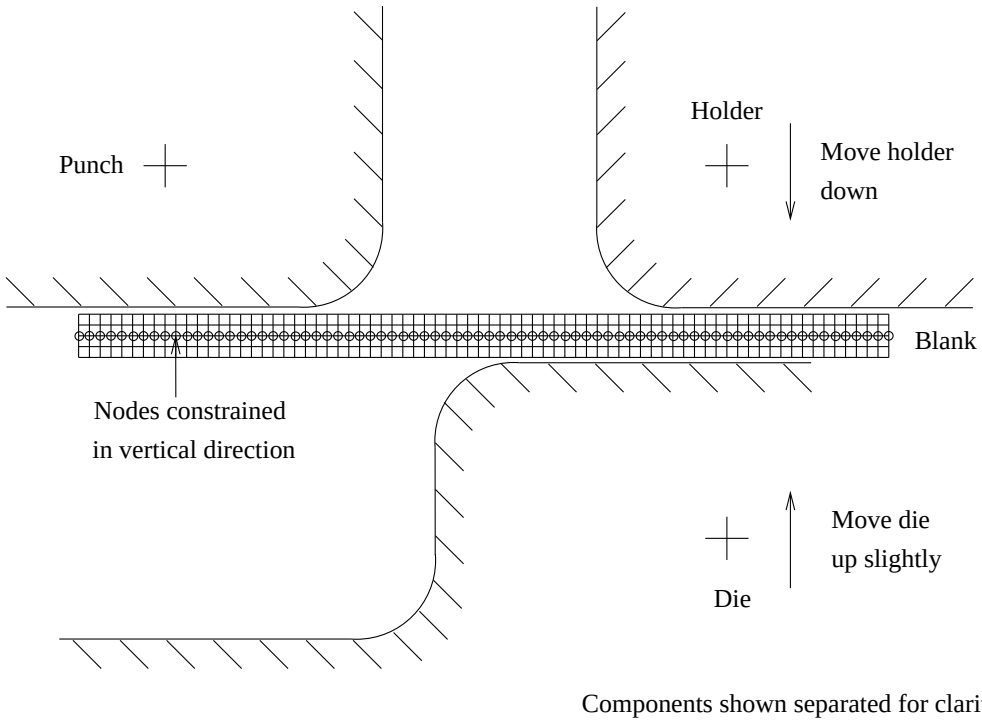

Figure 5.16: Contact analysis example from Abaqus/Answers. A metal blank has to be constrained along its central nodes before it can be clamped between a holder and a die, once contact is established and this constraint removed, the punch can be used to form an S-bend in the blank.

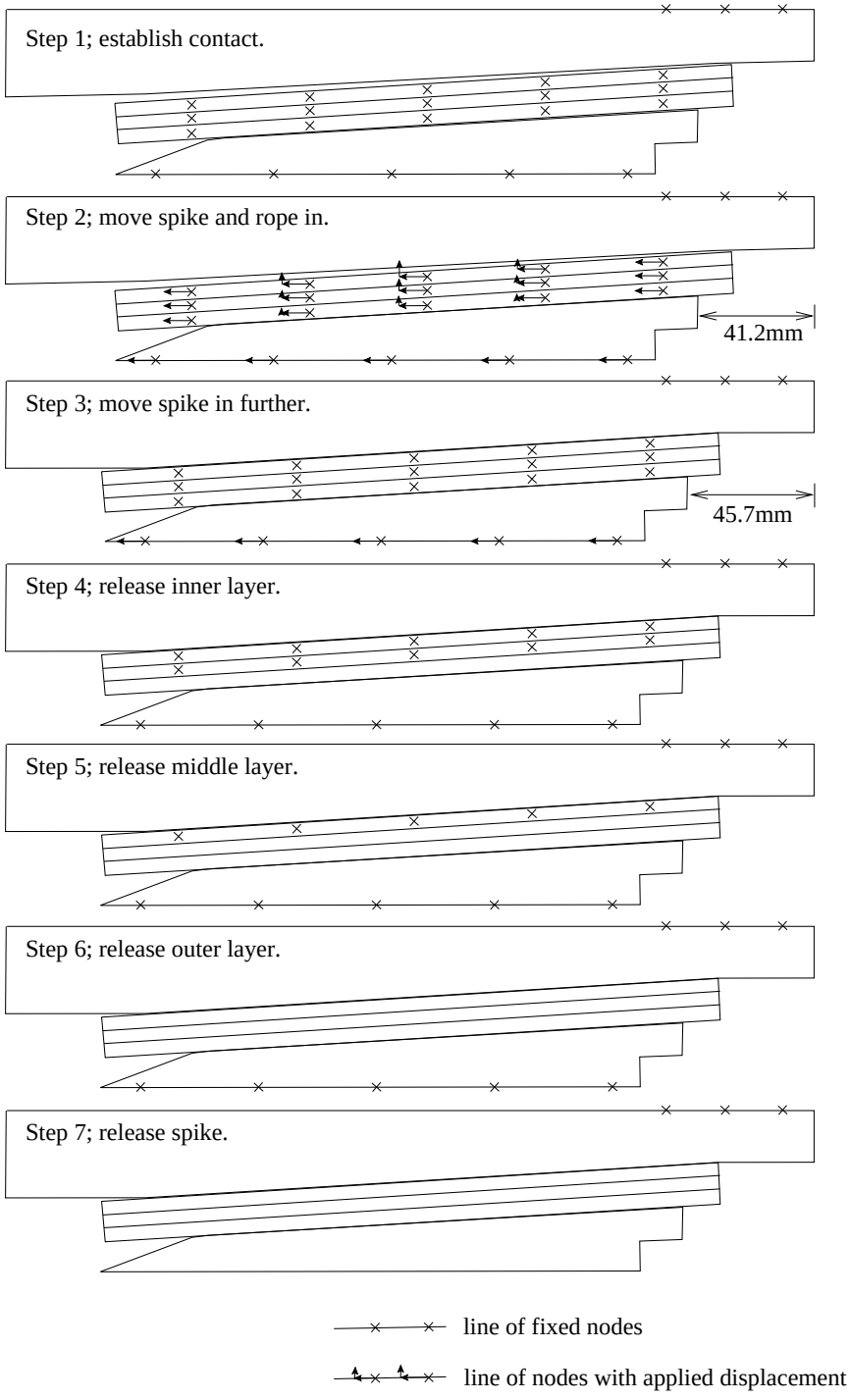

Figure 5.17: Schematic diagram of the initialisation process to establish contact. Seven steps are needed to bring the layers into contact under control and then release the constraints one by one to avoid chattering.

Chapter 6

Results from the finite element analysis.

6.1 Introduction.

This chapter presents the results of a finite element analysis on an aluminium 60 tonne Parafil G spike-and-barrel termination. These results are used to outline the mechanics at work within the termination, both on first-loading and when the load is cycled.

The chapter starts with a presentation of the contact between the rope and the spike, as this contact makes the most significant contribution to the workings of the termination. The stresses in the spike, rope and barrel, are then detailed along with the contact between the rope and the barrel.

The strains and displacements are presented later in Chapter 7, where they are compared with experimental data on actual 60 tonne terminations.

The chapter concludes with a summary of the salient conclusions derived from this study.

6.2 Spike results.

6.2.1 Relative slip between the rope and the spike.

By observing the relative slip between the rope and the spike it will become apparent that a significant insight into the behaviour of the termination as a whole can be obtained. The slip between the rope and the barrel is less detailed as shown in Section 6.4.

The relative slip is directly related to the magnitude and direction of the friction. As the rope moves in one direction, the friction and elastic slip will increase linearly, with the stiffness in stick, until the limits of friction and elastic slip are reached (as was seen in Figure 5.10). Beyond the limit of elastic slip, true slip occurs, and the total displacement between the two surfaces is the sum of the two slips. It should be remembered (from Section 5.4.4.1) that the elastic slip and the friction are related by the equation:

$$\tau_1 = \frac{a_s \sigma^{\beta_s}}{\gamma_{crit}} \gamma_1^{el} \qquad \text{(5.6 bis)}$$

and that γ_{crit} are τ_{crit} not related — the critical slip, γ_{crit}, remains constant throughout the analysis. The critical friction is pressure dependent, $\tau_{crit} = a_s \sigma^{\beta_s}$ or $a_d \sigma^{\beta_d}$; thus when the contact pressure rises, as the spike beds down, the critical friction will rise. Therefore, by looking at the slip that takes place, rather than the friction, the overall situation can be simplified by removing the factor of the rising contact pressure.

In general, the rope slips over the spike over its entire length on initial loading, slips backwards and forwards over the nose portion during cycling; then slips forward again along the entire length, on initial loading beyond the preload.

When the direction of movement is reversed, the friction and elastic slip both reduce in value, such that they are no longer critical. If the reversal in direction is greater than twice the critical elastic slip, then true slip will occur in the opposite direction. So the total displacement from the initial

situation is now the true slip that occurred during the bed-down minus the true slip that has subsequently occurred, minus the elastic slip.

The elasticity of the termination also comes into play; as the load is increased the rope stretches, and the spike also deforms as it moves between tension and compression during the loading history.

6.2.1.1 Description of the elastic slip - true slip graphs.

The sketches in Figures 6.1, 6.3 and 6.5 show schematically the values of elastic slip, true slip, and displacement from initial position, for seven locations along the spike, at salient points during the loading history. Four of these points are identical to the four 'salient' points for later graphs in this chapter. These are 'at the nose', 'near the nose', 'in the middle' and 'at the base.' The other three points show intermediate locations, as shown on the figure below the icons. (The exact values of slip can be derived from later graphs.)

At each point the heavy vertical line represents the initial condition; no true slip and no elastic slip. The darker shaded triangles represent the elastic slip that is present at this location at the current stage in the loading history. If the elastic slip exceeds the critical limit then true slip occurs. True slip is shown by the lighter shaded rectangles, with the magnitude being represented by the length along the base line. The true slip displaces the origin from which the elastic slip occurs. The total relative displacement is the sum of the true slip and the elastic slip, which is represented along the top of each icon. If the elastic slip reverses, then the elastic slip triangle moves back over the true slip rectangle, and the total relative displacement reduces. If slipping occurs in the reverse direction then true slip occurs and the size of the true slip rectangle reduces. The dashed lines are used to represent previous extremes of true slip for reference.

The numbers along the top, and letters down the side are used to reference

each individual icon. For example cell E3 represents the first unloading to about 35% UTS 'near the nose' of the spike.

6.2.1.2 Behaviour from initial assembly to a preload of 60%, then unloaded.

Figure 6.1 shows the relative slip between the rope and spike during pretensioning from 0% to 60% and back down to 5%.

By 20% preload, the rope is slipping elastically in to the termination, along the entire length of spike. At the nose, the critical limit has been reached and slip is about to occur, $\gamma_1^{el} = \gamma_{crit}$ and $\tau_1 = \tau_{crit}$.

By 40% the critical region has extended along the spike to cell B3, cell B2 experiences some true slip, and cell B1 even more. The slip along the rest of the spike remains elastic.

By 60% the critical region has now progressed into the middle of the spike, with cells C1→C5 all experiencing true slip, with the greatest slip at the nose and the least slip in the middle. It should be noted that there is minimal slip, and hence friction, at the base of the spike, cell C7. The forces on the spike are such that it is pulled in to the termination by the friction over the nose; equilibrium is maintained by the contact pressure tending to push the spike out of the termination.

On unloading, the load in the rope pad drops off fastest at the nose of the spike. This is because the friction on the rope hinders the movement of the rope backwards. This retains the extension that is present in the loaded fibres, and therefore the load in the fibre pad is also retained. Once global sliding is occurring then the extension in the rope can reduce and the load can fall. This retention of load therefore feeds back into the friction that the rope exerts on the spike, which is manifested by the elastic slip in these diagrams.

On unloading from 60% to 50% the nose of the spike has attained zero elastic slip and therefore zero friction, although the true slip accumulated so far remains. The accumulated slip will only change if further true slip occurs in either direction. Further along, in cell D2, there is still some elastic slip present acting into the termination; more still is retained in cells D3 and D4, and in D5 in the middle of the spike, the rope is still at the critical limit. Beyond this point the spike moves backwards relative to the rope, due to the load at the nose reducing; this causes the elastic slip to increase as observed in cells D7 and D8. On unloading the whole spike moves backwards relative to the barrel due to the frictional pull along its length reducing. Indeed due to the friction reversal, the nose of the spike now starts to be pushed backwards; the contact pressure remains constant as seen in Section 6.2.3, therefore the only way for the forces on the spike to remain balanced is for the friction at the base to increase.

On unloading further from 50%, this trend in the slip-reversal progresses; by 35% the slip at the nose is now critical in the reverse direction; slip of the rope is about to occur back over the spike. The elastic slip in cell E2 has reversed in direction, but it has not yet reached the critical limit; this hysteresis is due to the friction acting along the rope, between E1 and E2, and due to the elasticity of the yarn as it relaxes. Further along in cell E3, the elastic slip has just reversed in direction, whilst that in cell E4 has not. Cell E5 remains the same. The elastic slip in cells E7 and E8 increases further as the base of the spike moves even further back relative to the rope on unloading.

Position 5 is a very significant location — the magnitudes of the true slip and the elastic slip remain constant here throughout the cycling regime; the slip only alters once reloading past the initial preload is performed. Between position 5 and the nose, slip back and forth occurs during cycling; between this position and the base of the spike, the elastic slip varies in magnitude but not in sign. The magnitude of slip at the base changes as the spike is effectively pulled in and out by the changing load at the nose. That there

is one position where the slip remains unchanged may be an oddity of this analysis; at some point along the termination, the rope and the spike must be moving together, however this particular point does not have to remain static on the spike throughout the cycling.

Once the load has dropped to 20%, true slip has started to occur at the nose in the opposite direction to before; thus the accumulated true slip reduces. The elastic slip at cell F2 has reached the critical level but slip has not yet started. The elastic slips in F3 and F4 have become slightly more negative. F5 remains the same, and F6 and F7 increase slightly.

On reaching the unloaded limit of 5%, the limit of slip has been reached all the way along the spike to cell G3, slip occurring in cells G1 and G2. Cell G4 now has no friction at all, the elastic slip has reduced to zero. G5 remains the same; the elastic slip near the base increases further, such that G6 now reaches the critical limit.

Hence in an unloaded termination, there is slip of the rope over the spike in two directions. This occurs at the nose where the rope moves back, and over a region in the middle where the spike moves back due to the reversal of friction at the nose. Thus in the unloaded state the spike has friction acting in opposite directions at either end, this leads to a large compressive force in the spike of 48kN as noted in Section 6.2.4 below. This region in the centre of the spike will not be the critical one in an abrasion regime as the magnitude of the true slip here is minimal compared to that at the nose.

Figure 6.2 shows the frictional stress acting along the length of the spike during the pretensioning phase to 60%. As was shown in Figure 6.1 for levels A, B and C, a region of true slip grows down the spike from the nose on loading; by 60% this has reached as far as 140mm. The base of the spike is at 40mm, the nose at 220mm. The zero point, for the finite element analysis, was arbitrarily set at the start of the conical surface inside the back of the barrel. (The length along the axis, in this and the similar graphs later in this chapter, is taken to move with the spike, rather than being a fixed position.

Therefore no superimposed bed-down is shown, for clarity.)

At the nose of the spike the relative displacement between the rope and the spike exceeds γ_{crit} and so true slip occurs. The rest of the spike has elastic stick occurring with no true slip. This slipping region can be seen as the plateau in Figure 6.2 between 220mm and 165mm. At the 60% preload this slipping region has extended along the spike to the 150mm point.

The kink that exists at 180mm is a by-product of the initial assembly, arising from the slip that occurred when the spike was pushed into the rope. It is 'ironed out' by the time the load reaches 30%, and does not influence the analysis further. The ripples seen between the slipping plateau near the nose, and the elastic region near the base, are due to the static frictional limit being greater than the dynamic one. Once sliding occurs, the stress drops to the level of the dynamic friction on the slipping plateau. The slipping plateau rises with load as the contact pressure rises (Section 6.2.3). The unloading curves are not shown; they are similar to the unloading curves in the cycling region presented next.

6.2.1.3 Behaviour on cycling between 5% and 50%.

Figure 6.3 shows the relative slip between the rope and spike during a cycling regime from 5% to 50% and back to 5%. The same regime is observed to occur for the first and second load cycles, so it may be assumed that this regime will continue without any ratchetting until abrasion changes the geometry of the termination. The states at the two limits, 5% and 50%, remain constant regardless of the number of cycles. Therefore from a slip point of view there is no difference in loading to failure immediately, or cycling to 50% twice then loading to failure.

Figure 6.4 can be used to quantify the magnitude of the friction on the spike during the cycling phase. It shows the force along the length of the spike for each increment of the analysis during the unload-reload cycle. The reloading

increments are represented by dashed lines; the unloading by dotted lines. When loaded, all the friction acts to pull the spike into the barrel as seen in cells J1→J7. On unloading the friction at the nose reverses in sign. 'In the middle' there is no change in the frictional force during cycling; this correlates with there being no change in the relative slip here, as seen in the cells at position 5.

On reloading to 20% a lag in slip between the nose and further along the spike occurs. This is observed as the elastic slip in cell H1 increasing to zero, i.e. the rope is no longer slipping backwards and there is now no friction present at all; whereas the elastic slip in cell H2 is still negative, and more so in cell H3. This delay in slip between the nose and further along the spike is similar to that on unloading. The lag explains the behaviour at the nose of the spike in the plot of frictional stress along the spike as seen in Figure 6.4 between positions 200mm to 220mm. The slip that was occurring at 5% at the nose ceases, as the rope is pulled in again (cells G1 and H1); the true slip that occurred at G6 also stops as the spike is now pulled in again by its nose, and so stops moving back relative to the rope at the base.

Further loading to 35% brings the rope at the nose of the spike to the point of slipping, at 50% true slip occurs. By 50% the limit of slip has also been reached at position 2, but no actual slip takes place, the rope is again slipping elastically over the spike at positions 3 and 4, position 5 remains unaltered, and the slip at the base of the spike has reduced as the spike is pulled in at its nose. It can be seen that the magnitude of true slip at the nose from 60% to 5% is less than that from 5% to 50%; so both positions 1 and 2 remain behind their maximum displacements. (Position 2 is situated at the level where the slip is just about to occur; this can be seen in Figure 6.4 as the plateau of slipping between 210mm and the nose at 220mm.)

On unloading a similar pattern occurs, with the only true slip occurring at the nose between 20% and 5%. This global movement of elastic slip near the nose region can be seen by the global movement of the frictional stress curve

downwards in Figure 6.4, complete with the kink where the plateau ended. The nose unloads faster than the rest as noted above, and this leads to an exaggerated kink at 210mm, it can then be seen that for the last four loading increments the friction reaches a plateau. The final load increment (5%) is represented by the plateau at 0.011kN/mm^2; the penultimate increment is the dashed line just above this — it has the same plateau between 220mm and 210mm. Two increments before this, the unloading curve just reaches the slip plateau. On reaching the slip plateau, little peaks can be observed where the higher static frictional limit still applies.

Looking at the base of the spike in Figure 6.4, it can also be noted that there is a kink at 125mm where the frictional limit was reached on first-loading the rope; this plateau extends along to the middle at 165mm. On loading this kink remains; however, only elastic slip is occurring – the kink is just a residual indication of the plateau that has occurred in the middle region. The tensions in the rope on either side of this kink are slightly different due to the slip that occurred on one side only, it is this discontinuity in tension that manifests itself as the kink. It can also be seen that the friction and hence elastic slip is higher at 5% than it is at 50% and moves back and forth uniformly on cycling the load; this equates with the changes in relative slip seen at position 7.

6.2.1.4 Behaviour on loading from 5% to failure.

Figure 6.5 shows the relative slip schematics for the final loading phase to 100%.

Loading from 5% to 50% is the same as mentioned in Section 6.2.1.3. By 60% the situation on first-loading has been recovered, with an identical slip and frictional arrangement being in place. Slip is occurring along the length on the nose of the spike right back to the middle; the elastic slip at the base has dropped off to the low levels that it was at previously. By the time the

load reaches 100% this friction at the base has dropped off to zero.

On loading from 60% to 80% and 100%, which are first-loadings, the magnitude of true slip at the nose increases dramatically as the rope slides over the spike; the slip region also extends down the spike to cell R6. This growth in the slip plateau can also be seen in Figure 6.6. Figure 6.6 shows the frictional stress along the spike on loading from 5% to 100%. The shaded area represents the region where true slip is occurring; this is at the nose on reloading, followed by a sudden growth down the spike once the preload has been exceeded. By comparing Figures 6.2 and 6.6, it can be seen that the first-loading patterns from 60-100% are a continuation of those from 0-60%; the intervening cycle having had no effect on the behaviour. Figure 6.6 also shows the drop in friction at the base of the spike, which is shown by cells R7 and S7.

6.2.2 Slip between the rope and the spike.

The overall slip between the spike and the rope for the whole loading history is shown in Figure 6.7. This graph gives magnitudes for the slip that was shown schematically in Figures 6.1, 6.3 and 6.5. The slips at the four significant positions identified in Figure 6.4 are shown, with the zero displacement for each curve located in the centre of the cycling regime for clarity. At the nose, on loading, the rope slips over the spike (0.4mm), slips back and forth a bit (0.1mm) when cycled, then slips further when loaded to breaking (0.7mm). It can be seen that the unloading from 60% and the unloading from 50% are different curves as mentioned in Section 6.2.1.3: the rope does not regain its preload slip during the cycling regime. On loading to failure, however, it rejoins the original loading curve at the 60% mark, then continues rising. There is hysteresis during the cycling phase due to the slip that occurs.

Near the nose, the rope slips 0.35mm on loading, slips back and forth a bit during cycling with no hysteresis – the slip is all elastic, and then slips a further 0.35mm on loading to failure. There is less slip in the middle,

0.15mm to 60% and a further 0.15mm to failure, with a noticeable zero slip on cycling at this salient point. There is minimal slip at the base.

6.2.2.1 Cycling.

Figure 6.8 shows the frictional stress relative to the slip that occurs during cycling, with a sub-plot for each of these four salient points. The horizontal portions on Figure 6.8 indicate where true slip occurred, the inclined portions are due to the stiffness-in-stick modelling that is used. On loading from zero frictional stress a movement of γ_{crit} will take place before any true slip will occur. For this analysis γ_{crit} was set to be 0.06mm. It can be seen that between slip reversals an elastic slip of $2\gamma_{crit}$ or 0.12mm is present. The true slip that occurs in this regime is about 0.08mm, out of the total 0.2mm relative movement between the rope and spike. As mentioned in Section 5.4.7, once the elastic slip limit is exceeded the value of γ_{crit} is insignificant, so although the elastic slip makes up a significant portion of the graph it does not influence the end result.

Near the nose $\gamma = -\gamma_{crit}$ on unloading to 5%, therefore it is on the point of sliding but it does not quite reach γ_{crit} on reloading to 50%.

At the base of the spike the direction of the loading-unloading curve is reversed relative to the curves at the nose, however it can be seen that the gradient is the same; this is because the same stiffness-in-stick is present along the spike. The stiffness-in-stick is pressure dependent because the effective coefficient of friction is determined by the contact pressure, and the contact pressure is almost uniform along the length of the spike (Section 6.2.3).

6.2.2.2 Behaviour on loading to 100%.

Once the preload level has been exceeded, the region of true slip extends along the spike as noted in Section 6.2.1.4. The plateau not only increases in length,

but also in magnitude, due to the rising contact pressure (Section 6.2.3).

6.2.3 Contact force between the rope and the spike.

Figure 6.9 shows the variation in contact pressure with the varying load in the rope. For each of the four salient points selected in Section 6.2.1.1 the curve of the contact pressure has the same overall shape; an almost linear increase in the contact pressure with load on first-loading; and an almost uniform contact pressure when unloading-reloading.

The rise in contact pressure at the nose on first-loading can be linearised to give an equation for use in the prediction of the lifetime under a cyclic loading (Equation 7.12).

Figure 6.10 shows the variation in contact pressure along the length of the spike for salient load cases; the initial loading to 30%, 60% and 100%, and the cyclic limits of 5% and 50%.

Due to the geometry and the modelling, the fibres are more compressed at the nose and the base than in the middle. However, the contact pressure is almost symmetrical; it is not significantly greater at one end than at the other. Figure 6.10 also shows the increase in contact pressure as the spike is drawn in by the increasing load, and the retention of contact pressure as the spike is unloaded.

The contact pressure on the barrel is very similar to the pressure on the spike due to the low shear strength across the rope; all the pressure on one side of the rope is transferred directly across to the other side.

6.2.4 Force in the spike.

Figure 6.11 shows the variation in force along the length of the spike, for salient load cases during the loading history. It can be seen that the force in the spike is zero at both ends throughout the analysis as would be expected;

there can be no resultant force on the spike. This force is calculated by summing up the resolved contact forces (normal and frictional) along the length of the spike from the nose to the given location.

On loading the spike goes into tension — it is being pulled at the nose, and restrained at the base. At 30% preload it has a maximum tension of 21kN; at 60% this has risen to 42kN, and rises to 80kN at the failure load. These maxima are all located towards the base of the spike at about 120mm.

On unloading, due to the slip reversal, the rope pushes the nose of the spike back, whilst the base is still held firm, so the spike goes into compression; it reaches a maximum compressive force of -48kN, near the nose of the spike, at 175mm.

Figure 6.12 shows the force along the spike for the second load cycle; both load cycles give virtually identical curves. The intermediate load increments are plotted to show that there is no significant difference in the unloading-reloading shapes.

It can be seen that the curve for a reloading to 50% has a slightly different shape from the first-loading curves; this is because the frictional slip between the spike and the rope is different on reloading as explained in Section 6.2.1.3.

Figure 6.13 shows how the force in the spike varies during the analysis at the four locations identified earlier in this chapter (note the force axes have different scales). It can be seen that there is hysteresis in the force at the nose when cycling the load due to the frictional slip that takes place. For all locations the spike goes into tension when the rope is loaded and into compression when the rope is unloaded.

6.2.5 Stresses in the spike.

The stresses presented in this section for the spike are taken from the central integration point for the elements on the surface of the spike, at the four

salient points identified in Section 6.2.1.1.

The radial and hoop stresses in the spike (Figures 6.14 and 6.15) are almost identical along the length of the spike (as would be expected for a cylinder loaded externally). They rise linearly to a peak of roughly -0.13kN/mm^2 at failure, and maintain their compression of roughly -0.07kN/mm^2 when unloaded and reloaded from the 60% pre-load. No hysteresis is present. Note the similarities between these curves and those of the contact pressure (Figure 6.9).

For most of the spike the axial stress goes into tension on loading and then into compression on unloading (Figure 6.16). At the nose the stress is compressive throughout, which is due to localised deformation of the surface of the spike at the edge of the contact zone; this stress is negligible however, and does not affect the overall analysis. For the other three locations, the curves have identical shapes to those of the force in the spike (Figure 6.13), as would be expected.

The shear stress curves (Figure 6.17) highlight the change in the direction of friction along the spike; at the nose the rope slips over the spike into the termination on loading and the shear stress rises, while on unloading the slip reverses in direction and the shear stress becomes negative. At the base of the spike the spike slips over the rope into the termination as it is drawn in by the nose on loading, so the shear stress is negative. On unloading the magnitude of the shear stress reduces to zero; this coincides with the axial stress also reducing to zero. These curves have similar shapes and magnitudes as those for the inner layer of rope (seen later in Figure 6.35); both are sheared relative the outer layers of rope.

6.3 Contour plots of stress.

Figures 6.18 and 6.19 show the variation in axial, shear, hoop and radial stress in the spike and barrel at three loads; preloaded to 60%, unloaded to

5% and loaded to 100%, just before failure.

At the 60% preload, the spike and barrel both go into tension axially with only small amounts of localised compression at the ends of the contact zones, and around the tapped hole in the spike. On unloading both spike and barrel go into compression in the middle, due to the loading from the trapped rope. The rope remains in tension, Section 6.5.1, because it started from a much higher stress than the metal bodies. On loading to failure, tension is again present in the centre of the termination, with the maximum value feeding from the anchorage through the barrel into the rope and thence into the spike.

The maximum shear stresses are present at the ends of the contact regions; the magnitude and size of these zones do not alter much between these three load cases. It can be seen that at 100% there is a large shear along the inner surface of the barrel, where the load is transferred out of the rope; there is insignificant shear in the corresponding region of the spike.

The radial stresses in the spike and barrel are all compressive due to the spike bedding down. Similarly the hoop stresses are compressive in the spike and tensile in the barrel due to the bed-down. As both sets of stresses are bed-down dependent they remain constant when the load in the rope is reduced, i.e. throughout the cycling regime; because reducing the load does not affect the bed-down (Figure 7.21) or the contact pressure within the termination (Figure 6.10).

There is a uniform zone of radial compression in the spike of 0.08kN/mm^2 when a load of 60% has been reached, which remains on unloading, and rises to 0.12kN/mm^2 at 100%. Similarly there are uniform zones of hoop compression of 0.05 and 0.10kN/mm^2 at the same stages.

The radial and hoop stresses in the barrel are gradated from maxima at the contact surface to minima on the outside edge. There is negligible stress in the two ends.

Figure 6.20 shows the variation in axial stress on cycling the load between 5% and 50%.

6.4 Barrel results.

6.4.1 Relative movement between the rope and the barrel.

In contrast to the movement of the rope over the spike there is only one salient feature for the movement of the rope over the barrel. This is the division between true slip occurring adjacent to the nose of the spike, and the region adjacent to the base of the spike where only elastic slip occurs.

Figure 6.21 shows the relative displacements between the rope and the barrel during the whole analysis; Figure 6.22 shows an enlarged view of the cycling portion. Zero displacement is arbitrarily taken to be in the middle of the cycling regime to aid clarity. The rope slips over the barrel by 13mm along the whole of its length on loading to 60%. The spike moves less than 0.5mm relative to the rope during the same period (Figure 6.7), and so it too moves in about 13mm — this is the bed-down (c.f. Figure 7.21). On cycling negligible slip occurs. On loading to failure a further 4.5mm of slip occurs along the whole termination.

When cycled, the loading and unloading slopes (Figure 6.22) all have the same gradients and directions; the contact pressure varies by less than 20% along the length, therefore the stiffness in stick is almost uniform.

As with the spike, true slip will start after an elastic slip reversal of $2\gamma_{crit}$ (= 0.12mm) has occurred. However the true slip that then occurs is larger, at the nose a back and forth slip of 0.24mm is calculated. There is no true slip between the middle and the base of the termination; this region stays stuck when cycled, so no abrasion will occur here.

6.4.2 Friction between the rope and the barrel.

Figures 6.23 and 6.24 show the variation in frictional stress along the length of the barrel for various loads, with the four locations used elsewhere noted.

Figure 6.23 shows the friction attained for first loading to 30%, 60% and 100%, for unloading to 5%, and for reloading to 50% and 60%. On first-loading the slip is uniform along the length of the barrel. This plateau is due to slip occurring along the entire length. It is slightly raised at the two ends due to the geometry of the metal surfaces. As the contact pressure rises, the frictional stress rises.

Figure 6.24 shows the friction for the load increments whilst cycling the load on the rope. On unloading, the base half of the termination remains stuck; with the rope moving back and forth with elastic slip only, the friction remains below the critical stress. By 5%, at the base the friction has dropped to zero, in the middle the critical limit has just been reached in the reverse direction, and the start of the plateau indicates that sliding is occurring beyond this location. There is a similar hysteresis in the slip at the nose, as was seen over the spike in Section 6.2.2, although here it is more clearly demonstrated that the static friction is greater than the sliding friction, by the peaks labelled in the figure.

The kink at 155mm is situated at the limit that the true slip reached on unloading. Where the rope did slip backwards, it offset the equilibrium point from which the elastic slip oscillates. The same is true for the kink at 175mm which is due to the equilibrium point being offset by slip when reloading the rope. This kink is 'ironed out' when the rope reaches the point of slipping in the opposite direction on unloading.

6.4.3 Stresses in the barrel.

The stresses along the inner edge of the barrel are plotted in this section. Due to the nature of the discretisation of the finite element mesh, there is some fluctuation of the stresses at the integration points within a single element, as shown in Figure 6.25. This figure shows the axial stress present in an element on the inner surface of the barrel, adjacent to the nose of the spike. The stresses for three integration points are plotted; these lie parallel to the inner surface along the middle of the element. The figure only shows the stresses on first-loading to 60% and again to 100%; the cycling regions have been omitted for clarity (all the cycling regions are parallel to one another, but are offset according to the stress state that was present when the unloading commenced). These stresses can be seen to rise and fall as the rope is loaded; this effect arises from the rope, with its contact elements, sliding over the barrel element. These ripples are partly due to the interpolation used to transfer the load between the bodies, but are mainly due to the relatively course nature of the mesh used to model the barrel at the end of the contact zone. Within the contact zone the fluctuations are minimal, they only become significant where there is a discontinuity in the contact, arising from the rope and the barrel separating.

The edges and middles of the elements bordering the contact zone have different 'stiffnesses' and thus when one element 'rides over' another, the stresses within it are affected. The choice of nodes for linking the master and slave surfaces is determined automatically within Abaqus to be the nearest nodes; when the contact moves from node to node, the stresses will cycle accordingly. Each crest represents the movement of one element over another; from Figure 6.21 the total slip between the rope and the barrel is 18mm, the elements are 2.5mm in length, leading to relative movement of seven elements. It can be seen that there are seven crests and troughs for each integration point.

The mean of points 2, 5 and 8, is shown in Figure 6.26 on the 'near the nose'

sub-plot. On loading the axial stress is almost constant at -0.012kN/mm^2; on unloading from 60% the compression increases linearly to -0.02kN/mm^2 at a load of 20%, at which point slip starts occurring, and the stress drops to -0.015kN/mm^2. It drops further on loading, till a load of 30% is reached when slip starts again, at which point the axial stress is -0.006kN/mm^2; it then returns to the initial curve.

For the rest of this section, a mean of the integration points 2, 5 and 8, is plotted for an element at each of the four salient locations along the inside face of the barrel.

The radial stress is shown in Figure 6.27. This is compressive throughout. As the termination is loaded, and the spike is drawn in, the barrel is pushed outwards causing a compressive radial stress, and a tensile hoop stress as shown in Figure 6.28. On cycling the load, the position of the spike and the contact pressure do not change significantly; so the magnitudes of the radial and hoop stress remain constant, as seen in the figures.

The axial stress (Figure 6.26) does not behave in such a well-ordered manner as the radial and hoop stresses. On loading, the elements adjacent to the nose of the spike go into compression. This might at first seem to be counter-intuitive, but can be explained if a consideration is made about the forces exerted on the barrel by the rope. Along the length of the contact zone the barrel is pushed outwards by the rope, at either end of the barrel there is no such load, and these end regions restrain the centre portion from expanding radially. This restraint gives rise to localised bending at either end of the contact region; such that the regions in contact go into compression, whilst those regions on the inner surface but outside the contact zone, go into tension.

This can be seen in Figure 6.29 which shows the axial stress in the barrel after it has been unloaded from 100% to 0%. The barrel has been plotted with the displacements magnified by a factor of 100 to highlight the movement in the middle relative to the ends. The bending regions at the ends of the

contact zone can be clearly seen, with the rest of the spike having zero axial stress except for a small zone in the middle which is compressed by the rope on unloading.

6.4.4 Force in the barrel.

Figure 6.30 shows the force acting at four cross sections through the barrel. At the very base of the barrel the force will match the load in the rope as it is carried away into the anchorage. Further along the barrel the force will be less, and will indicate how much of the load has so far been transferred from the rope. At the very nose, before the rope makes contact with the barrel, the force will be zero. (Note the scales on these graphs are different due to the large variation in force along the barrel.)

On loading, the barrel goes into tension; and the force rises linearly for the initial loading stages. On unloading, the force in the barrel 'at' and 'near' the nose drops off rapidly, becoming compressive. Once slipping starts, however, the forces plateaus — this is because the force transferred into the barrel is equal to the frictional stress multiplied by the contact area on the rope side of that location, both of which remain constant. On reloading the force rises quickly, and plateaus when slip occurs again. Hence the hysteresis present in the cycling portions. In the middle a similar shape is observed with less hysteresis; no hysteresis is present at the base.

When the rope is unloaded, the barrel, like the spike, has a locked-in compression due to the friction from the rope unloading. Equilibrium is maintained by the rope staying in tension (Section 6.5.1).

For both the spike and the barrel it can be seen that the initial gradients of unloading from 50%, 60% and 100% and reloading from 5% are all the same for each given location. This is because the termination is acting as an elastic body before slip occurs.

6.5 Rope results.

6.5.1 Stresses in the rope.

Figure 6.31 shows the transverse stress-strain in the rope at various points along its length. The dashed line represents the stress-strain curve derived from experiments (Chapter 4), which is implemented by a user-subroutine for the material properties as detailed in Section 5.4.5. The change in moduli at the 30% preload can be seen on the figure where the initial segments of the loading curves are parallel to the first desired stiffness, and then change to lie parallel to the second desired stiffness. Due to the coarse nature of this switch, some elements overshoot the curve. As the stress is applied cumulatively by a summation of the changes from increment to increment, rather than by a universal formula, this overshoot remains throughout the analysis.

For all the locations, the inner layer of rope has the highest strain, and the outer has the lowest strain.

The hoop stresses are an order of magnitude less than the radial stresses and so are not detailed here.

6.5.1.1 Axial stress.

The mean axial stress in the rope is plotted against the load in the termination in Figure 6.32. At the nose the graph is a straight line as expected; the stress in the rope carries all the load. Moving along the termination some of the load has been carried out into the spike and barrel and so the curve deviates from a straight line; hysteresis being present due to the friction (albeit mainly stiffness-in-stick). When the rope is unloaded the axial tension in the spike, barrel and rope all drop off. The rope has a higher modulus (126.5kN/mm^2 c.f. aluminium 70kN/mm^2) than the spike and barrel, so for a given drop in strain, as the three entities unload together, it will lose more

stress than the aluminium bodies. However it starts from such a large stress that even when unloaded it remains in tension, whereas the spike and barrel both go into compression. It should be remembered that at any cross section through the whole termination the sum of all the axial forces will equal the load in the rope.

The stress in the rope drops going down the termination, such that at the base of the spike all the load has been transferred to the barrel and there is zero tension left in the rope.

6.5.1.2 Shear stress.

Figures 6.33, 6.34 and 6.35 show how the shear stress varies in the three rope layers as the load on the termination is changed. At the nose the inner layer is sheared in the opposite direction to the middle and outer layers on unloading, as it rubs back over the spike. The first-loading and loading-to-failure curves are similar, as the three rope layers move as one; it is only on unloading-reloading that most of the shear in the rope occurs. The hysteresis, due to the frictional stress plateauing when slip occurs, is clearly visible. When the friction reaches its limit, the shear also plateaus, as it is caused by the friction. The maximum shear stress observed in the analysis at the breaking load is about $22\mathrm{N/mm}^2$, which is comparable with the value which is believed to be used in designing the termination.

Near the base of the spike all three layers have the same shape graph, with an increasing negative shear on loading, and an increasing positive shear on unloading. This is due to the relative motions of the spike and barrel; the spike being pulled in on loading, then moving backwards on unloading.

6.6 Salient conclusions.

A finite element analysis has been formulated to model the behaviour of a Parafil spike-and-barrel termination. Using the results of this analysis, some salient conclusions can be made about the factors which govern the functioning of the termination.

6.6.1 Modelling.

- The rope has been modelled as three layers to allow for possible slip within the rope — no slip occurs.
- The contacting surfaces are successfully brought together by imposing displacements on the separate bodies. These displacements are removed once contact is established.
- The use of a user-defined material for the properties of the rope is employed, to follow the non-linear transverse stress-strain properties of the Kevlar 49. Figure 6.31 shows that the transverse stress-strain curves, which the elements follow, match those set using the data acquired in Chapter 4.
- The use of a user-defined friction has been employed to accurately model the slip between the rope and the spike, and the rope and the barrel. This enables the use of a modified Howell's equation of friction to be used, $\tau = a\sigma^{\beta}$. The stick-slip properties perform as expected.

6.6.2 Observations.

6.6.2.1 First-loading.

- The rope slips over the nose half of the spike; it remains stuck over the base half, with minimal friction.
- The rope slips over the barrel along the entire length.
- The spike beds down linearly.
- The contact pressure rises linearly, and is approximately uniform along the length of the contact zone.

6.6.2.2 Cycling the load.

- The rope slips back and forth over the nose of the spike. There is a salient point in the middle of the spike where no relative slip occurs. At the base of the spike the friction increases on unloading but no slip occurs.
- The rope slips back and forth over the barrel adjacent to the nose, with a similar relative slip to that over the spike. The friction adjacent to the base drops to zero on unloading, but no slip occurs.
- The spike bed-down remains constant.
- The contact pressure remains constant.

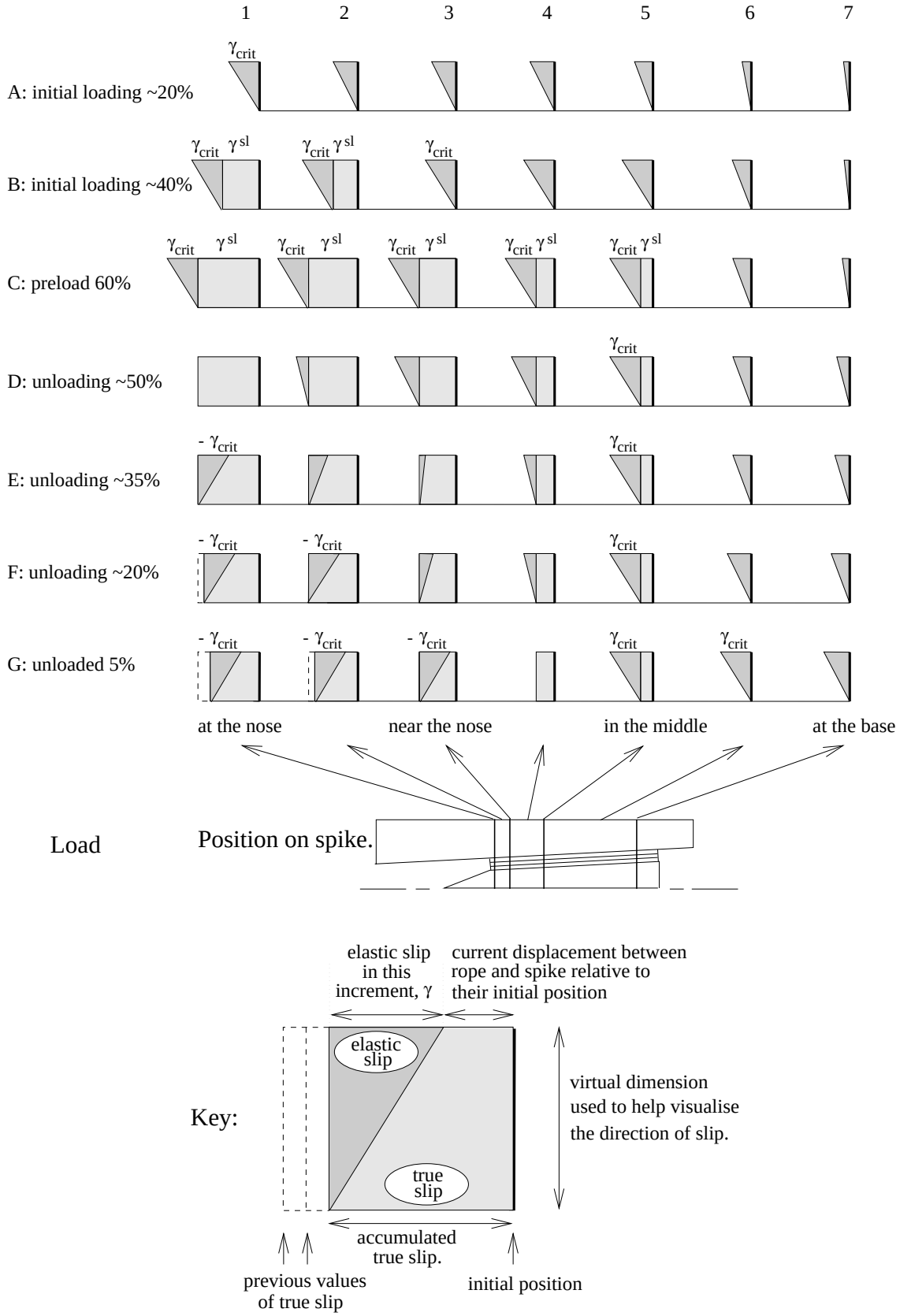

Figure 6.1: Schematic of the relative slip between the rope and spike during pretensioning, from 0 to 60% and down to 5%. The darker shaded triangles represent the elastic slip at seven points along the spike, the lighter shaded rectangles behind represent the amount of true slip that has accumulated at each portion.

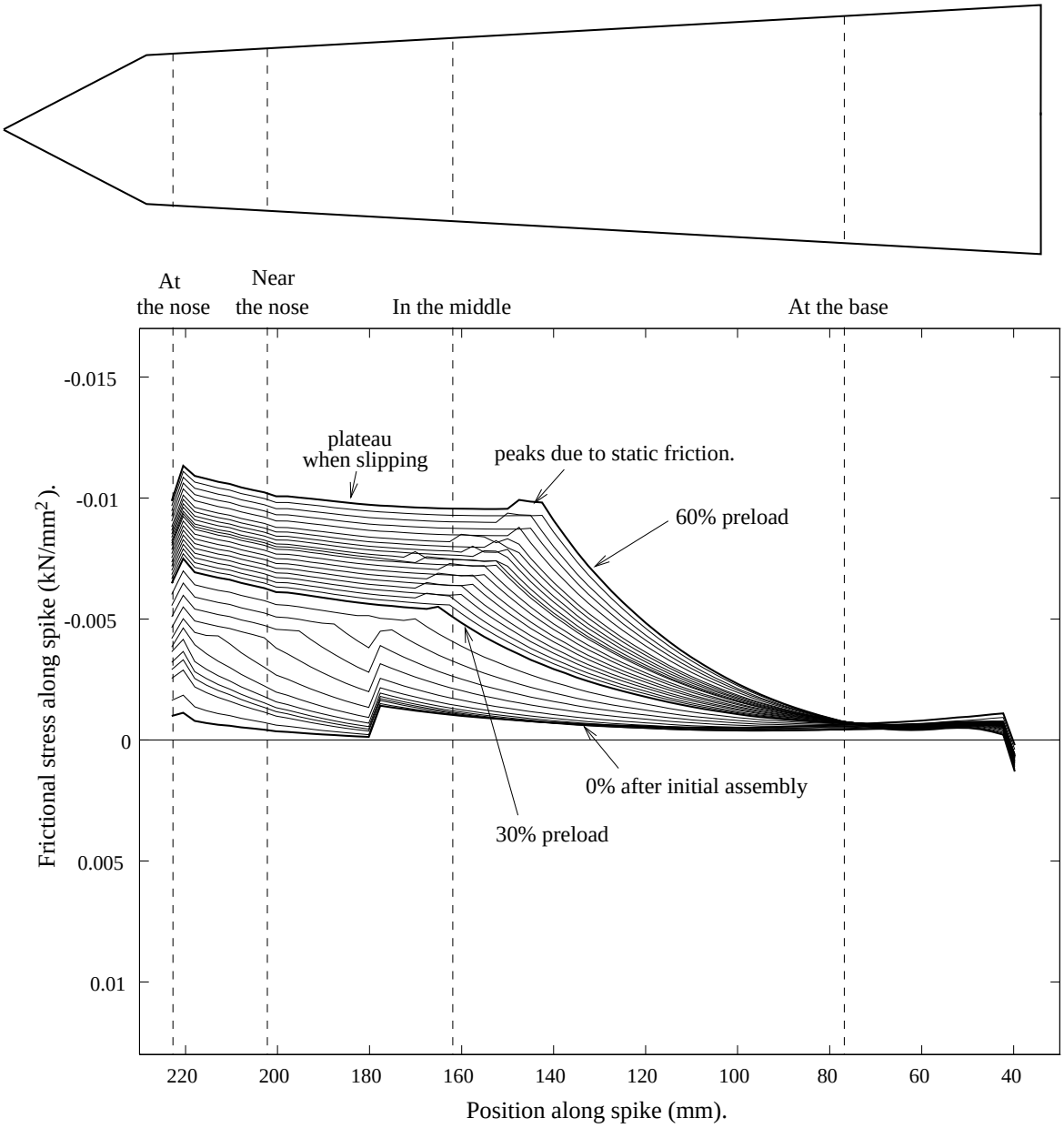

Figure 6.2: Frictional stress along the spike when the rope is pretensioned. The initial kink at 180mm is due to slip during the initialisation process, the later ripples between 30-60% load are due to the static friction being higher than the dynamic friction. The salient features used for all the later plots are labelled: **at the nose**, **near the nose** at the limit of the true slip, **in the middle** where no slip occurs during cycling, and **at the base**.

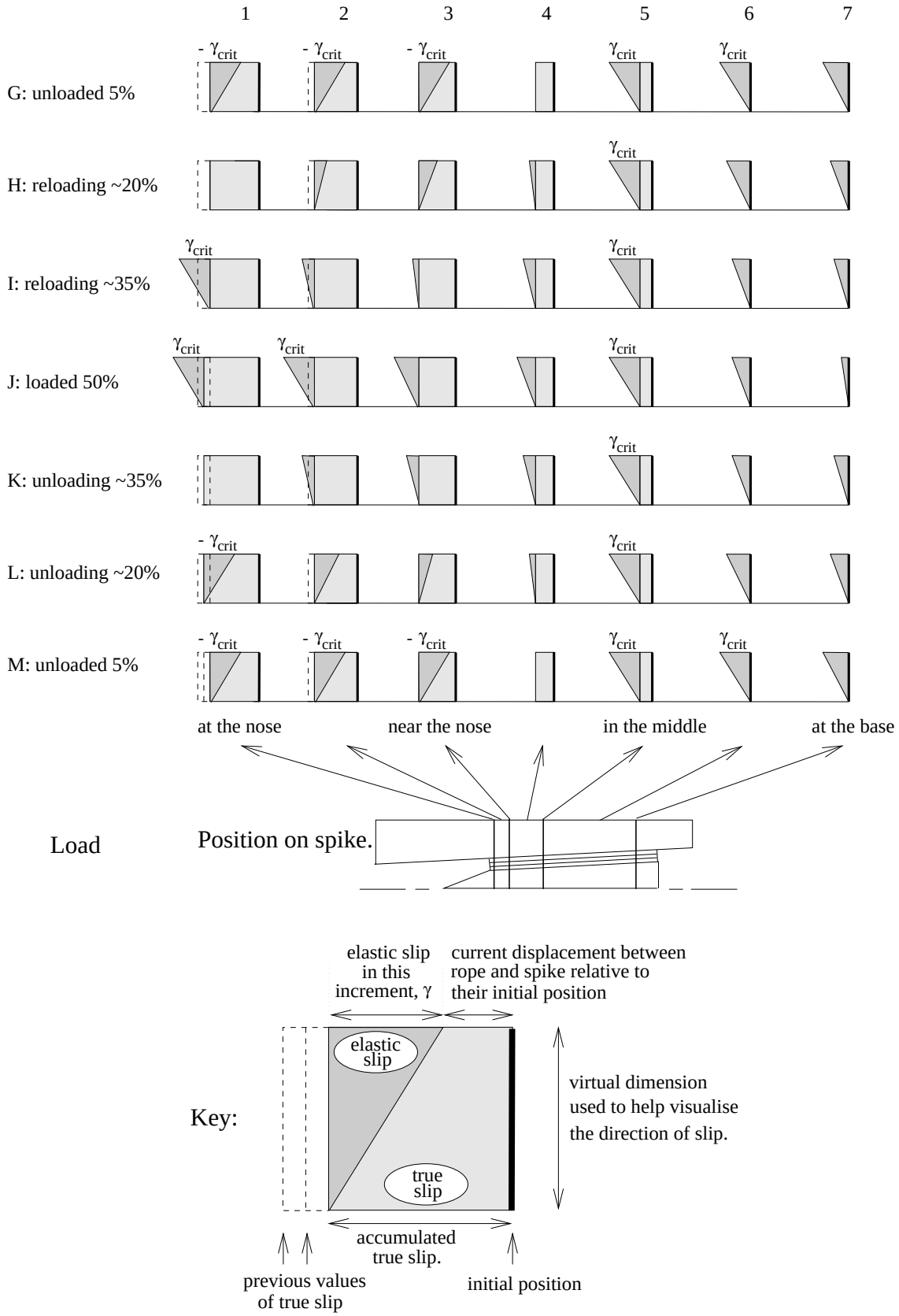

Figure 6.3: Schematic of the relative slip between the rope and spike during cycling of the load between 5-50%. The first and second cycle are identical.

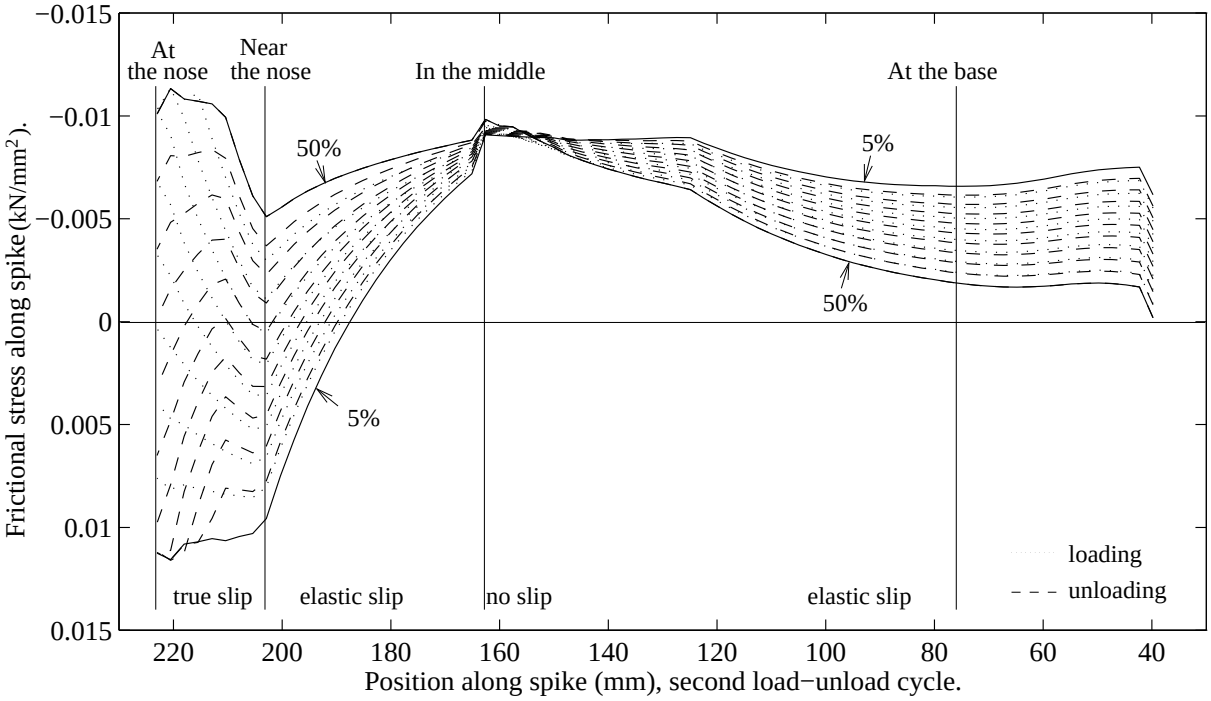

Figure 6.4: Frictional stress along the length of the spike during one cycle from 5% to 50% and down again.

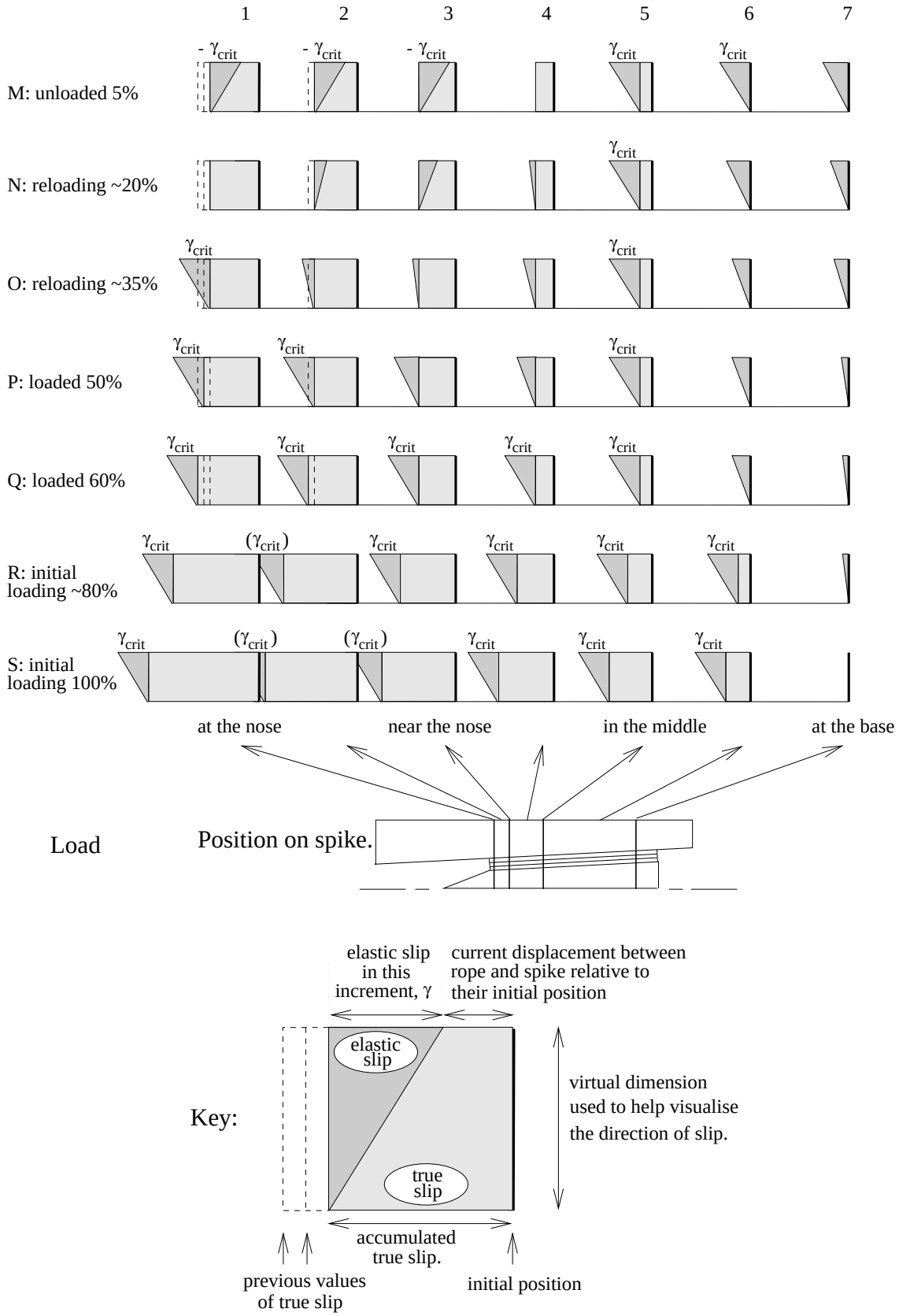

Figure 6.5: Schematic of the relative slip between the rope and spike taken to failure, after being pretensioned, cycled and unloaded.

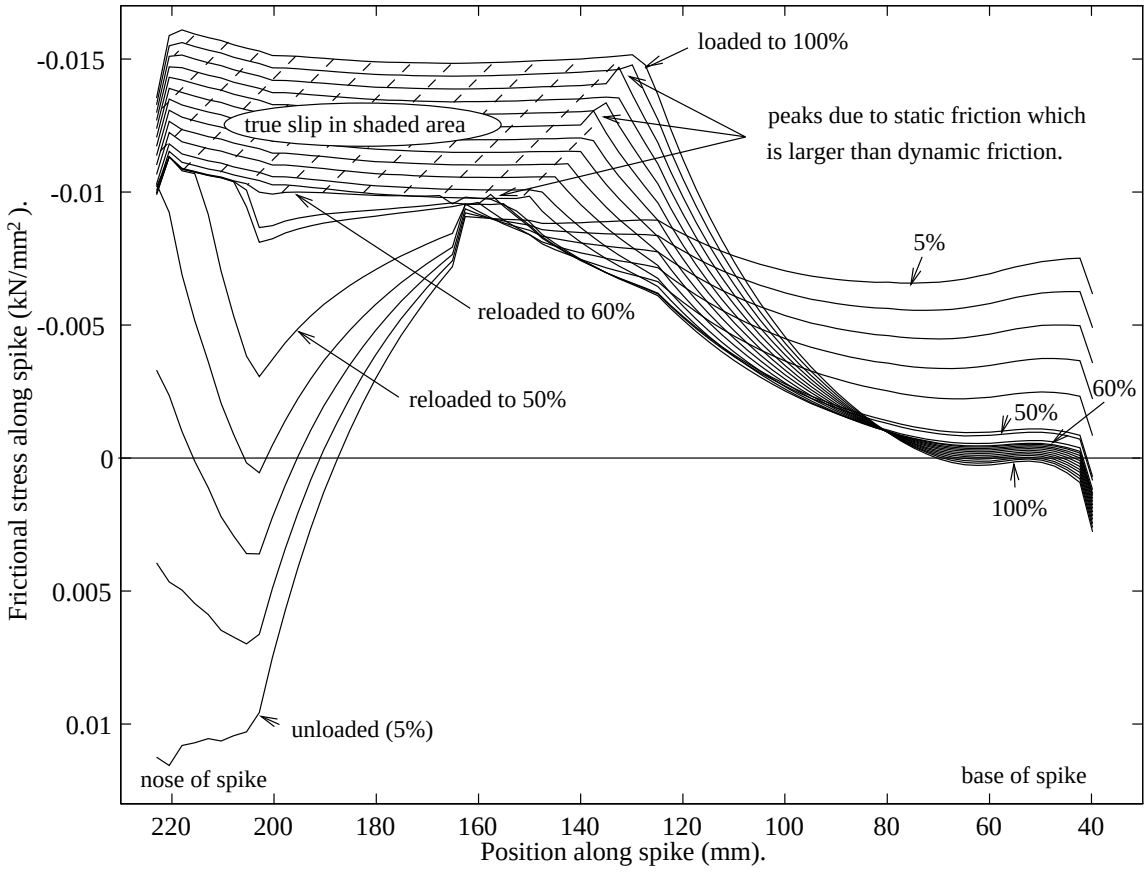

Figure 6.6: Frictional stress along the spike when the rope is loaded from 5% to failure load, having been pretensioned and cycled. The region of true slip at the nose of the spike grows rapidly down the length of the spike once the pretensioning load is exceeded, as indicated by the shaded area.

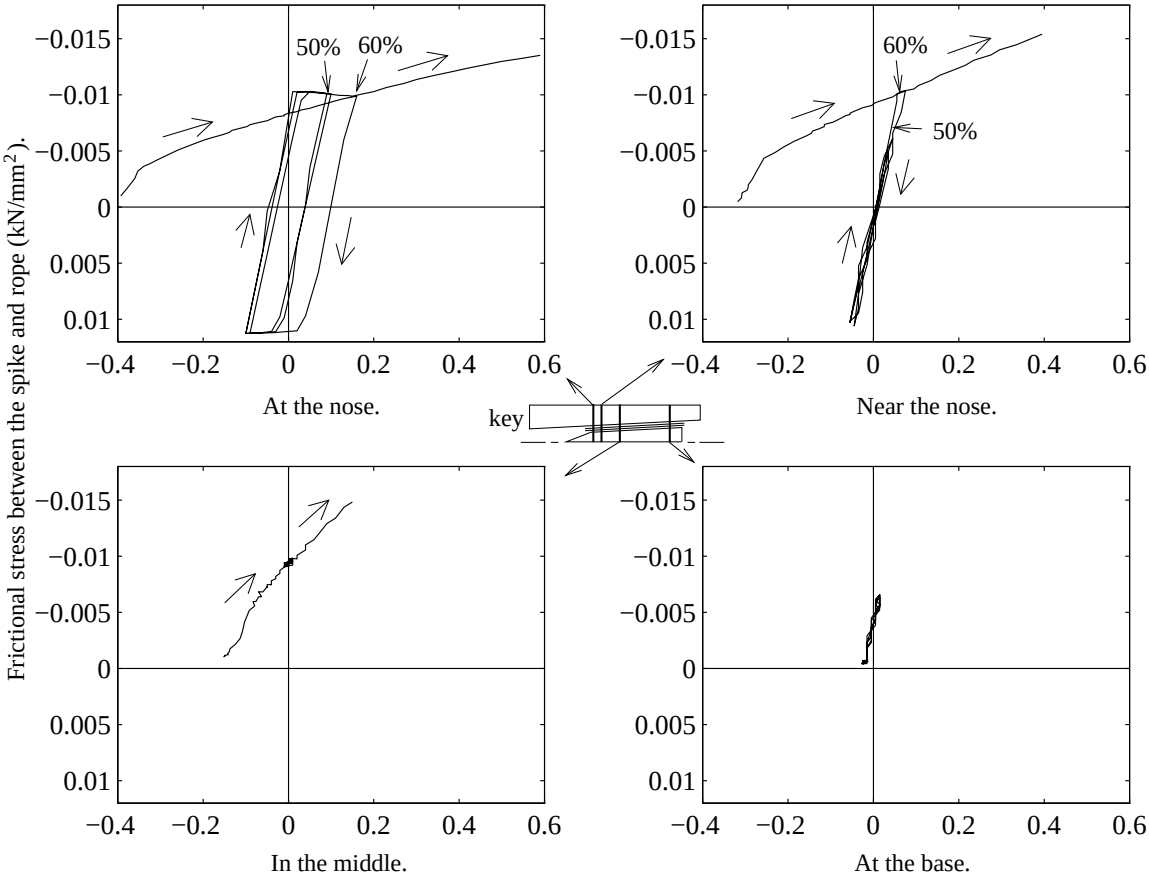

Figure 6.7: Frictional stress between the rope and the spike versus the relative displacement from the mid-point of the cycle, for the four salient locations identified in Figure 6.4.

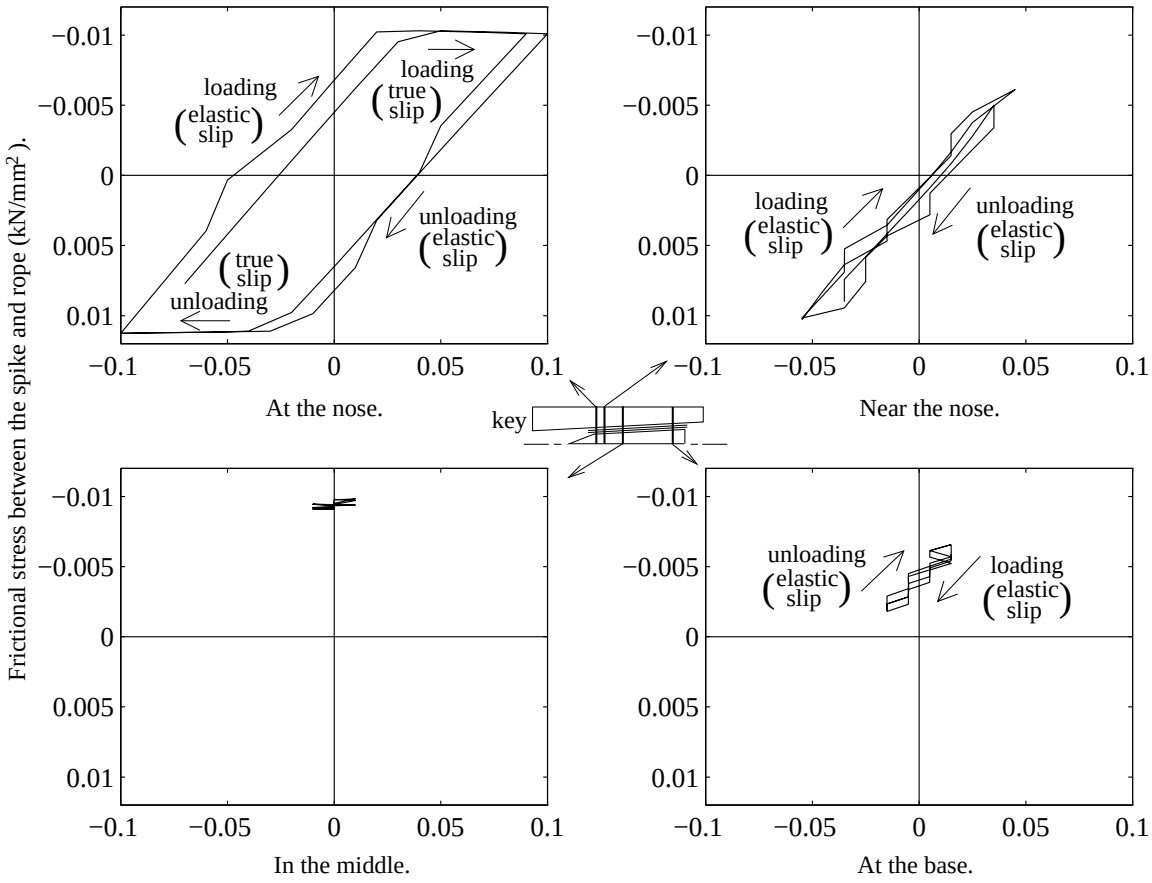

Figure 6.8: Frictional stress along the spike during cycling from 5% to 50% and down again, for the four salient locations identified in Figure 6.4.

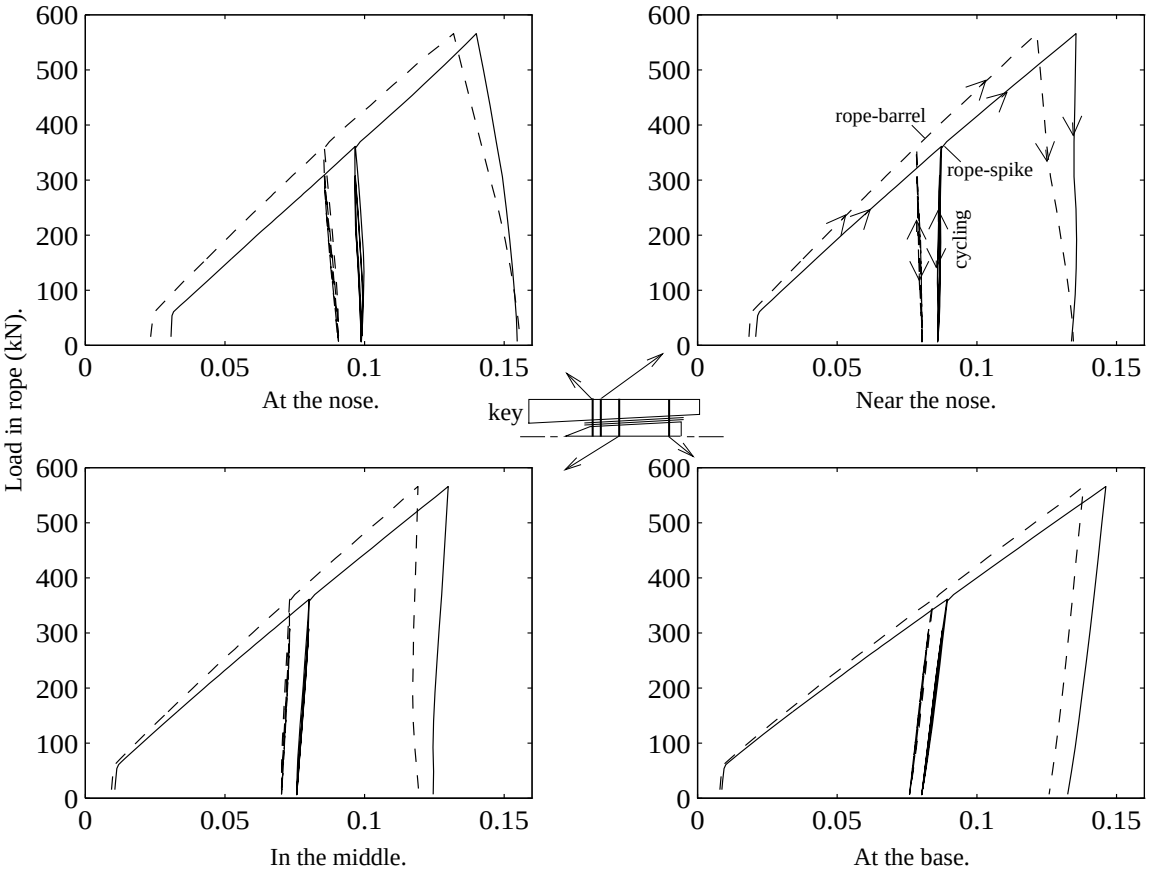

Figure 6.9: Contact pressures (kN/mm^2) throughout the analysis between the rope and the spike and the rope and the barrel. The pressures rise linearly on first-loading and remain approximately constant on unloading-reloading.

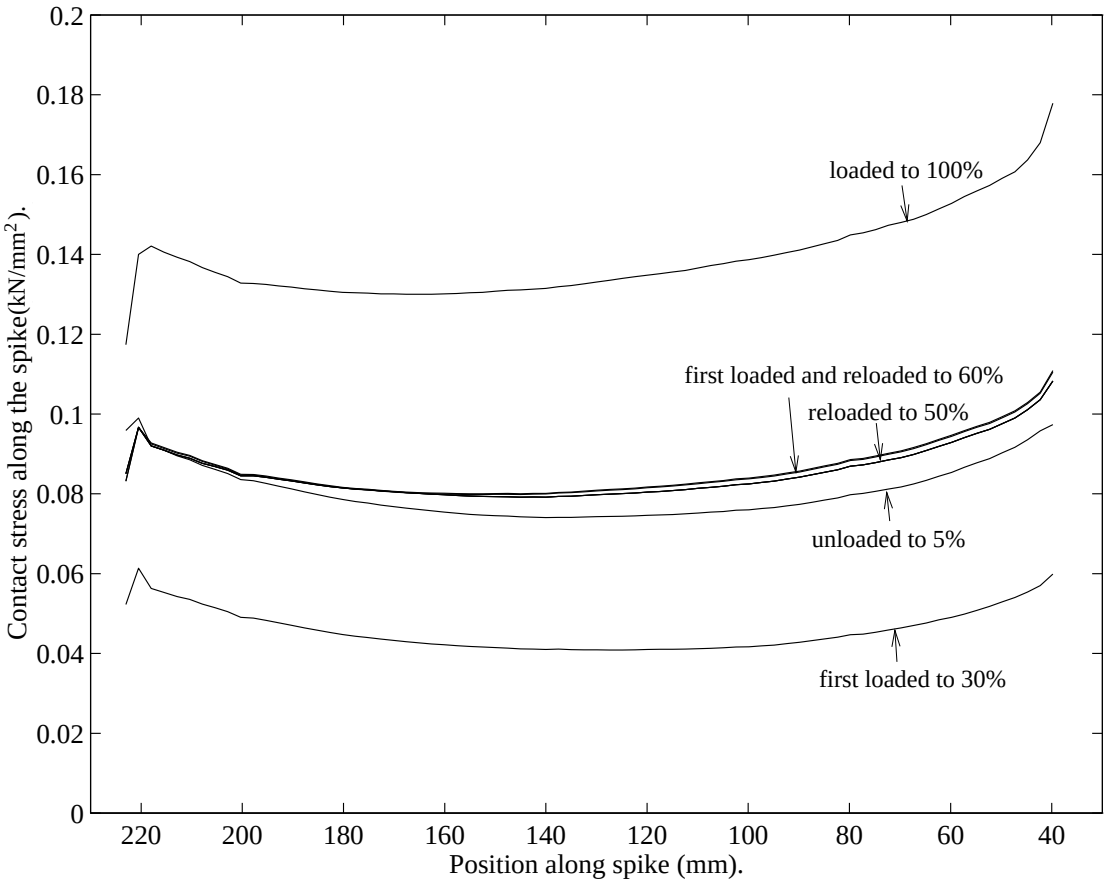

Figure 6.10: Contact pressures along the length of the spike at stages during the analysis, the contact pressure is almost uniform along the length of the spike, due to this being the design criterion. It can be seen to be slightly elevated at either end.

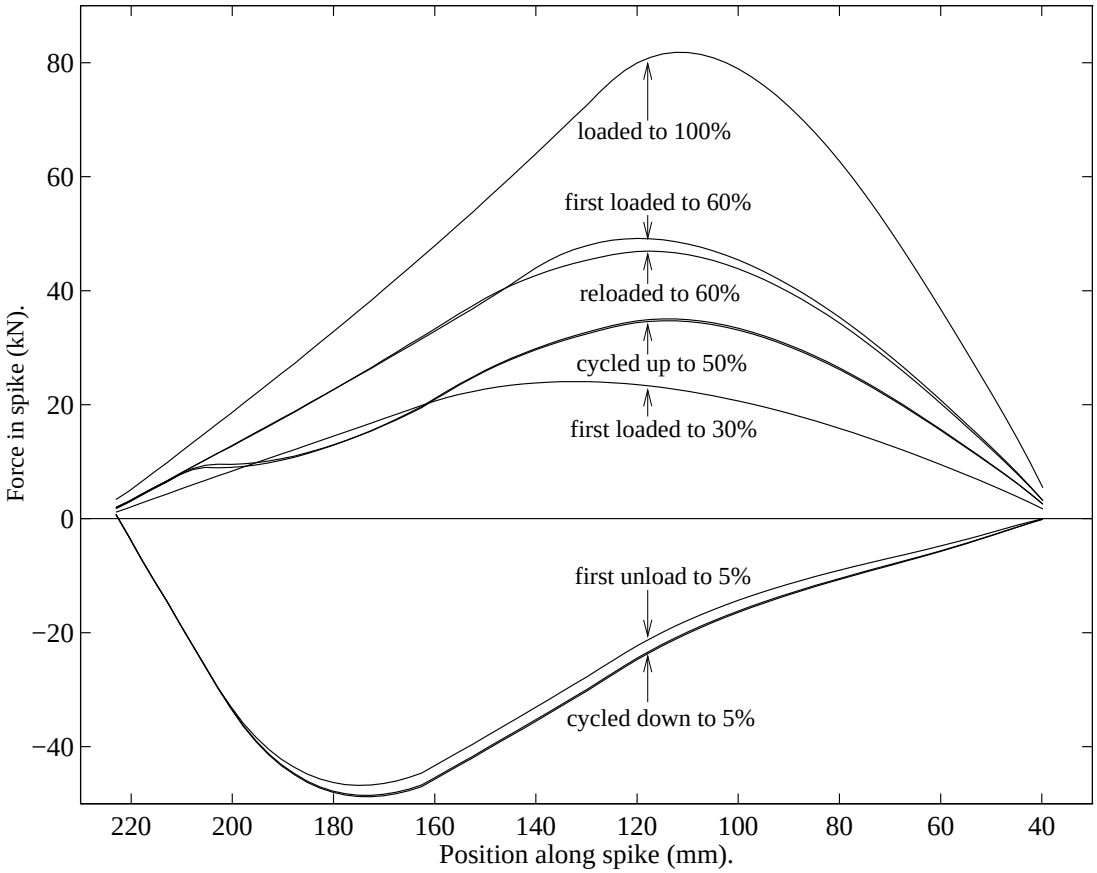

Figure 6.11: Variation in force along the spike for the whole analysis. This is the total force acting over the cross sections along the length of the spike. The tension on loading and compression on unloading can be seen.

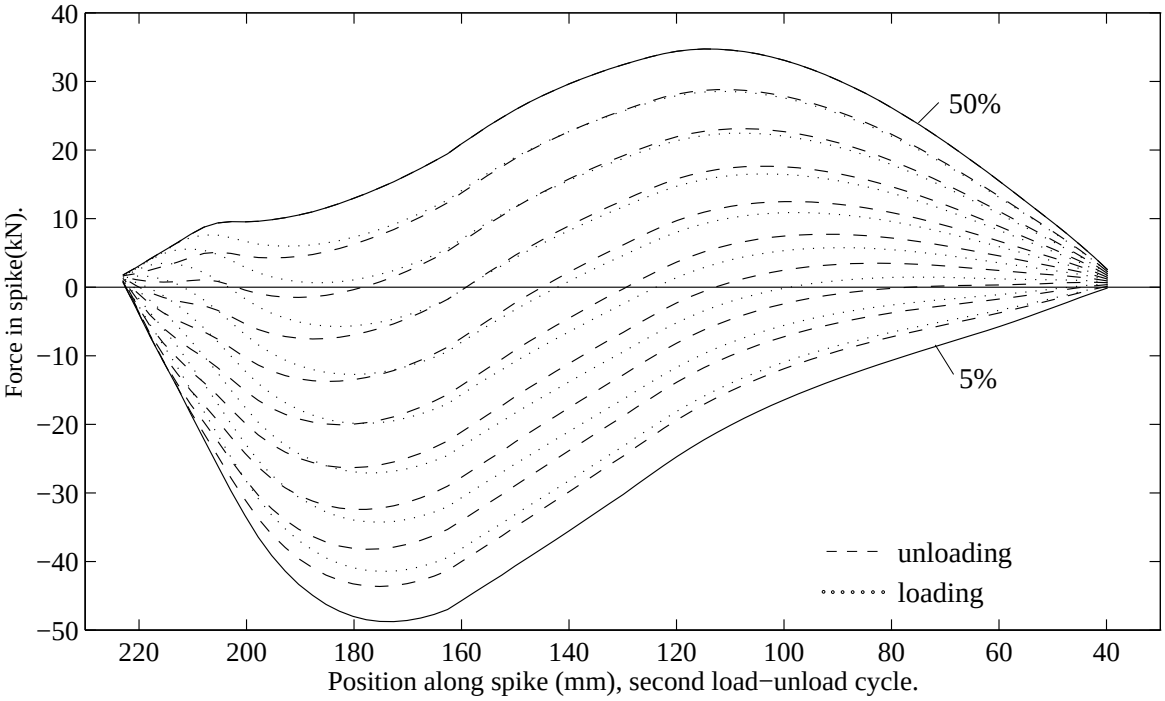

Figure 6.12: Forces along the spike during one cycling regime, showing intermediate curves for each increment in the loading history.

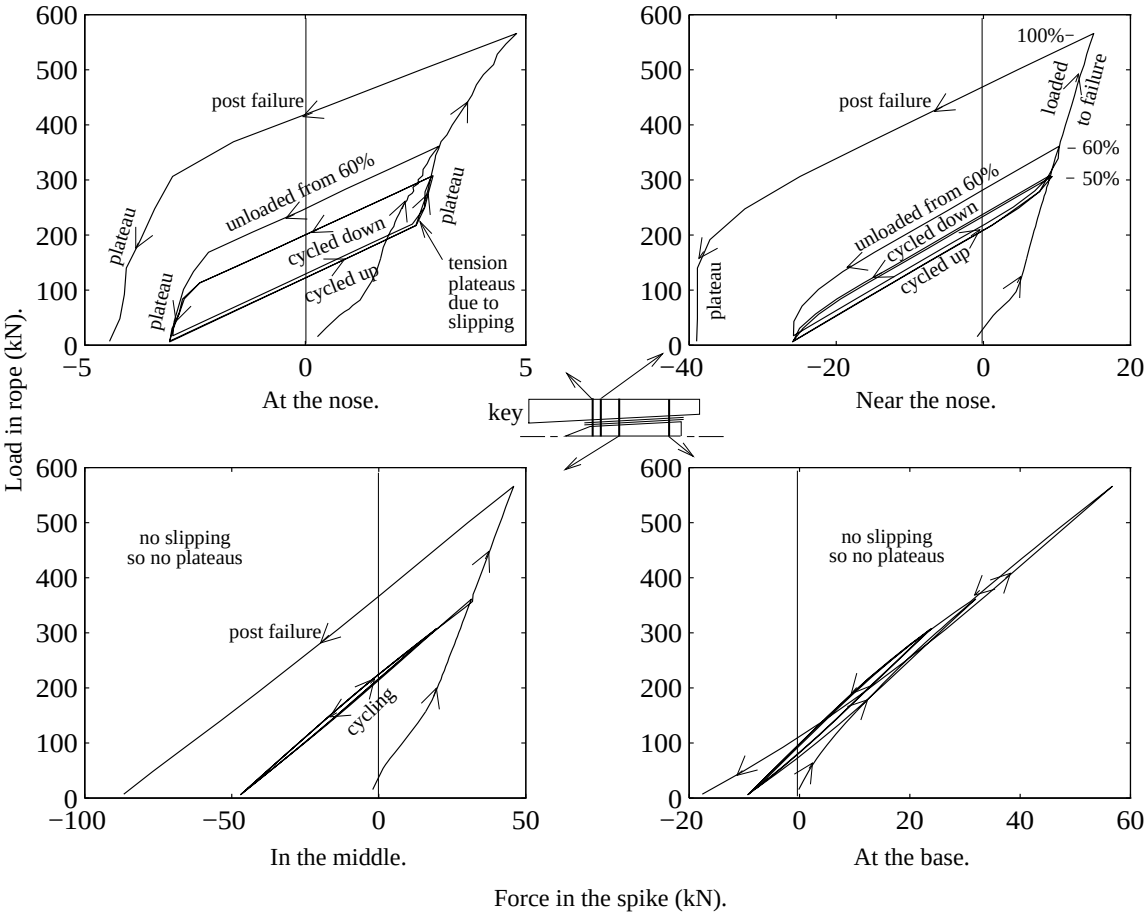

Figure 6.13: Forces at the four specified locations on the spike, plotted continuously throughout the analysis. **N.B.** the different scales. (c.f. Figure 6.12 which shows the discretised forces plotted continuously along the length of the spike.) Hysteresis at the nose during cycling can be observed where slip is occurring.

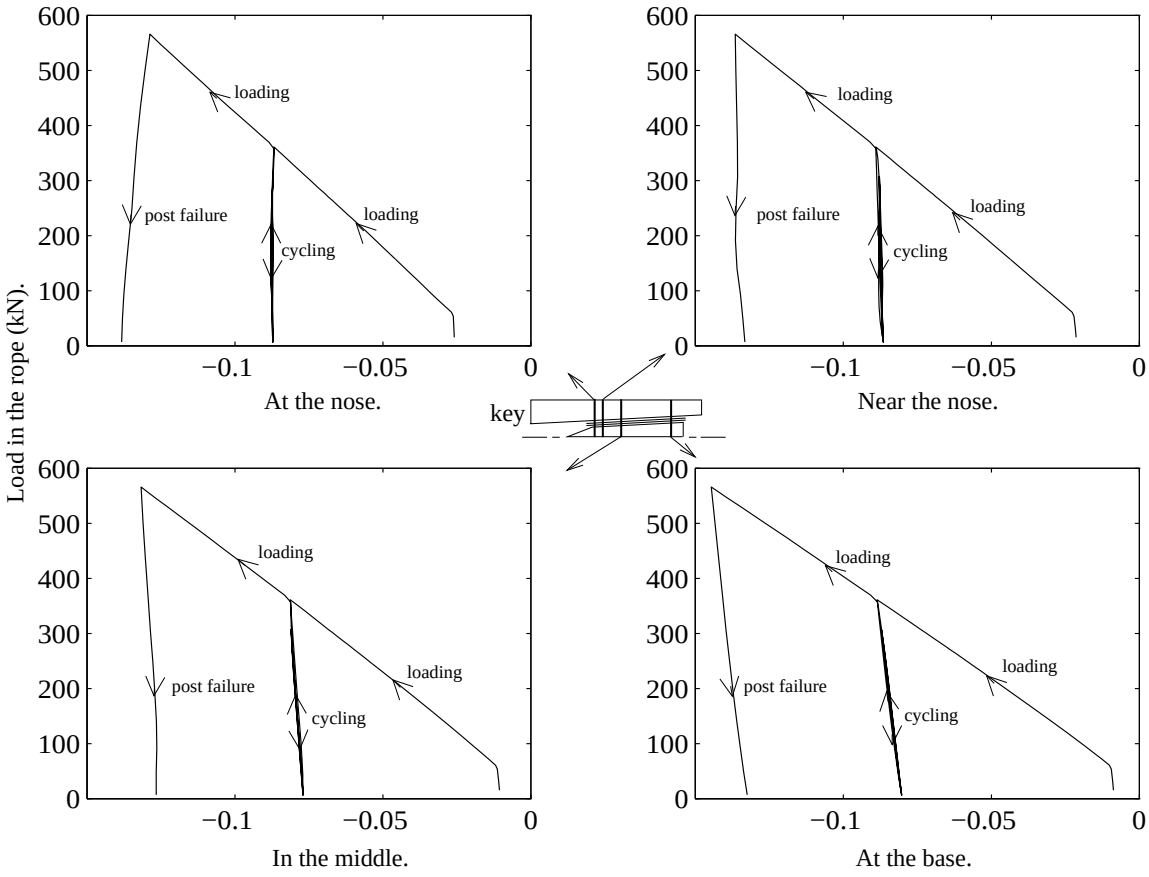

Figure 6.14: Variation of the radial stress (kN/mm^2) at the four salient points on the spike plotted throughout the analysis. The radial compression in the spike on first-loading is linearly proportional to the load in the rope, due to the linear rise in contact pressure (Figure 6.9) — similarly it remains constant on unloading-reloading.

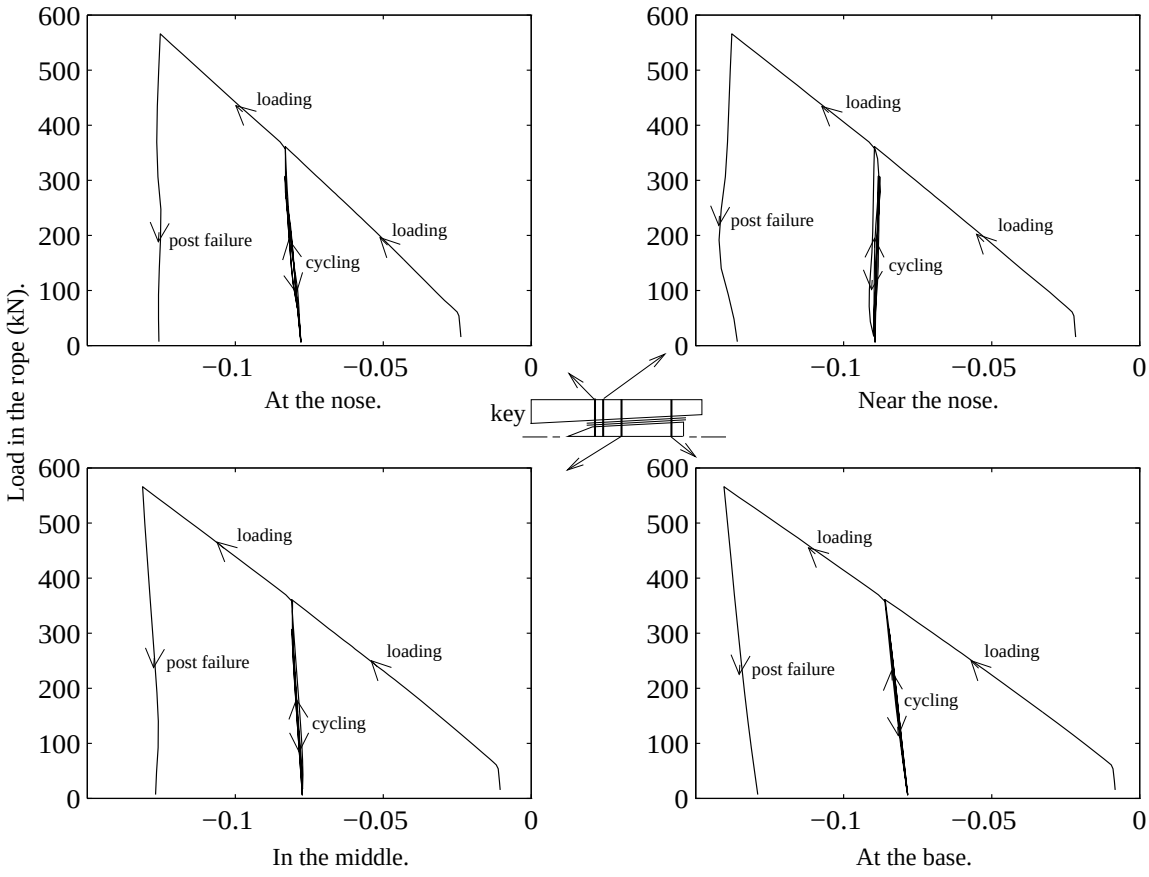

Figure 6.15: Variation of the hoop stress (kN/mm^2) at the four salient points on the spike plotted during the analysis. The hoop stress is compressive throughout and grows linearly on first-loading as the contact pressure rises (c.f. Figure 6.9), and remains constant on unloading-reloading.

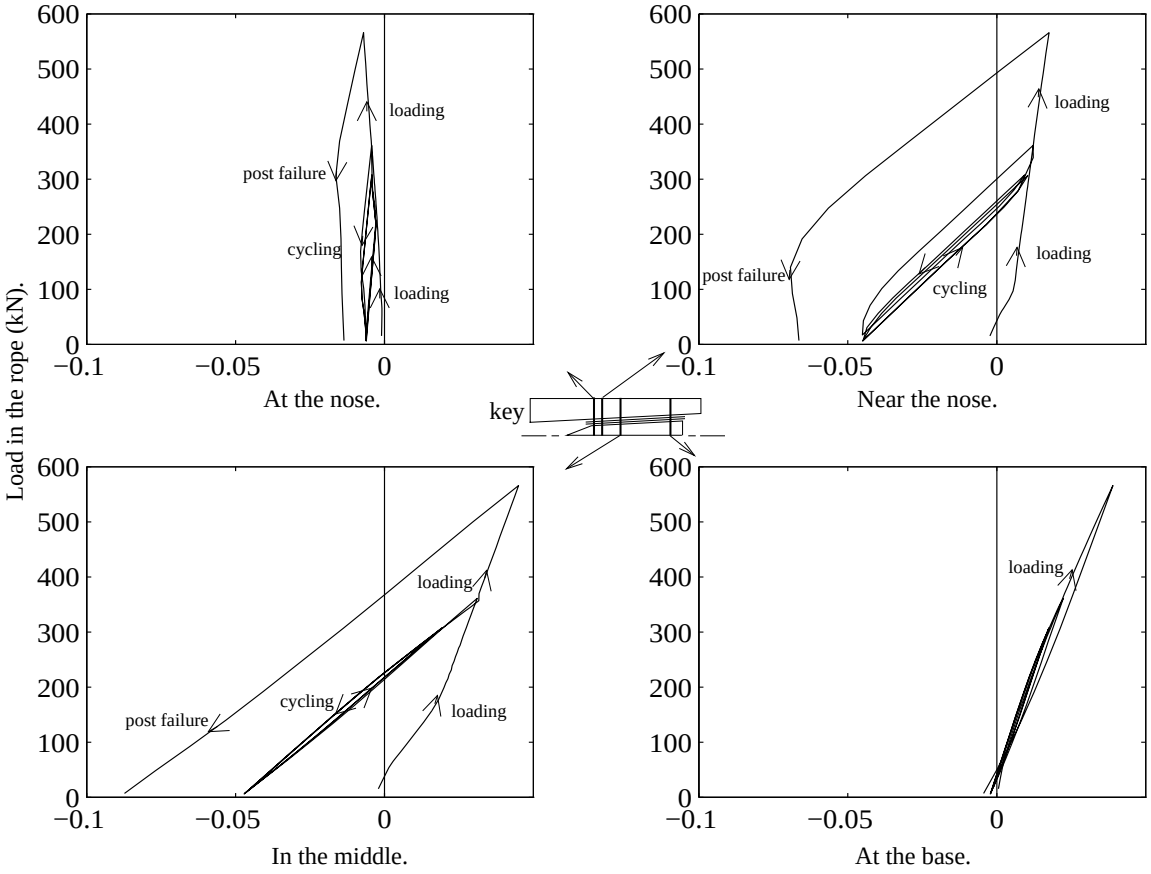

Figure 6.16: Variation of the axial stress (kN/mm^2) at the four salient points on the spike throughout the loading process. There is minimal stress at the ends, with tension on loading and compression on unloading in the middle as is also seen with the axial force in Figures 6.11 and 6.13.

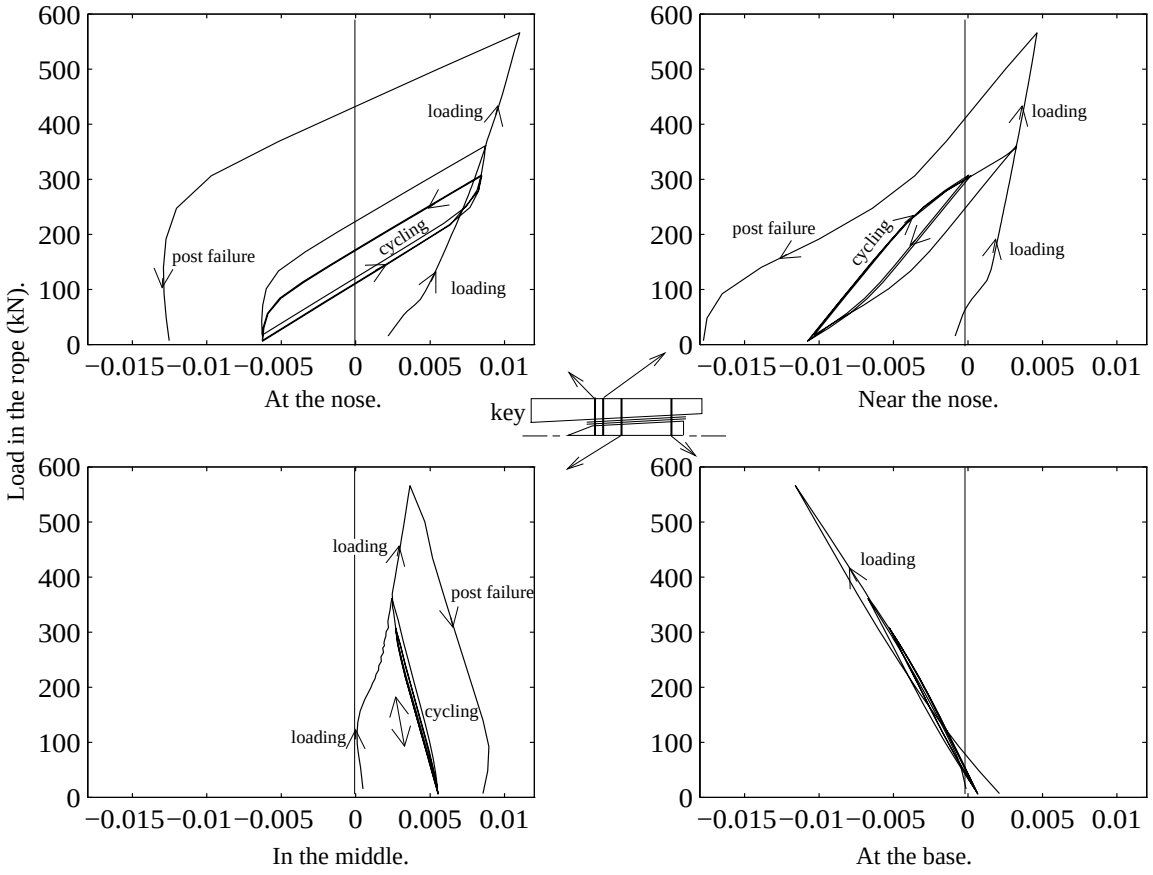

Figure 6.17: Variation of the shear stress (kN/mm^2) at four points on the spike throughout the analysis. These curves reflect the friction acting on the spike; hysteresis occurs on cycling where slip occurs, at and near the nose. These are essentially segments through Figures 6.6, 6.2 and 6.4, with time, for a given location.

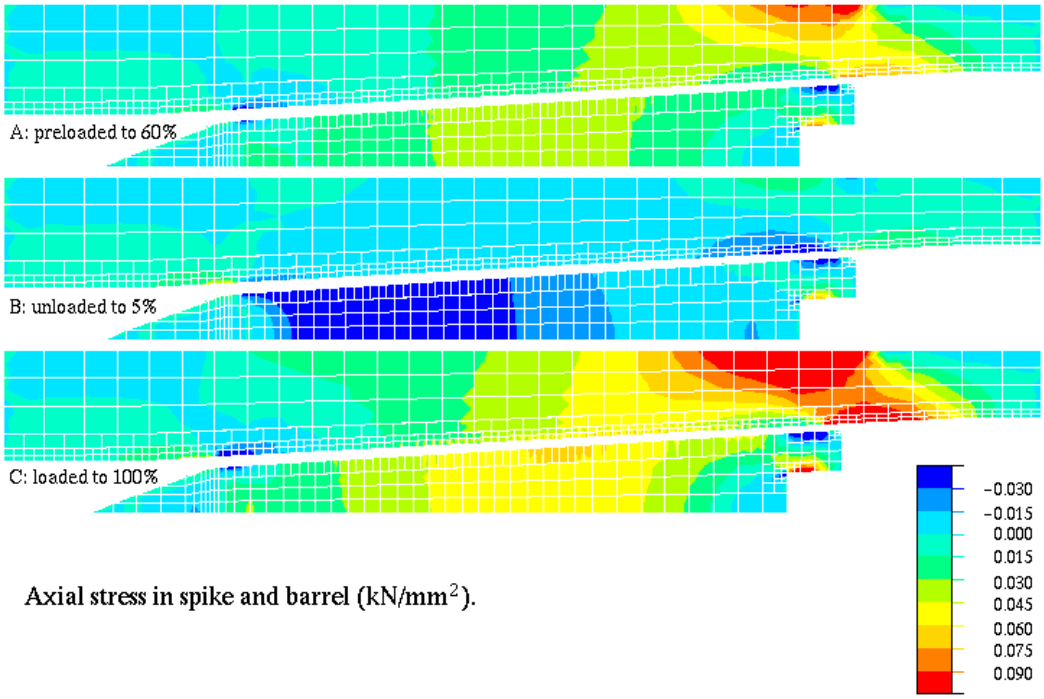

Axial stress in spike and barrel (kN/mm^2).

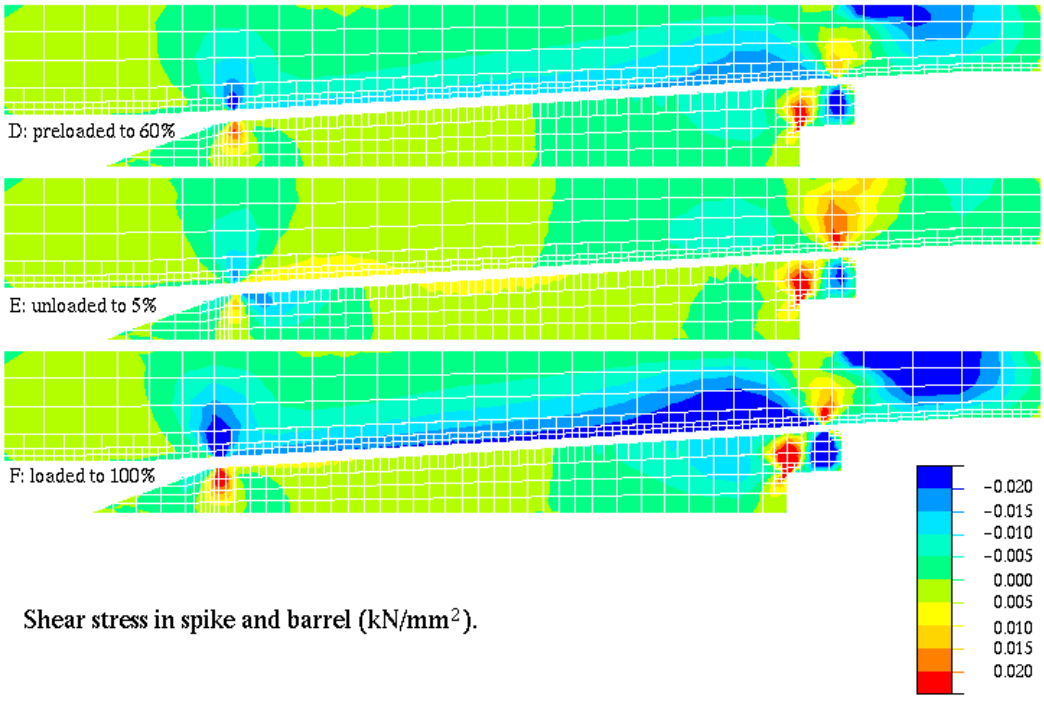

Shear stress in spike and barrel (kN/mm^2).

Figure 6.18: Axial and shear stresses in the termination at 60% pre-load, Unloaded to 5%, then loaded to 100%.

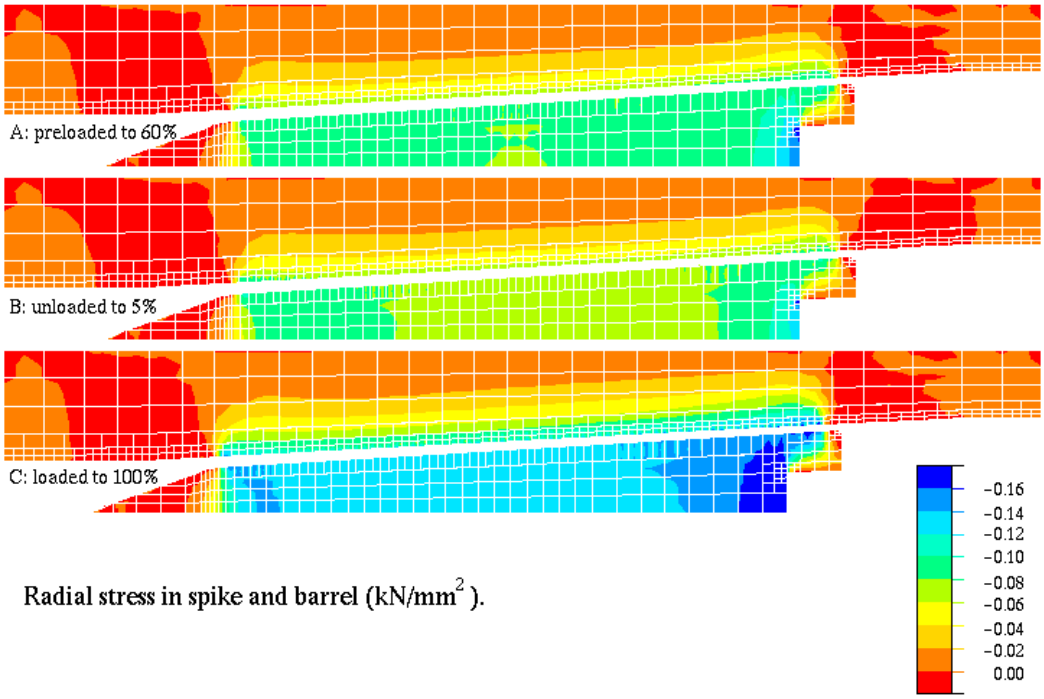

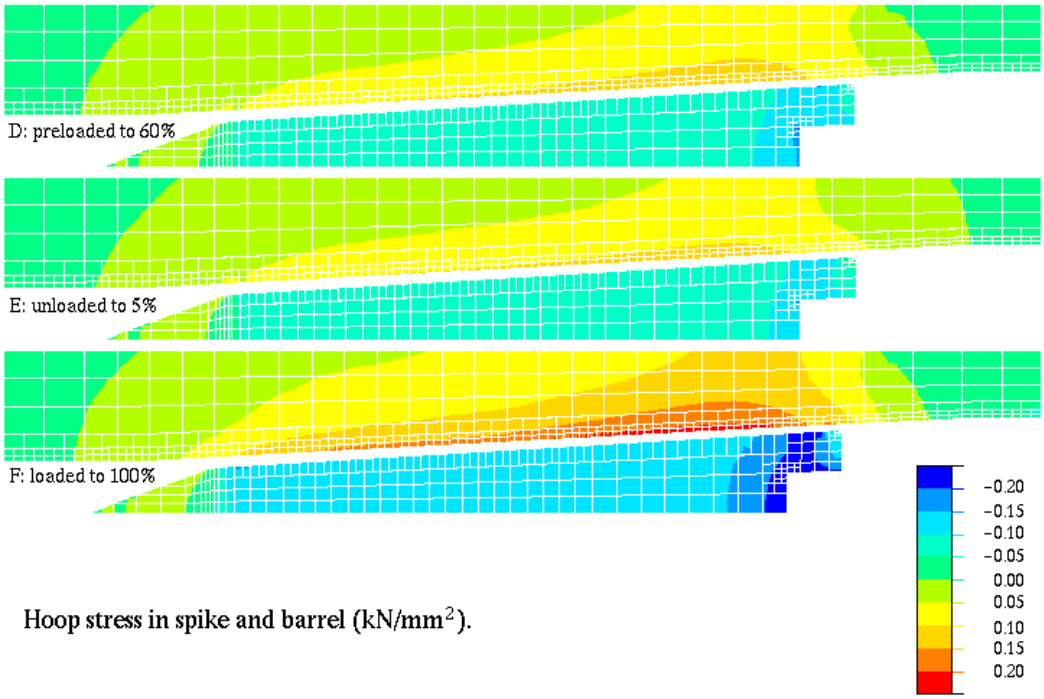

Figure 6.19: Radial and hoop stresses in the termination at 60% pre-load, Unloaded to 5%, then loaded to 100%.

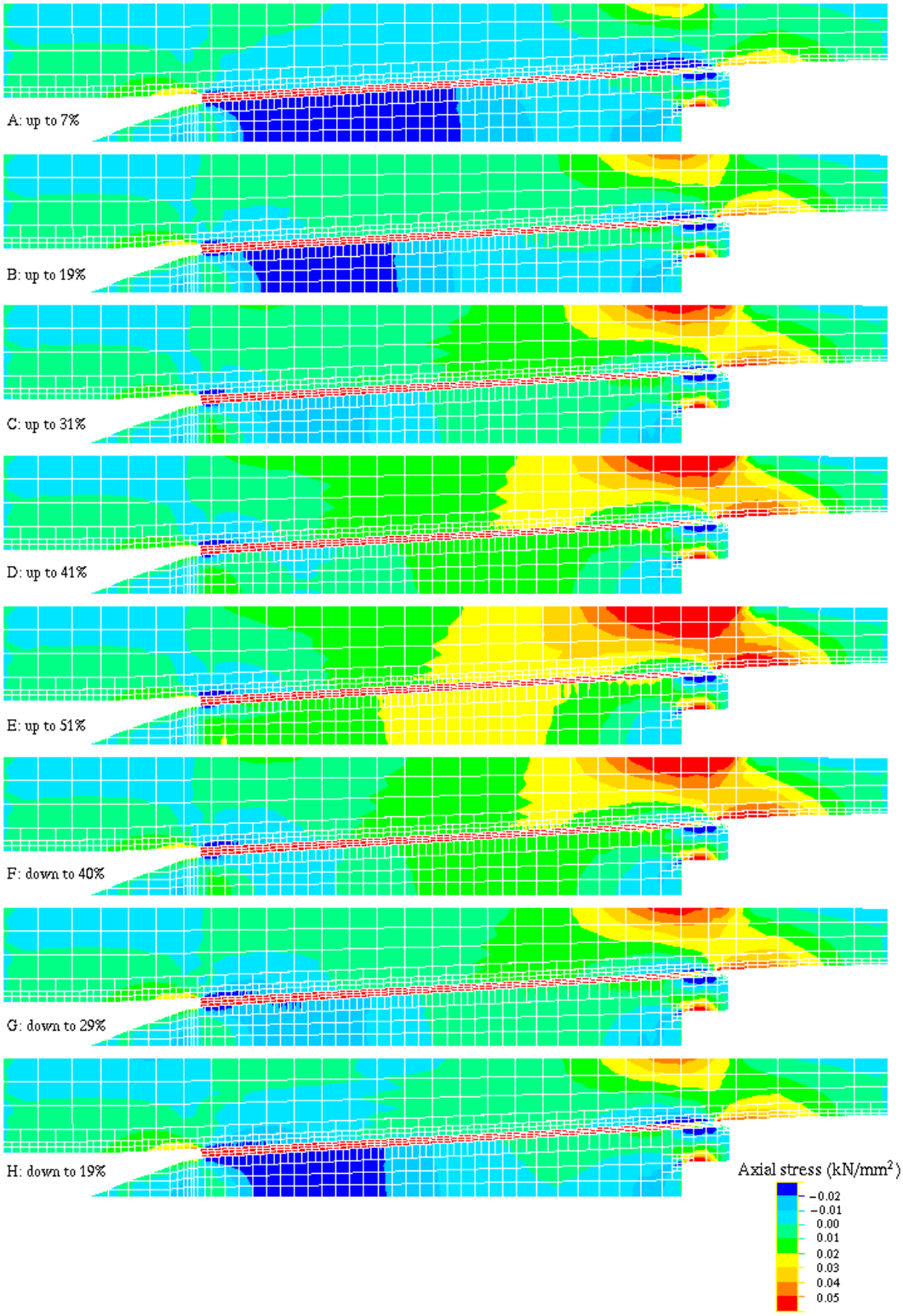

Figure 6.21: Variation in axial stress during cycling between 5% - 50%.

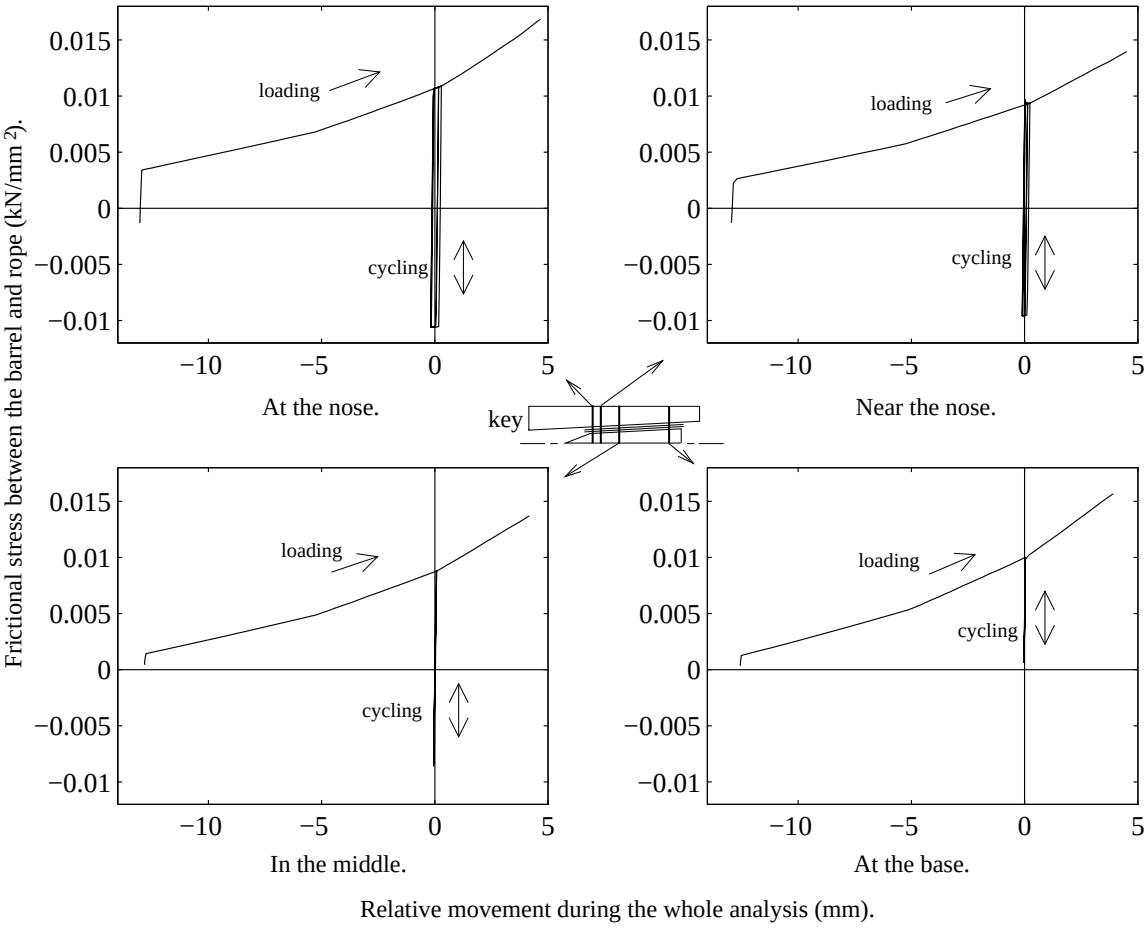

Figure 6.21: Relative slip of the rope along the barrel for the whole analysis. The zero is set at the mid point of the cycling regime.

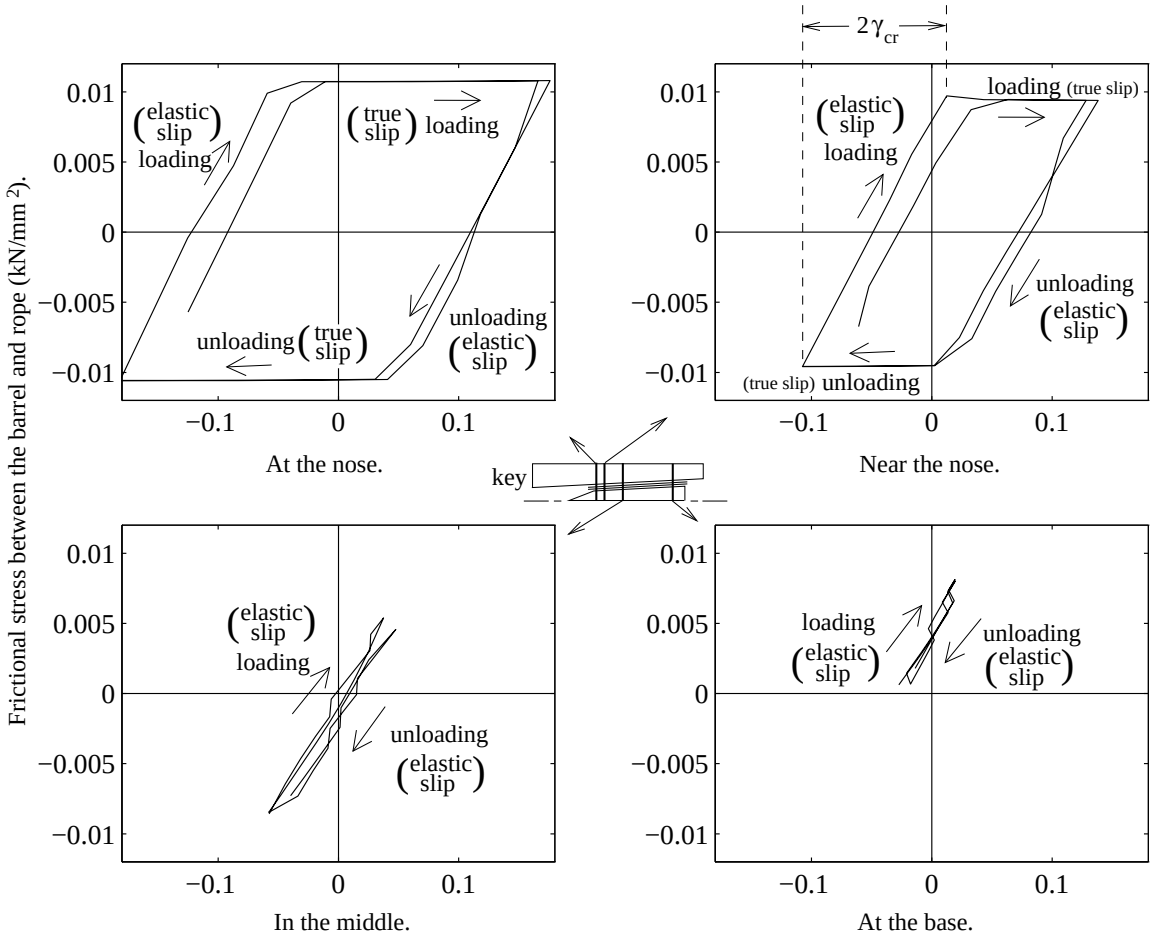

Figure 6.22: Relative slip of the rope along the barrel during cycling. Note the similarity of the elastic slip – true slip behaviour near the nose of the spike, and that observed in the verification tests in Figure 5.15.

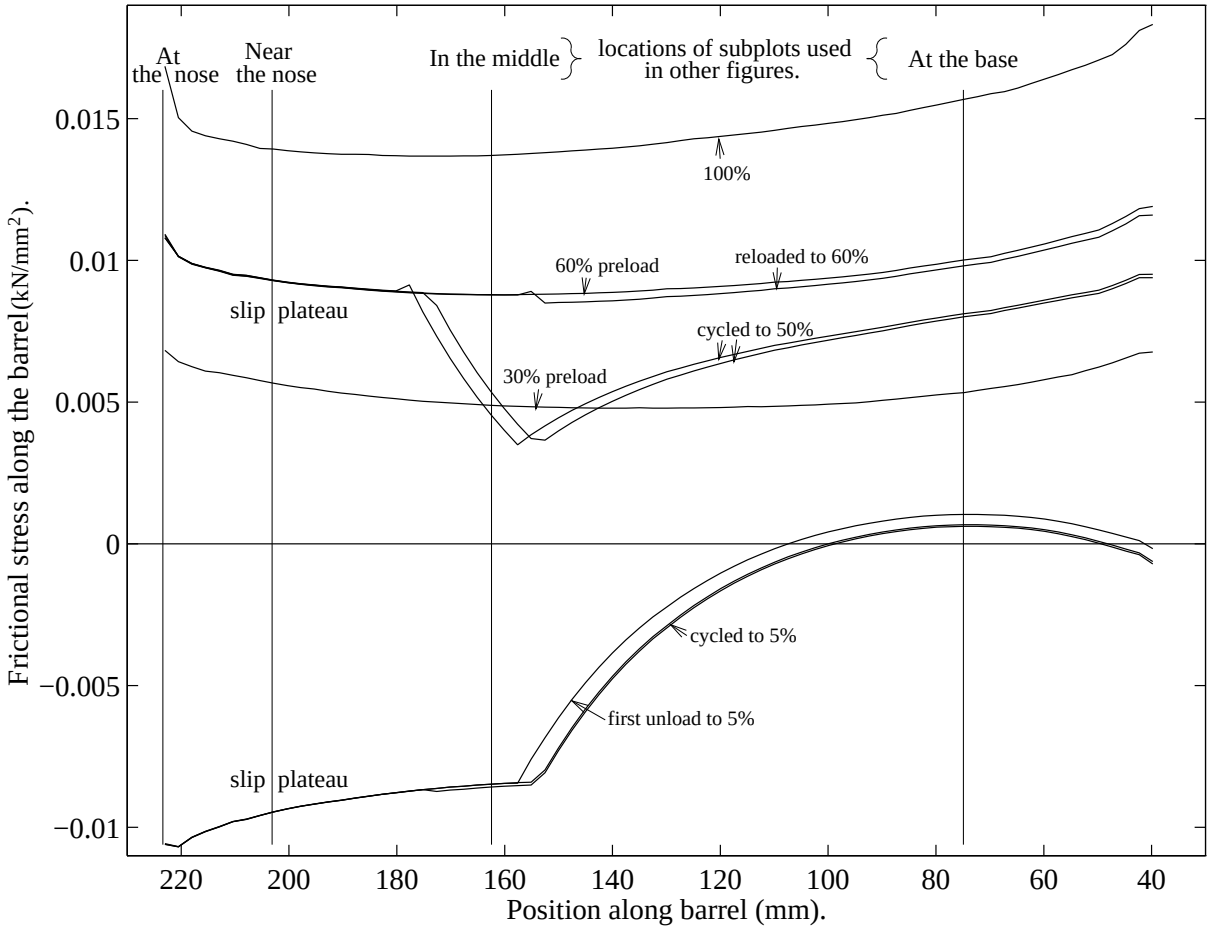

Figure 6.23: Frictional stress along the barrel for salient loads during the analysis. On first-loading, slip is occurring along the length of the barrel, so the friction is $a_d \sigma^{\beta_d}$ where σ is seen in Figure 6.9. Hence the frictional stress rises on loading from 30% to 60%. On cycling a slip reversal occurs near the nose. On reloading to 60% the preloaded state is regained; the stress plateauing along the entire length. On loading to 100% the plateau grows in magnitude further.

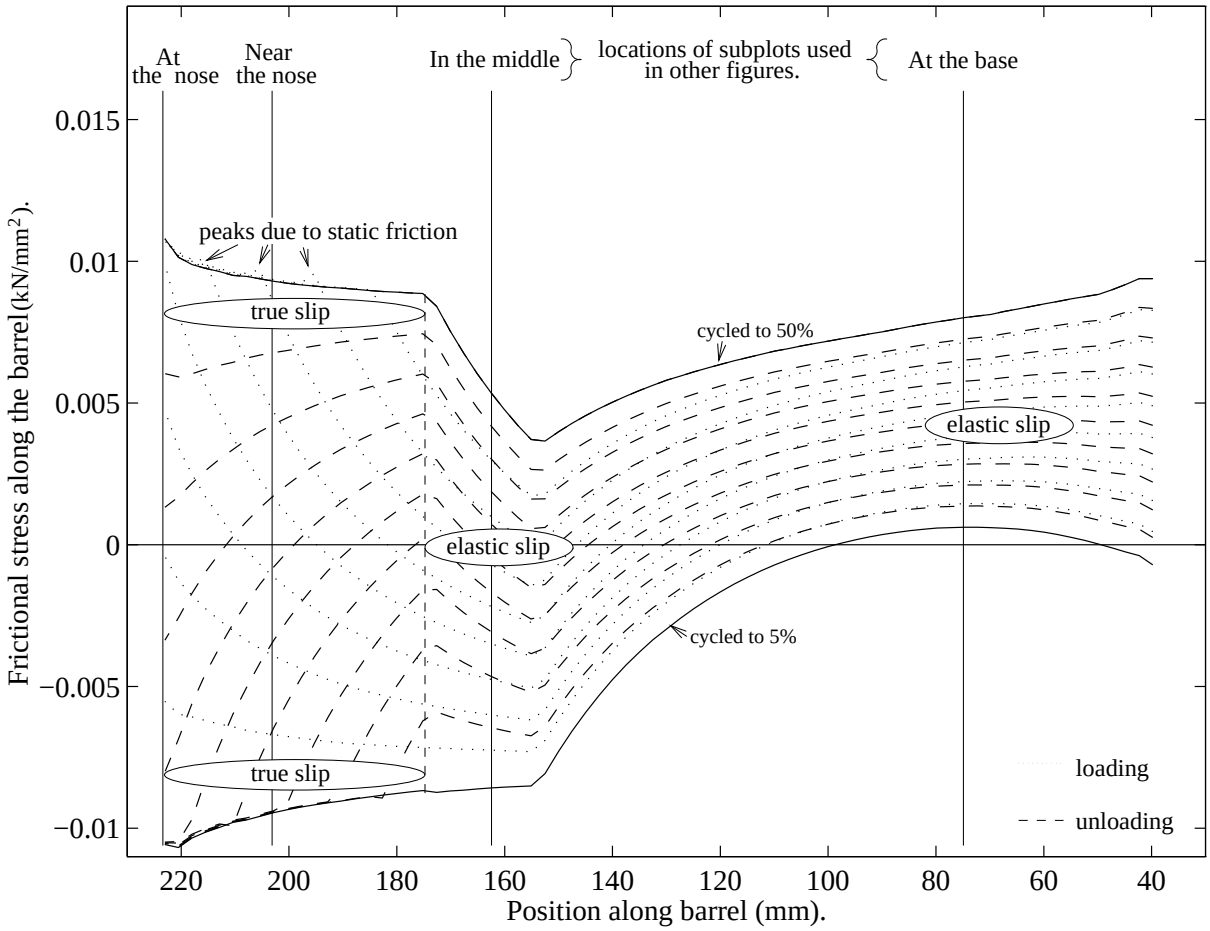

Figure 6.24: Frictional stress along the barrel during the cycling between 5 and 50%. The true slip at the nose where the slip plateaus at each end of the cyclic range can be observed. Note the large fluctuation in stress 'in the middle' compared with the zero slip that occurs between the rope and the spike (Figure 6.4).

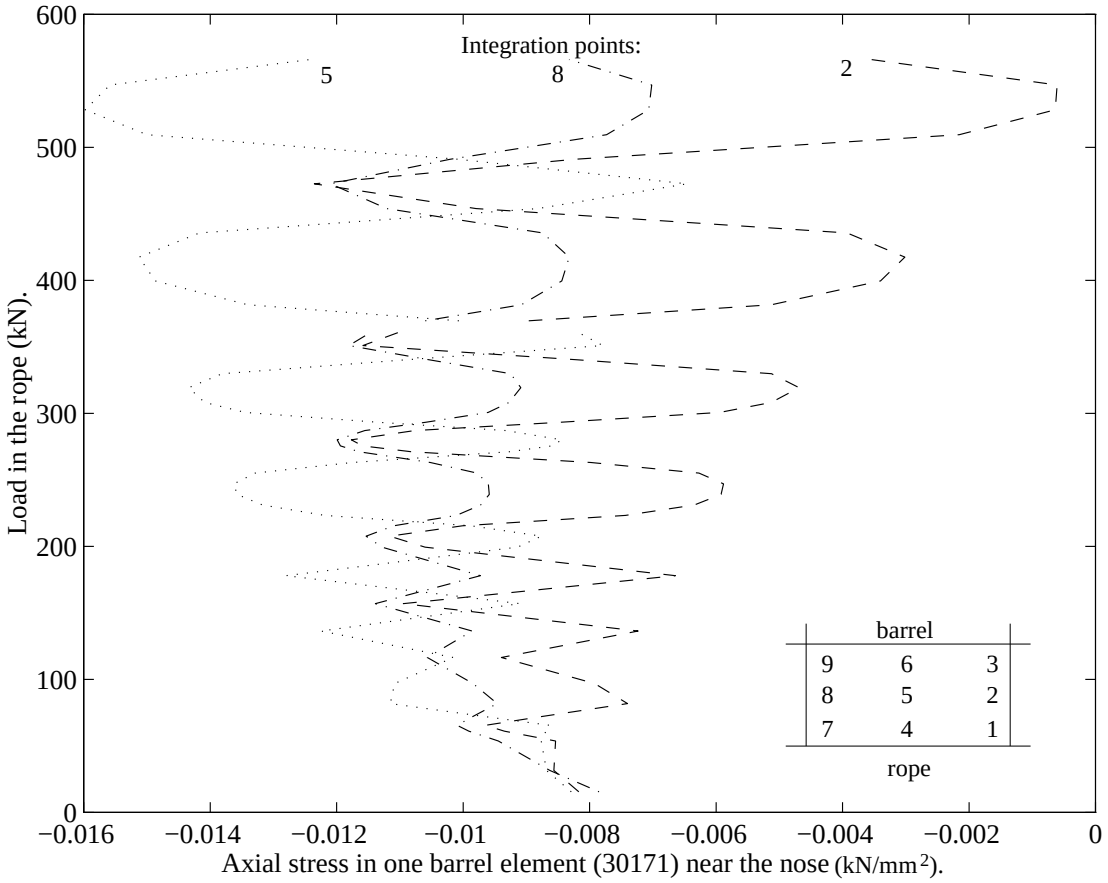

Figure 6.25: Variability in the axial stress for the integration points 2, 5 and 8, in barrel element 30171 near the nose of the spike. This shows the undulations caused by the interface element riding over the barrel element on first-loading, seven peaks correspond to seven elements moving past. This is a by-product of the local discontinuity at the end of the contact zone.

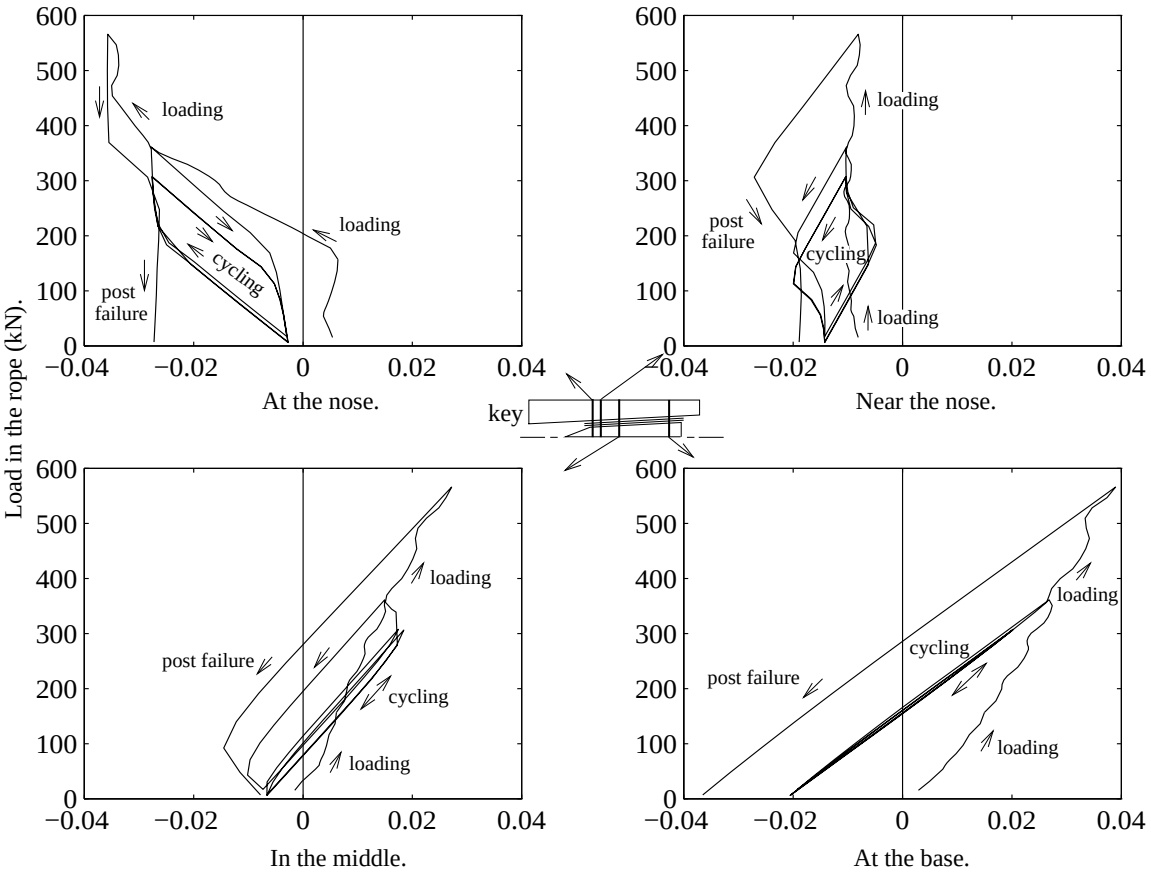

Figure 6.26: Variation of the axial stress (kN/mm^2) at four points on the inside of the barrel throughout the loading history. At and near the nose, the stress is compressive on first-loading due to the localised deformation seen in Figure 6.29, in the middle and at the base the stress is tensile on first-loading as the load is taken from the rope, going compressive on unloading as the relaxing rope compresses the barrel (Figure 6.30). The behaviour at the 'near the nose' location is also shown in Figure 6.25, the sum of those three curves gives the uniform stress of -0.01kN/mm^2 on first-loading here.

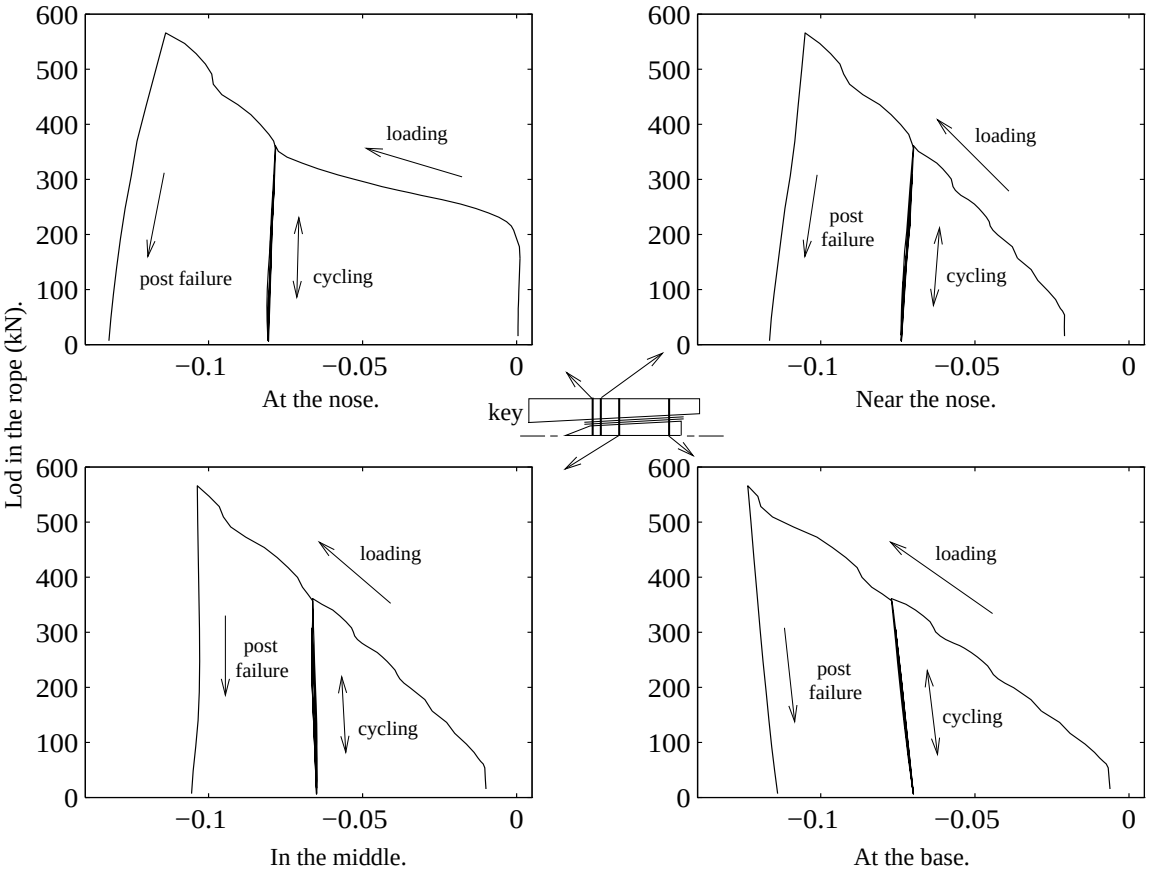

Figure 6.27: Variation of the radial stress (kN/mm^2) at four points on the inside of the barrel throughout the loading history. There is rising compressive radial stress in the barrel as the contact pressure rises on loading (Figure 6.9). On unloading-reloading the contact pressure and the radial stress remain constant.

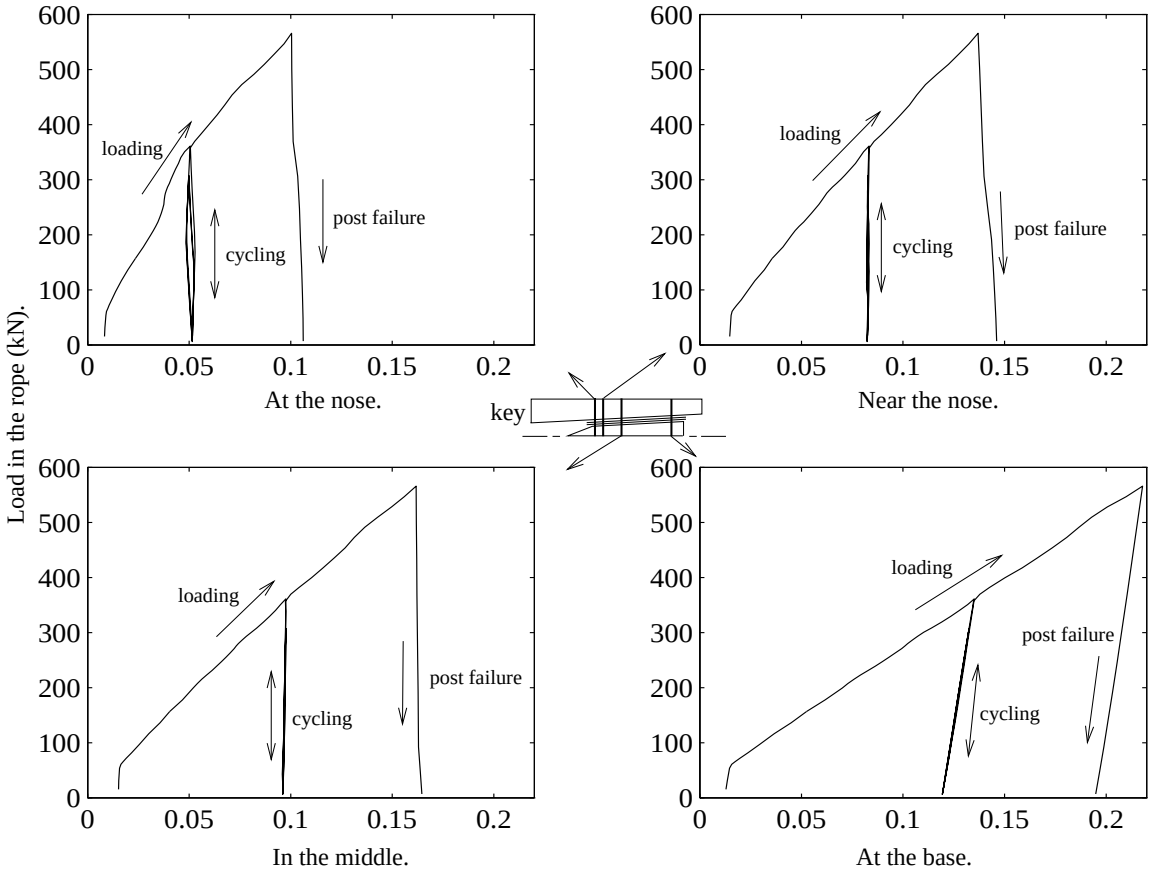

Figure 6.28: Variation of the hoop stress (kN/mm^2) at four points on the inside of the barrel throughout the loading history. There is rising tensile hoop stress in the barrel as the contact pressure rises on loading (Figure 6.9). On unloading-reloading the contact pressure and the hoop stress remain constant.

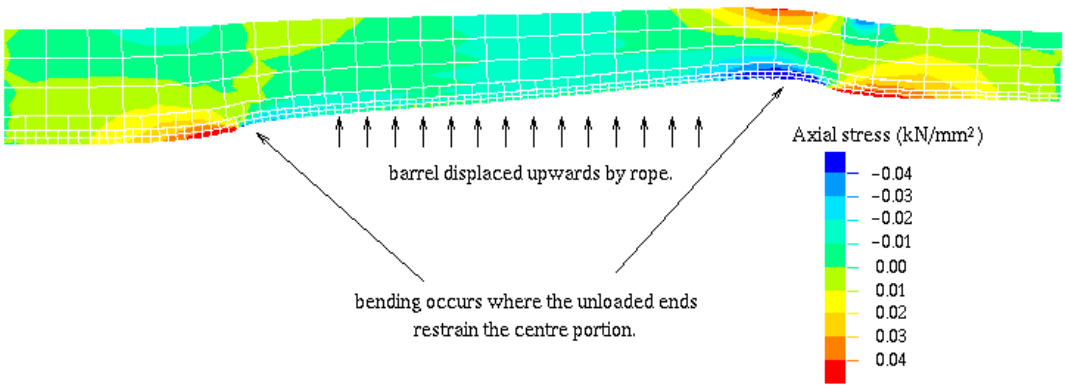

Figure 6.29: Axial stress in the barrel after unloading from 100%, displacements magnified 100 times. This stress plot highlights the local deformations occurring at the ends of the contact zone.

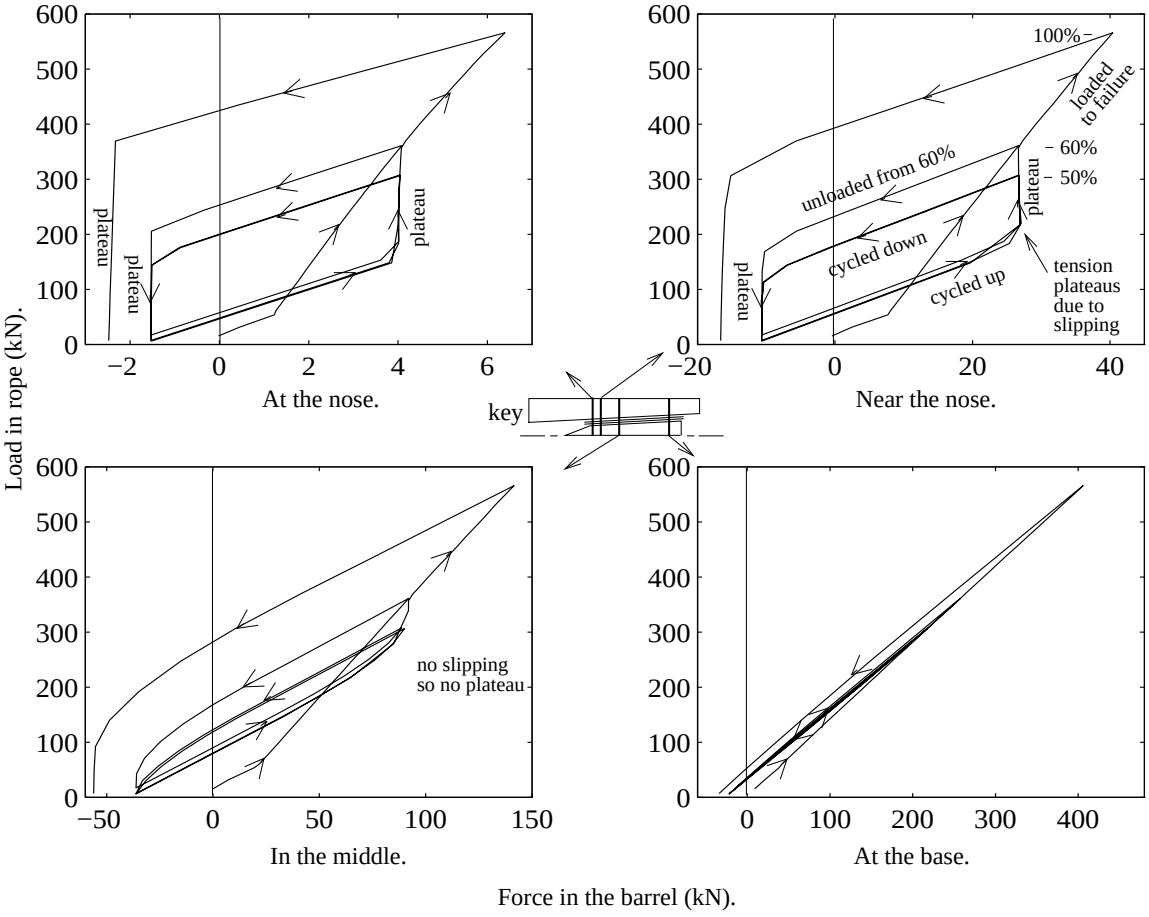

Figure 6.30: Force at the four points on the inside of the barrel throughout the analysis. **N.B.** different scales for each. The tensile force on loading reflects the amount of load that has been taken out at each location and is the sum of the friction on the rope side of that point. On unloading the friction reverses and the barrel goes into compression. At the very base the tension equals the tension in the rope. Hysteresis during cycling where slip occurs can be seen at and near the nose.

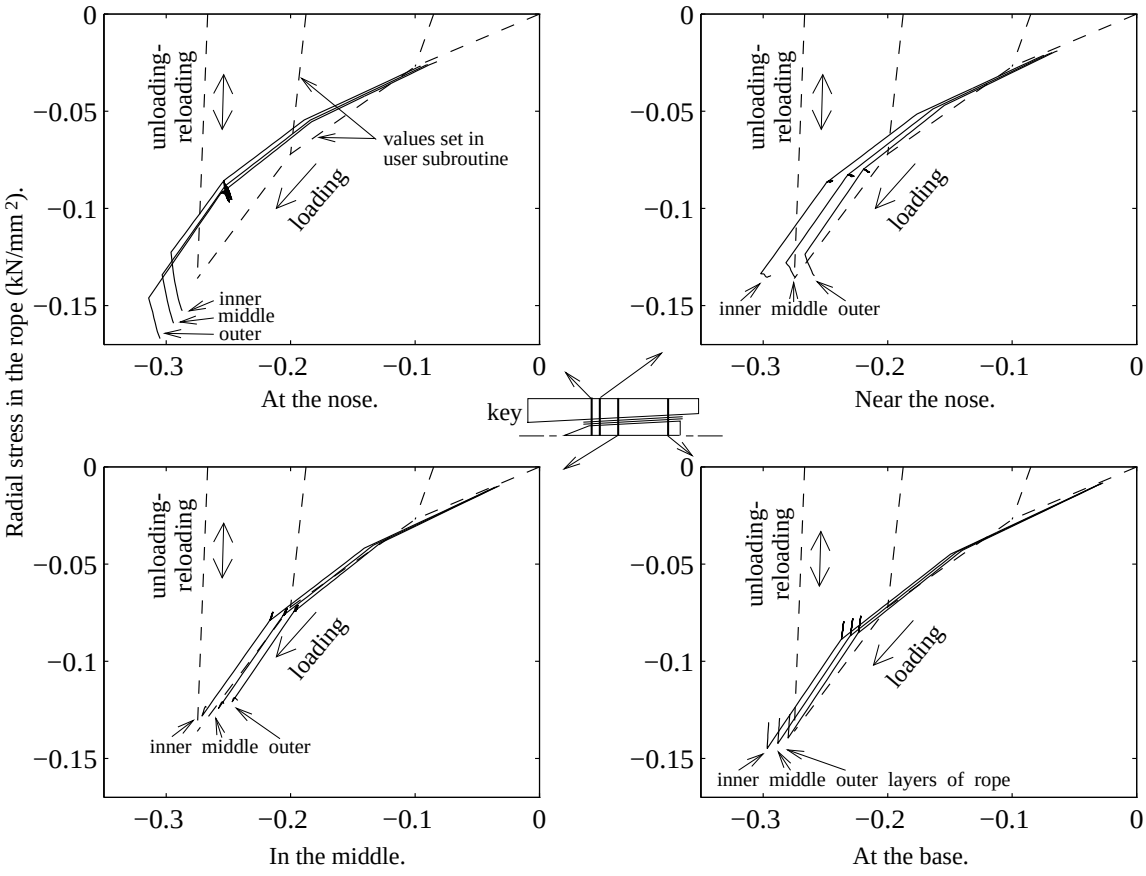

Figure 6.31: Transverse stress-strain in the rope throughout the loading history. The first-loading moduli are parallel to the values set in subroutine `UMAT` for the particular step. At the base the unloading-reloading moduli are parallel to the values set in `UMAT`. At and near the nose, however, a small discrepancy arises where the stress rises on unloading.

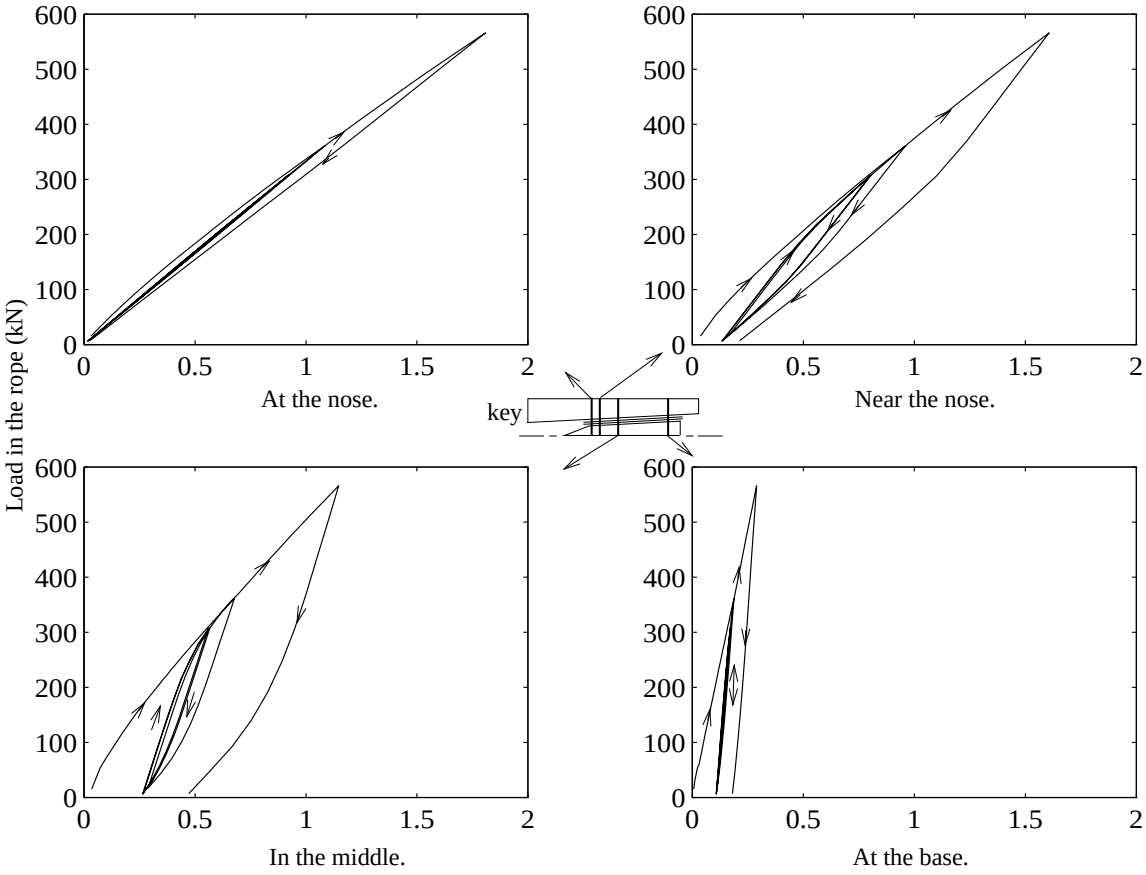

Figure 6.32: Mean axial stress (kN/mm^2) in the rope versus load throughout the loading history, averaged over the three layers. At the nose all the load is present in the rope, at the base most has been taken out into the barrel. In the middle hysteresis can be observed during the cycling of the load when slip occurs; tension remains on unloading which balances the compression in the spike and barrel.

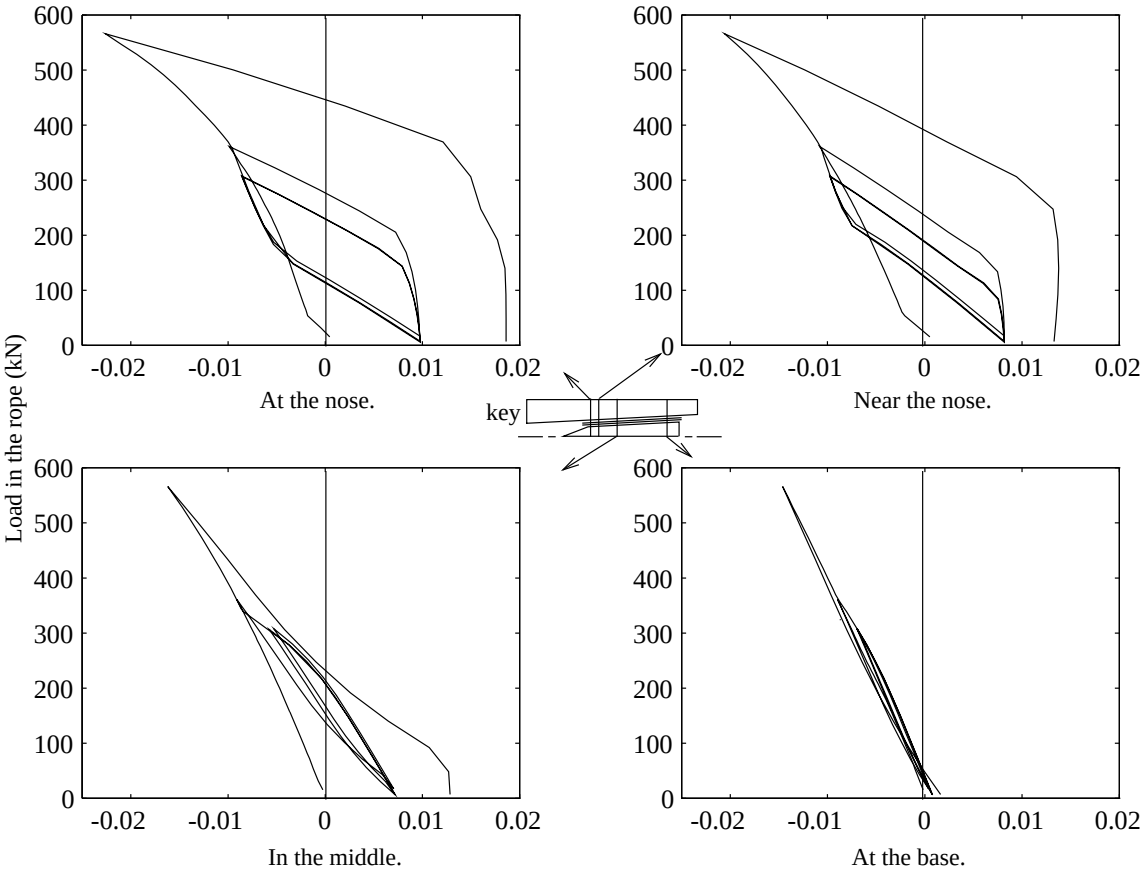

Figure 6.33: Shear stress (kN/mm^2) at the four salient locations in the outer rope layer throughout the loading history. At all points this is negative on first-loading due to the friction acting on this layer from the barrel (Figure 6.23). The shear becomes positive in sign on unloading the rope. Hysteresis can be observed at and near the nose where true slip occurs. (c.f. the shear on the inside surface of the barrel, Figure **??**, the corresponding curves have the same shape and magnitudes.)

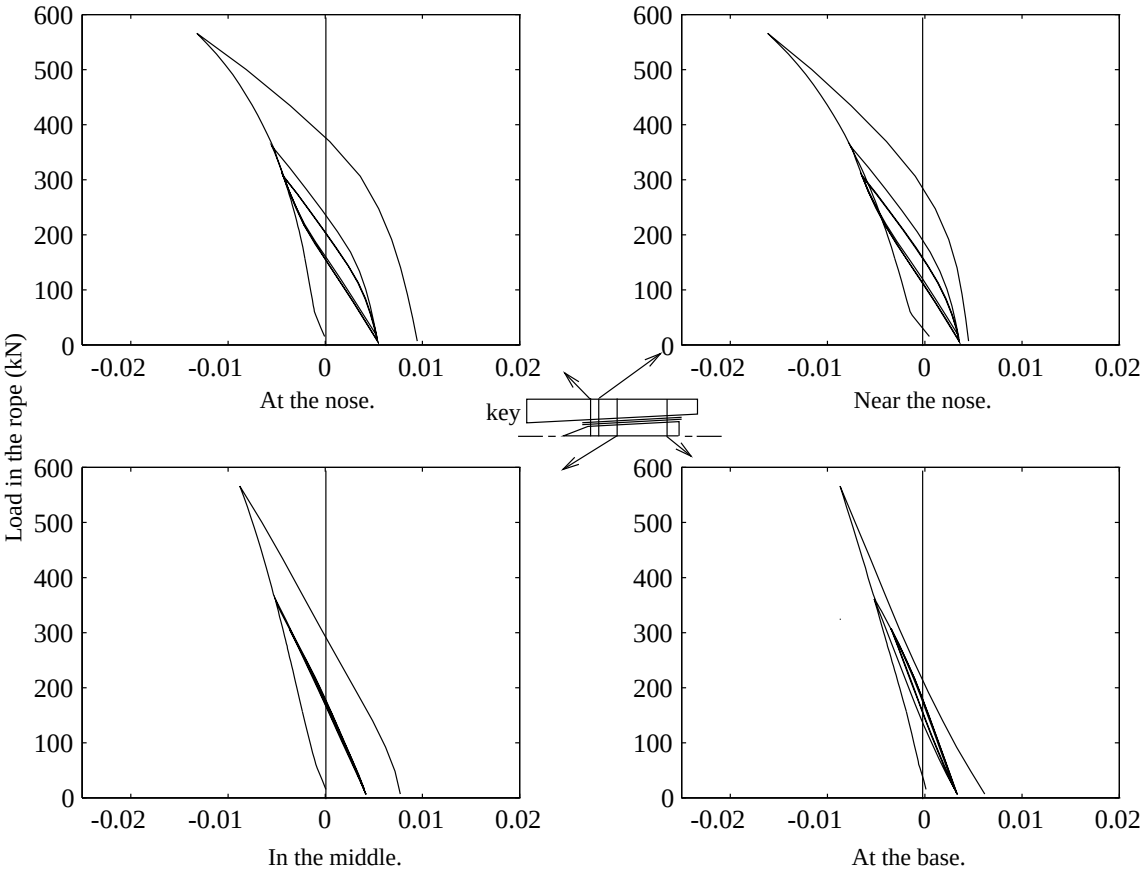

Figure 6.34: Shear stress (kN/mm^2) at the four salient locations in the middle rope layer throughout the loading history. Similar to the shear in the outer rope layer, Figure 6.33, this is negative on first-loading, going positive on unloading. This is due to the friction exerted on it by the outer rope layer.

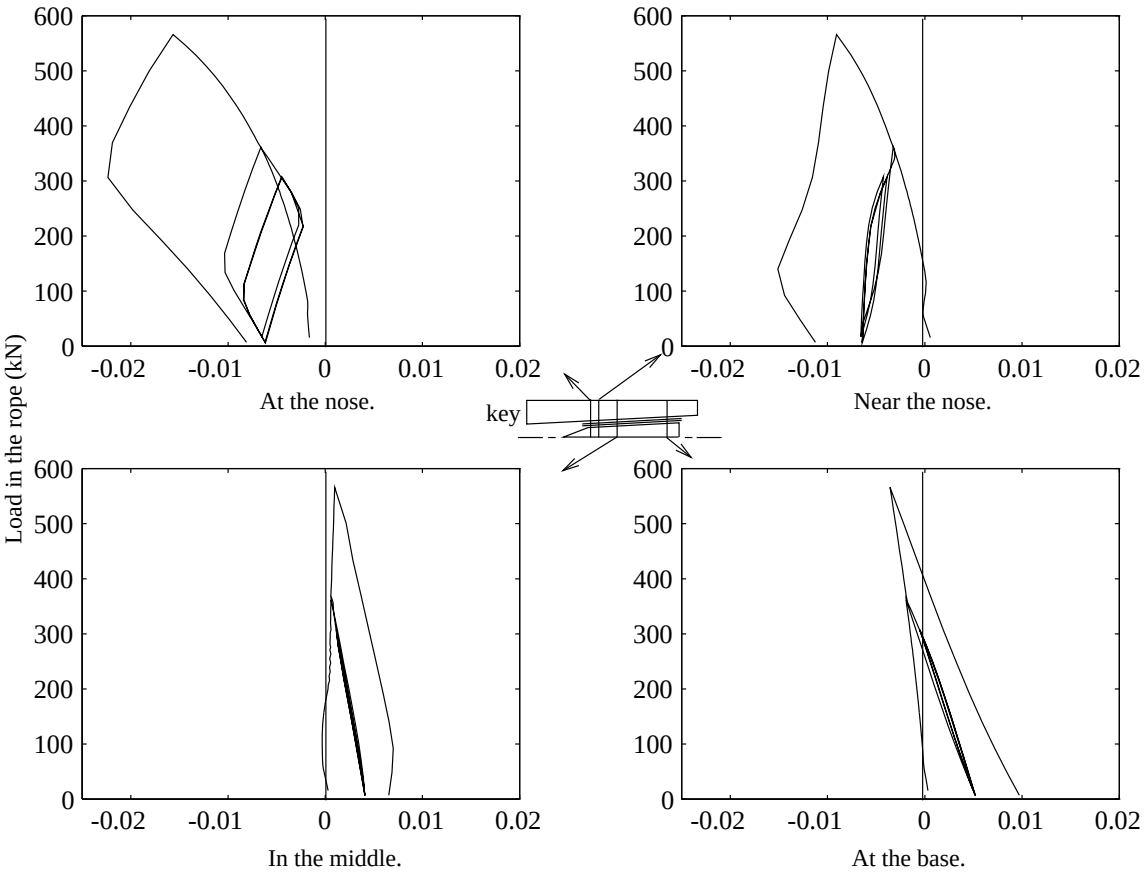

Figure 6.35: Shear stress (kN/mm^2) at the four salient locations in the inner rope layer throughout the loading history. On first-loading this is negative, being influenced by the shear from the barrel which is transmitted through the outer and middle layers of rope. On unloading, the friction from the spike dominates (Figure 6.8); such that at the nose, the shear increases negatively, with hysteresis on reloading due to the slip.

Chapter 7

Comparison between analysis and actual tests.

7.1 Introduction.

This chapter compares the results of the finite element analysis with experimental data; both that gathered here for a strain gauged termination, and data reported in the literature for lifetimes under cyclic loading.

The chapter starts with a discussion of three rope tests that have been carried out on 60 tonne Parafil G rope (Kevlar 49). The initial distances between the front faces of the barrels for the three tests were; 0.307m, 1.030m and 1.980m, respectively. The strains and displacements measured in one termination are then compared with the predicted values from the finite element analysis described in Chapters 5 and 6, and comments made regarding what happens in the terminations. The principal strains are calculated, and some suggestions are made regarding why the principal strains were not aligned with the axis of the spike.

The spike bed-down displacements for the three tests match those calculated by the finite element model very accurately. The strain gauge readings show a good correlation with the analytical values.

The chapter concludes by tying together the contact stresses and magnitudes of slip calculated with the finite element analysis (Chapter 6), along

with the abrasion results presented in Chapter 3. These are used to derive Equation 7.17, which predicts the lifetime of an actual termination given the rope size and the maximum and minimum loads of the cycle. This simple equation predicts the lifetimes reported in the literature very closely.

7.2 The strain gauging of a 60 tonne Parafil G termination.

One termination was strain gauged on the surface of the spike and the outside surface of the barrel. The inside surface of the barrel was not strain gauged as it was too difficult to place gauges there accurately. To reduce interference with the workings of the termination, four cavities were spark eroded into the surface of the spike; one at the nose, one at the base and two around the middle. Holes spark eroded through the middle of the spike carried the gauge wires out, via a high tensile steel connector in the base of the spike; this connector was required to pull the spike out of the barrel after the test. Once the gauges had been assembled, they were covered by a layer of epoxy resin shaped to match the shape of the spike; the fibres passing over the gauged region would experience minimal disturbance.

The spike and barrel were strain gauged as shown in the photograph in Figure 7.1. The locations were chosen based on a preliminary Abaqus analysis to be at salient points on the spike (Figure 7.2). Two gauges were located on opposite sides of the middle at 100mm from the base, which is close to where the maximum change in force between loading and unloading occurs. Opposite sides were used to detect asymmetry. Two more gauges were added at the nose and the base, at 170mm and 20mm from the base respectively; they were located at 90° and 270° relative to the others so that any one yarn would only pass over one gauge to minimise any interference between gauges. Rosettes were used at all locations to enable the principal axes of strain to be determined.

The locations of the gauges on the barrel were set such that they were approximately in line with the gauges on the spike. These coordinates were calculated in advance to account for the bed-down that occurred. The numbering system for the gauges referred to in this chapter is shown in Figure 7.3. The gauge readings may be affected by the contact pressure, the cavity geometry, and the epoxy covering as mentioned in Appendix A; but this is assumed to be minimal.

7.3 Readings from the spike.

The letters and arrow heads on the curves in this section are used to indicate the portions of the loading curves. These are:
a preload to 60%
b unloading to 5%
c first cycle up to 50%
d first cycle down to 5%
e second cycle up to 50%
f second cycle down to 5%
g loading to failure load 100%
h subsequent unloading to 0%

7.3.1 Nose of the spike, gauges 1→3.

Figures 7.4 and 7.5 show the variation in axial and hoop strain at the nose of the spike. The three tests are shown by various styles of broken line; the Abaqus prediction is shown by a solid line.

It can be seen that there is a significant variation from test to test in the absolute values of the strains at the nose of the spike; the Abaqus values lying between these. The corresponding curves all have the same shape however: the lateral shifting is most likely due to an asymmetric distribution of fibres around the spike. This asymmetry would cause bending and other

deformations in the spike and barrel as will be discussed in Section 7.5.

On first-loading, from 0-60% and 60-100%, the axial strain increases linearly in tension with the same gradient ($\sim 1500\mu\epsilon$ for 100% load) for all four curves. On unloading-reloading there is some hysteresis present due to the slipping of the rope over the nose of the spike. The strain becomes compressive on unloading due to the friction from the rope compressing the spike nose.

The hoop strains are compressive throughout, with the four curves being very similar in shape. The first-loading curves are linear to 100% at about $-1500\mu\epsilon$. On unloading-reloading, however, the curve has a steeper gradient, so the strain remains compressive. The hoop strain is linked to the contact force acting on the spike; this remains constant on cycling the load, therefore much hoop strain is retained whilst cycling.

7.3.2 Middle of the spike, gauges 4→9.

Where there are gauges on opposite sides, as in the middle of the spike, a mean strain can be calculated. There is a good agreement between the means and the estimates from the Abaqus analysis. The asymmetry between the readings is discussed later in Section 7.5.

Figure 7.6 shows the mean of the axial strains from test 3 compared with the Abaqus strains. On loading the spike is stretched, on unloading this stretch reduces but stays positive. The spike is under compression when the load is cycled down to 5% as was seen in Figure 6.16; however the large radial stress, Figure 6.14, means that the axial strain can remain positive even when the stress goes negative, due to Poisson's ratio effects. There is a good agreement between the shapes of the curves, although the Abaqus values underestimate the measured strains by about 20%. The gradients of the unloading-reloading curves are the same, except for a small amount of hysteresis in the actual termination.

7.3.3 Base of the spike, gauges 10→12.

Gauge 10 broke during the second test so there is not enough data from this gauge to make any useful comparisons of the axial strains. Gauge 11, however, continued working. Figure 7.7 shows the hoop strains at the base of the spike; the four curves represent the three tests and the Abaqus values. The predicted hoop strains from the finite element analysis underestimate the strains that are measured. The Abaqus strain at failure was nearly -2000$\mu\epsilon$ compared with a mean of about -3500$\mu\epsilon$ from the rope tests. All curves have the same shape however; the hoop strain increasing compressively in a linear manner on first-loading and remaining almost constant on unloading-reloading. The overall shape is identical to the shape of the hoop stress curve, seen previously in Figure 6.15. The rope test values may be elevated, compared with the Abaqus values, due to material being removed from an already thin section overlying the threaded hole. This would cause a stress concentration in the cavity, exactly where the gauge is located.

7.4 The barrel.

7.4.1 Middle of the barrel, gauges 13→24.

The mean of the axial gauges from test 3 in the middle of the barrel is compared with the Abaqus values in Figure 7.8. There is general agreement in the shape of the curves although the Abaqus values underestimate the maximum tensile and compressive strains measured in the termination.

The mean hoop strain around the middle of the barrel, from the four gauges in test 3, is shown against the Abaqus values in Figure 7.9. Both curves show a linear increase in strain on first-loading with a similar additional increase on unloading; the reloading sections all show a reduction in tensile hoop strain. Hysteresis is present for both curves; such that on reloading the strain is lower than it was whilst unloading.

The shear strains around the middle of the barrel, from the four gauges in test 3, are shown against the Abaqus values in Figure 7.10. The shapes of the curves are very similar, with the Abaqus strains lying within the range of the experimental values, for most of the loading history.

On first loading to 60%, the shear strain rises linearly to a maximum between 200-350$\mu\epsilon$. On unloading the shear strain rises further to between 600-700$\mu\epsilon$, falling to between 150-350$\mu\epsilon$ on reloading. There is hysteresis in the cycling portions. At 100% the shear strain has risen to 250-500$\mu\epsilon$ and reaches between 900 and 1100$\mu\epsilon$ on subsequent unloading.

7.4.1.1 The behaviour in the middle of the barrel.

The overall behaviour in the middle of the barrel can be explained by considering what is happening on the inside. On first-loading the spike is drawn into the termination, hence the barrel is stretched axially by the friction of the rope on the inside of the termination, and stretched in the hoop direction by the spike being pulled in. On unloading, the spike stays put and the contact pressure remains constant, whilst the contraction of the rope compresses the barrel axially. The results from the Abaqus analysis show that the conditions on the inner surface of the barrel do not change significantly whilst the rope is cycled; the contact pressure remains the same, and no radial displacement of the surface takes place. However, because the barrel is being compressed axially by the rope, the conditions on the outside surface do change; the barrel goes into compression axially and therefore into further tension circumferentially as it expands radially.

Because of these changes in the hoop and axial strains, the shear strain also rises on unloading, as would be expected from looking at the Mohr's circle (Appendix B).

7.4.2 Base of the barrel, gauges 25→30.

The axial and hoop strains at the base of the barrel have the same form as in the middle (see Figures 7.11, 7.12, 7.13 and 7.14). The strains are larger, adjacent to the base of the spike, because the barrel is experiencing the same contact pressure along its length on the inside, but the walls are thinner at the base.

7.5 Asymmetry within the termination.

Figure 7.15 shows the asymmetry that is present in the middle of the spike; in test 1, there is a difference of $2700\mu\epsilon$ in the axial strain, between the two gauges on opposite sides. Test 2 exhibits a difference of $420\mu\epsilon$, with only $270\mu\epsilon$ for test 3. In Appendix C, it is shown that a central spike displacement relative to the ends of 0.14mm can cause an axial strain of $1000\mu\epsilon$. This displacement is roughly 4% of the thickness of the rope, and so a small asymmetry in the distribution of fibres around the spike may cause the differences between opposite gauges, seen in Figure 7.15.

Figure 7.16 shows the axial strains measured at four points around the circumference of the barrel. The readings from gauges 16 and 22 are almost identical, differing by no more than $30\mu\epsilon$ throughout the test. The two other gauges do exhibit differences. Initially gauge 19 goes into compression, whilst gauge 13 on the opposite side reads the greatest tension out of the four gauges; thereafter the curves of axial strain for these two are of similar shape. This would indicate a simple bending. However, throughout the cycling regime between 5-50%, the adjacent gauges 19 and 16, have the greatest difference.

Figure 7.17 shows the deviation of the principal strain direction from the axial direction for these central gauges. Initially, the hoop and axial strains are comparable, which leads to a large fluctuation in this angle, but on further loading the angles settle down to less than 10^o for the remainder of the test.

As with the axial strains, the greatest difference is between two adjacent gauge locations rather than on opposite sides as might be expected from a simple bending of the barrel, so a more complex deformation is taking place.

Conversely the largest principal shear strains in the middle of the barrel (Figure 7.10) are on two opposite locations with the smallest occurring on the other two.

7.5.1 Possible asymmetric distributions.

If it assumed that a simple bending is taking place in the termination, with plane sections remaining plane, then the strain can be expressed by:

$$\epsilon = \epsilon_0 + x\kappa_x + y\kappa_y \tag{7.1}$$

where ϵ is the strain (either hoop, axial or shear), ϵ_0 is the mean strain, and x and y are the distances along the x and y axes which lie in the plane perpendicular to the axis of the termination. κ_x and κ_y are the curvatures in the x and y directions.

On the surface of the barrel this can be rewritten as:

$$\epsilon = \epsilon_0 + K_0 \sin(\theta - \theta_0) \tag{7.2}$$

where K_0 is a constant, θ is the angle around the barrel, and θ_0 is a phase shift.

If an additional term is included to allow for an additional distortion due to an oval distribution of fibres then:

$$\epsilon = \epsilon_0 + K_1 \sin(\theta - \theta_0) + K_2 \sin(2(\theta - \theta_0)) \tag{7.3}$$

A possible distribution that may lead to the sinusoidal form of Equation 7.3 is shown schematically in Figure 7.18. The thicknesses of rope around the spike will not be as extreme as in this diagram; when the termination is loaded everything will bed-down. However those regions that start off with

a greater thickness will end up with a higher transverse compression. This will lead to an asymmetric pressure on the inside of the barrel. This in turn leads to an asymmetric friction; where the contact pressure is greatest the limiting friction is greatest.

For the axial strain around the middle of the barrel, the least-squares best fit for an equation of the form of Equation 7.3 to the limits of the cycling regime (Figure 7.19) occurs when $K_1 = -25\mu\epsilon$, $K_2 = -32\mu\epsilon$ and $\theta_0 = 2$ radians. These are shown in the following equations:

$$\epsilon_{50\%} = 104 - 25\sin(\theta - 2) - 32\sin(2(\theta - 2)) \tag{7.4}$$

$$\epsilon_{5\%} = -232 - 25\sin(\theta - 2) - 32\sin(2(\theta - 2)) \tag{7.5}$$

There is also a variation in the hoop stresses as shown in Figure 7.20, however these would need a more complex curve fit.

The shortness of these ropes might also be a factor in this asymmetry; for test 3 a 2m length of rope was used. The two parallel faces applying the load to the lock nuts on the barrels allow for no initial mis-alignment, and any mis-alignment present would cause an asymmetric load on the terminations. This asymmetry can be reduced by inserting a universal joint between the loading head and the termination, although the geometry of the rig used ruled this out for the tests performed here.

7.6 Displacements.

Bed-down displacements could only be measured on the top termination (the gauged one) due to constrictions of space at the lower head. Three transducers were attached; one to measure bed-down of the spike relative to the barrel, one to measure displacement of the barrel relative to the other end, and as a check, one to measure the movement of the spike relative to ground.

7.6.1 Bed-down.

The bed-downs for all three tests and the Abaqus predictions are remarkably similar (Figure 7.21). The most notable feature for the Abaqus results is how the stiffnesses match the test results. There are five stiffnesses present, which correlate with the stiffness changes for the transverse moduli of the Kevlar. The stiffness is increased at 180kN and at 360kN for the loading phase, and increased substantially for the unloading-reloading phase, and again for the final unloading. The only deviation present is on reloading beyond the initial preload, for the tests the curves pass below the initial curves, such that for a given load there is a greater bed-down the second time round. This behaviour is most likely to be due to both creep and hysteresis which are a feature of polymer materials. The Abaqus model was only composed of linear-elastic portions, neither creep nor hysteresis were included for simplicity.

7.6.2 Force-displacement.

The force-displacement graphs (Figure 7.22) for the first two rope tests are as expected. Each graph is the sum of the bed-downs at the ends added to the elastic stretching of the rope in between. Test 1 is marginally stiffer due to the rope being shorter; however, the majority of the displacement is due to bed-down at both ends, rather than rope stretch.

Test 3 exhibits two notable events on reloading after being cycled, each being accompanied by a loud bang (Figure 7.23). The first two tests were not cycled and did not show this phenomenon. At 310kN an event must have occurred in the bottom (ungauged) termination as nothing unusual happened to the spike at the top. By measuring the shift from the previous loading curve before the event to the new loading curve, it can be determined that the rope lengthened by 2.7mm relative to the faces of the terminations. The second event occurred at 468kN with the rope again lengthening, this time by 5.4mm. At this event the spike moved backwards by 1.5mm, therefore

there was 6.9mm relative slip between the rope and the spike.

7.7 Anomalous spike movement.

The contact conditions between the spike and the rope, and the rope and the barrel are similar; on first loading slip is occurring of the rope over the spike and barrel in to the termination. If slip is initiated somehow, it is therefore likely to occur between both the rope and the barrel, and the rope and the spike. This was noted in Section 7.6.2 where relative movement occurs between both surfaces. This would imply that the spike can either end up further in, or further out. Both circumstances have been noted (c.f. Figure 2.6).

7.7.1 Limiting angle of friction.

An explanation for the anomalous behaviour of the spike, on further loading after a cycling regime, may be obtained by considering the limiting angle of friction, ϕ_f. As seen on Figure 7.24, ϕ_f is commonly defined as $\tan^{-1}(F/N)$, which gives:

$$\phi_f = \tan^{-1}(a_s \sigma^{1-\beta_s}) \tag{7.6}$$

Provided that ϕ_f is greater than the half angle of the spike, ψ, then the spike will remain in place. If the limiting angle of friction is less than ψ; then the frictional stress, holding the spike in place, will be unable to match the normal pressure acting to push it out, and slip will occur.

From Equation 7.6 two points may be noted; for a given contact pressure, and hence ϕ_f, there is a limiting angle on the spike above which a termination will not function. Similarly for a given spike angle, there is a contact pressure above which the termination will not function.

7.7.1.1 Limiting contact pressure for 3.5° spike.

For the friction used here, $\tau_s = 0.099\sigma^{0.91}$, with the half angle of 3.5°, Equation 7.6 can be used to derive an upper limit of $\sigma = 210\text{kN/mm}^2$ below which the termination will function. As this value is three orders of magnitude greater than that which will be experienced, this condition will always be satisfied so the spike should not jump due to a rise in contact pressure.

In a hypothetical case where the friction is halved, due to abrasion perhaps, to become $\tau_s = 0.05\sigma^{0.91}$, then the limit on σ reduces to 0.107kN/mm^2, i.e. once the contact pressure exceeds 0.107kN/mm^2 the rope will slip between the spike and the barrel. This is the same magnitude as the value predicted at ultimate load, both from the finite element model, and from an analysis of the hoop strains using Lamé's equations (Section 7.8). Therefore if the friction was to be halved then the spike may be expected to jump. (The order of magnitude changes dramatically due to σ being raised to the power of $1 - \beta_s$, which is close to zero.)

7.7.1.2 Limit on angle of spike.

For the current friction, $\tau_s = 0.099\sigma^{0.91}$, and the predicted maximum contact stress of 0.120kN/mm^2, the maximum spike half angle using Equation 7.6 equates to ψ=6.8°. If the designed half angle is greater than this, then the termination will be unable to reach the maximum load due to the spike slipping out of the back of the barrel.

7.7.2 Viscoelasticity.

The spike bed-down did not increase during successive cycles, nor did the strains change significantly; therefore no ratchetting occurred. The anomalous spike behaviour was not present for single cycles; the only differences being a small amount of abrasion of the rope over the spike and barrel, and

the extra time taken. The extra time taken is more likely to be the determining factor; due to the viscoelastic nature of Kevlar, under load between the spike and barrel, the stress will reduce over time. This drop in contact pressure will mean a reduction in the magnitude of limiting friction.

7.8 Prediction of contact pressure using Lamé's equations.

Assuming plane stress in a cross section through the barrel, the hoop strain on the outer surface of the barrel can be used to estimate the radial stress on the inner surface of the barrel using Lamé's equations.

Lamé's equations relate the stresses and strains as follows:

$$\sigma_r = A - \frac{B}{r^2} \tag{7.7}$$

$$\sigma_\theta = A + \frac{B}{r^2} \tag{7.8}$$

where σ_r and σ_θ are the radial and hoop stresses, at a radius, r. A and B are constants determined by the boundary conditions. On the outer surface of the barrel, $r = r_o$ and $\sigma_r = 0$; therefore from Equation 7.7:

$$A = B/r_o^2 \tag{7.9}$$

Using the elasticity equation, the outer hoop strain $\epsilon_{\theta o}$ can be expressed as:

$$\epsilon_{\theta o} = \frac{\sigma_{\theta o}}{E} - \nu\frac{\sigma_{ro}}{E} \tag{7.10}$$

but $\sigma_{ro} = 0$ and so an elimination of A from Equations 7.8 and 7.9 gives $B = E\epsilon_{\theta o}r_o^2/2$; substituting back into Equation 7.9 gives $A = E\epsilon_{\theta o}/2$.

Using these terms for A and B at the inner surface, $r = r_i$, Lamé's equations give:

$$\sigma_{ri} = \frac{E\epsilon_{\theta o}r_o^2}{2}\left(1 - \left(\frac{r_o}{r_i}\right)^2\right) \tag{7.11}$$

The mean hoop strain from test 3 in the middle of the barrel at the failure load (Figure 7.9), $\epsilon_{\theta o}$, is $500\mu\epsilon$. At this location, $r_i = 25$mm, $r_o = 50$mm

and $E = 70\text{kN/mm}^2$ therefore from Equation 7.11: $\sigma_{ri} = -0.13\text{kN/mm}^2$. This value corresponds very well to the Abaqus value of -0.12kN/mm^2 (Figure 6.9).

7.9 Lifetimes under cyclic loading.

Working from the finite element results, it is possible to predict a maximum yarn-on-spike amplitude of movement and contact pressure for each rope test. The contact pressure is determined by the maximum preload that has been applied, using Figure 6.9. It is not known what each maximum preload was for the literature data, so for this analysis it is assumed that the maximum load in the cycle is also the limit of the preload. It is assumed that the contact stresses in the termination are solely determined by the maximum load applied, and are not size dependent; i.e. a 6 tonne rope at 50% load will have the same contact pressure between the rope and spike as a 60 tonne rope at 50% load. Figure 6.9 can be linearised and non-dimensionalised to give:

$$\hat{\sigma} = 8.82 \times 10^{-3} + 6.85 \times 10^{-4} \lambda_{max} \tag{7.12}$$

where λ_{max} is the maximum percentage load factor applied ($100\times$maximum load/breaking load).

To estimate the amplitude of slip it may be noted from Chapter 6 that there is a position on the spike where no relative slip occurs. If it is assumed that this is the case for 6 tonne ropes as well, and for all the regimes, then the slip can be quickly estimated by analysing the portion of rope between this location and the nose of the spike. Figure 7.25 shows a schematic diagram of the forces that are present in the fibres at the load cycle limits for a 60 tonne Parafil G rope. From the finite element analysis it is noted that the rope remains static at 163mm and rubs over the nose at 220mm, so 57mm of rope is stretched.

At the salient non-moving location, the axial stress in the rope is assumed to

remain constant. (There is some variation (Figure 6.32), but this is minimal compared with the changes nearer the nose.) At the nose of the spike the load in the rope varies between λ_{max} and λ_{min}. The friction is taken to be uniform along the length of the slipping region. Therefore, the tension in the fibres will vary linearly along their length. Hence the load at the non-moving point will be the mean of λ_{max} and λ_{min}, as seen in Figure 7.25 (assuming an equal friction applies in both directions).

The extension in the fibres can be calculated by integrating the strain along the stretched portion. Due to the assumed linearity, the mean load in the rope can be used to calculate the extension. The maximum load case is equivalent to a uniform load of $(3\lambda_{max}+\lambda_{min})/4$, and the minimum to $(\lambda_{max}+3\lambda_{min})/4$. The difference between these gives the magnitude, λ_0, for an equivalent uniform cyclic loading of $(\lambda_{max}-\lambda_{min})/2$.

The failure strain, ϵ_y, of Kevlar 49 is 0.015, therefore the total cyclic strain ϵ_0, is:

$$\epsilon_0 = \frac{\lambda_0}{100}\epsilon_y = \frac{\lambda_{max}-\lambda_{min}}{2\times 100}\epsilon_y \tag{7.13}$$

Multiplying ϵ_o by the length of the stretched region, 57mm, gives the amplitude of slip, a_o;

$$a_o = 57\epsilon_0 = 4.28\times 10^{-3}(\lambda_{max}-\lambda_{min}) \tag{7.14}$$

For a 5-50% cycle in a 60 tonne rope this gives a displacement of 0.19mm compared with the finite element value of 0.20mm.

It is assumed that the areas of different sized terminations are scaled linearly, such that the cross sectional area of a rope of size, Q tonnes, will be related to a 60 tonne rope by the factor $Q/60$. Therefore the lengths will be scaled by a factor of $\sqrt{Q/60}$. Using this scaling factor and the non-dimensionalising yarn diameter, $d = 0.357$mm, Equation 7.14 can be generalised to predict the non-dimensionalised amplitude of abrasion ($\hat{a_o} = a_o/d$), from the percentage maximum load (λ_{max}), the percentage minimum load (λ_{min}) and the size of

the rope, Q tonnes:

$$\hat{a_o} = 1.55 \times 10^{-3}(\lambda_{max} - \lambda_{min})\sqrt{Q} \tag{7.15}$$

The compressed thickness of the rope at the nose of a 60 tonne Parafil G rope is 3.2mm from the finite element analysis (which is an annulus of 320mm^2 at a mean radius of 16mm). The non-dimensionalised thickness to be abraded, $\hat{\delta}$, that needs to fail from each side of the rope, for the yield stress to be reached in the remaining rope at the maximum load, is given (for a rope of size Q tonnes) by:

$$\begin{aligned} \hat{\delta} &= 3.2 \times \frac{100 - \lambda_{max}}{100} \times \frac{1}{2} \times \frac{1}{0.357} \times \sqrt{\frac{Q}{60}} \\ &= 5.79 \times 10^{-3}(100 - \lambda_{max})\sqrt{Q} \end{aligned} \tag{7.16}$$

Equations 7.12, 7.15 and 7.16 can be fed into Equation 3.23, to yield a simple formula for predicting the lifetime of any Parafil G rope with aluminium spike and barrels based on the current design:

$$\boxed{N = 4.59 \times 10^{11}(100 - \lambda_{max})Q^{-0.9}(12.9 + \lambda_{max})^{-1.1}(\lambda_{max} - \lambda_{min})^{-2.8}} \tag{7.17}$$

Figure 7.26 shows the lifetimes of 6 and 60 tonne Parafil G ropes under cyclic loading. This figure shows the predicted lifetimes derived from combining the finite element analysis and the abrasion tests performed for Chapter 3, along with experimental results from the literature presented earlier in Section 2.4. There is a very good correlation between these predictions and the experimental results, given the scatter associated with these fatigue tests and the assumptions made here. Indeed, the two 5-40% tests lasted 254,000 and 1,200,000 cycles.

The only deviations between the predictions and the experiments occur in the limits of the 60 tonne ropes. At high cyclic ranges the lifetime is overestimated by an order of magnitude, and is conversely underestimated by almost an order of magnitude for 5-30%. It may be that at high ranges in big ropes, which have to be tested slowly, creep rupture effects are important, due to

the time spent at the high loads. At low loads, the broken yarns may be shielding the surviving ones.

7.9.1 Predicted lifetimes for other size ropes.

Figure 7.27 shows the estimated effect of size on the lifetime of a Parafil termination using Equation 7.17; as the ropes become larger their susceptibility to abrasion damage becomes increasingly greater. Three different regimes are indicated to highlight the effect of severity on lifetime; it can be seen that reducing the cycle from 5-50% to 20-40% leads to an order of magnitude increase in lifetime.

7.10 Summary.

The finite element model closely predicts the strains that are measured in a 60 tonne Parafil G spike-and-barrel termination.

The spike bed-down displacements are very accurately predicted. The Abaqus values deviate by less than 1mm from the measured values once the analysis has begun. The gradient of the Abaqus bed-down curve changes as the transverse moduli of the rope are altered; the gradients are tangents to the measured values, though they are independently derived.

The Abaqus model does not however predict the asymmetric deformation that is seen, nor the anomalous spike movement that is observed when loading after a cycling regime. This asymmetry may be due to an irregular distribution of fibres around the spike; a bending strain of $1000\mu\epsilon$ is generated on the surface of the spike by a 4% offset of the rope (Appendix C). The anomalous movement of the spike is most likely due to the viscoelastic properties of Kevlar; over time the contact stress in the termination will fall, thus reducing the limiting friction — so rope-spike and rope-barrel slip may both occur.

Using the contact stresses and magnitudes of slip calculated with the finite element analysis (Chapter 6), and the abrasion results presented in Chapter 3, Equation 7.17 can be derived. This equation accurately predicts the lifetimes of actual 6 tonne terminations under cyclic loadings, given the size of rope, and maximum and minimum load limits.

The lifetimes under cyclic loading reduce with increasing size of rope, and with increasing load range; due to the increased amplitude of slip. The lifetimes also reduce with increasing maximum load, for a given load range, due to the increasing contact pressure within the termination.

Figure 7.1: Strain gauging of a 60 tonne Parafil spike and barrel. Six rosettes were placed around the outside of the barrel, four in the middle and two near the base. Four rosettes were placed in cavities on the surface of the spike, at the base, at the nose, and two in the middle; the connector used to pull the spike out after the test without damaging the wires can be seen.

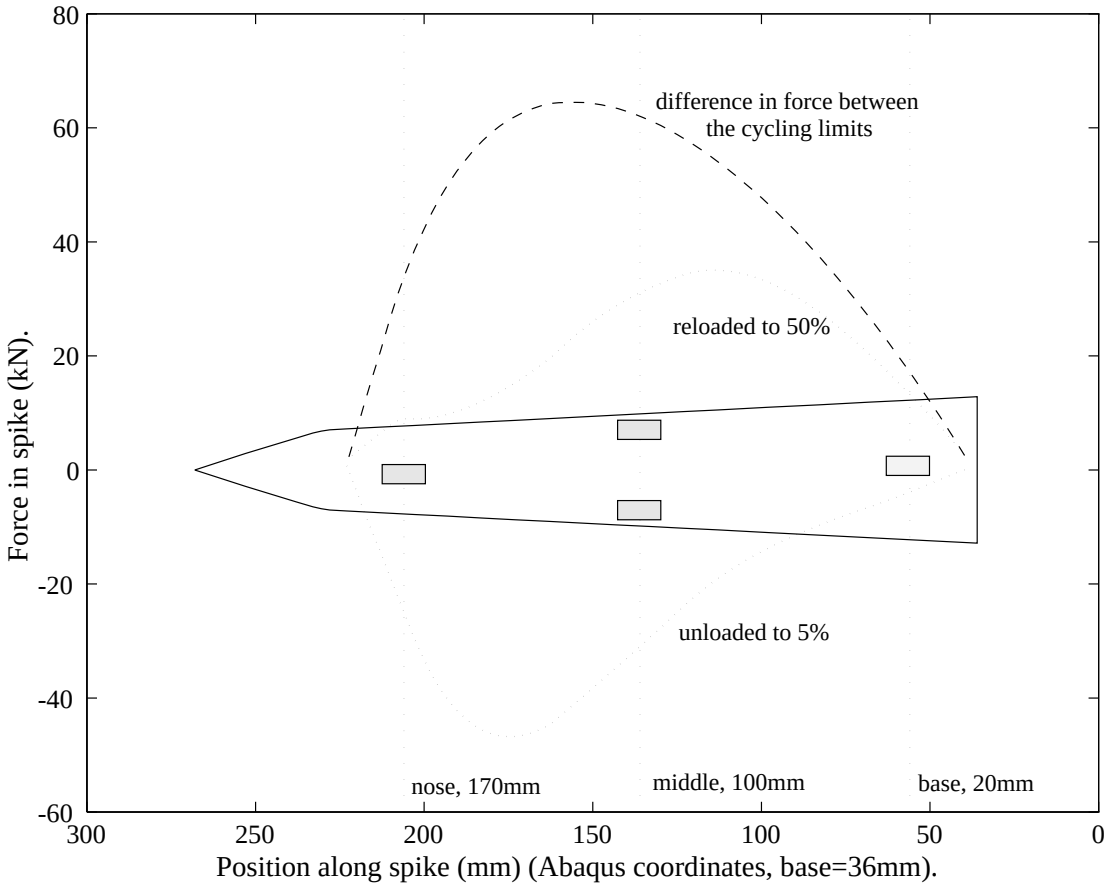

Figure 7.2: The locations of the strain gauges relative to the forces in the spike. The middle gauges are near to the maximum difference between the forces on cycling, these are positioned at 100mm from the base of the spike. The gauge at the nose, 170mm from the base, is located where the tension on loading plateaus due to the slip, a further gauge was located 20mm from the base.

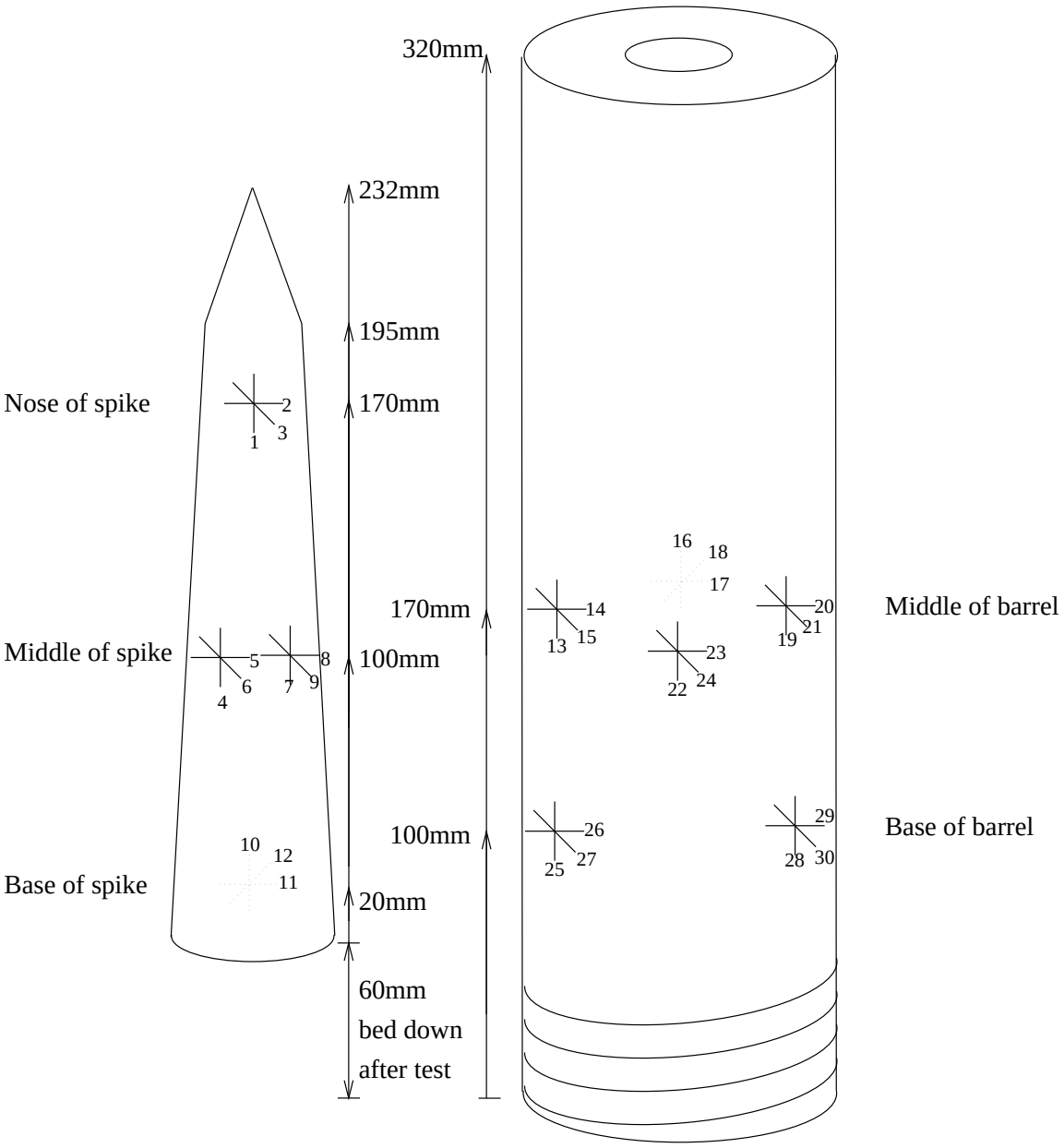

Figure 7.3: The numbering system used for the strain gauges. This shows the position of each rosette relative to each other, e.g. gauge 13 lies almost directly over gauge 4 in the assembled termination.

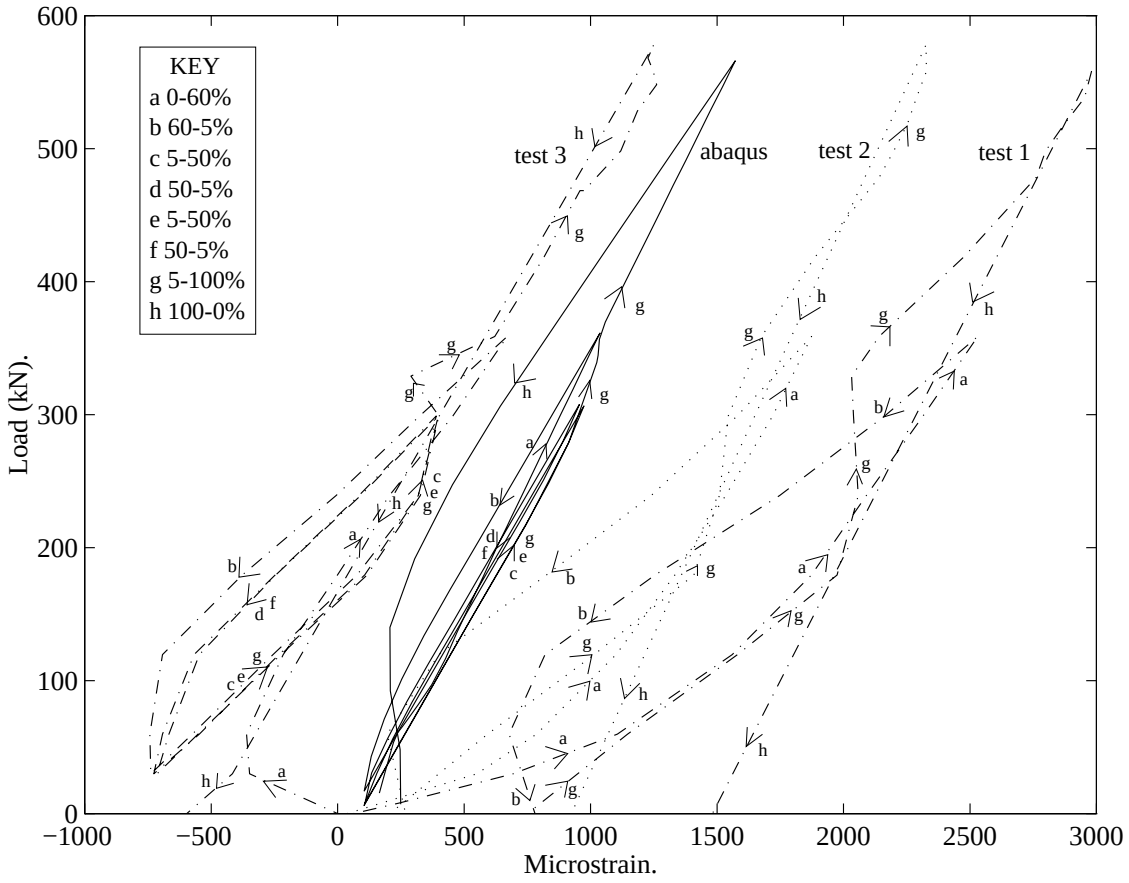

Figure 7.4: Axial strain at the nose of the spike. Comparison between the three rope tests and the Abaqus analysis; the gradients for all four are the same on first-loading, increasing in tension by $1500\mu\epsilon$ for full load, as the spike is stretched. However the rope tests all have different offsets from each other and the Abaqus values, due to asymmetry. On unloading-reloading, hysteresis can be observed for test 3, where the strain reverses rapidly before plateauing; less hysteresis is present in the Abaqus model, but both have a change in the compressive direction of $1000\mu\epsilon$ as the spike is compressed. The gradients between 100% and 0% are the same for all curves.

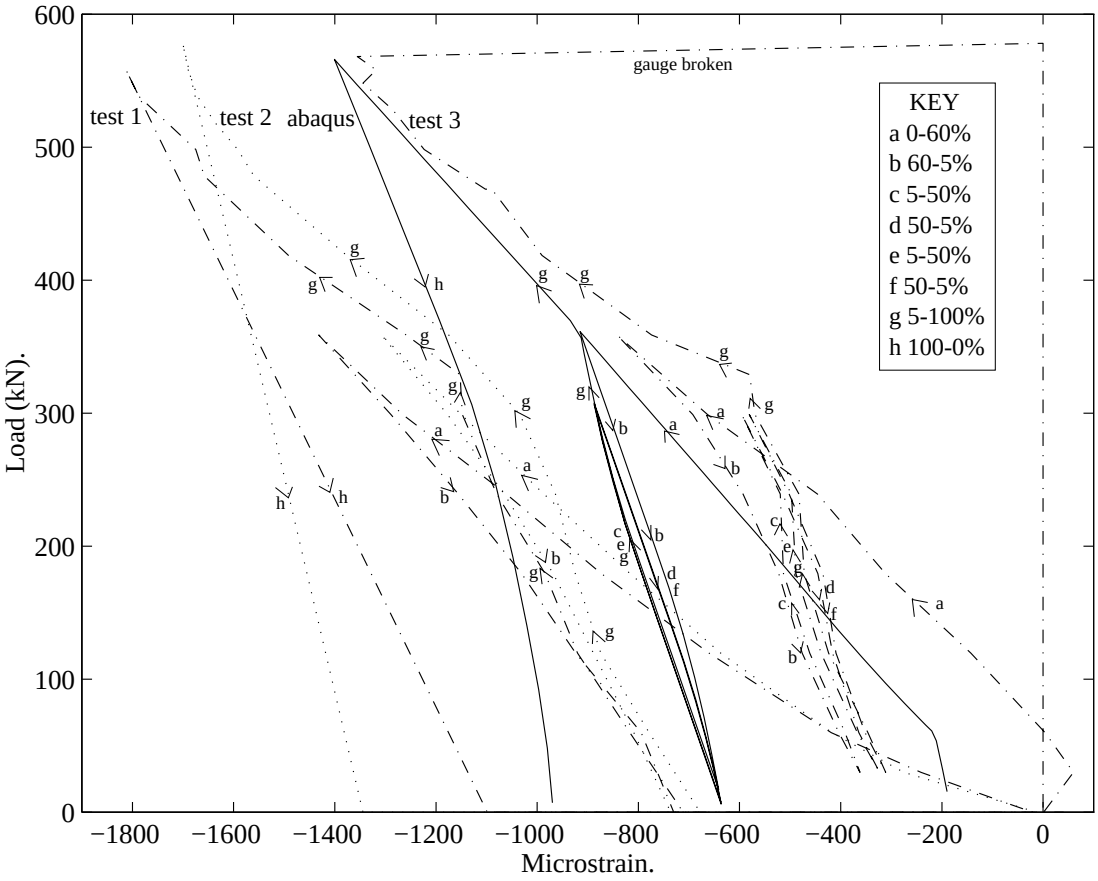

Figure 7.5: Hoop strain at the nose of the spike. The three tests and the Abaqus analysis all give similar load-strain curves; the hoop strain increases linearly in compression on first-loading as the spike is compressed in the radial and hoop directions. On unloading-reloading the magnitude of strain falls linearly, but at a steeper gradient, remaining compressive in the unloaded state. The experimental and analytical curves have approximately the same gradients throughout, except for a small offset present between the three tests for the pretensioning.

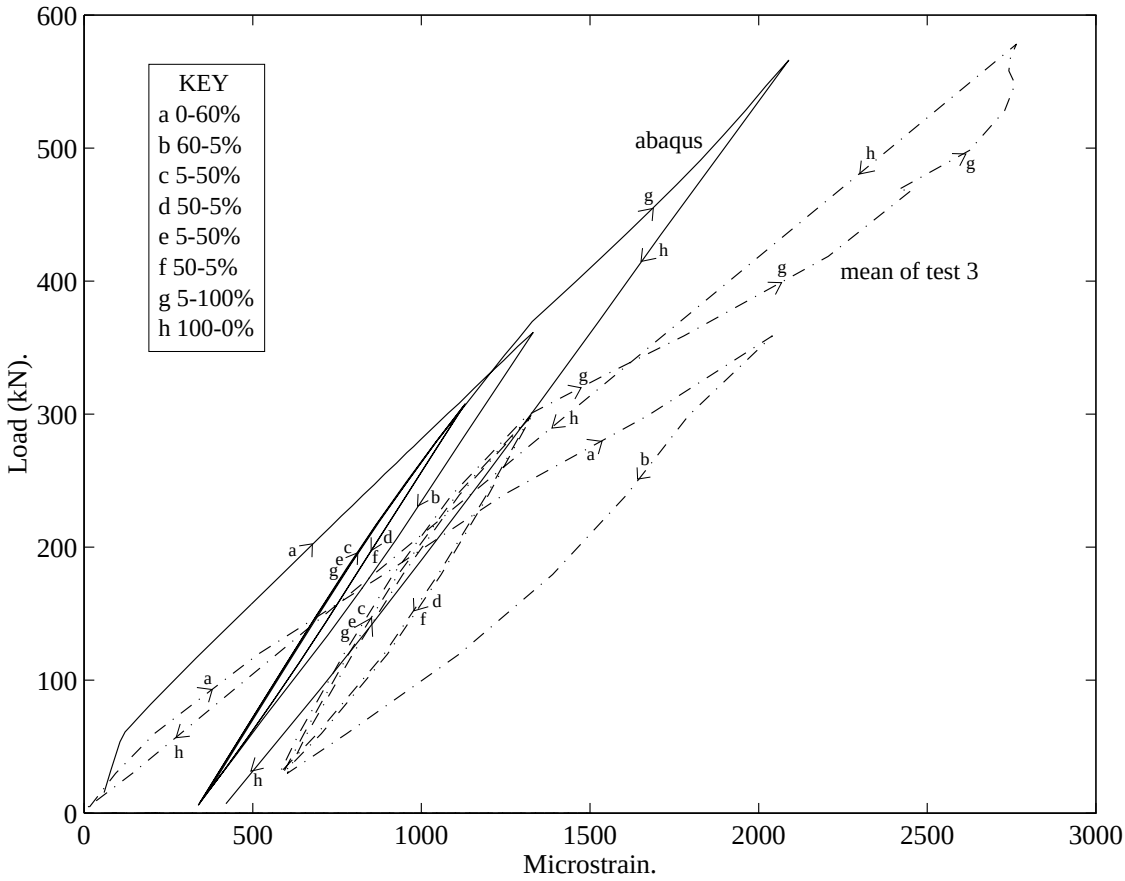

Figure 7.6: Axial strain in the middle of the spike, comparison between the mean of rope test 3 and the Abaqus analysis. Both curves have the same general shape throughout. The spike is axially stretched on loading, and compressed on unloading. Due to the large radial stress (Figure 6.14) and strain (similar to Figure 7.5), the axial strain remains positive even when the stress (Figure 6.16) becomes compressive. The cyclic portions have identical gradients and differ by only $200\mu\epsilon$.

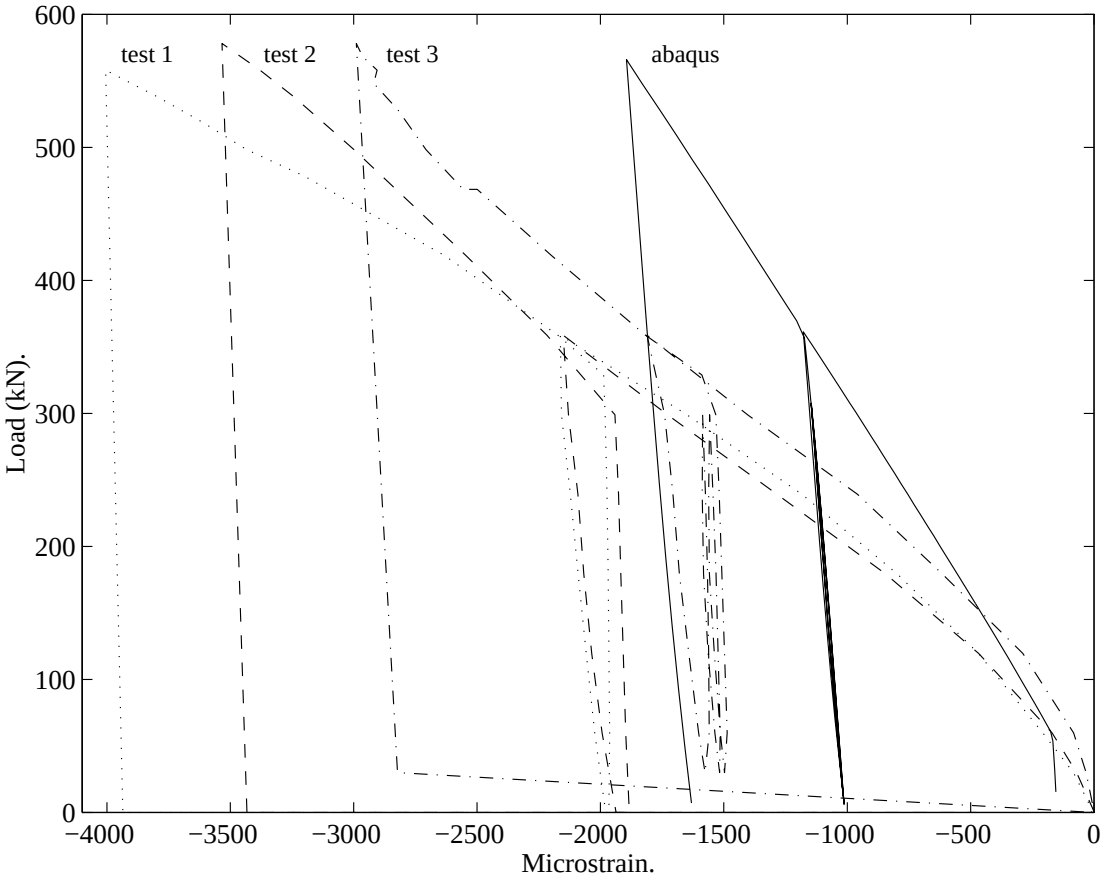

Figure 7.7: Hoop strain at the base of the spike. The three tests and Abaqus all give the same shaped curves; the hoop strain increases compressively in a linear manner on first-loading and remains almost constant on unloading-reloading. The only difference is the absolute magnitude; the gauges showing larger strains, possibly due to the cavities that they are in.

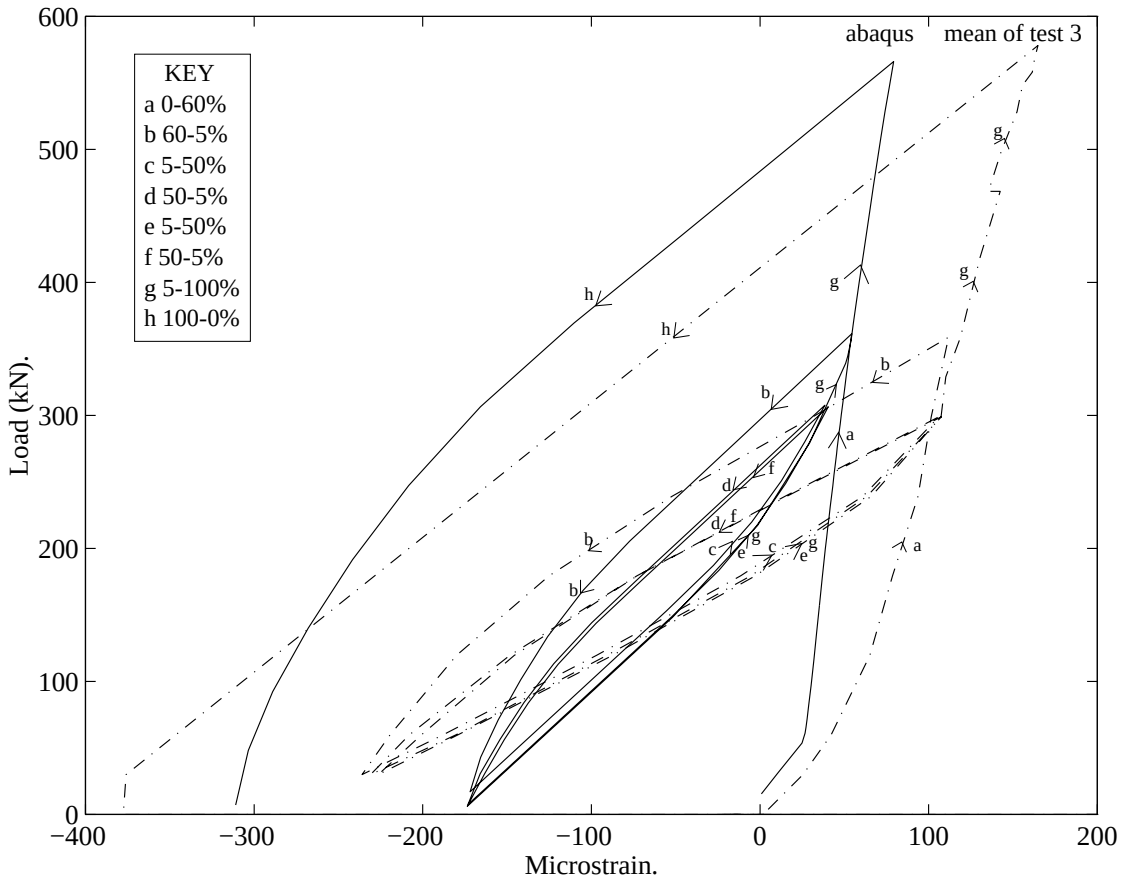

Figure 7.8: Axial strain in the middle of the barrel, comparison between the mean of rope test 3 and the Abaqus analysis. Both curves have the same general shape, going into a small tensile axial strain on loading ($\approx 100\mu\epsilon$), and a larger compressive axial strain on unloading ($\approx -350\mu\epsilon$ after failure) as the barrel goes into compression (as seen in Figure 6.30). The hysteresis on cycling takes the same form for both, with an initial rapid change in direction followed by a plateauing. The plateaus are less distinctive for both curves compared with the plateaus in stress, c.f. Figure 6.26.

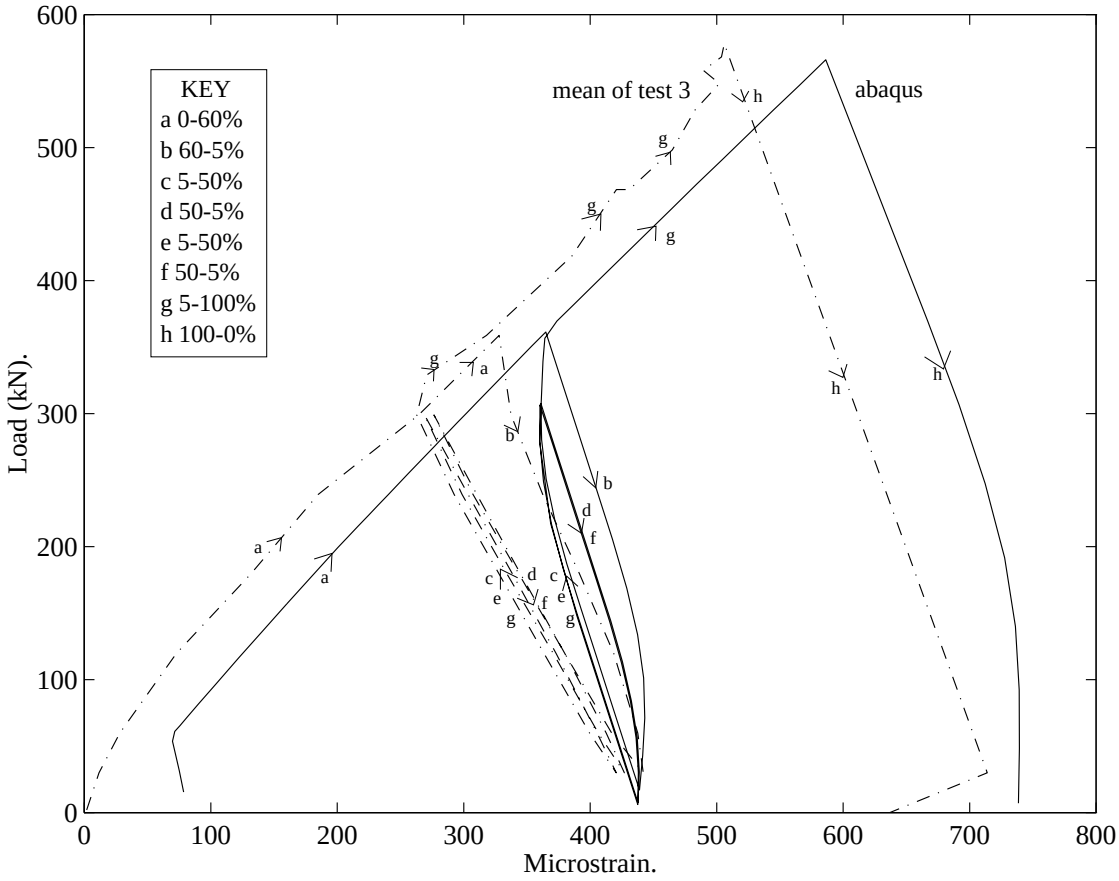

Figure 7.9: Hoop strain in the middle of the barrel, comparison between the mean of rope test 3 and the Abaqus analysis. The gradients on first-loading and unloading are identical, but with Abaqus giving a slightly greater strain. On cycling, Abaqus calculates a greater gradient for the unloading-reloading curves, such that the strains at 5% load are identical.

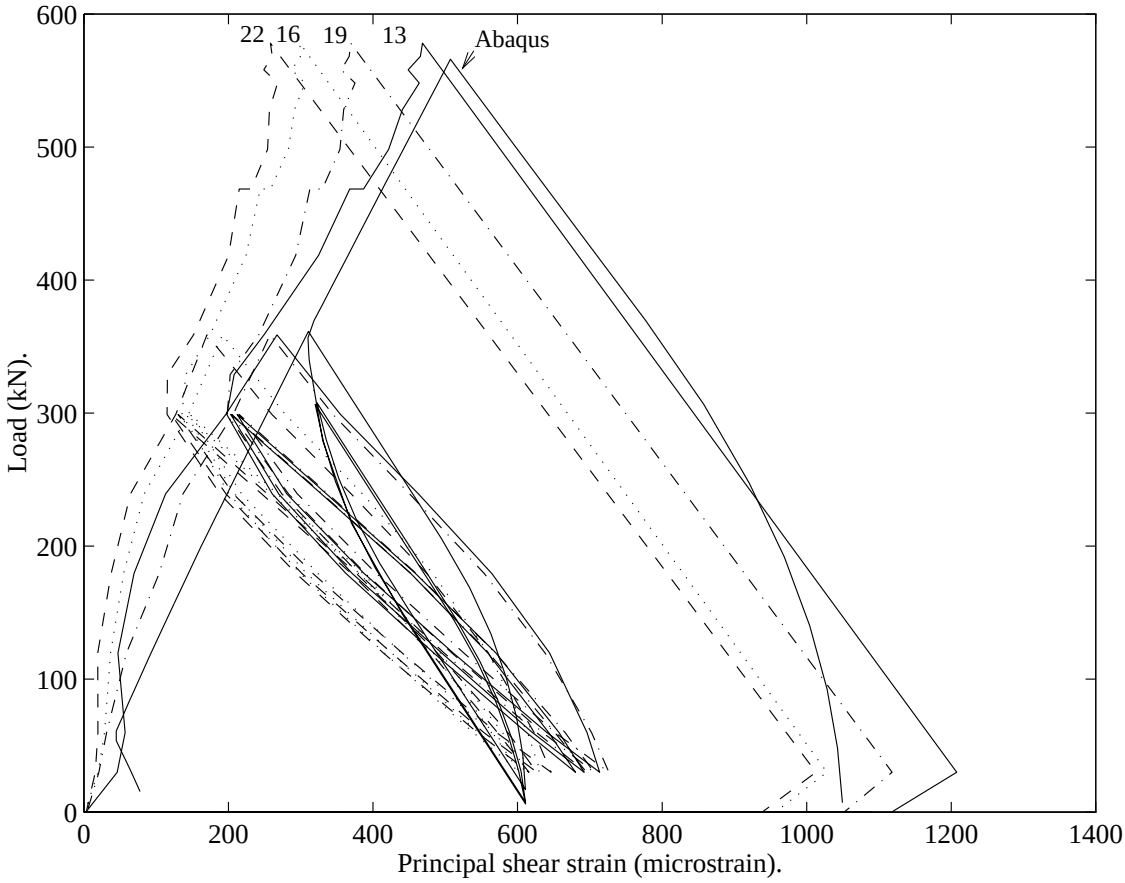

Figure 7.10: Principal shear strain in the middle of the barrel, comparison between the four values from rope test 3 and the Abaqus analysis. The first-loading curves are very similar, with the Abaqus strain being slightly greater. The curves in the cyclic region are also similar, with hysteresis present for all, due to the slip within the termination, the Abaqus gradient being slightly greater. The unloading gradients from 100% are also very similar.

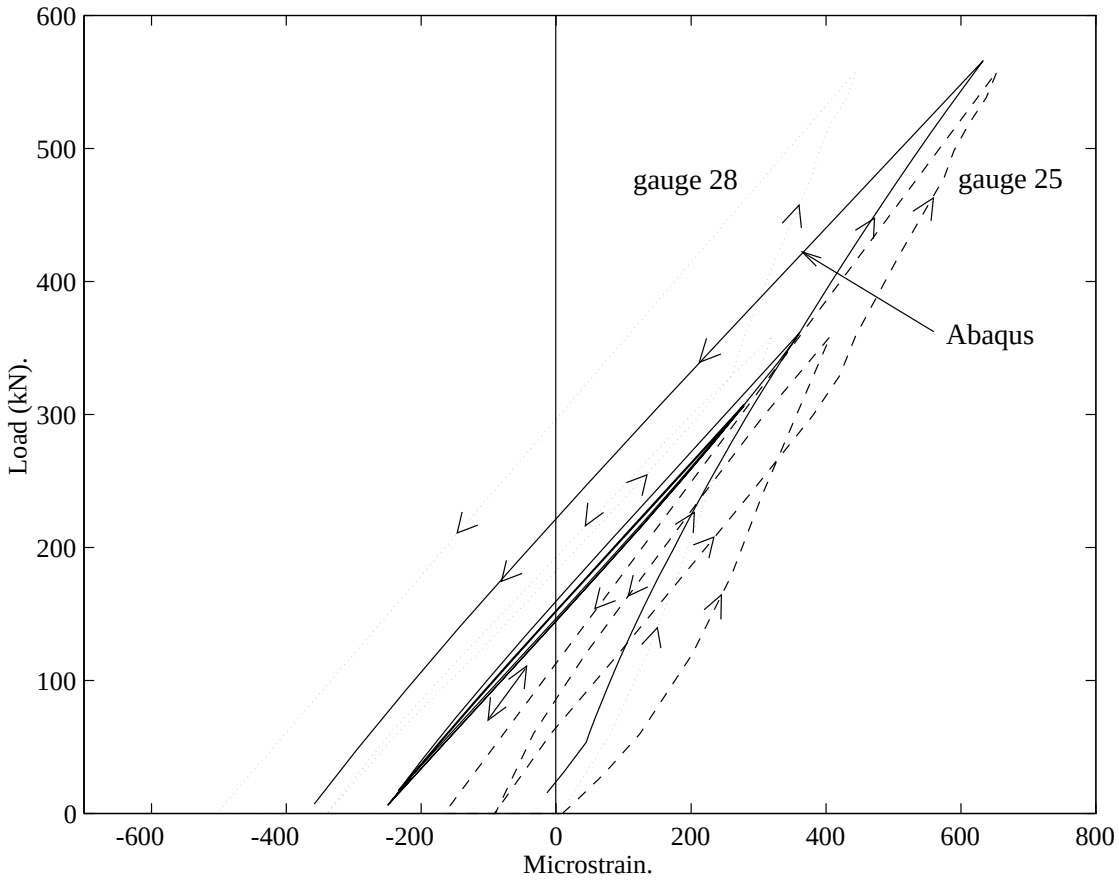

Figure 7.11: Comparison of axial strains at the base of the barrel from test 1, with the Abaqus analysis. All three curves here, and the curves for tests 2 and 3 (Figures 7.12 and 7.13) have the same shape; the axial strain is tensile on first-loading and goes negative on unloading, similar to the middle of the barrel (Figure 7.8). The Abaqus strains lie between the strains measured on opposite sides of the barrel for test 1, the test curves deviate slightly on first-loading whereas all the unloading-reloading gradients are the same.

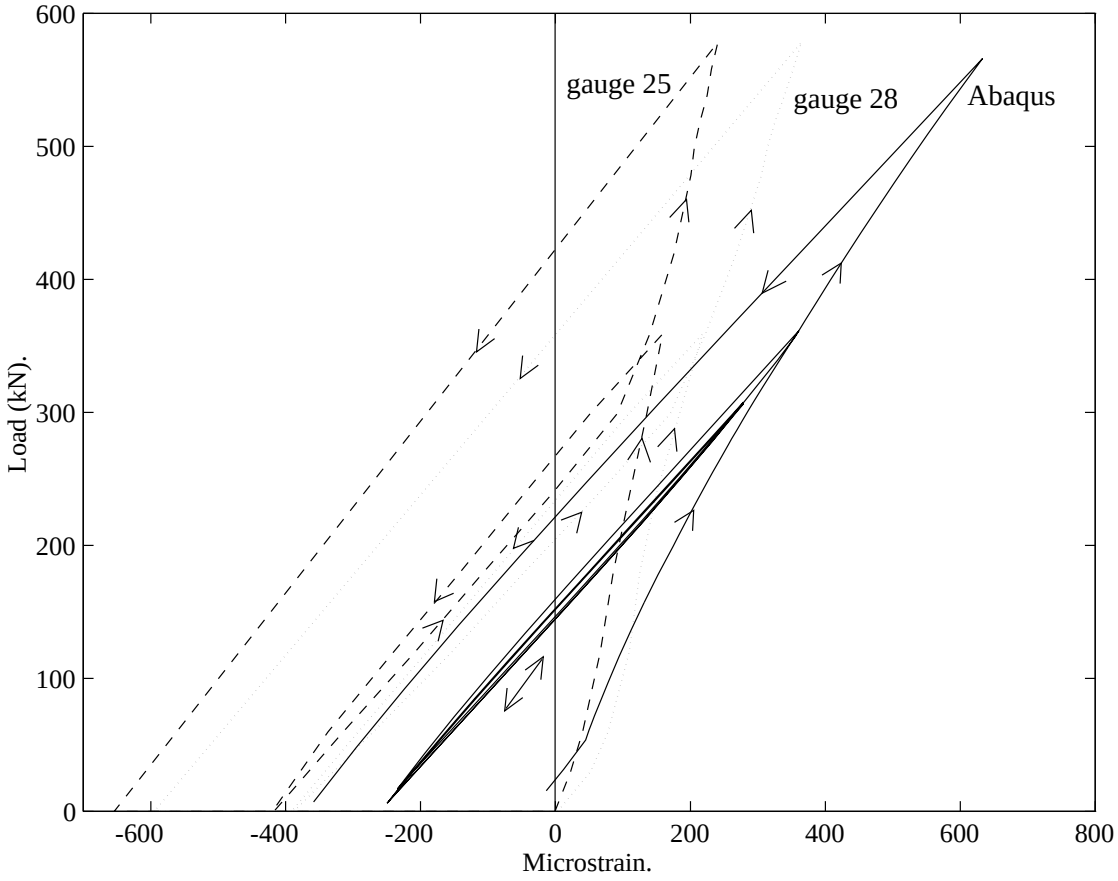

Figure 7.12: Comparison of axial strains at the base of the barrel from test 2, with the Abaqus analysis. The first-loading gradient of test 2 deviates further from the Abaqus strains than tests 1 and 3 (Figures 7.11 and 7.13), however the overall shapes are the same and the unloading-reloading gradients are identical.

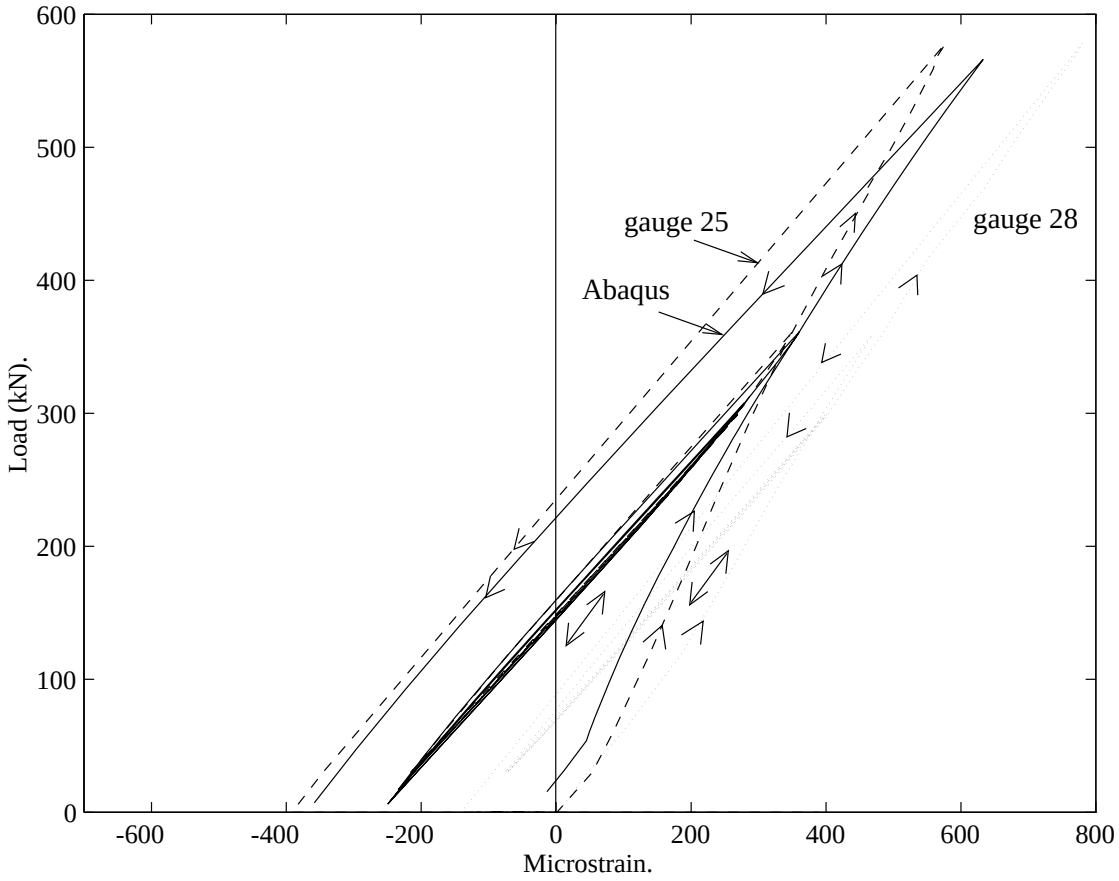

Figure 7.13: Comparison of axial strains at the base of the barrel from test 3, with the Abaqus analysis. The Abaqus strains show a very good agreement with the strains for test 3, indeed they differ from gauge 25 by less than $50\mu\epsilon$ throughout the whole loading history. Gauge 28 deviates slightly on first-loading but the unloading-reloading curves have the same gradient.

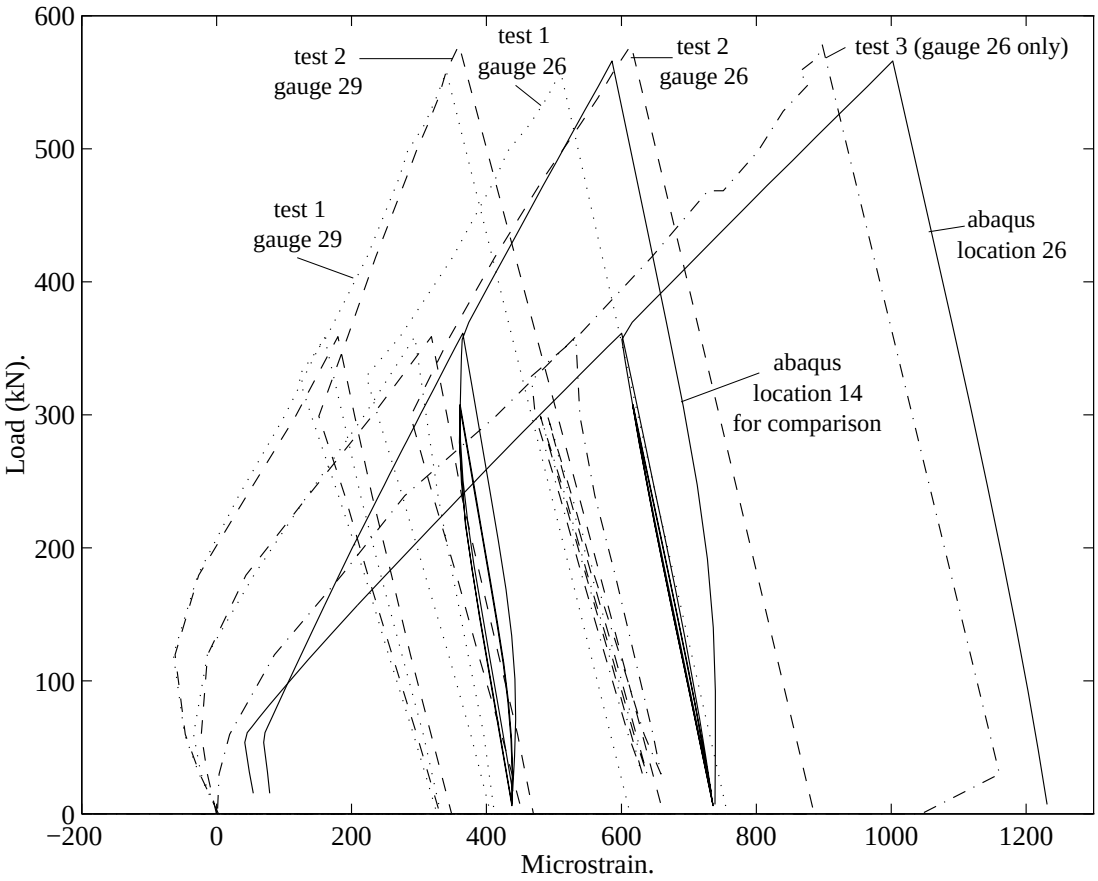

Figure 7.14: Comparison of hoop strains at the base of the barrel with the Abaqus analysis. The Abaqus hoop strains are very similar to the test 3 result. The Abaqus hoop strains at the base of the barrel are greater than the measured ones for tests 1 and 2, these tests lie a lot closer to the Abaqus values for the middle of the barrel, labelled 'location 14'. The shapes for all these curves are the same, an increasing tensile hoop strain on first-loading due to the rising internal contact pressure (Figure 6.30), with a further slight increase on unloading due to Poisson's ratio effects from the barrel going into compression axially.

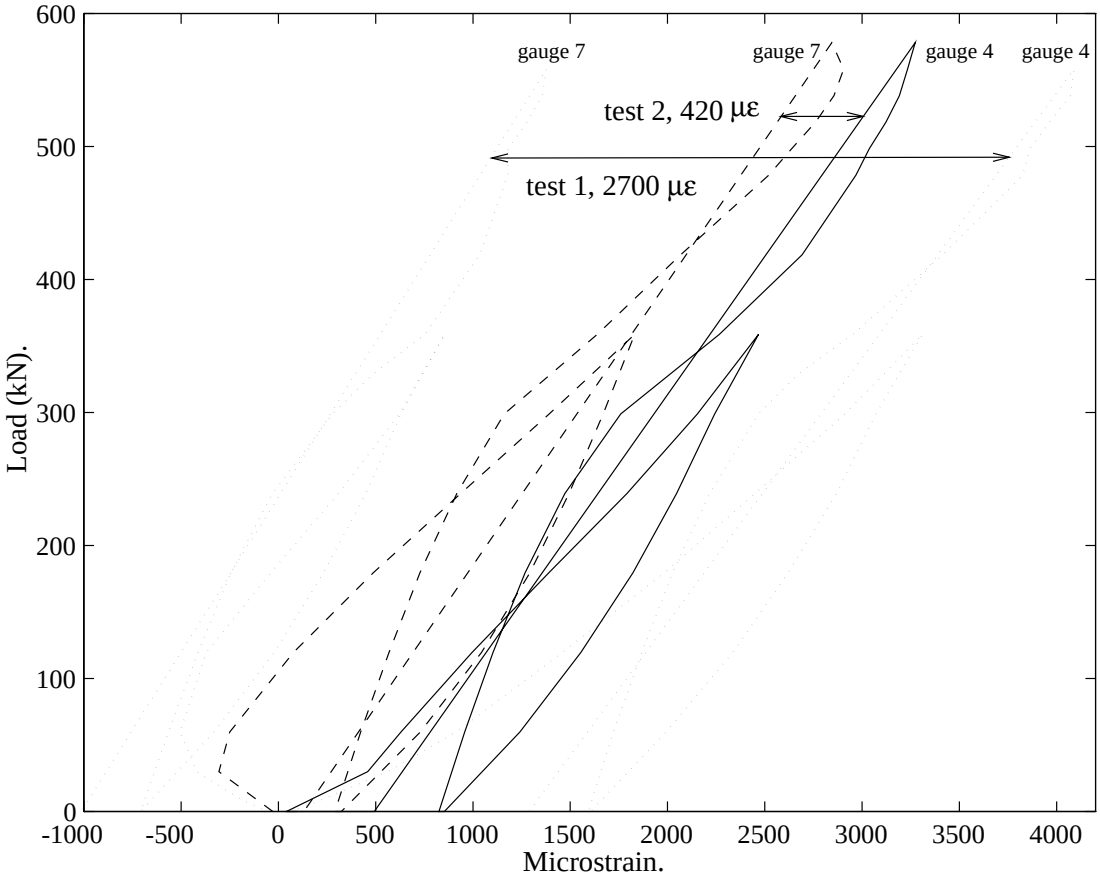

Figure 7.15: Axial strain in the middle of the spike, variation due to bending in rope tests 1 and 2. (Test 3 deviates by only $270\mu\epsilon$, see Figure 7.6 for the mean.) All four curves (and the two for test 3 not shown) have the same gradients throughout, after the initial preloading phase where they accumulate an offset, due to asymmetry within the termination. The means of all three tests are very close. The behaviour is compared with the Abaqus results in Figure 7.6.

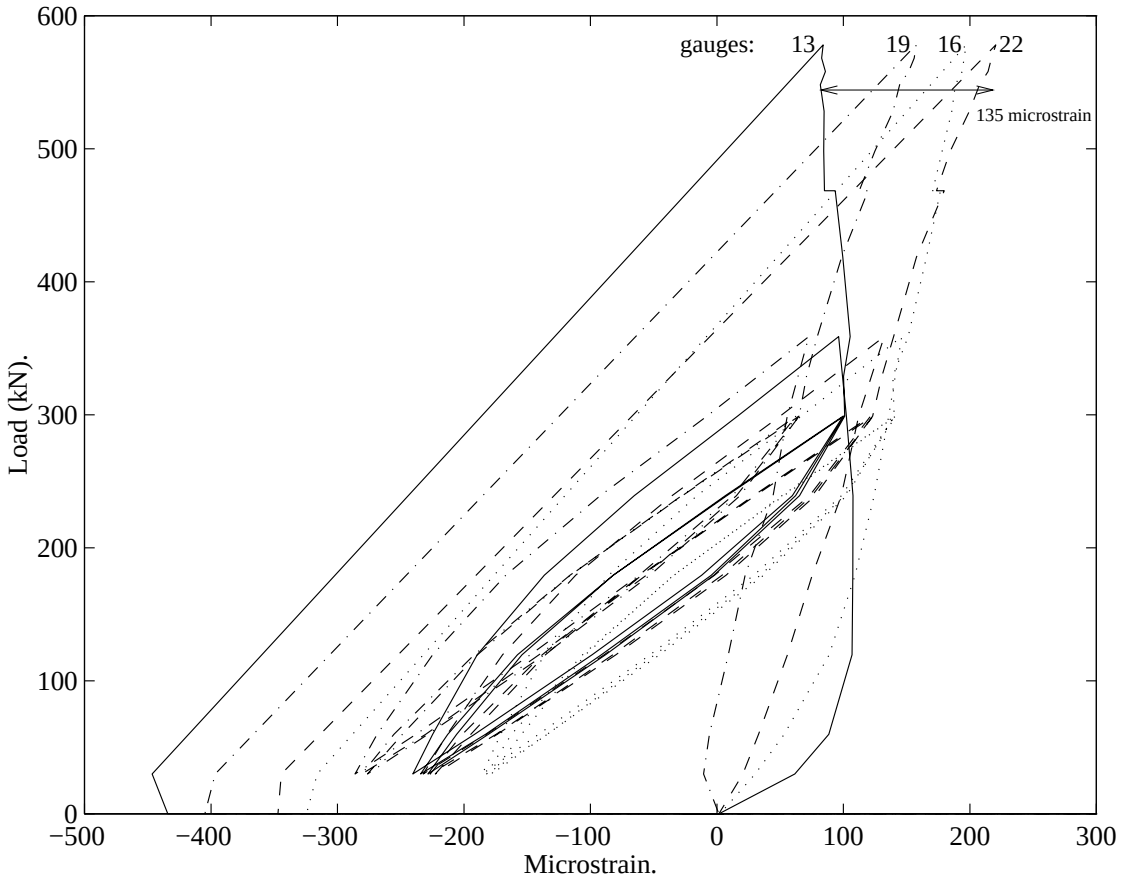

Figure 7.16: Axial strain in the middle of the barrel, showing curves for the four gauges from test 3. (The mean is compared with Abaqus in Figure 7.8.) Similar to the strains in the spike, these four curves have small offsets between them due to asymmetry. The deviation, of at most $135\mu\epsilon$, is much less than on the spike surface (Figure 7.15).

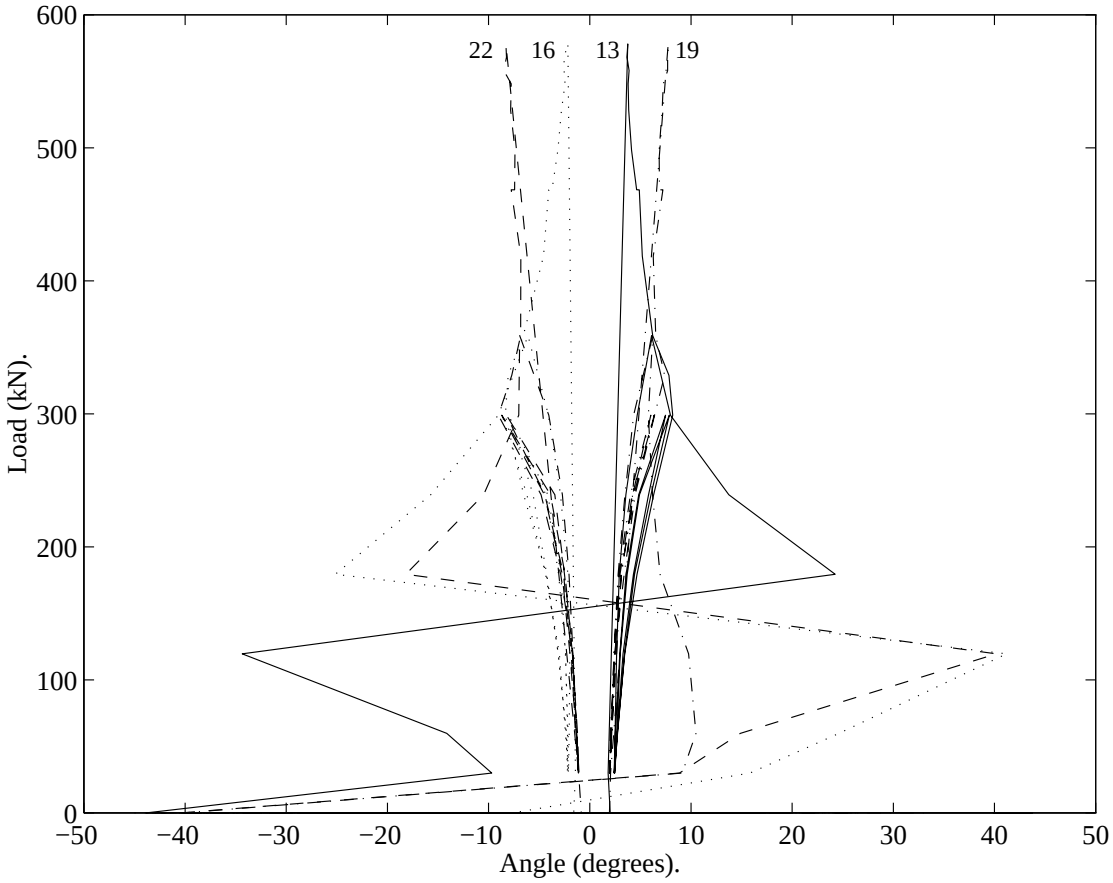

Figure 7.17: Deviation of the principal strain direction from the axial direction in the middle of the barrel for the four gauges in rope test 3. The 'switch-over' on first-loading for gauges 13, 16 and 22, is due to the axial and hoop strains being of equal magnitude, so the principal directions can jump by 90°. After preload, gauges 13 and 19 on opposite sides remain between 0° and 10°, whereas the other two gauges remain between 0° and -10°.

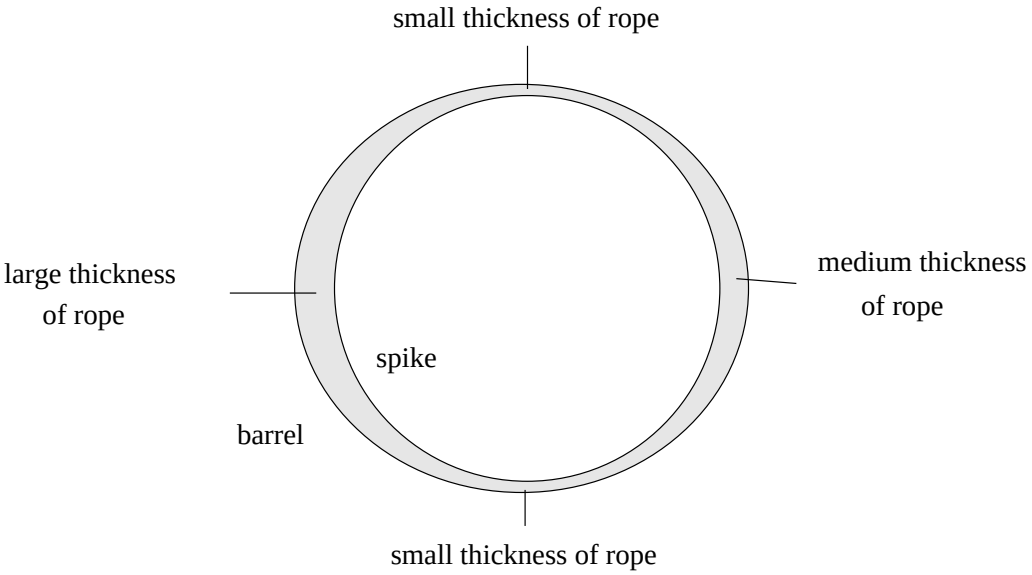

Figure 7.18: A schematic of an asymmetric distribution of fibres around the spike which would give rise to a double sinusoidal variation in the stress and strain of the form $\epsilon = \epsilon_0 + K_1 \sin(\theta - \theta_0) + K_2 \sin(2(\theta - \theta_0))$. The thickness of the rope varies such that it is smallest at two diametrically opposed points, and greater and greatest on the diagonal at right angles to this. The contact pressure will vary around the spike, and the barrel and spike will deform asymmetrically.

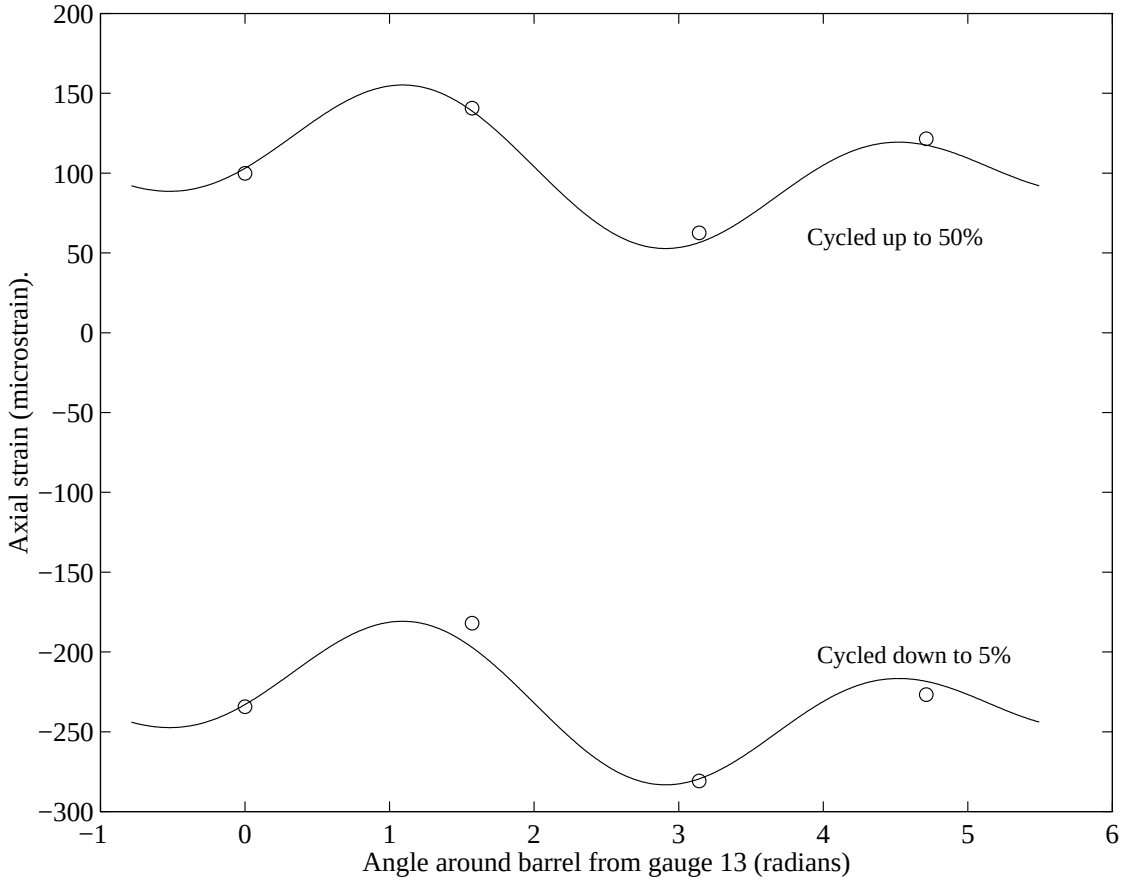

Figure 7.19: Variation in axial strain around the barrel at the limits of the cycling regime. A double sinusoidal variation in the strain of the form $\epsilon = \epsilon_0 - 25\sin(\theta - 2) - 32\sin(2(\theta - 2))$ is fitted where ϵ_0 varies between -232 and $104\mu\epsilon$ on cycling. This is consistent with an asymmetric distribution of fibres as shown in Figure 7.18, the distribution remaining fixed during cycling.

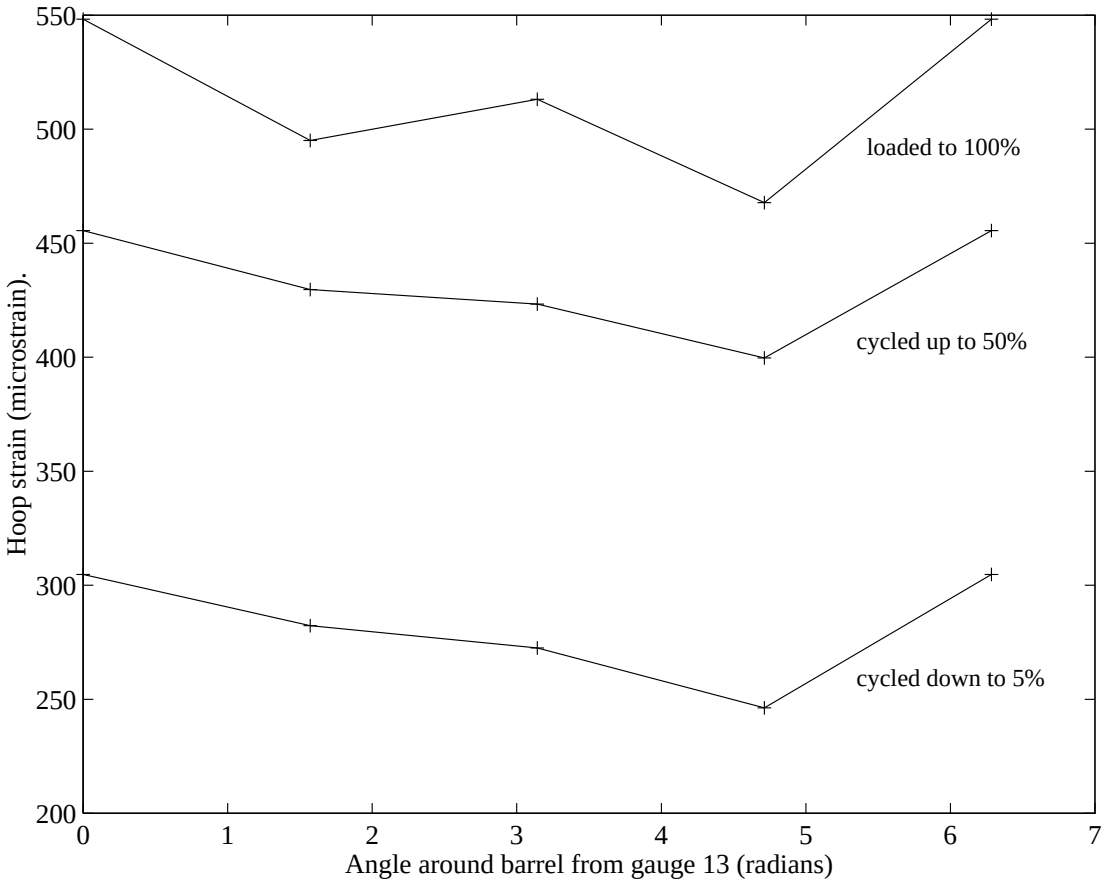

Figure 7.20: Variation in hoop strain around the barrel at the limits of the cycling regime, and at ultimate load. The behaviour here is more complex than a double sinusoidal function, but remains a second order effect superimposed on a mean strain.

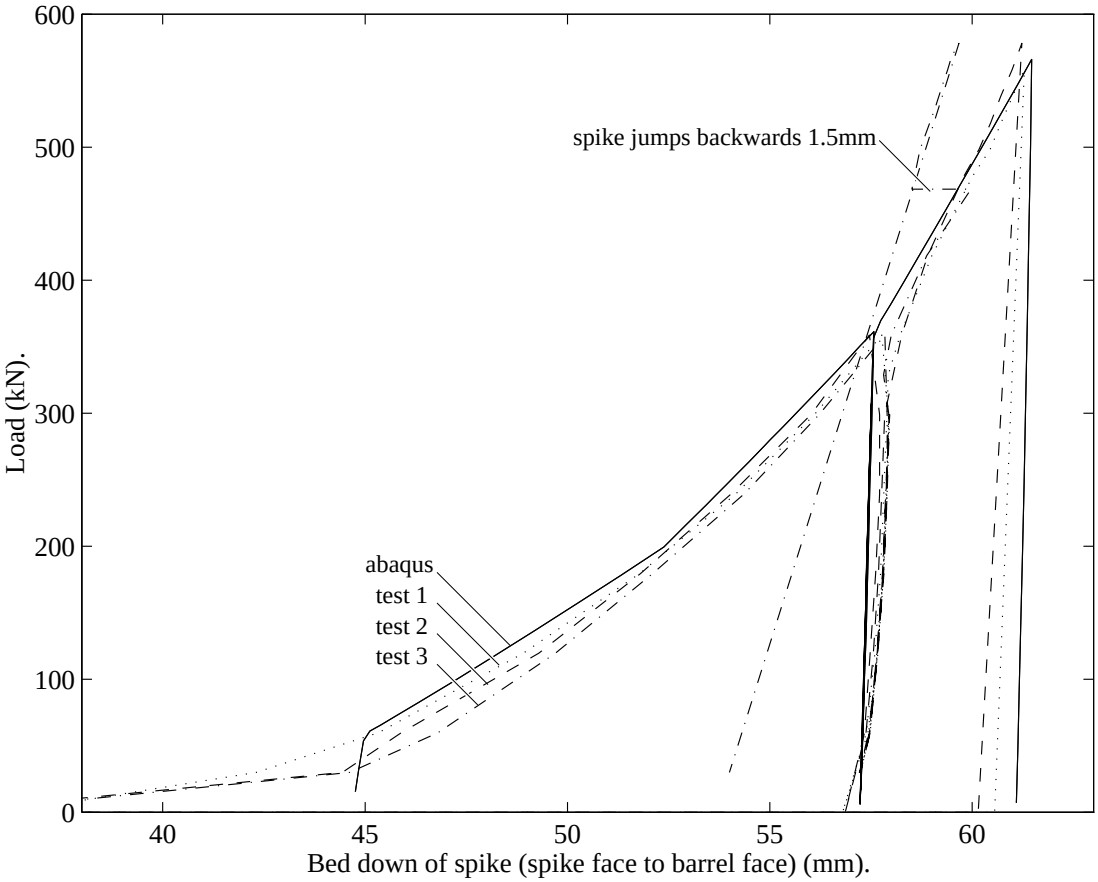

Figure 7.21: Spike bed-down displacements for the three rope tests compared with the Abaqus analysis, measured from the spike face to the barrel face. These curves show an excellent agreement, with the Abaqus result deviating less than 1mm from the measured values once pretensioning has begun. The only discrepancy is in test 3 where the spike jumps backwards by 1.5mm on loading to failure after the cycling. Five distinct Abaqus gradients can be seen; between 0-30%, 30-60% and 60-100% on first-loading, and on unloading from 60% and from 100%. These are due to the transverse modulus of the Kevlar being increased at these points.

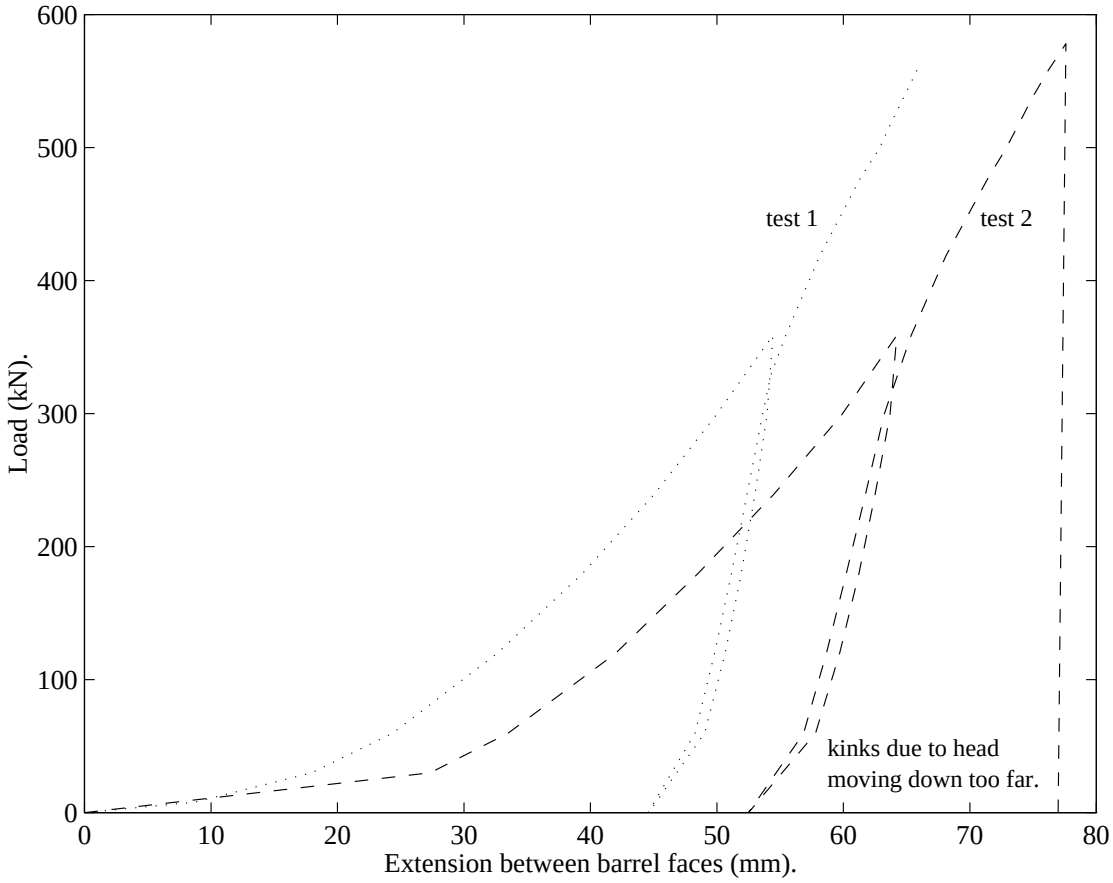

Figure 7.22: Rope extension for rope tests 1 and 2, barrel face to barrel face. The rope in test 2 was longer so the extension is greater. This graph is essentially a summation of the bed-downs in both terminations added to the stretch in the rope. On first-loading there is significant bed-down (Figure 7.21), on unloading the bed-down remains constant and the displacement is due solely to the elasticity in the rope.

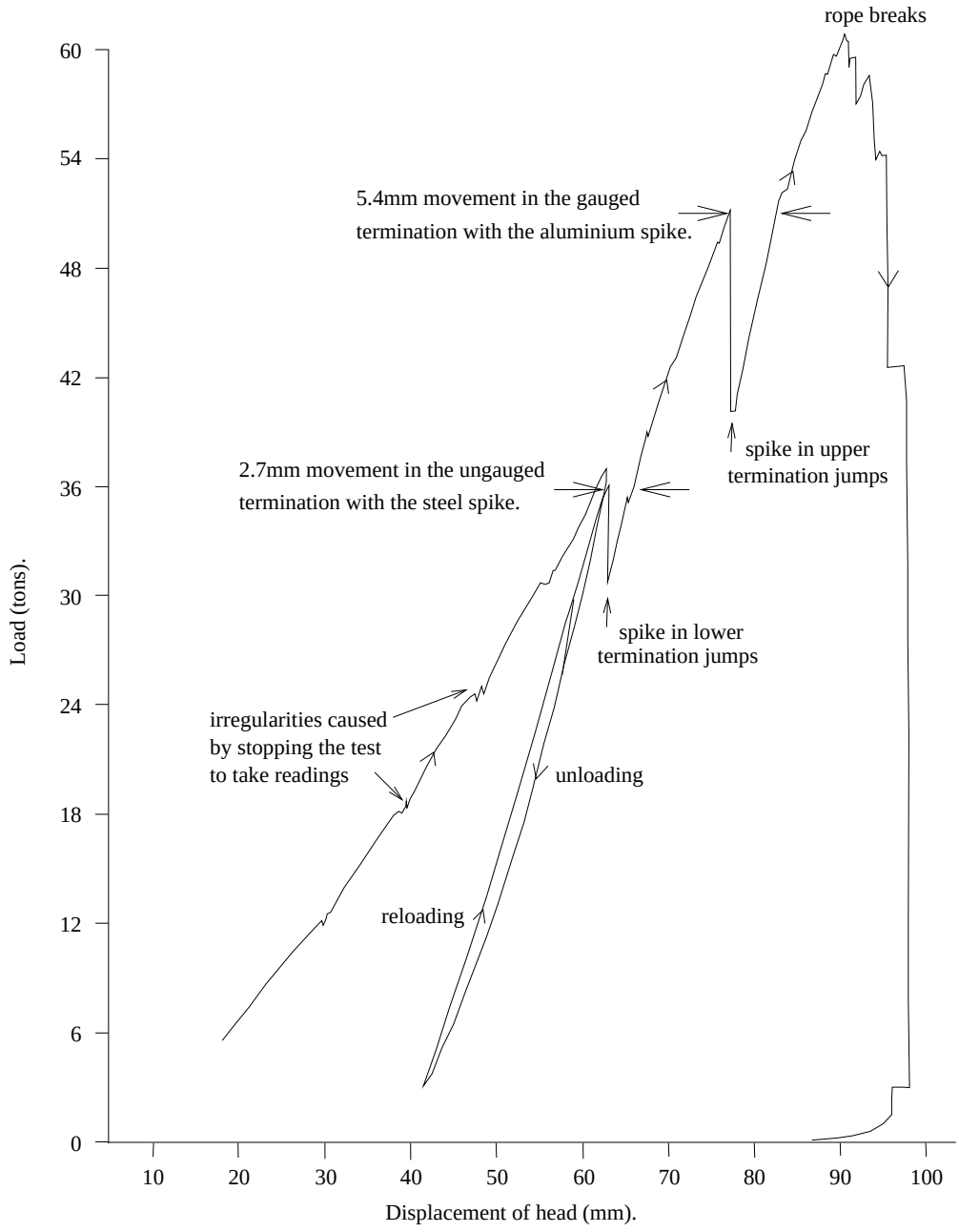

Figure 7.23: Force-displacement graph for rope test 3 recorded during test. This is similar to the first two tests (Figure 7.22). However on loading beyond the cycling portion, an event occurs in each end where the load in the rope suddenly drops; on further loading the load is regained but with an increased displacement.

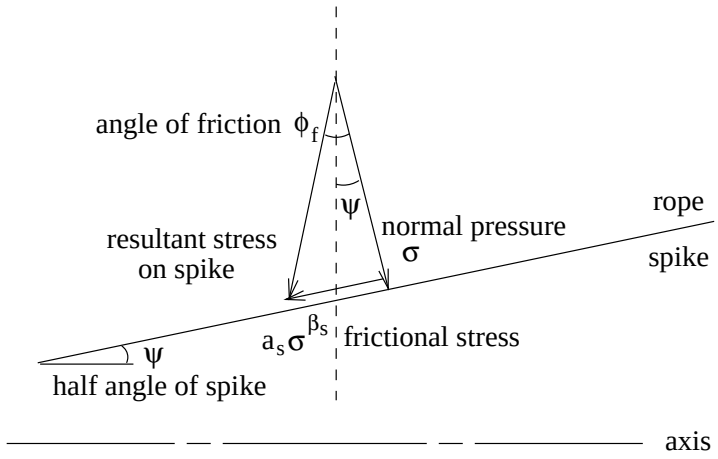

Figure 7.24: Stresses acting on the spike, showing the limiting angle of friction, ϕ_f. If ϕ_f is greater than ψ, the half angle of the spike, then friction will be able to stop the spike moving backwards. However, $\phi_f = \tan^{-1}(a_s\sigma^{1-\beta_s})$, and so reduces with increasing contact pressure.

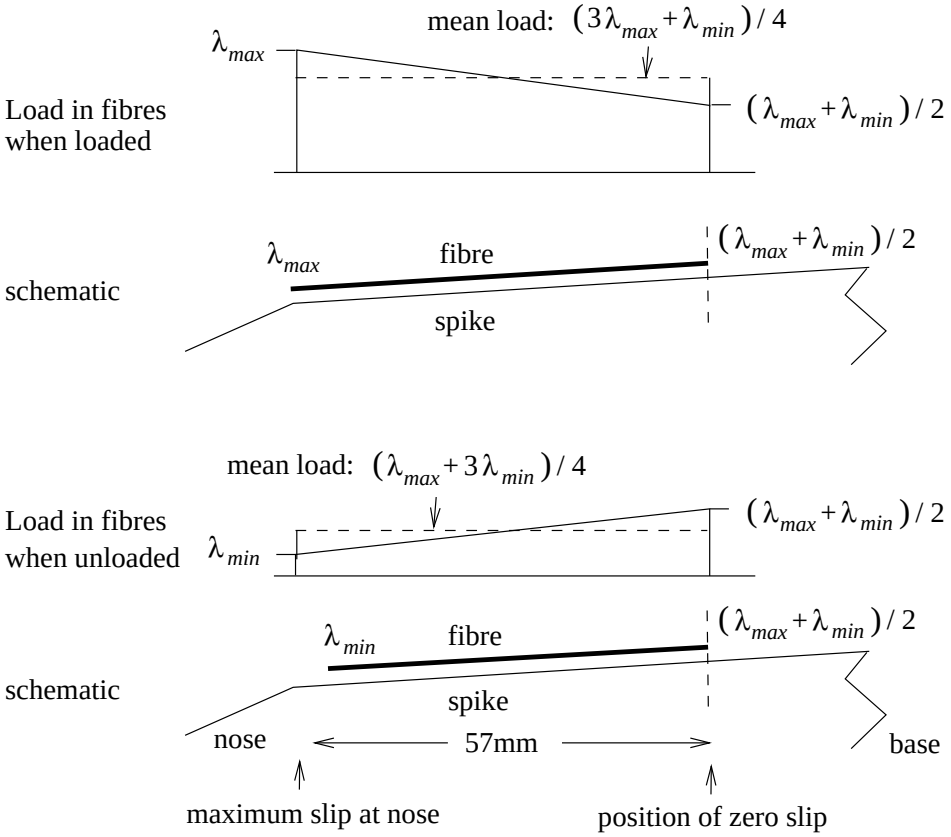

Figure 7.25: Schematic of the idealised load variation in the fibres at the limits of a cycle, between the load ratios λ_{max} and λ_{min}. At the rope end, the load cycles between λ_{max} and λ_{min}; at the position of zero slip, the load change is minimal, and approximates to $(\lambda_{max}+\lambda_{min})/2$. For a uniform rate of change in load along the spike, this gives a variation between the mean loads of $(\lambda_{max}-\lambda_{min})/2$.

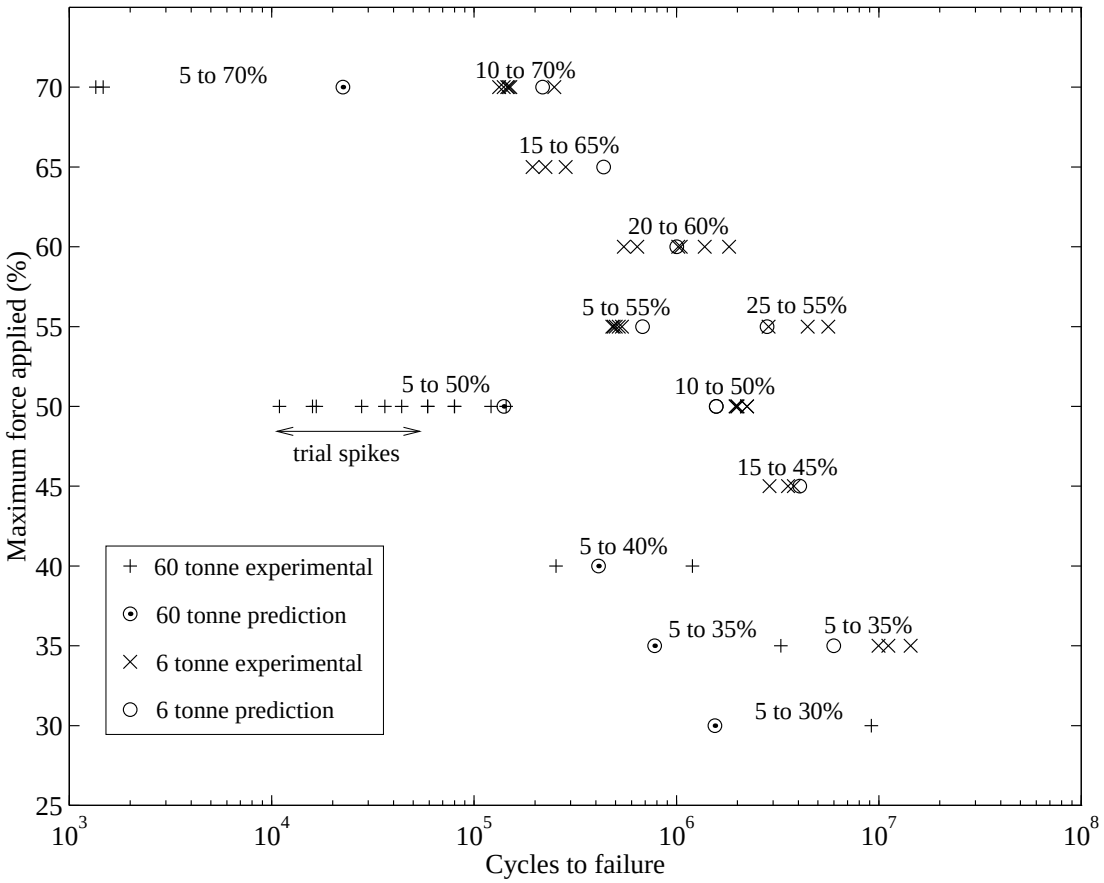

Figure 7.26: The lifetimes of 6 and 60 tonne Parafil G ropes subjected to cyclic loading. The experimental points from the literature were presented previously in Figure 2.7. The predictions are generated using Equation 7.17. There is an excellent agreement between the values predicted here and the literature for all the 6 tonne and most of the 60 tonne tests.

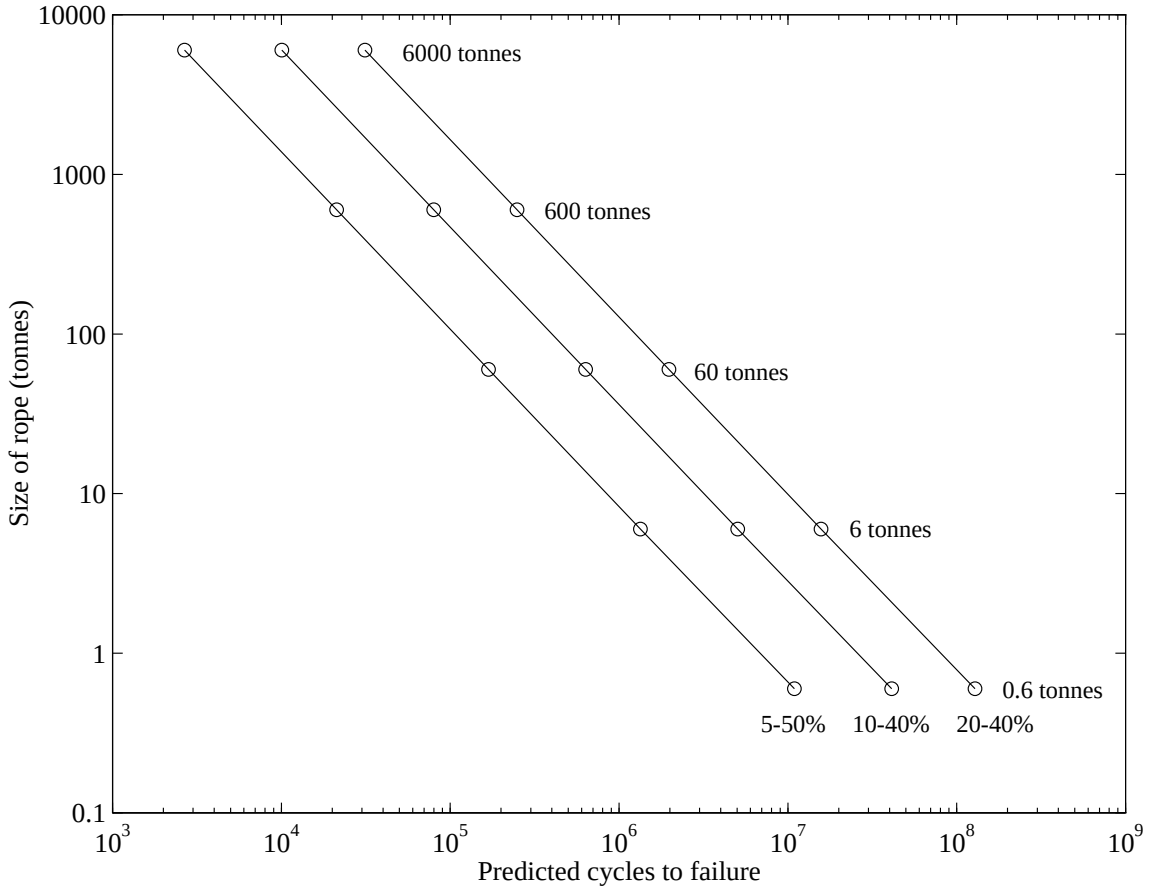

Figure 7.27: The predicted effect of size on the lifetimes of Parafil G ropes subjected to cyclic loading of λ=5 to 50%, 10 to 40% and 20 to 40%, using Equation 7.17. With an increase in cyclic range the lifetime falls for a given rope size due to an increase in the amplitude of slip. Similarly for an increase in the size of the rope for a given range the lifetime also falls due to an increase in the amplitude of slip.

Chapter 8

Discussion.

Spike-and-barrel terminations for parallel-lay ropes are much more complex than they first appear. What looks at first sight to be a simple arrangement, turns out on closer inspection to be highly complex; the functioning of which is heavily influenced by geometry, the material properties, and the frictional properties. Any alteration to any one of these factors alters the behaviour of the whole termination. Over their 25 year history, Parafil terminations have evolved into a sophisticated design which works well most of the time. To improve on their performance this study has probed inside the terminations and exposed hitherto unknown mechanisms and processes of slip and wear. This thesis shows that the finite element model can be used to predict the current behaviour of Parafil terminations. This work, which focussed on understanding behaviour, can therefore be extended to optimise the design.

This chapter contains a discussion focussed on what avenues are open to improve the termination design, both in terms of geometry and material selection. An overview of the aspects that may be improved to generate a better finite element model follows. The chapter concludes with a brief discussion of ways of further quantifying the asymmetry within the terminations and methods to reduce this.

8.1 Improvements to the termination design.

The design can be optimised in two main areas: using plastics for the spike and barrel in order to reduce the weight and improve the electro-magnetic

inertness of the termination; and increasing the lifetime for a given loading by varying the geometry, the materials, and the coatings applied to the fibres.

Once a particular set of materials has been chosen, the effects of varying the geometry and abrasion finishes can be varied quickly and simply by editing the data file for the analysis. Using the calculated severities and experimental abrasion data, the designer can predict the lifetime of the total termination. Trends can then be established which can be used to optimise the lifetime.

8.1.1 Modifications to the geometry.

The current focus in industry is in trying to refine the spike geometry. If successful, this would reduce the severities of abrasion at the nose of the spike, thus increasing the lifetime. Indeed McTernan [1986a] noticed increases in lifetime of a factor of 10 when modifying the spike for a 60 tonne rope cycled between 5% and 50% as seen in Figure 2.7.

In the current design, the contact pressure is almost uniform along the length of the spike (Section 6.2.3). However, this is not necessarily the optimal solution for maximising the lifetime of a cycled termination.

8.1.1.1 Adjusting the contact pressure.

The contact pressure may be controlled by varying the angles of the spike and barrel; such that at a certain load, the spike will bed-down to a position where the desired contact pressure distribution along the length will be achieved.

The finite element model, developed in this thesis, may be used to follow the bed-down of the spike; different spike and barrel geometries are likely to bed-down to different degrees depending on the distribution of pressure, friction, and slip, along the length during pretensioning.

The annulus that the rope occupies near the nose of the spike can be widened to reduce the contact pressure there; then, if everything else remains

constant, this would decrease the contact pressure factor in the severity of the abrasion. However this will also reduce the friction, so a longer slipping region will be needed; this will increase the amplitude factor in the equation of abrasion.

Alternatively, decreasing the annulus to increase the contact pressure and friction could reduce the length of the slipping region at the nose. This assumes that the nose of the spike takes out a certain force from the rope, from its tip to the no-slip position, regardless of the geometry. For a given spike angle, a higher friction will enable a shorter slipping region (Force $\propto$ frictional stress $\times$ length).

Using Equation 3.23, if the contact pressure and friction are increased by 10%, and the amplitude of movement is decreased by 10%; then the new cycles to failure, N_{new}, is related to the old cycles to failure, N_{old}, by the equation:

$$N_{new} = \frac{N_{old}}{1.10^{1.1}\frac{1}{1.10}^{2.8}} = 1.17N_{old} \tag{8.1}$$

Hence an increase in contact pressure of 10% can lead to an increase in lifetime of 17%, and is therefore desirable.

8.1.1.2 Adjusting the radius of spike.

Keeping the current half angle of about 3.5°, if the radius of the spike is decreased then it might be possible to decrease the overall diameter of the termination, saving much material. This would also have the benefit of increasing the thickness of rope between the spike and barrel, which would tend to increase the cyclic lifetime.

Conversely if the radius of spike is increased then the amplitude of slip may be reduced. For a constant annular area the thickness to be abraded is inversely proportional to the radius of the spike. If it is assumed that the force taken out over the nose portion of the spike is constant, then, for a given contact pressure (and friction), the length needed will be reduced due to the increased

circumference. A 10% increase in radius leads to a 10% decrease in thickness (so a 10% decrease in thickness to be abraded (from Equation 3.18)), and a 10% decrease in the slipping portion. Using Equation 3.23, this would lead to a 19% increase in lifetime as follows:

$$N_{new} = \frac{N_{old}\frac{1}{1.10}}{\frac{1}{1.10}^{2.8}} = 1.19N_{old} \tag{8.2}$$

Hence an increase in the width of the spike of 10% can lead to an increase in lifetime of 19%, and is therefore desirable.

8.1.1.3 Improved spike design.

A short fat spike will tend to have a longer lifetime under cyclic loading, than a long thin one. For an aluminium termination this design will be larger and more massive; however, if a plastic termination is employed this modification may be beneficial, as stated in Section 8.1.2.1.

8.1.2 Materials.

Replacing the aluminium spike and barrels with plastic ones will have the advantage of making Parafil rope assemblies more light-weight, corrosive-resistant and electro-magnetically inert.

8.1.2.1 Feasibility of non-metallic terminations.

The current 60 tonne aluminium spikes are easily capable of withstanding the calculated tensile load of 80kN; but if a plastic alternative is used, then not only its yield stress, but also its creep properties would have to be carefully assessed (Section 8.2.5). If the spike crept axially under load it would become longer and thinner, and the contact pressure would drop. It would then be liable to jump.

Using a shorter fatter spike as suggested in Section 8.1.1.3 to reduce the

severity of abrasion, would also alleviate these problems.

When moving from a strong material, such as aluminium, to a weaker one, such as epoxy, care must be taken that the yield stresses are not exceeded. To allow for this, the amount of material would need to be increased in line with the stresses indicated by the analysis. The real forte of the finite element model over the current build-it-and-see approach comes when the barrel is to be replaced by a reinforced plastic one. Using the finite element model it is simply a matter of performing several analyses with different reinforcing lay-ups to home in on the optimum design. Each distribution of reinforcement along the length of the barrel will feed-back into the mechanics of the termination, thus affecting the design.

If the elasticity of the barrel is changed then its behaviour under load will also change and it will assume a different geometry from before. The finite element model will automatically take into account the changing radius and changing surface angle, factors that would be very difficult to include in a simple analytical model.

8.1.2.2 Reduction in weight.

When the optimum contact geometries have been decided, excess material can be pared away from the outside of the barrel. For a fat spike it may be possible to have a hollow core as well, to save on materials and reduce weight.

8.1.2.3 Improvement of lifetimes.

The amplitude of slip is directly related to the length of yarn that rubs over the spike from the salient fixed point in the middle of the spike. The rope end, by definition, must cycle between λ_{max} and λ_{min}; the 'fixed point' on the rope experiences the same strain change as the adjacent point on the

spike, or else it would be slipping. The strain of the rope is determined by its material properties, and so there are two ways to reduce this slip: the first is to move this fixed point towards the nose of the spike. To do this the load must be taken out of the rope at a greater rate which means more friction is required. So a higher coefficient of friction between the rope and the termination might lead to an increase in lifetime, as was mentioned in Section 8.1.1.1. To increase the coefficient of friction it would be necessary to coat the nose of the spike with another material, or use a different material for the whole spike.

The second method of reducing the relative slip is to use a more flexible nose geometry for the spike, such that it deforms more and moves with the rope. The problem with this is that in moving with the rope, it does not take the load out of the rope as rapidly and so a longer portion would slip. It would also be necessary to retain the radial and hoop stiffnesses of the spike to maintain the contact pressure on the rope.

The yarns used in the tests referred to in Chapter 3 are from spools used to make Parafil ropes and so carry the finishes present in actual ropes. For optimisation of the termination lifetimes, these finishes can be varied to see their effect on the friction and the abrasion. These in turn can be coupled with the finite element model, to quantify their effect on the termination. The ideal finish would give a high frictional stress, whilst having a low abrasion.

Other researchers have considered coating the nose of the spike with PTFE or making the spike from Delrin [Mulcahy, 1996], both polymeric materials with a low coefficient of friction, with the expectation that the abrasion will be reduced. However there will still have to be a portion of rope that is stretched during the cycle to pass the load out into the spike, and so it is likely that higher magnitudes of slip and hence abrasion will occur elsewhere with these designs.

The transverse yield stress of Kevlar is lower than that of aluminium (Section 3.5), therefore Kevlar is the softer material and will suffer most of the

abrasion. If an alternative softer material is used for the spike and/or barrel, then these will abrade in preference to the fibres, and the analysis of Chapter 7 will not apply. If the termination itself is abraded, then its geometry will change; an analysis of the new geometry would be needed to see if it is capable of maintaining the maximum load. This change in geometry, accompanied by a deposition of wear material along the length of the spike, may lead to the spike jumping. It may also be possible that the friction characteristics of a softer material are such that the termination may not be able to hold the fibres at all. However, the major drawback to using a softer spike is that the only reason for the Kevlar not being abraded is that the spike is abraded first; this would lead to the overall abrasion rate being increased.

8.1.3 Prevention of anomalous spike movement.

8.1.3.1 Redesign.

If the barrel is made with a greater elasticity, then it will act like a spring, applying a uniform pressure on the rope regardless of how much the rope creeps transversely under load. With the current aluminium barrel, if the radial strain in the rope increases due to viscoelasticity, then the contact pressure will drop off due to the stiffness of the barrel. A more flexible barrel will retain the contact pressure.

8.1.3.2 Loading the spike.

It is possible to apply an external restraint to the spike to keep it pushed into the barrel. A simple lock, applied between the barrel and the spike, will not prevent the contact stress from changing. If, however, a large excess force is applied to the base of the spike by means of a compressed spring attached inside the barrel; then the contact pressure may be retained. A suitable spring may maintain a uniform force, even if the spike beds down further. The effects of adding a spring may be studied using the finite element model:

the spike by itself is no longer in axial equilibrium, and this will produce radical changes in the way the load is transferred out of the rope.

8.2 Improvements to the finite element model.

8.2.1 Extend range.

To study the effect of changing the materials and frictional properties, it is simply a matter of extending the range of data gathered for Chapters 3 and 4. For example, if it is proposed to replace the aluminium barrel with a fibre-reinforced polyester one for a Parafil F rope; then Kevlar 29-on-polyester friction and abrasion tests will need to be performed, to gather the yarn-on-solid data, and pads of Kevlar 29 will need to be squashed, to gather the anisotropic material data.

8.2.1.1 Yield of aluminium.

The model shows that the spike and barrel experience a stress close to their yield stress at maximum load, and the strain gauged 60 tonne termination also shows plastic deformation (Chapter 7). So a yield stress should be included. The onset of yield does not signify that the termination will fail; this will only occur once the yield has grown across a large region, and use of this can be made in paring down the design. Mulcahy [1996] reported yield in barrels by varying the spike design; when the new design was maintained subsequent assemblies operated elastically. The yield had caused a locked-in residual stress in the barrel, but not failure.

8.2.2 Range of friction measurements.

The maximum mean contact pressure applied here for the yarn-on-solid friction was only 16N/mm^2, compared with about 70N/mm^2 in an actual termination during the cycling phase. More tests at higher pressures should be

performed. For the tests here, the yarns were secured at either end by means of a knot, but it has subsequently been found that a more efficient method is to clamp the ends between two roughened aluminium plates, which are connected by six small bolts either side of the yarn. Using the clamps, the full yield stress of the yarn is attainable compared with only 60% from a knot. More tests should be performed at these higher stresses with discs of smaller radii (say 5mm, 10mm, 15mm).

8.2.3 Model yarn-on-yarn friction.

For a detailed analysis of a partly abraded large termination, it will be necessary to model the intra-rope friction. For this, yarn-on-yarn frictional data will be needed.

There are many ways of measuring inter-yarn friction: for example one yarn can be pulled from a bundle of yarns compressed under a known load [Taylor, 1955], or one surface of aligned yarns may be pulled across another [Speakman and Stott, 1931]. However for these two methods the surrounding yarns become abraded and so need regular replacing; in addition they cannot be cycled to measure abrasion. So the method developed by Lindberg and Gralén [1948] is preferable. Lindberg measured the tensions necessary to pull one fibre over another fibre when they had been intertwined. They showed that if Amontons' law and a double helix configuration are assumed then the following equation can be derived for slip to occur:

$$\mu = \frac{\ln T_{out}/T_{in}}{\pi\, n\, \beta} \tag{8.3}$$

where T_{out} and T_{in} are the tensions leaving and entering the intertwined region, μ is Amontons' coefficient of friction, and β is the angle between the yarns. Goksoy [1986] generalised this approach to yarns and wrapped the yarn back on itself by means of a pulley such that 'both' yarns are automatically replaced. Wu [1990] has used a similar arrangement to Goksoy to measure the friction between small braided ropes. Modelling the contact

region of intertwined yarns is very complicated, and so use of Amontons' friction rather than a modified Howell's friction should be sufficient.

8.2.4 Yarn-on-yarn abrasion.

A detailed analysis of yarn-on-yarn abrasion was not performed here. The rope yarns move as one body within the termination; the initial slip between individual yarns is negligible compared with the slip relative to the spike and barrel. Thus, it is reasoned here that the yarn-on-solid abrasion is the dominant factor in determining the overall lifetime. However yarn-on-yarn abrasion may come into play once some yarns have failed by abrasion over the spike and barrel. These yarns may remain in place, effectively shielding the surviving yarns. Thus yarn-on-yarn abrasion would become a significant failure mechanism. For most terminations it reasoned here that once yarns have broken, they will recoil away from the contact zone due to their elasticity; they are then ratchetted further away as the surviving fibres cycle back and forth. This would continuously bring fresh yarns into contact with the spike and barrel.

It is difficult to ascertain the severity of the yarn-on-yarn abrasion for the purposes of replicating it in the laboratory, because the failed yarns that may shield the remaining rope will also move back and forth, so the amplitude is uncertain. As more yarns fail, the stress in the remaining yarns will also rise as the load is carried by fewer yarns; this will lead to an increase in strain and the amplitudes of slip will change as abrasion continues.

Yarn-on-yarn abrasion experiments may be performed in a similar manner to the yarn-on-yarn friction measurements, by cycling an intertwined yarn against itself.

8.2.5 Hysteresis.

The Abaqus material model was only composed of linear-elastic portions; hysteresis was not included for simplicity. The axial and transverse stress-strain curves of Kevlar do, however, exhibit hysteresis; the strain on loading and unloading is different — energy is dissipated whilst cycling the load. If it is necessary to model this behaviour then it can be implemented in the Abaqus `UMAT` subroutine, if the relevant experiments are performed to obtain material data.

Axial hysteresis has been extensively studied [Amaniampong, 1992] so data is readily available should this be needed. Transverse hysteresis has not been studied; however, there is no unloading in the transverse direction, so any hysteresis in the loading is taken into account by the discretisation of the transverse loading curves performed here.

8.2.6 Viscoelasticity.

Synthetic fibres are viscoelastic [Chambers, 1986; Guimarães, 1988], so the 'elastic moduli' are time dependent.

For the finite element model there was assumed to be no viscoelasticity in the elastic compliances used. A time dependent term can be inserted into the compliances, based on experimental measurements taken after appropriate time intervals. For the time scales used for cyclic tests on large Parafil ropes, viscoelastic effects may well be important.

8.2.6.1 Transverse creep.

In Section 4.4.3.1 it was noted that when a pad of Kevlar fibres was loaded to 125N/mm^2 in 30 minutes, and the displacement maintained, a further 5 minutes saw the transverse compression load drop by 5%. When the pad of fibres was transversely loaded at 0.01mm/min, the runs took up to 10 hours, with

no noticeable change being observed when the full load of 125N/mm^2 was left applied for 24 hours. This loading rate was used for the determination of the transverse moduli. However, the 60 tonne rope tests presented in Chapter 7 were transversely loaded between these two rates, and so a viscoelastic effect is a possible explanation for the anomalous spike movement.

8.2.6.2 Axial creep.

Once the termination has been preloaded, there remains a locked-in axial stress in the middle of the rope of about 250N/mm^2 (Figure 6.32). Over time this stress will reduce thus affecting the functioning of the termination.

8.2.7 Discretisation of the transverse loading curve.

A variation in the transverse modulus in the finite element model along the length of the rope will be needed if the termination is designed to have a non-uniform contact pressure along its length.

It is possible to apply different moduli to different elements in the rope using the Abaqus subroutine `UMAT`, but care must be taken to avoid too much discontinuity between neighbouring elements.

8.2.7.1 Stress-strain at the nose.

The stresses and strains in the rope were shown in Figure 6.31. Over the rear half of the spike the rope behaves as expected; but near the nose of the spike, the rope is further compressed on unloading from the 60% preload. This rise is due to the axial contraction of the rope. Near the middle of the spike the rope remains fixed (Section 6.2.1.2); so as the rope contracts axially on unloading, more material is drawn into the contact zone over the nose, thereby increasing the radial stress and the contact stress (Figure 6.10). Thus, a first-loading modulus would have been more appropriate than the

unloading modulus.

8.2.8 Analysis of a partly abraded termination.

Whilst the rope is being abraded two factors come into effect. The severity of the contact stress may decrease as there are fewer yarns between the spike and the barrel; this is due to the broken yarns moving away into the main body of the rope. Conversely the severity of the amplitude will increase as the yarns that remain are exposed to a greater cyclic stress; at failure they will experience the yield stress.

No true slip occurs between the three layers of rope. This is partly due to γ_{crit} being set to 0.3mm, rather than 0.06mm as for the Kevlar-on-aluminium contact. The maximum elastic slip, however, is only 0.08mm; so little true slip would be occurring anyway. A higher value was used to speed up the solution as the layer-on-layer contact was not deemed to be as important as the rope-on-solid contact. Reducing the possibility of switching between stick and slip friction, within the rope, keeps the number of iterations down. For future analyses γ_{crit} can be reduced, especially if an analysis of a partially abraded termination is required.

8.3 Asymmetry.

Asymmetry is observed in the strain gauge readings of the termination in Chapter 7. It is also possible that the ropes tested under high cyclic loading, reported in the literature, fail sooner than predicted due to sensitivities in the assembly. If the spike is not central then abrasion will occur on one side more severely than expected, which will upset the geometry further leading to a rapid failure.

8.3.1 Future tests.

To study this asymmetry, tests should be performed with extra gauges around the barrel, at additional locations. These tests should also be performed with a regular spike, as the holes in the spike used here may play a small part in the anomalous strains and spike movement.

One termination should be restrained via a universal coupling; as the two flat faces used here do not allow for any rotational misalignment.

A longer rope would also alleviate any misalignment that is highlighted by the short ropes used here (less than 2m).

8.3.2 Mechanical assembly.

The terminations here were assembled with extreme attention to detail, as mentioned in Appendix D. Even with this care, it has not been possible to attain a uniform distribution of fibres around the spike. A remedy for this is to design a machine that can terminate ropes automatically. Indeed, rigs are already used in the assembly of larger rope terminations; to hold bundles of yarns during fabrication. A similar device could be totally mechanised for use on smaller ropes. It would be required to remove the sheath, secure the yarns whilst the spike is inserted into the exact centre of the rope, and then assemble the termination. Everything would be lined up perfectly, barrel, rope and spike; and known forces would be applied to the rope sheath and the spike. Use of this machine will then enable the manufacturer to give an increased guarantee for the terminations.

8.4 Summary.

All these ideas show that there is a large scope for experimentation to prolong the life of Parafil ropes. It should be possible to test hypotheses far more rapidly using the finite element model developed here, and with a greater

insight into what effect each modification has on the whole, than a pure experiment-only programme would be able to do.

The first hypothesis that should be tested from the indications of this work is to develop a short fat fibre-reinforced-plastic spike-and-barrel assembled by machine.

Chapter 9

Conclusions and recommendations.

In addition to being able to carry 100% of the desired load without any anomalous movement, a termination should be able to withstand a cyclic loading for an acceptable number of cycles. The objective of this thesis has been to gain an understanding of the factors involved in the functioning of a Parafil termination, and the role each factor plays.

The major factors that have been identified in this thesis are:

- Kevlar-on-aluminium friction
  - modified Howell's equation: $\tau = a\sigma^{\beta}$
- Kevlar-on-aluminium abrasion
  - amplitude of slip
  - contact pressure
  - thickness to be abraded
- transverse stress-strain behaviour of Kevlar
  - first-loading
  - unloading-reloading

Simple analyses of Parafil terminations are flawed by their simplifying assumptions. As the functioning of the termination is so dependent on all the factors mentioned above, any rounding-error applied to one of these factors will grossly affect the overall result. Therefore the only way to get an accurate analysis is to use a finite element model, with the requirement that both non-linear friction and non-linear material properties are included.

The use of a modified Howell's equation for friction $\tau = a\sigma^{\beta}$ as suggested here, can be proposed as a valid means of modelling the friction between polymeric materials. This re-expression of Howell's equation, in terms of stresses rather than a force per unit length of yarn, enables it to be used in the finite element analysis. The subroutine developed to follow the stick-slip non-linear friction is also an integral part of the analysis.

The modelling of the transverse compression of Kevlar fibres, en masse, is necessary in order to predict the behaviour of such a non-linear material. It is seen that there are two distinct ranges of transverse modulus; one set for first loading, which applies to the initial loading of the Parafil rope, and another set with a much higher modulus for the unloading-reloading, which applies to the cyclic loading of the rope. The moduli increase as the specimen is loaded due to the void ratio decreasing. It is possible to match these moduli by discretising the loading curves for insertion into the finite element analysis described in Chapter 5.

It can be deduced from the fact that an application of Lamé's equations to the strain gauge readings gives the same contact pressure within the termination as the finite element model, that the compression of the Kevlar is accurately predicted. Therefore the discretisation of the transverse loading curve into linear-elastic portions is justified.

Actual spike bed-down displacements are very accurately predicted by the finite element model. The Abaqus values deviate by less than 1mm from the measured values once the analysis has begun. The gradient of the Abaqus bed-down curve changes as the transverse moduli of the rope are altered;

the gradients are tangents to the measured values, although they are derived independently.

As presented in Chapters 3 and 4; frictional and material data were gathered for Kevlar 49-on-aluminium, for use in the finite element model. Due to the closeness of the results from the model and from the strain gauging of an actual 60 tonne Parafil G rope, discussed in Chapter 7, it is reasonable to assume that experimental data gathered here correlates with the properties inside a termination. It is also reasonable to assume that the finite element model itself is a valid analysis tool for predicting future alterations to the termination.

The finite element model can be used to give the contact stresses and magnitudes of slip in the areas of the termination where slip occurs. When these are coupled with the abrasion results of Kevlar 49 on aluminium capstans presented in Chapter 3, Equation 7.17 can be derived. This equation accurately predicts the lifetimes of actual 6 tonne terminations under cyclic loadings, given the size of rope, and maximum and minimum load limits. The lifetimes under cyclic loading reduce with increasing size of rope, and with increasing load range, due to the increased amplitude of slip. The lifetimes also reduce with increasing maximum load, for a given load range, due to the increasing contact pressure within the termination. These effects are shown both by data in the literature, and by Equation 7.17.

There is an asymmetric distribution of strains measured around the spike and barrel, which can not be predicted with the axisymmetric analysis performed here. This asymmetry is likely to be due to an irregular distribution of fibres around the spike; a bending strain of $1000\mu\epsilon$ is generated on the surface of the spike by a 4% offset of the rope.

The finite element model does not predict the anomalous spike movements. Movements of the spike, both into and out of the barrel are observed when the rope is loaded further after a cycling regime has been imposed. A study of the angle of friction shows that the half angle of the spike, 3.5^{o}, lies below

the limiting angle of 6.8°. If the spike subtends an angle greater than 6.8° then the contact pressure pushing the spike backwards would outweigh the friction holding it in place, and the termination would not function. The anomalous movement of the spike is most likely to be due to the viscoelastic properties of Kevlar; over time the contact stress in the termination will fall, thus reducing the limiting friction — so rope-spike and rope-barrel slip may both occur. Over a long period of time the axial stress in the rope will also reduce, affecting the locked in stresses.

This thesis shows that a scientific approach can be applied to the art of parallel-lay spike-and-barrel design to gain an insight into the mechanics within the termination. This analysis can now be used as a basis for future design modifications.

Appendix A

Factors affecting the gauge readings.

A.1 Contact pressure on gauges.

Any change caused by the pressure should affect all three cross gauges equally, because they all have the same geometry; only their orientations are different. Two simple things may happen, the readings are offset by the same amount, or they are multiplied by the same factor. An offset will not rotate the Mohr's circle of strain, and hence ϕ will remain unaffected. A multiplying factor will cause some rotation, but cannot reduce ϕ to zero. (The Mohr's circle is discussed in Appendix C.)

A.2 Elasticity of epoxy.

Aluminium alloy has a modulus, E, of 71000N/mm^2, and a yield stress, σ_y, of approximately 630N/mm^2; therefore the strain at first yield will be 8800$\mu\epsilon$. For the epoxy resin used to fill the strain gauge pits; E $\approx$ 3000N/mm^2 and $\sigma_y \approx$ 70N/mm^2; therefore the first yield will occur at a strain of 23000$\mu\epsilon$. Therefore the epoxy is still elastic when the aluminium reaches yield; so there should be no problems of the epoxy debonding prematurely from the aluminium.

Appendix B

Calculation of principal strains.

Figure B.1 shows the Mohr's circle of strain for a 45° strain gauge rosette. The individual gauges are labelled a, b and c; gauges a and c are at right angles to each other and are bisected by gauge b. The principal strains are labelled 1 and 2; they are offset by an angle ϕ from gauges a and c as shown on the figure. Let the strains measured by the gauges a, b and c, be ϵ_a, ϵ_b and ϵ_c. Let the principal strains be ϵ_1 and ϵ_2. The maximum shear strain is γ. It can be shown [Case and Chilver, 1971] that:

$$\phi = \frac{1}{2}\tan^{-1}\left(\frac{2\epsilon_b - \epsilon_a - \epsilon_c}{\epsilon_c - \epsilon_a}\right) \tag{B.1}$$

$$\epsilon_1 = \frac{(\epsilon_a + \epsilon_c) + \sqrt{(\epsilon_a + \epsilon_c)^2 - 4(\epsilon_a\epsilon_c - \frac{1}{4}(2\epsilon_b - \epsilon_a - \epsilon_c)^2)}}{2} \tag{B.2}$$

$$\epsilon_2 = \frac{(\epsilon_a + \epsilon_c) - \sqrt{(\epsilon_a + \epsilon_c)^2 - 4(\epsilon_a\epsilon_c - \frac{1}{4}(2\epsilon_b - \epsilon_a - \epsilon_c)^2)}}{2} \tag{B.3}$$

$$\gamma = \epsilon_1 - \epsilon_2 \tag{B.4}$$

Mohr's circle of strain.

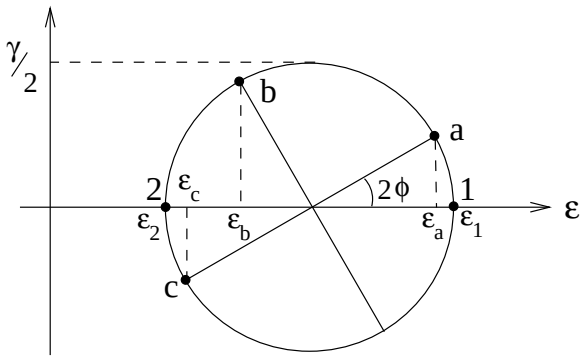

Strain gauge positions.

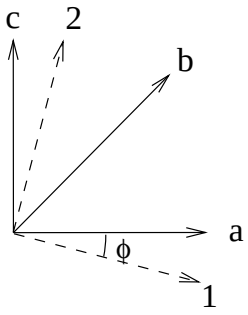

a, b, c: strain gauge rosette
1, 2: principal directions

Figure B.1: Mohr's circle of strain for a 45° strain gauge rosette.

Appendix C

Strains due to bending.

To determine whether it is possible for a strain of $1000\mu\epsilon$ to be generated on the surface of the spike by an asymmetric bending alone, a simple analysis can be performed. For this, the spike is assumed to be a uniform cylinder of radius, r, of length, l, with distributed loads, $W/2$, at the ends and the middle as shown in Figure C.1. The central deflection relative to the two ends, δ, can be shown to be:

$$\delta = \frac{0.011Wl^3}{EI} \tag{C.1}$$

where E is the Young's Modulus, and I is the second moment of area of the cyclinder ($I = \pi r^4/4$).

The central bending moment is:

$$M = \frac{Wl}{8} \tag{C.2}$$

The stress on the surface of the cylinder is, $\sigma = Mr/I$, and the strain is $\epsilon = \sigma/E$ (ignoring the hoop stress). Putting all these together gives:

$$\epsilon = \frac{8.2\delta r}{l^2} \tag{C.3}$$

Assuming a length of 150mm and a radius of 20mm, then a strain of $1000\mu\epsilon$ or 0.001 is associated with a central displacement of **0.14mm** which is definitely possible. Compare this with the thickness of rope near the nose of the spike which is 3.2mm (an annulus of 320mm^2 at a mean radius of 16mm); hence this displacement only requires **4%** ($100\times0.14/3.2$) of the rope to be offset.

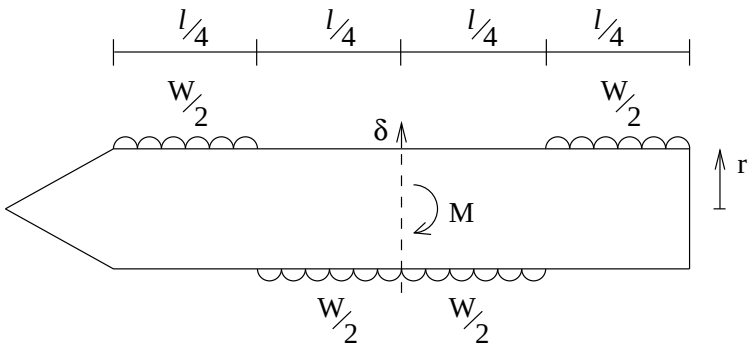

Figure C.1: Simple asymmetric loading applied to spike.

Therefore it is possible that the deviations of strain between each test are due to an asymmetric distribution of rope within the termination, causing bending and higher-order deformations in the spike and barrel.

Appendix D

Termination assembly.

The terminations here were assembled with the utmost care and attention, to ensure that as little asymmetry as possible was present. Three hours were spent untangling the yarns for each termination before assembly. Rearrangement is necessary because the twist in the individual yarns causes them to intertwine with their neighbours when the restraining sheath is removed.

After separating the yarns, they were evenly distributed around the circumference of the barrel. This was aided by placing a red dot in the centre of the rope before the sheath was removed; the fibres with red ends are then known to have come from the centre of the rope.

The spike was guided home as the rope was drawn through the barrel. For this the barrel was supported vertically and the sheath of the rope pulled down by hand. For the final assembly, the spike was tapped with a hammer while pulling the rope.

Much care was taken to ensure an even thickness and distribution of Kevlar around the spike; such attention to detail is not sought in terminations constructed in the industry.

References.

ABAQUS/ANSWERS (1993) "Spring-Summer." *Hibbit, Karlsson & Sorensen, Inc., 1080 Main Street, Pawtucket, RI 02860-4847.*

AMANIAMPONG, G. (1992) "Variability and Viscoelasticity of Parallel-lay Ropes." *Ph.D. Thesis, CUED.*

AMINIAN, P.K. AND WHITE, J.K. (1988) "A review of the properties of Type F (Kevlar 29) Parafil cables with reference to the design of cable structures." *Symposium on engineering applications of Parafil ropes, London.*

ASHBY, M.F. AND JONES, D.R.H. (1980) "Engineering Materials 1." *Pergamon Press.*

BAXTER, C. (1988) "Uses of Parafil ropes for mooring offshore platforms." *Symposium on engineering applications of Parafil ropes, London.*

BEERS, D.E. AND RAMIREZ, J.E. (1990) "Vectran fiber for ropes and cables." *Marine Technology Society '90 Proceedings, Washington.*

BOWDEN, F.P. AND TABOR, D. (1950) "The friction and lubrication of solids." *Clarendon Press, Oxford.*

BOWDEN, F.P. AND TABOR, D. (1974) "Friction: an introduction to tribology." *Heinemann, London.*

BRADBURY, E. AND REICHER, A. (1952) "High friction of extracted continuous filament yarn on clean glass surfaces." *Journal of the Textile Institute, Vol.43 No.7 T350-353*

BURGOYNE, C.J. (1988) "Structural applications of type G Parafil." *Symposium on engineering applications of Parafil ropes, London.*

BURGOYNE, C.J., HOBBS, R.E. AND STRZEMIECKI, J. (1989) "Tension bending and sheave bending fatigue of parallel lay ropes." *Eighth Interna-*

tional Congress on Offshore Mechanics and Arctic Engineering, The Hague. pp. 691-698

BURGOYNE,C.J., GUIMARÃES, G.B. AND CHAMBERS, J.J. (1991) "Tests on beams prestressed with unbonded polyaramid tendons." *Cambridge University, Department of Engineering, technical report no. CUED/D - Struct TR.132,1991.*

CASE, J. AND CHILVER, A.H. (1971) "Strength of Materials and Structures." *Edward Arnold.*

CHAMBERS, J.J. (1986) "Parallel lay aramid ropes for use as tendons in prestressed concrete." *Ph.D. Thesis, University of London.*

CRAWFORD, H. AND MCTERNAN, C.M. (1988) "'Fatigue' properties of Parafil." *Symposium on engineering applications of Parafil ropes, London.*

DE WITTE, A. (1990) "The design and construction of an exhibition glasshouse in the Netherlands." *Presented at the Fourth Rail Bridge Centenary Conference, August, Heriot-Watt University, Edinburgh. (Ed. B.Topping) (Not in Proceedings.)*

DOBB, M.G. AND ROBSON, R.M. (1990) "Structural characteristics of aramid fibre variants." *Journal of Material Science, 25, pp. 459-464.*

DRISCOLL, A.H. (1990) "A decade of synthetic fibres in the deep ocean." *Marine Technology Society '90 Proceedings, Washington.*

DU PONT (1976) "Characteristics and uses of Kevlar 29 aramid." *E.I. Du Pont de Nemours and Co. Inc., Wilmington, Bulletin No. 375.*

DU PONT (1988) "Kevlar para-aramid; database for fibre optic and other cables." *E.I. Du Pont de Nemours and Co. Inc., Wilmington.*

FLORY, J.F., PARSEY, M.R. AND BANFIELD, S.J. (1990) "Factors affecting life of synthetic fiber ropes in marine service." *Marine Technology Society '90 Proceedings, Washington.*

GARRITY, S.W. AND GARWOOD, T.G. (1990) "The test performance of a full scale prestressed brickwork bridge abutment." *Developments in Structural Engineering, E.&F.N.Spon, Chapmann and Hall, London.*

GOKSOY, M. (1986) "A study of yarn-on-yarn abrasion." *PhD. Thesis, University of Manchester.*

GUIMARÃES, G.B. AND BURGOYNE C.B. (1996) "Stress-rupture data for aramid fibres." *Advanced Composite Materials in Bridges and Structures. M.M. El-Badry, Editor; Canadian Society for Civil Engineering, Montreal, Quebec.*

GUIMARÃES, G.B. (1988) "Parallel-lay aramid ropes for use in structural engineering." *PhD. Thesis, University of London.*

HADLEY, D.W., PINNOCK, P.R. AND WARD, I.M. (1969) "Anisotropy in oriented fibres from synthetic polymers." *Journal of Material Science, 4, pp. 152-165.*

HAJI-DEHABADI, M.R. AND WHITE, J.K. (1988) "Use of parallel cable as a ground anchor tendon." *Symposium on engineering applications of Parafil ropes, London.*

HANAOR, A. (1990) "Design analysis and response of double layer tensegrity grids." *Developments in Structural Engineering, E.&F.N.Spon, Chapmann and Hall, London.*

HEARLE, J.W.S. (1967) "Fatigue in fibres and plastics (a review)." *Journal of Material Science, 2, pp. 474-488*

HEARLE, J.W.S., GROSBERG, P. AND BACKER (1967) "Structural mechanics of fibres, yarns, and fabrics Volume 1." *John Wiley and Sons, New York.*

HEARMAN, R.F.S. (1956) *Advanced Physics, 5, p. 323.*

HOWELL, H.G. (1953) "The general case of friction of a string round a cylinder." *Journal of the Textile Institute, Vol. 44 No. 8/9*

HOWELL, H.G. AND MAZUR, J. (1953) "Amonton's law and fibre friction." *Journal of the Textile Institute, Vol. 44 No. 2*

KALANTAR, J. AND DRZAL, L.T. (1990) "The bonding mechanism of aramid fibres to epoxy matrices." *Journal of Material Science, 25, pp. 4186-4193*

KAWABATA, S., SERA, M., KOTANI, T., KATSUMA, K., NIWA, M. AND XIAOXIN, C. (1993) "Anisotropic Mechanical Properties of Advanced High Performance Fibers Obtained by a Single Fiber Testing System." 9th *International Conference on Composite Materials, Spain.*

KAWABATA, S. AND SERA, M. (1993) "Torsional Fatigue of Aramid Fibers." *Proceedings International Conference on Advanced Composites, Wollongong University, Australia.*

KENNEY, M.C., MANDELL, J.F AND MCGARRY, F.J. (1985) "Fatigue behaviour of synthetic fibres, yarns, and ropes." *Journal of Material Science, 20, pp. 2045-2059*

KINGSTON, D. (1988) "Development of parallel fibre tensile members." *Symposium on engineering applications of Parafil ropes, London.*

KINGSTON, D. AND MATTRASS, F. (1973) "Patent Specification 1341013; Rope Fittings" *The Patent Office, London.*

KRAGELSKY, I.V., DOBYCHIN,M.N. AND KOMBALOV,V.S. (1982) "Friction and wear, calculation methods." *Pergamon Press, Oxford.*

LINCOLN, B. (1952) "Frictional and elastic properties of high polymeric materials." *British Journal of Applied Physics, Vol. 3 Aug.*

LINDBERG, J. AND GRALÉN, N. (1948) "The dynamic friction between cellulose acetate yarn and a cylindrical metal surface." *Textile Research Journal, Vol. 18 p. 287.*

LINEAR COMPOSITES LIMITED. (1977) "Parafil rope; technical notes." *Linear Composites Limited, Vale Mills, Oakworth, W.Yorkshire.*

LU, T.J. (1996) "Continuum Mechanics Lecture Notes." *Cambridge University Engineering Department.*

LYNE, D.G. (1955) "The dynamic friction between cellulose acetate yarn and a cylindrical metal surface." *Journal of the Textile Institute, Vol. 46 No. 1*

MCTERNAN, L.M. (1986) *Private correspondence with D. Kingston, Linear Composites Ltd.*

MCTERNAN, L.M. (1986a) "Second Interim Report on Testing of 60 tonne Parafil Type G (Kevlar 49) Rope and Terminations." *National Engineering Laboratory.*

MCTERNAN, L.M. (1992) "Comparative Tests on 6 tonne Type G Parafil Cables and Terminations." *National Engineering Laboratory — private correspondence with D. Kingston, Linear Composites Ltd.*

MEREDITH, R. AND HEARLE, J.W.S. (1959) "Physical methods of investigating textiles." *Textile Book Publishers, New York.*

MULCAHY, P.T.A. (1996) "Terminations of Parallel-Lay ropes - analysis and testing." *Fourth Year Project, Cambridge University Engineering Department.*

NAAMAN, A.E. (1982) " Prestressed Concrete Analysis and Design." *McGraw-Hill.*

ODEN, J.T. AND PIRES, E.B. (1983) "Nonlocal and Nonlinear Friction Laws and Variational Principals for Contact Problems in Elasticity." *Journal of Applied Mechanics, Vol. 50, pp. 67-76.*

O'BRIEN, E.J AND DIXON, A.S. (1995) "Reinforced and Prestressed Concrete Design." *Longman Scientific & Technical.*

PETERSON, C.W. (1990) "High performance parachutes." *Scientific American, May.*

PHOENIX, S.L. AND SKELTON, J. (1974) "Transverse Compressive Moduli and Yield Behavior of Some Orthotropic, High-Modulus Filaments." *Textile Research Journal, pp. 934-949.*

PILLER, B. (1973) "Bulked yarns." *Textile trade press, Manchester.*

RICHMOND, B.R. AND SHAM, S.H.R. (1994) "Present and future developments in cable supported bridge technology using new materials." *Cable–Stayed and Suspension Bridges, Deauville. AFPC. October, pp. 79-90*

SARKAR, A.D. (1980) "Friction and Wear." *Academic Press, London.*

SCHICK, M.J. (1975) "Surface characteristics of fibres and textiles. Part I." *Marcel Dekker, Inc. New York.*

SCHICK, M.J. (1977) "Surface characteristics of fibres and textiles. Part II." *Marcel Dekker, Inc. New York.*

SCHIERLE, G.C. (1990) "Prestressed trusses: analysis, behaviour and design." *Developments in Structural Engineering, E.&F.N.Spon, Chapmann and Hall, London.*

SINHA, B.P. (1990) "Behaviour of prestressed brickwork pocket type walls under lateral loading." *Developments in Structural Engineering, E.&F.N.Spon, Chapmann and Hall, London.*

SPEAKMAN, J.B. AND STOTT, E. (1931) *Journal of the Textile Institute, Vol. 44 T399.*

STIDD, J. (1990) "Mechanical properties of Technora aramid fiber and ropes." *Marine Technology Society '90 Proceedings, Washington.*

TAYLOR, D.S. (1955) *Journal of the Textile Institute, Vol. 46 p. 59.*

TECHNOMARE (1996) *Private correspondence with D. Kingston, Linear Composites Ltd.*

VAN LEEUWEN, IR.JOOP,H. AND VAN DER BURG, A.J. (1990) "Bending fatigue behaviour of Twaron aramid ropes." *Marine Technology Society '90 Proceedings, Washington.*

WU, H.C. (1990) "Modelling of fibrous assemblies — tensile and bending behavior." *Ph.D. thesis, M.I.T.*